A graphite particle-filled viscoelastic composite layer for active/passive constrained layer damping treatment of structural vibration

A
Thesis Submitted in
Partial Fulfillment of the Requirements
for the Degree of

DOCTOR OF PHILOSOPHY

by

Abhay Gupta
(Roll No: 156103004)

DEPARTMENT OF MECHANICAL ENGINEERING
INDIAN INSTITUTE OF TECHNOLOGY GUWAHATI,
GUWAHATI-781039, INDIA
November, 2021

Department of Mechanical Engineering
Indian Institute of Technology Guwahati
Guwahati-781039 INDIA

CERTIFICATE

It is certified that the work contained in the thesis entitled "**A GRAPHITE PARTICLE-FILLED VISCOELASTIC COMPOSITE LAYER FOR ACTIVE/PASSIVE CONSTRAINED LAYER DAMPING TREATMENT OF STRUCTURAL VIBRATION**" submitted by **Abhay Gupta (Reg. No. 156103004)** to the Indian Institute of Technology Guwahati for the award of the degree of Doctor of Philosophy has been carried out under my supervision in the Department of Mechanical Engineering, Indian Institute of Technology Guwahati. This work has not been submitted elsewhere for the award of any other degree or diploma.

26/11/2021

(Dr. Satyajit Panda)
Professor
Department of Mechanical Engineering
Indian Institute of Technology Guwahati
Guwahati-781039
INDIA

Declaration

I Abhay Gupta (Roll no: 156103004) declare that the present written submission is my thoughts in my own words. I have adequately cited and referenced the original sources, where others ideas have been involved. I also declare that I have adhered to all principles of academic honesty and integrity and have neither fabricated nor falsified any idea/data/fact/source in my submission. I understand that any violation of the above will be cause for disciplinary action by the Institute and can also evoke penal action from the sources which have thus not been properly cited or from whom proper permission has not been taken when needed.

(**Abhay Gupta**)

Date: 23/11/2021

Roll No: 156103004

Dedicated to

My grandparents, parents and teachers

Acknowledgments

The work presented in this thesis has been possible with my close association with several people. I would like to express my heartfelt gratitude and appreciation towards all those who made this Ph.D. thesis possible.

First and foremost, I would like to express my deepest sense of appreciation and thanks for my thesis supervisor Dr. Satyajit Panda, who has been a remarkable mentor for me. His continuous support, enthusiasm, inspiration, encouragement and never give-up attitude has made a deep impression on me. During the course of interaction for last six years at IIT Guwahati, I have learnt a lot from him including how to approach a problem in a systematic way. I am really pleased to be associated with a mentor like Dr. Satyajit Panda in my life.

I am also thankful to Prof. Debabrata Chakraborty, Prof. Anjan Dutta and Dr. Poonam Kumari for their careful review and suggestions in their capacity as doctoral committee members. I am also grateful to past and present departmental heads Prof. A. K. Dass, Prof. S. K. Dwivedy and Prof. S. Senthilvelan for providing me enough facilities during my Ph. D. program.

The financial support provided by the Ministry of Education, Government of India for research work at IIT Guwahati is gratefully acknowledged.

I express deepest gratitude to my mother Smt. Poonam Gupta, father Sri Ajay Kumar Gupta and brother Nitish for their constant love, support and encouragement towards my research work.

Finally, I would be the grateful to my fellows of research group Dr. Pavan, Dr. Ambesh, Dr. Manish, Shashi, Bharat, Nitin and Rahul for their continuous sleepless, unfatigued, energetic, and fruitful discussions.

Above all, I am thankful to the Almighty God.

Abhay Gupta

Date: 23/11/2021

(**Abhay Gupta**)

Abstract

In this dissertation, a viscoelastic particulate composite (VEPC) is proposed with the objective of improved constrained layer damping treatment of structural vibration. This VEPC is comprised of micro-sized graphite particles that are dispersedly distributed within the Butyl rubber matrix. The effective material properties of this VEPC are estimated using a differential scheme and the elastic-viscoelastic correspondence principle. The corresponding results reveal increased effective storage modulus and decreased effective loss factor of a viscoelastic medium for the inclusion of graphite particles. With these material characteristics of the VEPC, its damping capability is first investigated in the constrained layer damping (CLD) treatment of a sandwich beam where the damping layer lies at the core. A finite element (FE) model of the sandwich beam is derived for analysing the passive damping in the beam. This analysis reveals that the passive damping in the sandwich beam increases significantly for the inclusion of graphite particles within the viscoelastic core, and also an optimal volume fraction of inclusion (VFI) corresponding to the maximum damping in the sandwich beam appears. Further study on the optimal utilization of VEPC patches within the core of the sandwich beam reveals a minimal change of weight of the overall beam for the replacement of patches of conventional viscoelastic material by VEPC patches while this replacement yields a significant improvement of passive damping in the sandwich beam.

Next, the VEPC layer is applied in the CLD treatment of parametric instability of a beam operating under the periodically varying dynamic axial compressive load. The beam is composed in the layered configuration where the viscoelastic damping layers are constrained between the substrate layers. The stability analysis of the layered beam is performed by deriving its FE model based on the layer-wise deformation theory, and the results reveal significantly improved dynamic stability of the layered beam for an increase in the VFI of graphite particles. However, it occurs up to a certain value of increasing VFI where an optimal value of VFI arises for the maximum improvement of dynamic stability. The inclusion not only improves the dynamic stability of the beam but also provides significantly enhanced static stability of the same beam. Also, the VFI acts as a tuning parameter to control the dynamic instability of the layered beam by shifting the parametric instability region aside from the operating frequency range of interest.

The same VEPC layer is subsequently utilized in the active constrained layer damping (ACLD) treatment of a plate, where the VEPC layer is constrained by an extensional mode piezoelectric actuator layer. This actuator layer is activated according to the velocity feedback control law, and a closed-loop FE model of the overall plate is derived for the analysis. The results reveal that the inclusion of graphite particles not only causes an improved transfer of active action from the piezoelectric layer to the substrate plate but also enhances the energy-dissipation capability of the constrained viscoelastic layer. It is found that the maximum transfer of active action and the maximum passive damping capability of the VEPC layer arise almost at the same VFI. So, an optimal VFI is obtained for significantly improved ACLD treatment of the overall plate.

The usefulness of the VEPC layer in the shear actuation-based active-passive hybrid damping treatment of structural vibration is also studied. This study is performed through the flexural vibration analysis of a sandwich plate-strip where the core is made of a laminate of active layers and VEPC layers in two different stacking sequences. The active layers are comprised of shear mode piezoelectric actuator patches that are activated according to a shear-based velocity feedback control strategy. The analysis is performed by deriving a closed-loop FE model of the sandwich plate-strip, and it reveals that the hybrid damping is significantly dependent on the stacking sequence of active and passive damping layers at the core. However, the inclusion of graphite particles not only provides augmented passive damping but also causes enhanced transfer of shear actuation force from the active layers to other layers. As a result, a significantly improved shear actuation-based hybrid active-passive damping is achieved due to the inclusion. The effectiveness of this hybrid damping treatment is also presented by configuring the active and passive damping elements within the core in an optimal manner.

Finally, the performance of the present VEPC layer in the CLD/ACLD treatment is compared to that for an existing viscoelastic composite by the name of 0-3 viscoelastic composite. The overall study in this thesis presents a novel viscoelastic particulate composite layer for the improved CLD/ACLD treatment of structural vibration.

Table of Contents

List of Figures

List of Tables

List of Symbols

List of symbols used throughout the thesis are listed. List of symbols less frequently used, or that have different meaning or different forms at different contexts, are defined where they are used.

E	Young's modulus
E'	Storage Young's modulus
E''	Loss Young's modulus
G	Shear modulus
K	Bulk modulus
v	Poisson's ratio
ρ	Mass density
ϕ	Volume fraction of inclusion
η_c	Viscoelastic material loss factor
N_0	Static axial compressive load
N_{cr}	Critical buckling load
λ	Dynamic load parameter
N_F	Number of harmonic terms
r_p	Static load parameter
w_I	Width of instability region
L	Length of the sandwich beam/plate-strip
a	Length of the plate
b	Width of the plate/plate-strip
v_p	Volume fraction of actuator patches
h_f	Thickness of face layer of sandwich beam
h_v	Thickness of viscoelastic layer
k	Number of layers
k_d	Feedback control gain
$\boldsymbol{I}$	Identity matrix
$\boldsymbol{O}$	Null matrix
$\boldsymbol{L}$	Operator matrix
$\boldsymbol{K}$	Stiffness matrix
$\boldsymbol{M}$	Mass matrix

$\boldsymbol{N}$	Shape function matrix
$\boldsymbol{T}_t, \boldsymbol{T}_r$	Transformation matrices
$\boldsymbol{d}^e$	Elemental nodal displacement vector
$\boldsymbol{P}_M^e$	Elemental mechanical load vector
$\boldsymbol{P}_E^e$	Elemental electro-elastic load vector
$\boldsymbol{d}$	Global general displacement field vector
$\boldsymbol{D}$	Electrical displacement field vector
$\boldsymbol{E}$	Electric field vector
$p(t)$	Transverse harmonic load
δT_K	Variation of total kinetic energy
δT_P	Variation of total potential energy
u , v , w	Displacements components in coordinate directions
V	Applied voltage
$V_{\max}$	Maximum control voltage
$W_{\max}$	Maximum transverse displacement amplitude
$\dot{w}$	Sensing point velocity
$\boldsymbol{X}$	Global nodal displacement vector
W_f	Resonant displacement-amplitude
$\boldsymbol{\varepsilon}$	Strain vector
$\boldsymbol{\sigma}$	Stress vector
ω	Operating frequency
ω_n	Fundamental natural frequency of vibration
η_i	Total loss factor for i^{th} mode of vibration
n_g	Number of graphite wafers along the x and y directions
n_p	Number of shear-actuated piezoelectric patches
$u^k / v^k / w^k$	Displacement along $x / y / z$ direction within k^{th} layer
$u_0 / v_0 / w_0$	Displacement along $x / y / z$ direction at any point on reference surface
$\varepsilon_x / \varepsilon_y / \varepsilon_z$	Normal strain along $x / y / z$ direction
$\varepsilon_{xy} / \sigma_{xy}$	In-plane shear strain/stress in the xy-plane

$\sigma_{xz} / \sigma_{yz}$	Transverse shear stress in xz / yz plane
$\boldsymbol{\sigma}_b / \boldsymbol{\sigma}_s$	Bending/shear stress vector
$\boldsymbol{C}_b^k / \boldsymbol{C}_s^k$	Bending/shear stiffness matrix for k^{th} layer
$\sigma_x / \sigma_y / \sigma_z$	Normal stress along $x / y / z$ direction
$\varepsilon_{xz} / \varepsilon_{yz}$	Transverse shear strain on xz / yz plane
$\boldsymbol{\varepsilon}_b / \boldsymbol{\varepsilon}_s$	Bending/shear strain vector

Superscript:

e	Element
i	A State of deformation
R	Real
I	Imaginary
T	Transpose

Subscript:

b	Bending
s	Shear
v	Viscoelastic
d	Particle inclusion
m	Matrix phase

Abbreviations:

UCLD	Unconstrained layer damping
CLD	Constrained layer damping
PCLD	Passive constrained layer damping
ACLD	Active constrained layer damping
FE	Finite element
FSDT	First-order shear deformation theory
VEPC	Viscoelastic particulate composite
VEC	Viscoelastic composite
VEM	Viscoelastic material
VFI	Volume fraction of inclusion

Chapter 1

Introduction

Viscoelastic materials possess an important property of energy dissipation during their time-dependent deformation, and it is immensely exploited in damping out the vibration of thin-walled structures. Generally, these damping materials are attached to a thin-walled structure in two different layered configurations. In the first configuration, a viscoelastic layer is attached to the surface of a host structure, and it is commonly known as the unconstrained layer damping (UCLD) treatment (El-sabbagh and Baz, 2014; Lee and Hwang, 2004; Narayanan et al., 1981; Roy and Ganesan, 1993; Ungar and Edward, 1964). However, in the second layered configuration, a viscoelastic layer is constrained by a stiff layer against the host structure surface so that it is commonly called the constrained layer damping (CLD) or passive constrained layer damping (PCLD) treatment (Ferreira et al., 2013; Huang et al., 2016; Kerwin, 1959; Patel and Ganapathi, 2001 Pradhan et al. 2016; Ramesh and Ganeshan, 1994; Swallow, 1939; Zhang et al., 2020). However, the energy dissipation capability of a viscoelastic material reduces in its operation at low frequency (Azvine et al., 1995; Trindade, 2011). So, the utilization of the viscoelastic materials along with the piezoelectric actuators has been recommended in a good number of research reports (Baz and Ro, 1993; Lam et al., 1997; Plattenburg et al., 2015; Shi et al., 2004; Trindade, 2011) to achieve the structural vibration control in a wide range of the frequency, and it leads to different kinds of hybrid active-passive damping treatments (Arafa and Baz, 2000; Baz and Ro, 1995; Gentilman et al., 1994; Ghoneim, 1993). Among these different hybrid damping treatments, active constrained layer damping (ACLD) (Baz and Ro, 1995) is the most popular one, as a great deal of research on this kind of damping treatment has been addressed in the literature.

In this introductory chapter, first, a brief introduction is presented on the viscoelastic materials and piezoelectric materials. Next, a literature review on the development of UCLD, PCLD, and ACLD treatments is presented. On the basis of this literature review, the scope of the present research has been identified, and the objectives of the present thesis are furnished. The contributions in the field of viscoelastic damping of structural vibration made towards the preparation of this

dissertation have been delineated thereafter. In the end, the organization of the thesis is outlined.

1.1 Viscoelastic materials

Viscoelastic materials are homogeneous and isotropic materials, which exhibit both the elastic and viscous damping properties during their time-dependent deformation. These materials are composed of long intertwined and cross-linked molecular chains, where each chain contains thousands or millions of atoms. However, the position of some part of the long polymer chain changes during the deformation of the material, and the corresponding rearrangement of the part of polymer chain results in time-dependent strain of the material, which is known as the creep phenomenon. However, a back stress develops during the rearrangement of the part of polymer chain. When the magnitude of this back stress becomes equal to that of the applied stress, the material does not undergo further creep. The same back stress also causes the material to return to its original form once the applied stress is relieved. Here, the creep phenomenon yields viscous properties of the material, while the recovery of the same material to its original form signifies elastic property, and thus this material is commonly known as a viscoelastic material.

The linear constitutive behaviour of an elastic material can be described by the linear stress-strain curve, as shown in Fig. 1.1 by the line aob. However, in the case of a viscoelastic material, the aforesaid creep phenomenon arises along

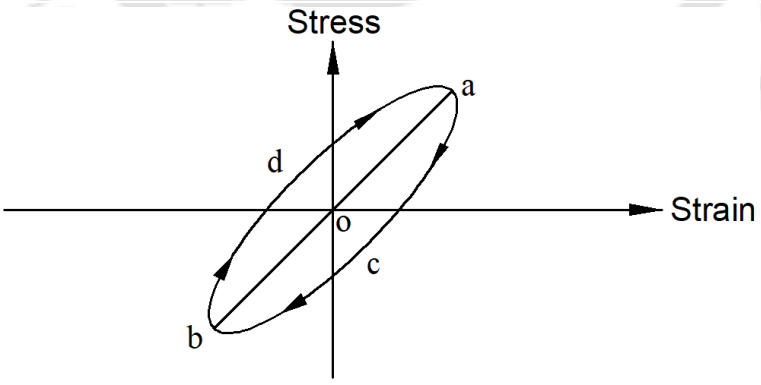

Fig. 1.1 Stress-strain plot for a viscoelastic material under the periodic load at low-stress limit.

with the elastic deformation so that the stress-strain curve appears in the form of the ellipse for every cycle of the periodically varying stress/strain, as shown in Fig. 1.1 by the curve acbd. This enclosed elliptical curve is commonly known as the hysteresis loop for viscoelastic materials, where the area within the enclosed curve denotes the dissipated-energy per unit volume of the material over every cycle of periodic stress/strain (Jones, 2001). In Fig. 1.1, the slope of the major axis of the ellipse is the measure of the stiffness or modulus of elasticity of a viscoelastic material, while the ratio of minor and major axes of the same ellipse is a measure of the dissipated-energy per cycle of periodic stress/strain. This dissipated-energy per cycle of periodic stress/strain is identified as the material damping, and it is denoted by different parameters, namely loss factor, quality factor, damping ratio, etc. Of these, the commonly used one is the loss factor that is defined by the ratio of the dissipated-energy per radian (area of hysteresis loop/ 2π) and the peak strain energy in a cycle of periodic stress/strain (Ungar and Kerwin, 1964; Thomson, 1993).

Generally, the properties of a viscoelastic material vary with the operating frequency and temperature (Christensen 1982; Lakes 1998, 2009). Figures 1.2(a) and 1.2(b) illustrates the effect of temperature on the storage modulus (E') and loss factor (η_c), respectively, at a constant frequency. Here, the constitutive behaviour of a viscoelastic material within a wide range of temperature is defined by three regions, namely glassy, transition and rubbery regions. In the glassy region or low temperature region, the storage modulus (E') appears with a high magnitude and decreases slowly with the increasing temperature, while the loss factor (η_c) increases (Fig. 1.2(b)). However, at the high temperature region, the rubber-like behaviour of a viscoelastic material appears, where both the storage modulus (E') and loss factor (η_c) of the material decreases with the increasing temperature. At the temperature region corresponding to the transition from glassy to rubbery state, the peak value of the loss factor (η_c) arises (Fig. 1.2(b)) (Christensen 1982; Lakes 1998, 2009; Nashif et al. 1985). However, the influence of the operating frequency on the constitutive behaviour of a viscoelastic material is demonstrated in Figs. 1.3(a) and 1.3(b) through the variations of the storage modulus (E') and loss factor (η_c), respectively, with the frequency. At the low frequency region, a viscoelastic material behaves like a rubber-like material having a low value of the material loss factor (η_c). However, the stiffness of the

viscoelastic material increases with the increasing frequency resulting in the transition from rubbery to glassy state (Fig. 1.3(a)), and the material loss factor (η_c) appears with its maximum value within this transition zone (Fig. 1.3(b)).

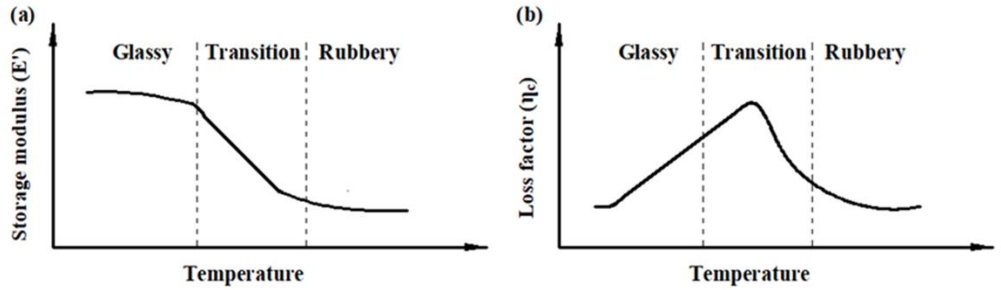

Fig. 1.2 Effect of temperature on the (a) storage modulus (E') and (b) material loss factor (η_c) of a viscoelastic material.

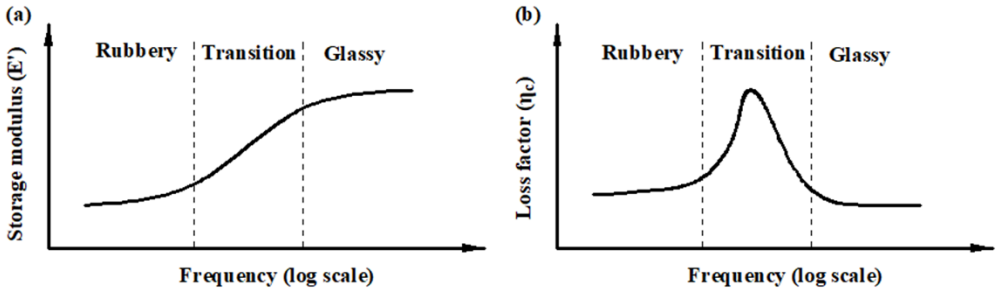

Fig. 1.3 Effect of frequency on the (a) storage modulus (E') and (b) material loss factor (η_c) of a viscoelastic material.

The commonly used viscoelastic materials in structural damping applications are Paracril-BJ, Polymer Blend, butyl rubber, Viton-B, Styrene-butadiene rubber (SBR), Soundcoat N5, 3M-467, LD-400, etc. (Jones, 2001). For defining the constitutive behaviour of these viscoelastic materials, various mathematical models are available in the literature like Maxwell model, Kelvin–Voigt model, Zener model, Poynting–Thomson model, augmenting thermodynamic fields (ATF) model, anelastic displacement field (ADF) model and Golla-Hughes-McTavish (GHM) model (Christensen 1982; Flügge 1967; Golla and Hughes, 1985; Haddad 1995; Lakes 1998, 2009; Lesieutre and Bianchini,1995; Lesieutre and Mingori, 1990; McTavish and Hughes, 1993; Zener 1948). These viscoelastic material models are usually used for modelling the material behaviour in the time-domain and extensively utilized for the transient analysis of viscoelastic

structures. However, the frequency domain analysis of similar structures is usually carried out using the complex stiffness model of the viscoelastic materials. This viscoelastic material model is established through the dynamic test of the material, where a viscoelastic material is considered to operate under a sinusoidal stress. The corresponding sinusoidal strain appears with the same frequency but has a retarded phase (δ) (Chawla and Meyers, 1999). These stress and strain can be written in terms of their amplitudes (ε_0 and σ_0), operating frequency (ω) and phase difference (δ) as (Chawla and Meyers, 1999),

$$\varepsilon = \varepsilon_0 \exp j(\omega t),\ \sigma = \sigma_0 \exp j(\omega t + \delta),\quad j = \sqrt{-1} \tag{1.1}$$

The stress and strain can also be expressed according to Hooke's law as,

$$E^* = \frac{\sigma}{\varepsilon} = \frac{\sigma_0}{\varepsilon_0}(\cos\delta + j\sin\delta) = (E' + jE'') \tag{1.2}$$

where, E' and E'' denote the real and imaginary counterparts, respectively, of the complex modulus (E^*). These real (E') and imaginary (E'') counterparts are also known as storage and loss moduli, respectively. The ratio of loss modulus (E'') to storage modulus (E') is denoted as the material loss factor (η_c). So, the complex constitutive relation (Eq. (1.2)) for a linear isotropic viscoelastic material can also be written as follows (Tomlinson, 1990),

$$E^* = (E' + jE'') = E'(1 + j\eta_c) \tag{1.3}$$

$$G^* = (G' + jG'') = G'(1 + j\eta_c),\ E' = 2(1+\nu G') \tag{1.4}$$

In Eqs. (1.3) and (1.4), the symbols G and ν denote shear modulus and Poisson's ratio, respectively. However, the material properties of a viscoelastic material are conventionally expressed in terms of E' and η_c through the temperature-frequency nomogram that can be generated following a simple methodology based on the principle of temperature-frequency equivalence (Jones, 2001; Nashif, 1985).

1.2 Piezoelectric materials

Piezoelectric materials belong to a special class of ceramics that possess an important property of energy conversion from mechanical to electric field or vice versa. This property makes them valuable ceramics in the development of sensors and actuators particularly in the vibration or shape control of structural elements.

In 1880, Curie brothers (Jacques and Pierre) first demonstrated the piezoelectricity phenomenon in natural materials such as quartz and Rochelle salt. It was observed that, when the mechanical strain is imposed on these materials, they produce electrical output. This property is known as the direct piezoelectric effect. Further, in 1881, Gabriel Lippmann theoretically proposed the converse piezoelectric effect, where an electrical input produces mechanical strain in these materials. However, the existence of converse piezoelectric effect in the piezoelectric crystals was experimentally confirmed by Curie brothers. The piezoelectric materials were first introduced in the practical application of sonar devices during World War I. Over the next few decades, some new piezoelectric materials and their applications were explored. During World War II, various research groups in the US, Russia, and Japan discovered a new class of synthetic materials, known as ferroelectrics. These synthetic materials exhibit a significantly greater piezoelectric effect than those in natural piezoelectric materials. Some examples of these synthetic piezoelectric materials are lead zirconate titanate (PZT), barium titanate, lead niobrate, lead lanthanum zirconate titanate (PLZT), ammonium dihydrogen phosphate, lithium sulfate, polyvinylidene fluoride (PVDF or PVF2), etc. (Tzou et al., 2004).

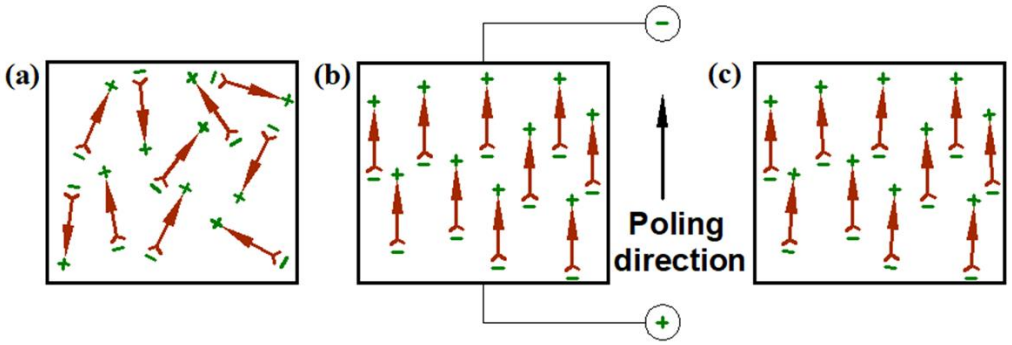

Fig. 1.4 Schematic diagrams of a typical domain of piezoelectric material, (a) before polarization, (b) polarization under the externally applied electric field, (c) remnant polarization after the removal of the externally applied electric field.

The synthetic piezoelectric materials are the isotropic materials at their raw stage where molecular dipoles are randomly oriented with zero dipole density or polarization (Fig. 1.4(a)). However, under the externally applied electric field (>2000 V/mm) at a high temperature, molecular dipoles are aligned in the direction of the applied electric field, and this direction is called as poling direction

(Fig. 1.4(b)). On the removal of the externally applied electric field, the alignment of a major part of the molecular dipoles does not alter resulting in a remanent polarization (P_R) in the material. The material with this remanent polarization exhibits piezoelectric properties (Fig. 1.4(c)). However, this phenomenon of polarization (P) can be expressed through the applied electric field (E) vs polarization (P) hysteresis loop, as shown in Fig. 1.5(a).

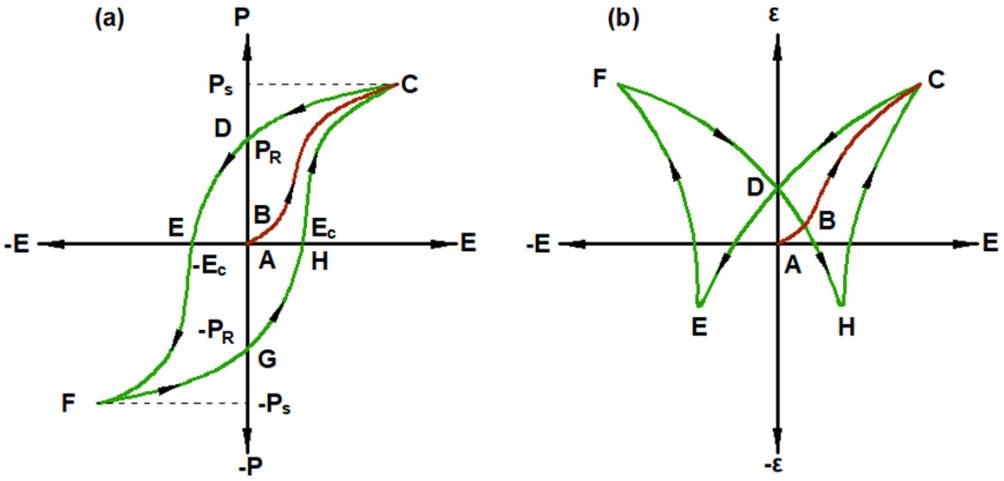

Fig. 1.5 (a) Electric field (E) vs polarization (P) hysteresis loop, (b) electric field (E) vs strain (ε) butterfly curve for a piezoelectric material.

Figure 1.5(a) illustrates the increase in polarization linearly from its zero-value with the increasing applied electric field (line AB). For further increase in the applied electric field, the polarization switches towards the applied electric field leading to nonlinear polarization response with the continuous increase in the applied electric field (curve BC, Fig. 1.5(a)). This nonlinear polarization occurs up to a point C, called as saturation (P_S) point. If the applied electric field decreases from this point (C), some of the molecular dipoles switch back although the polarization remains nonzero after the complete removal of the applied electric field. The polarization at this stage known as remanent polarization (P_R, Fig. 1.5(a)). However, zero polarization can be obtained with the negative electric field. The applied electric field for the zero polarization is commonly known as coercive electric field ($-E_c$), as shown in Fig. 1.5(a) (point E). Further decrease in the applied electric field causes a new alignment of dipoles as well as saturation of polarization ($-P_s$, Fig. 1.5(a)).

In parallel to the electric field (E) vs polarization (P) hysteresis loop, the strain (ε) of the piezoelectric material also varies with the applied electric field (E), and the corresponding electric field (E) vs strain (ε) curve is known as butterfly curve, as shown in Fig. 1.5(b). In Fig. 1.5(b), the stain increases and reaches to the saturation point C through the path ABC for the increase in the applied electric field. As the applied electric field decreases from point C, the material expands until a practical strain limit (F, Fig. 1.5 (b)). However, for the practical application of a piezoelectric ceramic as the material of sensor/actuator, the applied electric field is usually kept below the coercive electric field (point E or H in Fig. 1.5(a)). Otherwise, depoling takes place leading to the material behaviour differently. In addition to this restriction over the applied electric field in the application of piezoelectric ceramics for sensor or actuator, the operating temperature must not exceed a certain limit that is usually known as the Curie temperature (Chaudhry and Rogers, 1995).

The linear constitutive relations for piezoelectric materials under constant temperature can be expressed in terms of the field parameters like stress ($\boldsymbol{\sigma}$), strain ($\boldsymbol{\varepsilon}$), electric displacement ($\boldsymbol{D}$) and electric field (E). On the basis of these field parameters ($\boldsymbol{\sigma}, \boldsymbol{\varepsilon}, \boldsymbol{D}, E$), thermodynamic potentials like internal energy (U), enthalpy (H), Helmholtz free energy (F) and Gibbs free energy (G) can be defined, as given in Eq. (1.5) (Chee, 2000).

$$dH = \boldsymbol{\sigma} d\boldsymbol{\varepsilon} - \boldsymbol{D} d\boldsymbol{E}, \quad dU = \boldsymbol{E} d\boldsymbol{D} + \boldsymbol{\sigma} d\boldsymbol{\varepsilon},$$
$$dF = \boldsymbol{E} d\boldsymbol{D} - \boldsymbol{\varepsilon} d\boldsymbol{\sigma}, \quad dG = -\boldsymbol{\varepsilon} d\boldsymbol{\sigma} - \boldsymbol{D} d\boldsymbol{E} \tag{1.5}$$

These piezoelectric constitutive formulations (Eq. (1.5)) are utilized depending on the natural variables in an application of the material. In the case of the structural application, the natural variables are usually considered as strain ($\boldsymbol{\varepsilon}$) and electric field (E). The corresponding constitutive relations can be expressed using the thermodynamic potential H as (Chee, 2000),

$$\boldsymbol{\sigma} = \boldsymbol{C}\boldsymbol{\varepsilon} - \boldsymbol{e}\boldsymbol{E} \tag{1.6}$$

$$\boldsymbol{D} = \boldsymbol{e}^{\mathrm{T}}\boldsymbol{\varepsilon} + \in \boldsymbol{E} \tag{1.7}$$

In Eqs. (1.6)-(1.7), $\boldsymbol{C}$ is the stiffness matrix for a constant electric field (E); $\boldsymbol{e}$ is the piezoelectric matrix for the constant strain ($\boldsymbol{\varepsilon}$) or the constant electric field (E); $\in$ is the electrical permittivity matrix for the constant strain ($\boldsymbol{\varepsilon}$). Here, Eq. (1.6) represents the converse piezoelectric effect, while the direct piezoelectric effect is represented by Eq. (1.7). These converse (Eq. 1.6) and direct (Eq. 1.7)

piezoelectric effects are utilized in the development of piezoelectric actuators and sensors, respectively, for structural applications (Thakkar and Ganguli, 2004b).

However, the practical piezoelectric actuators are commonly made in the form of thin wafer, as shown in Fig. 1.6 where a piezoelectric wafer is poled (P) either vertically (Fig. 1.6(a)) or horizontally (Fig. 1.6(b)). These piezoelectric actuators are usually activated by the application of external electric field (E_z) through their top and bottom fully electrode surfaces. Here, for the vertically poled piezoelectric wafer (Fig. 1.6(a)), the primary actuation forces appear as the electrically induced normal stresses in the plane of the wafer. So, it is called as the extensional mode piezoelectric actuator. In other type, i.e. for the horizontally poled piezoelectric wafer (Fig. 1.6(b)), the primary actuation forces appear as the electrically induced shear stresses in the transvers (xz or yz) planes of the wafer, and thus it is known as the shear mode piezoelectric actuator (Benjeddou et al., 1997; Sun and Zhang, 1995).

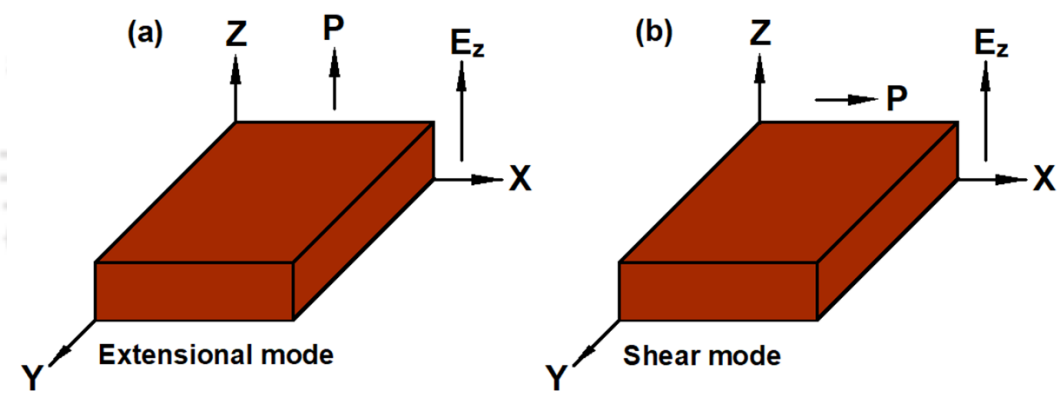

Fig. 1.6 Schematic diagrams of the (a) extensional mode and (b) shear mode piezoelectric actuators.

1.3 Passive damping of structural vibration using viscoelastic materials

The energy-dissipation property of viscoelastic materials is extensively exploited in attenuation of structural vibration, where good passive damping can be achieved for vibration control at a low cost. However, in this context, viscoelastic damping materials are utilized in different forms like tuned damper, edge damping, free/unconstrained layer damping (UCLD), constrained layer damping (CLD), etc. (Grootenhuis, 1970; Nakra, 2000). Among these various techniques, the UCLD and CLD treatments are the popular ones to control the bending mode

of vibration of thin-walled flexible structures. A literature review on these UCLD and CLD treatments is carried out and presented in the following sections.

1.3.1 Unconstrained layer damping (UCLD) treatment

In the UCLD treatment, a viscoelastic damping layer is freely attached to the surface of the host structure (Fig. 1.7(a)). As this layered structure undergoes bending mode of vibration, the damping in the structure arises through the extensional/compressional deformation of the viscoelastic layer (Fig. 1.7(b)). The concept of UCLD treatment was proposed by Oberst and Frankenfeld (Oberst and Frankenfeld, 1952). Later, this concept of viscoelastic damping was utilized for vibration suppression of various thin-walled structures (Nakra, 1984; Nakra, 1998; Rao, 2003; Sun and Kari, 2010). However, Ungar and Edward (1964) reported that the damping performance of the UCLD treatment can be dependent on the thickness deformation of the viscoelastic layer. This additional mechanism of damping in the UCLD treatment may appear in the case of a thick

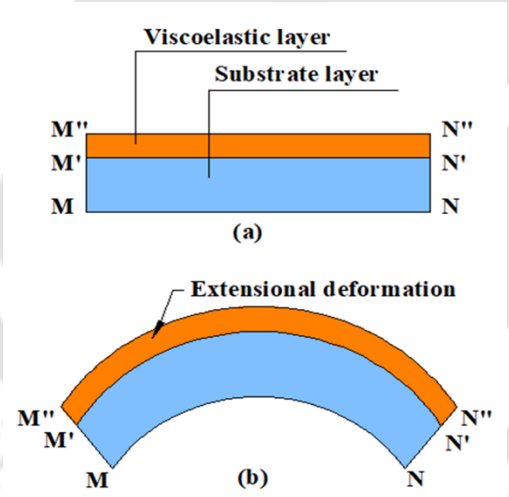

Fig. 1.7 Schematic diagrams of the (a) undeformed and (b) deformed substrate layer integrated with a viscoelastic layer (UCLD treatment).

viscoelastic layer. Besides, the shear deformation of the viscoelastic layer also occurs but its contribution to the damping in the layered structure is significantly lesser than that by the extensional/compressional strain (Reddy, 1979). Therefore, the damping in the UCLD treatment appears mainly through the alternate extension and compression of the viscoelastic layer.

Narayanan et al. (1981) presented the UCLD treatment of free vibration of a beam with thin-walled hollow cross-section, where the transverse vibration and the coupled bending-torsion oscillation of the beam are analysed. It was reported that the modal loss factor for coupled bending-torsion oscillation depends on the mode number; however, at lower modes, the modal loss factor for the coupled bending-torsion oscillation is higher than that for the transverse vibration mode. Okazaki et al. (1994) analysed the passive damping in a cylindrical shell integrated with the UCLD treatment, where they considered both the transverse shear and extensional deformations of the viscoelastic layer. This study reveals the influence of the transverse strains in the viscoelastic layer on the passive damping in the cylindrical shell, especially for a thick viscoelastic layer. Ravi et al. (1996) proposed a computationally efficient formulation for the analysis of partial or full UCLD treatment. In the same line, Cortes et al. (2008) presented a mathematical model of a beam integrated with a thick viscoelastic damping layer using fractional-order derivative viscoelastic constitutive model. However, a comparative study over different analytical methods was presented by Mead (2007) for the theoretical estimation of passive damping in the UCLD treatment of plate and beam structures. Zarraga et al. (2019) studied the dynamic characteristics of a plate integrated with a thick viscoelastic damping layer and reported that the mathematical model based on Kirchhoff–Love thin plate theory can estimate the passive damping in the UCLD treatment accurately. Recently, Sun et al. (2018) carried out an analysis of the UCLD treatment of plate vibration and suggested to consider frequency dependent properties of the viscoelastic layer in the UCLD treatment, especially for the vibration response around a resonant frequency.

The aforesaid studies on the UCLD treatment of structural vibration is carried out by taking the viscoelastic damping materials in the layer form. However, the same damping treatment is also utilized with different geometrical and material configurations, particularly for achieving its enhanced passive damping capability. Mead and Pearce (1961) achieved superior damping in a UCLD treated structure by providing the viscoelastic damping material around the location of the maximum bending moment within the structure. Markuš (1976) presented the UCLD treatment for a cylindrical shell, where the viscoelastic material is attached to the inner or outer surface of the shell. It was observed that the outside coated shell possesses significantly higher passive damping than that

in the inside coated shell. Lunden (1979) demonstrated an optimal distribution of the UCLD material over the length of a beam element for effective attenuation of resonant vibration amplitudes. In the same line, Yildiz and Stevans (1985) also demonstrated the optimal region in a plate to attach the viscoelastic material for the UCLD treatment. Parthasarathy et al. (1985) reported superior damping by the conversion of UCLD treatment from full to the partial one provided that the mass of damping material would not be altered and the damping material in the partial one is to be attached to the host structure surface following the locations of high extensional deformation. Roy and Ganesan (1993, 1996) reported improved attenuation of vibration amplitude of plates by increasing the thickness of the viscoelastic damping layer in the partial UCLD treatment.

Cheng and Lapointe (1995) studied partial UCLD treatment of a panel structure and reported that the performance of the damping treatment could be increased by optimal cutting shapes of the viscoelastic layer. In this line, Lumsdaine and Scott (1998) used sequential quadratic programming (SQP) algorithm to obtain the optimal design of the viscoelastic layer and reported significant damping in the UCLD treated laminated beams/plates. Lee and Hwang (2004) presented an optimal UCLD configuration for improved damping in beams. El-sabbagh and Baz (2014) presented topology optimization of a UCLD treated plate to obtain the optimal distribution of the viscoelastic material over the host plate-surface towards the improved damping. Liang et al. (2020) used a stand-off layer between the surface of a cantilever beam and the free viscoelastic damping layer to enhance the damping capability of the UCLD treatment.

1.3.2 Constrained layer damping (CLD) treatment

The UCLD treatment is a light-weight and low cost passive damping treatment. It can also be installed easily over the surface of a host structure. However, for better utilization of the viscoelastic damping materials, a stiff constraining layer is attached to the free surface of the viscoelastic layer, as shown in Fig. 1.8(a). As this layered structure undergoes bending mode of vibration, the constrained viscoelastic layer mainly undergoes transverse shear deformation (Fig. 1.8(b)). The corresponding damping in the layered structure is significantly better than the passive damping in the UCLD treatment (Grootenhuis, 1970). This arrangement of viscoelastic damping is commonly known as constrained layer damping (CLD). It is also called the passive constrained layer damping (PCLD) since a passive

constraining layer is used to constrain the viscoelastic layer for achieving its good transverse shear deformation during the bending deformation of the layered structure. Because of the significantly greater damping in the CLD treatment compared to that in the UCLD treatment, the CLD treatment is widely utilized for vibration attenuation of many engineering structures/systems. Some of these engineering structures/systems may be mentioned here as outlet guide vane in turbines (Tomlinson, 1990), compression blades in turbines (Sun and Kari, 2010), machine tool (Marsh and Hale, 1998; Shi et al., 2017), spinning disks (Seubert et al., 2000), energy absorbent devices, blast protective military equipment, wind energy system, radio frequency antenna, biomedical devices, etc. (Birman and Kardomatea, 2018; Herrmann et al., 2005). The CLD treatment is also utilized in the automobile and aircraft industries for door panels, floor panels, brake covers, skin, stringers, frames of fuselage section in commercial aircraft (Rao, 2003) and flutter suppression of aeronautical panels (Cunha-Filho et al., 2016).

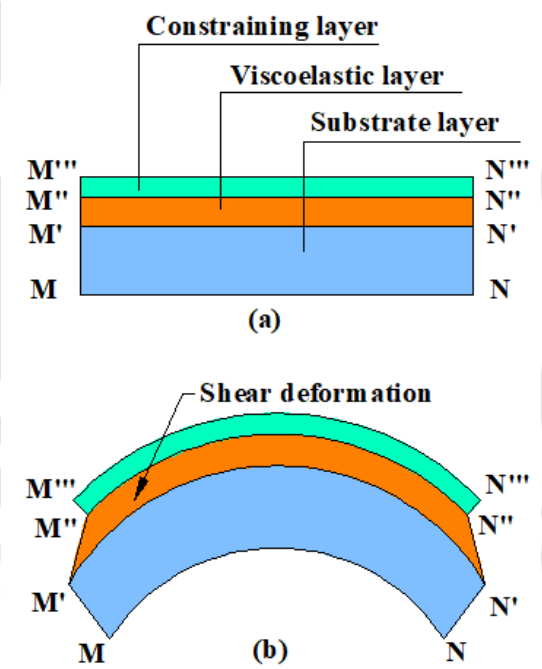

Fig. 1.8 Schematic diagrams of (a) undeformed and (b) deformed substrate layer integrated with a CLD layer.

1.3.2.1 Literature on the theoretical/experimental analysis of CLD treatment

The concept of PCLD/CLD treatment was introduced by Swallow (1939), while Kerwin (1959) first reported its mathematical formulation. At the same time, Ross et al. (1959) proposed a mathematical model of the CLD treatment where the relationship among the motions of component layers in the CLD treatment and the modal loss factor was established. Further, Mead and Markus (1969) derived a six-order differential equation in terms of the transverse deflection of a sandwich beam with the viscoelastic core. In the same line, many other works are also available in this early stage of development of CLD treatment (Jones and Salerno, 1966; Lu et al., 1979; Pan, 1969; Yin et al., 1967; Yu, 1963). However, Douglas and Yang (1978) reported negligibly small influence of compressional deformation of the constrained viscoelastic layer on the passive damping in a sandwich beam, where the viscoelastic layer lies at the core of the sandwich beam. Further, Sylwan (1987) suggested to consider both the transverse shear and compressional deformations of the viscoelastic layer in the estimation of passive damping in the CLD treated beams. Later, Huang et al. (2001) suggested that the accuracy in estimation of damping can be improved by the consideration of thickness deformation of the constrained viscoelastic layer, especially for a thick damping layer. However, in this concern of theoretical estimation of passive damping in the CLD treatment, a great deal of research has been carried out by many researchers leading to various analytical models of layered structures having constrained viscoelastic damping layers (Alam and Asnani 1984a, 1984b; Cai et al., 2004; Meunier and Shenoi, 2003; Xiang et al.; 2008; Yang, 2015). Cao et al. (2011) introduced the wave propagation approach to solve the vibration problem of a PCLD treated cylindrical shell and reported that it is a simple and straight forward approach compared to other existing approaches. Hamdaoui et al. (2019) demonstrated a discrete adjoint-based gradient method to estimate viscoelastic properties of a sandwich beam with the viscoelastic core. Jin et al. (2015) presented the benchmark solutions for the damping characteristics of a PCLD treated shell with restraints and intermediate ring supports, where the analytical model of the shell is derived using modified Fourier-Ritz method. Zhai et al. (2020) also presented the benchmark solutions for free vibration of a five-layered composite sandwich plate with two constrained viscoelastic layers, where the governing equation of motion is solved using the closed-form Navier method. Zhai et al. (2019) also used the closed-form Navier method to solve the equation of

motion of a doubly-curved sandwich shell and addressed appropriate values of the geometrical and material parameters of the shell in having maximum passive damping. Further, Wang et al. (2020) demonstrated the effects of geometrical and material parameters of a co-cured composite structure on the passive damping in the overall structure, where the layered structure is composed of multiple constrained viscoelastic membranes, and the corresponding analytical model is derived based on the zig-zag theory and Rayleigh-Ritz method.

Besides the aforesaid various analytical models, finite element (FE) method has also been utilized extensively to analyse dynamic characteristics of the CLD treated structures. Johnson and Kienholz (1982) presented FE models of three-layered beam, plate, and ring structures with the constrained viscoelastic layer and demonstrated the accuracy of the FE model in estimation of damping with reference to the analytical results. They introduced the modal strain energy method (MSE) for numerical estimation of damping in a CLD treated structure. However, Shin and Maurer (1991) used this MSE method in the FE framework for analysing the damping in a CLD treated plate and reported that the MSE method might overestimate the damping in the plate with reference to experimental results. Similar studies were also carried out by Imaino and Harrison (1991) and Wilson et al. (1992). Sun et al. (1990) derived an FE model of a CLD treated laminated beam where offset-beam elements were introduced to estimate the shear deformation of the constrained viscoelastic layer. The accuracy of this FE model in estimation of damping was also verified with reference to the experimental results. Ramesh and Ganeshan (1994) proposed an FE modal of a CLD treated cylindrical shell and demonstrated the variation of the modal loss factor with the circumferential modes. The same authors (Ramesh and Ganeshan, 1995) also suggested to consider the in-plane extensional deformation of the constrained viscoelastic layer for improved estimation of damping characteristics of the CLD treated structure. Similar FE analysis in the estimation of damping in CLD treated laminated beams, and conical/spherical sandwich shells were presented in Korjakin et al., 2001; Ren et al., 2020; Xie and Shepard, 2009; Zhang and Chen, 2006.

Moreira et al. (2006) presented a FE formulation using facet type quadrangular shell finite elements to model multi-layered laminated structures with constrained viscoelastic layers. Alvelid and Enelund (2007) introduced an interface finite element model for the modelling of viscoelastic rubber layer in

sandwich beams/plates. Hu et al. (2008) addressed the appropriateness of different theories such as classical lamination theory (CLT), first-order shear deformation theory (FSDT), high-order theories (HOTs), and Zig-Zag theory for the analysis of CLD treated sandwich beams. Manconi and Mace (2010) used wave finite element (WFE) method for estimating the dissipated energy from a laminated panel with constrained viscoelastic layers and reported that WFE method provides the advantage of lesser computational time compared to the conventional FE procedure. Ferreira et al. (2013) presented a FE model of sandwich plate with the viscoelastic core using Carrera's Unified Formulation (CUF) and demonstrated the advantages of the developed FE model to analyse the damping in the plate. In the same line, Filippi et al. (2016) also derived higher-order finite elements for the FE analysis of CLD treated beams. Liu et al. (2017) proposed a differential quadrature hierarchical finite element (DQHFE) model based on the layer-wise theory to analyse the constrained layer damping in a sandwich plate. This DQHFE modal provides highly accurate results using few nodes on the boundary of the substructural elements. Li et al. (2019) proposed the reduced FE model of the sandwich plate with viscoelastic core using Golla-Hughes-McTavish (GHM) approach and reported that this FE model has greater accuracy compared to the classical FE models based on the GHM approach. Zhao et al. (2019) proposed a simplified FE model of a CLD treated plate using single-layer equivalent material properties and demonstrated the accuracy of this modelling approach.

Besides the above analytical and numerical studies, a good number of experimental studies on the CLD treatment have also been reported in the literature. Yin et al. (1967) conducted a series of experimental studies for CLD treatment of beam, plate, and tubular structures and demonstrated the corresponding passive damping in the structures. Rao and He (1993) also carried out an experimental study to validate their analytical results in estimation of damping in a laminated composite beam having multiple constrained viscoelastic layers. Kung and Singh (1998) proposed an analytical model of a beam integrated with multiple CLD patches and investigated the effects of size and locations of the patches over the host structure-surface on the passive damping in the overall beam. The corresponding analytical results were validated through experimentation. Huang et al. (2001) experimentally investigated the effect of thickness deformation of the viscoelastic layer in the CLD treatment on its damping effectiveness and suggested to consider the thickness deformation of the

constrained viscoelastic layer for estimation of damping, especially for thick damping layers. Similar experimental investigation is also carried out in Sisemore and Darvennes, 2002. Granger and Ross (2009) conducted an experimental study for the partial CLD treatment of a beam and validated their analytical model for the same beam, where the analytical model was derived by defining the viscoelastic material properties according to the Prony series. Similar study for partial CLD treatment of curved panels/shells was also carried out by Li et al., 2020 and Kumar and Singh, 2010. Ojha and Dwivedy (2019) fabricated the leptadenia pyrotechnica rheological elastomer (LPRE), and its damping capability to attenuate the vibration of a sandwich plate was demonstrated experimentally. It was reported that the LPRE viscoelastic core could be used for the improved damping in a sandwich plate with the isotropic face layers.

1.3.2.2. Literature on different geometrical/material configurations of CLD treatment

In order to augment damping capability of the CLD treatment, it is utilized in various geometrical configurations. Plunkett and Lee (1970) introduced a CLD treatment by cutting the constraining layer into appropriate lengths, particularly for the augmented damping treatment. It was reported that the damping is dependent on the length of the constraining layer, loss factor of the viscoelastic material and stiffness of the constraining layer. Similar study through the segmentation of CLD layer was also carried out by Al-Ajmi and Bourisli, 2008; Lepoittevin and Kress, 2010; Trompette and Fatemi, 1997. However, Tian et al. (2016) reported that damping improvement in the CLD treatment through its segmentation can only be effective for thin viscoelastic layer, where the improved damping arises by the increase in the shear strain of the viscoelastic layer.

The performance of the CLD treatment can be improved using multiple viscoelastic layers, where the damping layers and stiff constraining layers are stacked alternatively in a laminate configuration (Torvik and Strickland, 1972). However, it is important to decide a suitable number of damping layers in symmetric or asymmetric layered configuration looking into the improvement of damping with the minimum possible increase in the weight of the layered structure (Alam and Asnani, 1984a, 1984b). In this line, Rao and He (1993) analysed the dynamic responses of a composite beam having multiple constrained viscoelastic layers and reported that the natural frequency and modal loss factor

were influenced by ply orientations of laminae and thickness of damping layers. A similar study for a multi-layered cylindrical shell was also presented by Zheng et al. (2014).

Whittier (1959) introduced a standoff/spacer layer between the viscoelastic damping layer and the host structure-surface for augmented damping in the CLD treatment. The standoff layer enhances the shear strain in the constrained viscoelastic layer, and it results improved damping capacity of the CLD treatment. Rogers and Parin (1995) analytically and experimentally investigated the CLD treatment of a panel structure using a stand-off layer, and suggested thicker stand-off layer for greater damping in the CLD treatment. Garrison et al. (1994) analysed the partial CLD treatment of a plate by incorporating spacer/stand-off layer and reported that the standoff layer facilitates to reduce the size of the CLD treatment, where a good damping can be maintained with the advantage of less weight of the damping arrangement. Similar observations were also reported by Masti and Sainsbury (2005).

Nokes and Nelson (1968) introduced the partial PCLD treatment of a structure for reducing the mass of the viscoelastic damping treatment, and they reported that the passive damping for the partial coverage may be more than that for the full coverage of the PCLD treatment. Markuš (1974) reported the same observation for the PCLD treatment of a beam. However, Lu (1977) utilized the partial PCLD treatment over the outer surface of a pressurized liquid-filled cylindrical shell and observed significant attenuation of vibration of the cylindrical shell. El-Rehab and Wagner (1986) used thin axial strips to constrain the viscoelastic layer over the outer surface of a cylindrical shell and observed a good energy-dissipation from the overall shell through the relative motion between strips and host structure-surface. Lall et al. (1987, 1988) reported that the performance of the partial PCLD treatment in attenuation of vibration of beams and plates is significantly dependent on the shear modulus of viscoelastic material and size of PCLD patches. Marcelin et al. (1992) presented an optimal arrangement of the partial PCLD treatment to achieve maximum passive damping in beam and panel structures. Similar studies are also available in Chen and Huang, 1999, 2001; Cheng and Lapointe, 1995; Khalfi and Ross, 2016; Xu et al., 2020; Zheng et al., 2005, 2006.

The CLD/PCLD treatment is basically comprised of a viscoelastic layer that is sandwiched between two stiff layers. So, the aforesaid research on this subject

is mainly carried out based on the variations of material properties and geometrical arrangement of the viscoelastic damping material. However, the influence of material properties of the stiff constraining or substrate layers on the damping performance of the CLD/PCLD treatment is also addressed in a few available studies. Moita et al. (2018) studied the damping characteristics of a sandwich plate and a cylindrical panel, where the core is made of a viscoelastic material and the face layers are made of a functionally graded material (FGM). It was observed that the modal loss factor of the sandwich structures significantly varies with the change in the volume fractions of component materials in the FGM. In the same line, Sahu et al. (2020) considered an FGM constraining layer for the PCLD treatment of a doubly curved shell and observed that the damping in the PCLD treated shell changes significantly with the variations of the volume fractions of component materials in the FGM. Zhang et al. (2020) performed dynamic analysis of a porous FGM sandwich plate with the viscoelastic core and reported that porosities within the FGM face layers may significantly affect the passive damping in the overall sandwich structure.

1.3.2.3 Literature on CLD treatment of dynamic instability of flexible structures

Vibration of structural elements through parametric resonance is a commonly known phenomenon in many engineering structures like drill string in a high-speed drilling process (Huang and Kuang, 2007), ribs in aircraft wing (Vasiliev et al., 2012), rotating disk in external memory drives (Jiang et al., 1990), turbine blades (Sakar and Sabuncu, 2004), shaft-rotor-bearing system in the power transmission machinery (Young et al., 2007), fluid conveying pipes (Vaz and Rizzo, 2011), etc. In these applications, a structural element operates under various dynamic forces while its dynamic instability may evolve through the parametric resonance resulting in the commencement or the enhancement of vibration of the structural element. This kind of dynamic instability is generally known as parametric instability. The available studies on this context address primary, secondary and combinatory parametric instabilities (Nayfeh and Mook, 2008). Among these different parametric instabilities, the critical one is the principal primary parametric instability (Bolotin, 1964). However, a great deal of research on the parametric instability of various structures has been reported in the literature (Dey and Singha, 2006; Ganapathi et al., 1999; Ke et al., 2013; Langthjem and Sugiyama, 2000; Mohanty et al., 2012; Patel et al., 1999;

Pradyumna and Bandyopadhyay; 2011), where it is revealed that the parametric instability may lead to the failure and/or improper functionality of structural elements during operation. So, a good number of studies on the control of parametric instability have also been reported by many researchers. In this aspect of controlling parametric instability, a majority of the available studies have been carried out utilizing various active materials like electrorheological (ER) fluid (Yeh et al., 2004), magnetorheological (MR) material (Yeh and Shih, 2006), piezoelectric actuators (Chen et al., 2002; Pradyumna and Gupta, 2011).

However, the utilization of active materials imposes the complex arrangement of sensors, actuators, controller and external power supply. So, the passive damping materials are usually preferred for simple control arrangement at low cost. But, in this line, a limited number of studies are available in the literature utilizing the viscoelastic damping materials. In an early work, Steven and Iwanawski (1969) used viscoelastic damping for improved dynamic stability of a column operating under a dynamic compressive load. Later, similar studies were also carried out by Saito and Otomi (1979).

However, Ray and Kar (1995) utilized viscoelastic material through the CLD arrangement for passive control of parametric instability of a symmetric sandwich beam. This available study shows reduced stability region with the increase in the material loss factor of the viscoelastic core. A similar study was also reported by Dwivedy et al. (2007). However, Ray and Kar (1996) also studied the dynamic instability of multi-layered beams made of elastic and viscoelastic layers, and they reported that the critical buckling load and dynamic stability region improve with the increase in the number of layers within the multi-layered beams. Shih and Yeh (2005) carried out the dynamic stability analysis of a viscoelastic beam and observed that the instability region reduces with the increase in the viscoelastic beam length. Pradhan et al. (2016) analysed the dynamic instability of a CLD treated asymmetric sandwich beam and reported that the dynamic stability of the beam improves with the increasing material loss factor as well as the ratio of moduli of viscoelastic and substrate layers. Recently, Ojha and Dwivedy (2020) presented the performance of LPRC viscoelastic material layer for the CLD treatment of parametric instability of a sandwich plate where the viscoelastic material lies at the core.

1.4. Hybrid active-passive damping treatments

Piezoelectric actuators (Figs. 1.6) are enormously utilized in the active control of structural vibration. Generally, a piezoelectric actuator is attached to or embedded in a host structure and provides the actuation force to counteract the deformation of the overall structure when it is activated by supplying external electric field according to a control strategy (Dash and Singh, 2009). However, as mentioned in section 1.2, there are two kinds of piezoelectric actuators, namely extensional mode and shear mode piezoelectric actuators (Fig. 1.6). The extensional mode piezoelectric actuators are usually attached to the surface of a host structure and provide the actuation force in the form of the electrically induced in-plane normal stresses to attenuate the vibration/deformation of the overall structure (Benjeddou et al., 1997; Brahem et al., 2020; Hwang and Park, 1993; Khdeir and Aldraihem, 2001; Raja et al., 2004; Trindade, 2007; Zhang et al., 2016). In contrast, shear mode piezoelectric actuators provide the actuation force in the form of electrically induced transverse shear stress. So, generally, the shear mode actuators are embedded in the host structure following the location of maximum value of the mechanically induced transverse shear stress within the structure (Aldraihem and Khdeir, 2003; Baillargeon and Vel, 2005; Benjeddou and Deu, 2001b; Lezgy-Nazargah, 2016; Li and Yang, 2007; Nikoei and Hassani, 2020; Panda and Dubey, 2020). However, the available studies in this context show good control capability of both kinds of piezoelectric actuators in attenuation of structural vibration, but they do not work well at a high frequency (Azvine et al., 1995; Trindade, 2011). It basically shows the appropriateness of a piezoelectric actuator in control of structural vibration at low frequency region. On the other hand, viscoelastic materials possess good energy-dissipation capability at high frequency region (Shi et al., 2004) since the material loss factor of these damping materials decreases at a low frequency (Fig. 1.3(b)). On the basis of these two facts, the utilization of piezoelectric actuators in combination with viscoelastic materials has been recommended by many researchers to achieve structural vibration control in a wide range of frequency. It leads to various hybrid damping treatments, where the damping appears in a combination of active and passive actions in the piezoelectric and viscoelastic materials, respectively.

The commonly known hybrid active-passive damping treatments are electro-mechanical surface damping (EMSD) (Ghoneim, 1993, Hagood and Flotow, 1991),

conventional active piezoelectric damping composite (CAPDC) (Gentilman et al., 1994), active piezoelectric damping composite (APDC) (Arafa and Baz, 2000) and active constrained layer damping (ACLD) (Baz and Ro, 1995). All these hybrid damping treatments are developed using extensional mode piezoelectric actuators, while a few studies are available in the open literature on the utilization of shear mode piezoelectric actuators in combination with viscoelastic damping materials towards the shear actuation-based hybrid damping treatment. Batra and Geng (2002) considered two different arrangements for the active-passive damping treatment of a plate. The first one is a sandwich plate where a shear mode piezoelectric actuator layer is covered by two identical viscoelastic layers at the core. In the second one, the host plate is covered by two identical viscoelastic layers that are constrained by the extensional mode piezoelectric actuator layers. Through these configurations of the hybrid plate, they investigated the effectiveness of the shear mode piezoelectric actuator in comparison to that of the extensional mode piezoelectric actuator for the active-passive damping treatment. This study revealed that the shear mode piezoelectric actuators can also be used for an effective hybrid active-passive damping treatment in attenuation of structural vibration. In another study, Trindade (2011) used a shear mode piezoelectric actuator along with a viscoelastic material for controlling a sandwich beam, where a shear actuator patch is inserted at the core, and the rest of the core is filled by the viscoelastic material. From the corresponding experimental results, the author (Trindade, 2011) suggested that the shear mode piezoelectric actuator may be a good choice for active-passive damping treatment of structural vibration in a wide range of operating frequency.

However, among the aforesaid available hybrid damping treatments, the popular one is the ACLD as extensive research on this hybrid damping treatment is reported in the literature. The arrangement for the ACLD treatment using the extensional mode piezoelectric actuators is similar to that for the PCLD treatment, where the constraining layer is made of the piezoelectric actuator instead of a passive material. The damping in this arrangement mainly appears through the transverse shear deformation of the constrained viscoelastic layer; however, the actuation force in the piezoelectric constraining layer enhances the shear deformation of the viscoelastic layer resulting in augmented damping in the treatment (Baz and Ro, 1995). Unlike the PCLD treatment, ACLD treatment needs an additional feedback control arrangement to activate the piezoelectric

constraining layer by supplying external electrical voltage according to a control strategy. This ACLD treatment is widely used in aircraft, naval and automobile industries (Herdic et al., 2005; Kwak et al., 1999; LaPlante, 1998). Moreover, it is most efficient to control the structural vibration over a wide range of frequency (Azvine et al., 1995). A detailed literature review on the development of this ACLD treatment is furnished in the following section.

1.4.1 Literature review on ACLD treatment

The concept of ACLD treatment was proposed by Baz and Ro (1993, 1995). Subsequently, its damping performance was investigated by many researchers in comparison to the active damping through surface-bonded piezoelectric actuators and the passive damping through PCLD treatment. It was observed that ACLD arrangement provides significantly greater damping than that for any of the other two cases (Chen and Baz, 1996; Tomlinson, 1996). In this line, Lam et al. (1997) also proposed a similar hybrid damping treatment using the piezoelectric actuator layer and PCLD layer. They arranged these two layers either over the top surface of a substrate beam or over the top and bottom surfaces of the same beam. Among these two arrangements, the later one provides better attenuation of vibration of the overall beam; however, further work on this arrangement of hybrid damping treatment is not observed in the open literature. The ACLD treatment is usually made of soft viscoelastic layers having high material loss factor. So, although the actuation force is primarily utilized to enhance the shear deformation of the constrained viscoelastic layer, it cannot transfer to the host structure effectively because of the low stiffness of the intermediate viscoelastic layer. Therefore, the direct actuation of the host structure by the piezoelectric actuator layer does not appear effectively. It basically implies underutilization of the actuator. This issue was reported by Liao and Wang (1996), and they introduced edge elements/anchors to enhance the transfer of actuation force resulting in a new arrangement of ACLD treatment named enhanced active constrained layer damping (EACLD). EACLD treatment provides better damping than that for the ACLD treatment; however, a little decrease in the passive counterpart of the total active-passive damping appears (Liao and Wang, 1996; Liao and Wang, 1997; Liu and Wang, 1998). Fang et al. (2021) also carried out a comparison study between the ACLD and EACLD treatments to control a rotating FGM beam and observed better damping performance in the EACLD. Further, Kumar et al. (2011a) used

the stand-off layer between viscoelastic layer and base structure-surface within the EACLD arrangement, and observed significant damping improvement.

Yellin and Shen (1996) introduced the self-sensing active constrained layer (SACL) damping treatment, where the constraining piezoelectric layer is utilized to act as sensor and actuator simultaneously. Balamurugan and Narayanan (2002) used both the SACL and edge elements for vibration attenuation of a beam element and observed significantly improved damping compared to that for the SACL only. Gao and Liao (2005) studied the dynamic characteristics of a beam integrated with full/partial EACLD treatment, where also the self-sensing actuators were utilized. It was observed that the damping is mainly dependent on the control-gain, location and coverage of self-sensing actuators. Liu and Wang (2000) proposed active-passive hybrid constrained layer (HCL) treatment, where passive and active materials were used together to constrain the viscoelastic material layer in place of pure piezoelectric layer constraining layer. A significant improvement of damping was observed through the HCL treatment by proper selection of active and passive materials, as well as the length of the constraining material. These researchers (Liu and Wang, 2002) also integrated both EACL and HCL treatments to achieve a better hybrid active-passive damping treatment. Kumar et al. (2011b) used precompressed damping layer within the ACLD treatment and found that the damping performance of the ACLD treatment improves significantly. Kumar (2013) proposed a robust controller to enhance the damping performance of ACLD treatment. A stand-off layer was also used in this damping arrangement, and the corresponding results were validated through an experimental study. The results in this study revealed improved hybrid damping with a significant decrease in the required control voltage.

However, Baz and Ro (1993) introduced the partial ACLD treatment of flexible beams. Subsequently, a good number of studies on the use of the partial ACLD treatment in an optimal manner arrived in the literature (Huang et al., 1996; Ray and Baz, 1997; Sun and Tong, 2002; Veley and Rao, 1996; Zheng et al., 2011). Lesieutre and Lee (1996) utilized ACLD treatment in the segmented form for vibration attenuation of a beam and reported that the segmented ACLD treatment possesses an advantage of controlling several modes of vibration. Li et al. (2008) also addressed better damping in the segmented ACLD treatment than that for the same treatment in full layered form. Similar studies for vibration attenuation of cylindrical shells and plates were also addressed in Lu et al., 2017;

Ni et al., 2013; Yuan et al., 2010. Kumar and Singh (2009) studied the partial ACLD treatment to control a beam and suggested proper selection of viscoelastic layer thickness and locations of ACLD patches over the host structure-surface for achieving effective vibration control. However, Plattenburg et al. (2015) placed the active and passive damping patches side-by-side over the surface of a substrate plate and demonstrated the corresponding damping characteristics in the overall plate. Recently, the arrangement of EACLD treatment in the patch form has been demonstrated by Li et al. (2019).

The aforesaid studies on the ACLD treatment address the development in the design of the ACLD treatment. Besides, a great deal of research on the mathematical modelling and theoretical estimation of dynamic characteristics of the ACLD treatment for various structures has also been addressed in the literature (Datta and Ray, 2016, Lam et al., 1995; Moita et al., 2011; Park and Baz, 1999; Park and Baz, 2001; Ray et al., 2001; Saravanan et al., 2001; Shi et al., 2004; Sun and Tong, 2004; Trindade et al., 2001; Van Nostrand et al., 1994; Vasques et al., 2006; Yuan et al., 2010). Among many others, Van Nostrand et al. (1994) developed an FE model of ACLD treated beams using a viscoelastic material modelling approach as Augmenting Thermodynamic Fields (ATF). Lam et al. (1995) developed a mathematical model of ACLD treated beams based on the Galerkin approach and Golla-Hughes-McTavish (GHM) method. Trindade et al. (2001) presented an FE model of a multi-layered beam with the piezoelectric actuator and viscoelastic damping layers, where the viscoelastic layer is modelled using anelastic displacement fields (ADF) method. The accuracy of this FE model was also verified with the results obtained from experimentation. Sun and Tong (2004) proposed the compressional-shear model of an ACLD treated layered beam to investigate the effect of the compressional vibration on the active-passive damping. It was observed that compressional vibration may significantly affect the damping in the overall beam particularly for higher modes of vibration. However, Datta and Ray (2016) presented a FE model of an ACLD treated laminated composite plate where the viscoelastic layer is modelled using fractional order derivative (FOD) constitutive relation. Further, the same authors (Datta and Ray, 2018) also analysed the ACLD treatment of a laminated composite shell based on the Novozhilov nonlinear shell theory and FOD viscoelastic constitutive model. It was reported that the FOD constitutive model of viscoelastic materials

provides the advantage of low computational time in the nonlinear transient analysis of ACLD treated structures.

1.5 Viscoelastic composites for UCLD/CLD/ACLD treatment

In most of the available studies on the UCLD/CLD/ACLD treatment, monolithic viscoelastic materials are utilized. However, some available studies address viscoelastic composites in place of the monolithic viscoelastic material for having better damping capability of the UCLD/CLD/ACLD treatment. In this line, the first viscoelastic composite appeared in the form of a nanocomposite. It is comprised of single-walled/multi-walled carbon nanotubes (CNTs) embedded in the epoxy matrix, where the improved material damping appears due to the stick-slip mechanism (de Borbón et al., 2014; DeValve and Pitchumani, 2014; Khan et al., 2011; Rajoria and Jalili, 2005). The damping effectiveness of this kind of viscoelastic nanocomposite was demonstrated in a few studies through the CLD arrangement, where it is revealed that the damping capability of the neat epoxy can be augmented by the inclusion of CNTs (de Borbón et al., 2014; Rajoria and Jalili, 2005). Another type of viscoelastic composite appeared by the inclusion of soft viscoelastic particles within the stiff elastic matrix (Attipou et al., 2013). The stiff elastic matrix provides high stiffness of the composite, while the material damping of this composite arises due to the inclusion of viscoelastic particles. Further, silica nanoparticles and rubber particles were embedded in a fiber/epoxy composite to improve its damping properties (Huang and Tsai, 2015). Here, the rubber particles provide improved damping properties of the fiber/epoxy composite but the stiffness of the composite decreases due to the inclusion of rubber particles. So, it is compensated by the inclusion of silica nanoparticles.

In any of the aforesaid composites, the material for matrix phase is taken with high stiffness and a very low material loss factor. So, although the inclusion yields improved material damping, these composites are not capable of providing good passive damping as that appears in the conventional CLD treatment. Generally, the CLD treatment is made of soft viscoelastic material with high material loss factor, especially for achieving high damping in the treatment. However, using this type of viscoelastic material for the matrix phase, two types of composites, namely 0-3 and 1-3 viscoelastic composites (VECs), were addressed in Kumar and Panda, 2016; Kumar et al., 2018a, 2018b. These available studies

show a significantly improved CLD/UCLD/ACLD treatment for the use of the 0-3/1-3 VEC instead of the monolithic viscoelastic material.

1.6 Motivation and objectives of the present research

A literature survey is performed and presented in the aforesaid sections for understanding the state-of-art research on the utilization of viscoelastic damping materials in attenuation of vibration of thin-walled structures. It is observed from this literature survey that viscoelastic damping materials are extensively utilized for passive damping of structural vibration mainly through two damping arrangements, as free/unconstrained layer damping (UCLD) and passive constrained layer damping (PCLD/CLD). However, the passive damping in the PCLD/CLD treatment is significantly more than that in the UCLD treatment (Grootenhuis, 1970), and thus most of the available studies in this context have been carried out using PCLD/CLD arrangement. These available studies reveal various mathematical modelling approaches for theoretical analysis of PCLD/CLD treatment of different kinds of structures besides the studies on the experimental verification. Moreover, different geometrical and material configurations of the PCLD/CLD treatment have been developed by many researchers, in particular, to achieve augmented passive damping. In this line, popular ones are multi-layered CLD treatment (Alam and Asnani, 1984a, 1984b; Torvik and Strickland, 1972; Zheng et al., 2014), partial PCLD (Khalfi and Ross, 2016; Marcelin et al., 1992; Nokes and Nelson, 1968), CLD with standoff/spacer layer (Masti and Sainsbury, 2005; Rogers and Parin, 1995; Whittier, 1959), segmented constraining layer (Plunkett and Lee, 1970) and segmented damping layer (Lepoittevin and Kress, 2010; Tian et al., 2016; Trompette and Fatemi 1997).

Generally, viscoelastic damping materials do not work well in suppression of structural vibration at a low operating frequency, while piezoelectric actuators can fruitfully be used in the low frequency range (Azvine et al., 1995; Trindade, 2011). So, the viscoelastic damping materials are utilized along with piezoelectric actuator materials for achieving the structural vibration control effectively in a wide range of operating frequency (Azvine et al., 1995). In this line, the viscoelastic and piezoelectric materials are utilized in different geometrical configurations leading to various hybrid active-passive damping treatments like electro-mechanical surface damping (EMSD) (Ghoneim, 1993), conventional active piezoelectric damping composite (CAPDC) (Gentilman et al., 1994), active

piezoelectric damping composite (APDC) (Arafa and Baz, 2000) and active constrained layer damping (ACLD) (Baz and Ro, 1995). Of these, most popular one is the ACLD treatment as the open literature shows a great deal of research on this hybrid active-passive damping treatment for numerous structural elements. Further, the ACLD treatment is available in different configurations, where the poplar ones are partial ACLD (Baz and Ro, 1993; Li et al., 2008; Zheng et al., 2011), stand-off layer damping (Kumar et al., 2011a), pre-compressed layer damping (Kumar et al., 2011b), HCL damping (Liu and Wang, 2000), EACL damping (Balamurugan and Narayanan, 2002; Liao and Wang, 1996; Liu and Wang, 1998), segmented ACLD (Lesieutre and Lee, 1996) and SACL damping (Yellin and Shen, 1996).

Through the aforesaid research, the CLD/ACLD treatment is now well developed, and it becomes an eminent means to exploit the energy-dissipation properties of viscoelastic materials in control of structural vibration particularly for thin-walled flexible structures. This development of CLD/ACLD is achieved mostly by using monolithic viscoelastic damping materials. However, two types of viscoelastic composites (VECs), namely 1-3 VEC and 0-3 VEC, are now available in the literature (Kumar and Panda, 2016; Kumar et al., 2018a, 2018b). These VECs significantly improve the damping capability of CLD/ACLD treatment when they are used in place of the conventional monolithic viscoelastic damping materials. Here, the inclusion of graphite wafers within the VEC layers mainly enhance the transverse shear deformation of the viscoelastic phase resulting in augmented damping. But, it needs a precise arrangement of macro-sized graphite wafers within the actively/passively constrained 0-3/1-3 VEC layer, where a micro-gap between two consecutive wafers is to be maintained. This requirement of the precise arrangement of graphite wafers within the viscoelastic matrix phase may pose difficulties in fabrication of the 0-3 and 1-3 VEC layers, and it seems to yield expensive CLD/ACLD treatment.

However, instead of graphite wafers, if the micro-sized graphite particles are dispersedly incorporated within the viscoelastic matrix, then the resulting particulate composite can be fabricated using the conventional fabrication procedure at a low cost (German, 2016; Sabu and Ranimol, 2010). But, the damping characteristics of the CLD treatment will certainly alter for the use of this viscoelastic particulate composite (VEPC) instead of 0-3 or 1-3 VEC. Here, the VEPC can be characterized as a macroscopically homogeneous and isotropic

material similar to a conventional particulate composite, and thus the passive damping mechanism in the use of VEPC remains the same as that appears for the monolithic viscoelastic layer in the CLD treatment. But, the change in the effective material properties of the viscoelastic damping layer due to the inclusion of graphite particles would have certain effect on the damping characteristics of the CLD treatment. An investigation on this issue may provide a new viscoelastic damping material towards the improved CLD treatment, and thus the first objective of this research is decided to investigate the damping characteristics of the CLD treatment by incorporating graphite particles in the constrained viscoelastic damping layer.

A good number of studies on the CLD treatment of parametric instability of thin-walled flexible structures have been observed in the literature, where the control of principal primary parametric instability is addressed in most of the studies, as presented in section 1.3.2.3. In these applications of CLD treatment, the corresponding passive damping is utilized to stabilize a flexible structure by reducing the principal primary parametric instability region, where the width of instability region reduces and the origin of instability shifts towards a high amplitude of the applied dynamic force. Apart from these two aspects of controlling the principal primary parametric instability region, another potential way is to shift the instability region out of the frequency range of operation. It basically needs a shift of natural frequency (ω_n), since the origin of instability region appears at an operating frequency (ω) that is equal to $2\omega_n / q$ ($q = 1, 2, 3, ...$) (Bolotin, 1964). However, for this additional functionality of the CLD treatment, it would be capable of regulating the stiffness of the CLD treated structure besides its (CLD) sufficient passive damping capability. This capability of the CLD treatment may be achieved by the use of VEPC layer where the stiffness of the CLD treated structure can be regulated by varying the volume fraction of inclusion of graphite particles. The corresponding investigation is performed at present, and it is taken as the second objective of this research for the development of CLD treatment in control of parametric instability of flexible structures.

In the ACLD treatment, the piezoelectric actuation force is primarily used to enhance the shear deformation of the constrained viscoelastic layer for augmented passive damping (Baz and Ro, 1995). However, this actuation force cannot transfer from the piezoelectric layer to substrate structure effectively

because of the intermediate soft viscoelastic damping layer. So, the direct actuation of the substrate structure by the piezoelectric layer appears weakly (Liao and Wang, 1996). It basically shows the underutilization of the piezoelectric actuation force in the hybrid active-passive damping treatment. In this concern, edge elements were used in an earlier study (Liao and Wang, 1996) for improved transfer of the actuation force. However, an alternative potential way is to increase the stiffness of the viscoelastic layer by the inclusion of graphite particles. Here, the inclusion would facilitate enhanced transfer of actuation force resulting in effective utilization of the piezoelectric actuator. But, there is a possible decrease in the passive damping since the same inclusion yields reduced material loss factor of the viscoelastic damping layer. In combination of these two facts, the total active-passive damping either increase or decrease depending on the volume fraction of inclusion. A detailed study in this concern may provide a potential VEPC damping layer for the improved ACLD treatment. Therefore, the third objective of this research is decided to investigate the damping characteristics of the ACLD treatment using the VEPC layer.

In most of the available studies on the ACLD treatment, the hybrid active-passive damping is achieved using the extensional mode piezoelectric actuators; however, the utilization of the shear mode piezoelectric actuators in the same hybrid damping treatment is not well explored. The corresponding literature review is furnished in section 1.4, where it is observed that the shear-actuated active-passive damping treatment is achieved by the use of a shear mode piezoelectric actuator layer that is sandwiched between two identical viscoelastic layers. Further, the viscoelastic layers are covered by the substrate material layers. Although this configuration provides a good shear-actuated hybrid active-passive damping (Batra and Geng, 2002), it can further be improved by alleviating two major shortcomings. The first shortcoming arises in deciding an appropriate stacking sequence of the active and passive damping layers within the corresponding layered structure. Here, both the active and passive actions appear through the transverse shear strain so that the appropriate location of active layer within the stack of layers coincides with that of the passive damping layer. However, the second shortcoming arises in the underutilization of the actuator layer, as the shear actuation force does not transfer to other layers effectively through the soft viscoelastic damping layers. Looking into these shortcomings, the fourth objective of this research is decided to address a fruitful design of the

shear-actuated active-passive damping treatment using the VEPC damping layer, in particular, to utilize the shear actuation force and passive damping materials effectively for achieving an improved shear actuated active-passive damping.

The aforesaid four objectives of the present research imply the development of a graphite particle-filled viscoelastic composite for a potential material of passive damping layer in the CLD and ACLD treatments. However, as mentioned earlier, another viscoelastic composite by the name of 0-3 VEC is also available in the literature, and this 0-3 VEC enables the CLD/ACLD treatment to have an excellent damping capability (Kumar et al., 2018a, 2018b). So, it is evident to verify the performance of the viscoelastic particulate composite in comparison to that of the 0-3 VEC in the CLD and ACLD treatments. It is taken as the fifth objective of this research.

In order to fulfil the aforesaid objectives in this research, the following theoretical studies have been carried out.

(a) Constrained layer damping in sandwich beams with a graphite particle-filled viscoelastic core.

(b) Passive control of parametric instability of sandwich beams using viscoelastic particulate composite (VEPC) damping layers.

(c) Active constrained layer damping treatment using the inclusion of graphite particles within the viscoelastic damping layer.

(d) Shear actuation-based hybrid active-passive damping in sandwich structures using a graphite particle-filled viscoelastic layer.

(e) Comparative performance of VEPC and 0-3 VEC in the active/passive constrained layer damping treatment.

1.7 Contributions

The following contributions in the field of viscoelastic damping of structural vibration have been made towards the preparation of the dissertation.

1. A novel graphite particle-filled viscoelastic composite (VEPC) layer is proposed for improved CLD and ACLD treatments of thin-walled flexible structures.

2. An analytical formulation is presented for estimation of effective properties of the graphite particle-filled viscoelastic composite (VEPC).

3. A computational strategy for determination of optimal size and locations of VEPC patches in the partial CLD treatment of beams is proposed in the finite element framework.

4. A new strategy in passive control of parametric instability is introduced by the use of the constrained VEPC layer, where the instability region not only reduces but also shifts aside from the operating frequency range depending on the volume fraction of inclusion in the VEPC layer.

5. An augmented ACLD treatment of structural vibration is presented by the inclusion of graphite particles within the actively constrained viscoelastic layer, where both the active and passive counterparts of the total active-passive damping increase significantly for an optimal volume fraction of inclusion in the viscoelastic layer.

6. A fruitful layered arrangement of shear mode piezoelectric actuator and viscoelastic damping layers is presented for effective utilization of these component materials in the shear-actuated active-passive damping treatment of structural vibration.

7. The usefulness of the graphite particle-filled viscoelastic layer in augmentation of shear-actuated active-passive damping is demonstrated for control of plate vibration.

8. The utility of the present VEPC layer in comparison to that of the other existing viscoelastic damping layers for the CLD/ACLD treatment is evaluated and presented.

1.8 Organization of the thesis

A brief introduction of the viscoelastic materials and piezoelectric materials is presented in Chapter 1. This is accompanied by a literature review on the uses of these materials for the UCLD, PCLD and ACLD treatments of structural vibration. On the basis of this literature review, the scope of the present research has been identified, and the objectives of the present thesis are outlined.

Chapter 2 deals with the CLD treatment of a sandwich beam where the core is made of the present VEPC. First, an analytical formulation is presented to estimate the frequency-dependent effective properties of the VEPC. Next, an FE model of the sandwich beam is derived to analyse the change in the passive damping characteristics of the beam due to the inclusion of graphite particles within the viscoelastic core. Subsequently, an optimal partial CLD treatment of the sandwich beam is demonstrated using the viscoelastic patches made of VEPC.

In Chapter 3, the VEPC layer is applied for the CLD treatment of parametric instability of layered beams operating under the periodically varying dynamic compressive load. First, the FE equations of motion of the layered beams are derived based on the layer-wise deformation theory, and then the method of solution for evaluation of the parametric instability region is demonstrated. Subsequently, numerical results are presented for investigating the usefulness of the present VEPC in passive control of parametric instability of layered beams.

Next, in Chapter 4, a study on the ACLD treatment of a substrate plate is carried out using the present VEPC layer. First, a closed-loop FE model of the substrate plate integrated with the ACLD layer is derived based on the layer-wide deformation theory and the velocity feedback control law. Next, the numerical results are presented to explore the advantages of the VEPC layer over the conventional monolithic viscoelastic layer in the ACLD treatment of plate vibration.

Chapter 5 presents the shear actuation-based active-passive damping treatment of a sandwich plate-strip where the core is made of a laminate of active layers and VEPC layers. The active layers are comprised of shear mode piezoelectric actuator patches. First, different layered arrangements of the active and VEPC layers at the core are presented. Next, a closed-loop FE model of the sandwich plate-strip is developed based on a shear actuation-based feedback control strategy. Subsequently, numerical results are presented mainly for demonstration of two concerns. The first concern is to address a fruitful layered arrangement of shear mode piezoelectric actuator and viscoelastic layers at the core for their effective utilization in having a good shear actuation-based hybrid damping treatment. The second concern is the usefulness of the present VEPC for achieving an augmented shear actuation-based hybrid damping treatment.

Chapter 6 deals with a study on the comparative performance of 0-3 VEC, VEPC and conventional monolithic viscoelastic damping layers in the CLD/ACLD treatment of plate vibration. First, the CLD/ACLD arrangement in symmetric and asymmetric sandwich plate configurations is presented, and the FE models of these sandwich plates are derived based on the layer-wise deformation theory. Subsequently, numerical results for the modal loss factor and frequency responses of the symmetric/asymmetric sandwich plates are presented for each of the aforesaid three kinds of damping layers towards a comparative study on their damping performance.

Finally, the important conclusions from work carried out and the future scope of the present thesis work are outlined in Chapter 7. The list of references is provided at the end of the thesis.

Chapter 2

Constrained layer damping in sandwich beams with a graphite particle-filled viscoelastic core

2.1 Introduction

The literature survey in the previous chapter shows a substantial number of studies on the constrained layer damping (CLD) treatment of thin-walled flexible structures. In almost all these available studies, monolithic viscoelastic materials are utilized for the CLD treatment. However, in the quest of better viscoelastic damping materials for the improved CLD treatment, two kinds of viscoelastic composites (VECs), namely 0-3 and 1-3 VECs are introduced in recent studies (Kumar and Panda, 2016; Kumar et al., 2018b). These VECs perform well to augment the passive damping capability of the CLD treatment, and this improved CLD treatment appears through a special arrangement of macro-sized rectangular graphite wafers within the viscoelastic matrix of 0-3/1-3 VEC damping layer, where any two consecutive wafers are laid with a precise micro-gap. This requirement of the precise arrangement of thin graphite wafers within the viscoelastic matrix phase may raise difficulties in fabrication of the 0-3 and 1-3 VECs leading to expensive CLD treatment.

Looking into this shortcoming, micro-sized graphite particles may be incorporated dispersedly within the viscoelastic matrix instead of graphite wafers, and then the resulting particulate composite can be fabricated using the conventional fabrication procedure at a low cost (German, 2016; Sabu and Ranimol, 2010). But, the damping characteristics of the CLD treatment will certainly be altered for the use of the viscoelastic particulate composite (VEPC) instead of 0-3 or 1-3 VEC, and this difference will appear mainly because of the corresponding changes in the effective material properties of the constrained damping layer. Generally, a particulate composite is characterized as a macroscopically homogeneous isotropic material. So, the mechanism of damping in the CLD treatment for the use of the VEPC layer will be the same as that appears in the use of a monolithic viscoelastic damping layer. However, the improvement or deterioration of damping capability of the CLD treatment for the inclusion of dispersed graphite particles in the constrained viscoelastic damping

layer can be estimated following the theory of linear viscoelasticity if the effective linear properties of the VEPC layer are considered in an application.

According to the theory of linear viscoelasticity, the dissipated-energy per cycle of steady-state vibration of a viscoelastic material system is equal to the stored energy in the same cycle multiplied by the loss factor of the system. Here, the viscoelastic material system stores energy elastically, and this ability of the material is characterized by a material constant named as storage modulus, while the ability of the same material system to dissipate energy is characterized by another material constant known as loss modulus. The ratio of loss and storage moduli is the loss factor that characterizes the dissipated-energy as a fraction of stored energy. Now, the inclusion of dispersed graphite particles within the viscoelastic matrix obviously yields improved effective storage modulus of the resulting VEPC layer, while the effective loss factor of the same VEPC is expected to decrease. Therefore, the energy-dissipation capability of the CLD treatment either improves or deteriorates depending on the variations of the effective properties of VEPC with the volume fraction of the inclusion of graphite particles. A detailed study in this concern may produce a potential VEPC layer for improved CLD treatment of structural vibration. So, in this chapter, a VEPC layer is considered with the inclusion of dispersed graphite particles in the viscoelastic matrix. This VEPC layer is taken as the constrained damping layer for the CLD treatment of a simply-supported/fully clamped sandwich beam, and the damping characteristics of the sandwich beam are investigated theoretically mainly for the variation of the volume fraction of inclusion of dispersed graphite particles within the constrained viscoelastic layer. This study is carried out considering both full and partial CLD treatments of the sandwich beam.

In section 2.2, a mathematical model of the sandwich beam with VEPC core is derived using finite element procedure. Subsequently, a solution procedure for the estimation of passive damping in the sandwich beam is presented in section 2.3. In the next section, i.e., in section 2.4, first, the variations of storage modulus and material loss factor of the VEPC with the volume fraction of inclusion of dispersed graphite particles are presented. Next, the damping capability of the constrained VEPC layer in the CLD treatment of the sandwich beam is investigated. Additionally, an optimal partial CLD

treatment of the sandwich beam using VEPC patches is also presented. Finally, a summary of the overall analysis is delineated in section 2.5.

2.2 Mathematical model of a sandwich beam with VEPC core

Figure 2.1(a) shows a sandwich beam with the VEPC core. The thickness, width and length of the sandwich beam are denoted by h, b and L, respectively. Within the overall thickness (h) of the sandwich beam, the thicknesses of face layers and VEPC core are indicated by h_f and h_c, respectively. For deriving a mathematical model of the sandwich beam, the bottom surface of the sandwich beam is taken as the reference plane, and the origin of the reference Cartesian coordinate system (xyz) is located at the middle point (o) of one edge of the reference plane (Fig. 2.1(a)). The face layers are considered to be made of an elastic isotropic material. The ends of the sandwich beam are considered either as simply-supported or as fully clamped ends, and the overall beam is

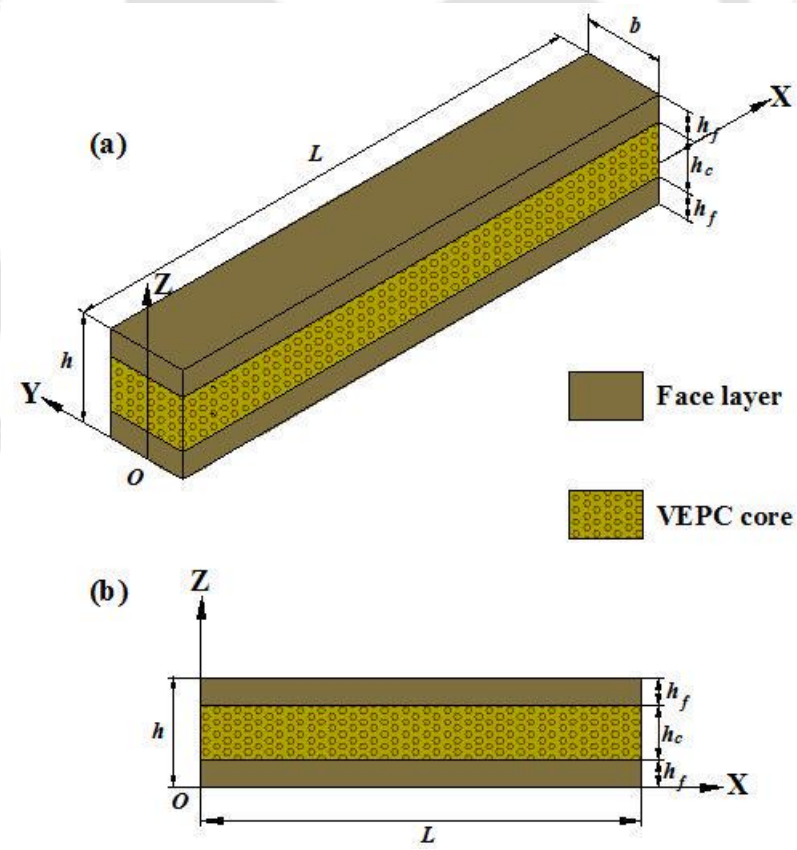

Fig. 2.1 Schematic diagrams of (a) a sandwich beam with the VEPC core and (b) a typical vertical plane in parallel to the xz -plane of the sandwich beam.

considered to be subjected to a uniformly distributed transverse harmonic load ($p(t)$) at its top surface. With this configuration of the sandwich beam, its material properties, geometrical properties and boundary conditions do not vary along the y-direction. The beam operates under the uniformly distributed transverse load and there is no body-force in any direction. Also, there is no externally applied force at the boundary surfaces in parallel to the xz–plane. Under these conditions, the boundary surfaces in parallel to the xz-plane can be assumed as stress free ($\sigma_y = \tau_{yx} = \tau_{yz} = 0$) surfaces. Now, because of a very small width (in y-direction) of the beam compared to its length, there can be a little variation of the stress components ($\sigma_y, \tau_{yx}, \tau_{yz}$) across the width so that they ($\sigma_y, \tau_{yx}, \tau_{yz}$) would be approximately zero throughout the entire region (Sadd, 2009). However, the other stress components ($\sigma_x, \sigma_z, \tau_{xz}$) may vary in the y-direction, but it would be a little variation of the stresses across a very small width of the beam. Accordingly, the state of strain ($\boldsymbol{\varepsilon}$) and the state of stress ($\boldsymbol{\sigma}$) at any point within the xz-plane can be written as,

$$\boldsymbol{\varepsilon} = \{\varepsilon_x \quad \varepsilon_z \quad \gamma_{xz}\}^{\mathrm{T}} \tag{2.1a}$$

$$\boldsymbol{\sigma} = \{\sigma_x \quad \sigma_z \quad \tau_{xz}\}^{\mathrm{T}} \tag{2.1b}$$

where, ε_x and ε_z are the normal strains along the x and z directions, respectively; σ_x and σ_z are the normal stresses along the x and z directions, respectively; γ_{xz} and τ_{xz} are the shear strain and shear stress, respectively over the xz-plane. The linear strain-displacement relations at any point in the xz-plane can be written as,

$$\boldsymbol{\varepsilon} = \boldsymbol{L}\boldsymbol{d} \tag{2.2a}$$

$$\boldsymbol{d} = \{u \quad w\}^{\mathrm{T}}$$

$$\boldsymbol{L} = \begin{bmatrix} \partial/\partial x & 0 & \partial/\partial z \\ 0 & \partial/\partial z & \partial/\partial x \end{bmatrix}^{\mathrm{T}} \tag{2.2b}$$

In Eq. (2.2b), u and w are the displacements at any point in the xz-plane along the x and z directions, respectively; $\boldsymbol{d}$ and $\boldsymbol{L}$ are displacement vector and operator matrix, respectively.

2.2.1 Material properties of different layers of the sandwich beam

The VEPC layer at the core of the sandwich beam is presently supposed to be comprised of uniform spherical solid particles that are dispersed within the viscoelastic solid matrix. The solid particles and viscoelastic matrix are considered to be made of homogeneous isotropic materials such as graphite and Butyl rubber, respectively. The linear constitutive behaviour of these constituent materials is considered. The material properties of Butyl rubber are dependent on the operating temperature and frequency so that the effective material constants of the VEPC are also dependent on the same parameters. Presently, the sandwich beam is considered to operate at room temperature, and thus the effective material constants of VEPC are dependent on the operating frequency only. Now, if the matrix phase of this particulate composite is made of an elastic material instead of the viscoelastic material, and the volume fraction of inclusion is very small in comparison to 1, then the effective material constants of the composite like shear modulus (G), bulk modulus (K), Young's modulus (E) and Poisson's ratio (ν) are given by (Hsiao-Sheng and Acrivos, 1978; Walpole, 1972),

$$G = G_m\left[1+\phi f_G\left(G_d, K_d, G_m, K_m\right)\right],$$
$$f_G = \left[\frac{5\left(G_d - G_m\right)\left(3K_m + 4G_m\right)}{6G_d\left(K_m + 2G_m\right) + G_m\left(9K_m + 8G_m\right)}\right] \tag{2.3a}$$

$$K = K_m\left[1+\phi f_K\left(G_d, K_d, G_m, K_m\right)\right],$$
$$f_K = \left[\left(\frac{3K_m + 4G_m}{3K_m}\right)\left(\frac{3K_d - 3K_m}{3K_d + 4G_m}\right)\right] \tag{2.3b}$$

$$E = \frac{9KG}{3K+G},\ \nu = \frac{3K-2G}{2\left(3K+G\right)} \tag{2.3c}$$

where, G_m and G_d represent shear modulus of the matrix phase and inclusion, respectively; K_m and K_d denote bulk modulus of the matrix phase and inclusion, respectively; ϕ is the volume fraction of inclusion. Equations (2.3a)-(2.3c) represent the analytical expressions for effective moduli of an infinitely dilute particulate composite where the volume fraction of inclusion is very small in comparison to 1. However, for an increased volume fraction of inclusion, the effective properties of a particulate composite can be computed using a

differential scheme (Bruggeman, 1935; Pal, 2005). Here, the particulate composite is theoretically achieved through the successive addition of an infinitely small number of new particles starting from the infinitely dilute system. The corresponding changes (dG and dK) in the magnitudes of effective moduli (G and K) for a differential increment ($d\phi$) of volume fraction of inclusion can be determined by (Bruggeman, 1935; Pal, 2005),

$$dG = f_G\left(G_d, K_d, G, K\right) G\, d\phi \tag{2.4a}$$

$$dK = f_K\left(G_d, K_d, G, K\right) K\, d\phi \tag{2.4b}$$

Equations (2.4a)-(2.4b) can be utilized for a low or moderate volume fraction of inclusion (Pal, 2005; Porfiri and Gupta, 2009). However, for a high volume fraction of inclusion, it is suggested in (Krieger and Dougherty,1959; Pal, 2005; Porfiri and Gupta, 2009) to consider the increment ($d\phi$) of volume fraction of inclusion in a special form as, $d\phi/\left(1-\phi/\phi_m\right)$, where ϕ_m is the maximum packing volume fraction of undeformed solid particles. Accordingly, Eqs. (2.4a)-(2.4b) can be written as,

$$\frac{dG}{d\phi} = f_G\left(G_d, K_d, G, K\right)\frac{G}{1-\phi/\phi_m} \tag{2.5a}$$

$$\frac{dK}{d\phi} = f_K\left(G_d, K_d, G, K\right)\frac{K}{1-\phi/\phi_m} \tag{2.5b}$$

For the consideration of the viscoelastic matrix phase instead of the elastic matrix phase, the effective moduli of the resulting VEPC can be obtained through Eqs. (2.5a)-(2.5b) by implementing elastic-viscoelastic correspondence principle (Christensen, 2012), where the moduli (G_m, K_m) of the elastic matrix phase in the analytical expressions (Eqs. (2.5a)-(2.5b)) are simply replaced by the complex moduli ($G_m^*(\omega)$, $K_m^*(\omega)$) of the viscoelastic matrix phase. Accordingly, Eqs. (2.5a)-(2.5b) can be written for effective complex moduli of VEPC as,

$$\frac{dG^*(\omega)}{d\phi} = f_G^*\left(G_d, K_d, G^*(\omega), K^*(\omega)\right)\frac{G^*(\omega)}{1-\phi/\phi_m} \tag{2.6a}$$

$$\frac{dK^*(\omega)}{d\phi} = f_K^*\left(G_d, K_d, G^*(\omega), K^*(\omega)\right)\frac{K^*(\omega)}{1-\phi/\phi_m} \tag{2.6b}$$

In Eqs. (2.6a)-(2.6b), the superscript (*) denotes a complex quantity and the effective complex moduli ($G^*(\omega)$), ($K^*(\omega)$) of VEPC are dependent on the operating frequency (ω) only because of the consideration of constant operating temperature. However, for an operating frequency and a specified volume fraction (ϕ) of inclusion, the corresponding effective complex shear ($G^*(\omega)$) and bulk ($K^*(\omega)$) moduli of VEPC can be computed by solving the nonlinear differential equations (Eqs. (2.6a)-(2.6b)), where the initial conditions may be considered as, $G^*(\omega)=G_m^*(\omega)$ and $K^*(\omega)=K_m^*(\omega)$ for $\phi=0$. Presently, Eqs. (2.6a)-(2.6b) are solved using MATLAB function ode45. According to the corresponding methodology, the input functions (f_1^*, f_2^*) are provided by separating their real and imaginary parts (Eq. (2.6c)) while the initial conditions (y_0 at $\phi=0$) are also provided in the similar format (Eq. (2.6d)). Here, the subscripts R and I denote real and imaginary counterparts of a complex quantity, respectively. For these inputs to the MATLAB function ode45, the solutions (y_n) for the complex moduli (G^*, K^*) at a given volume fraction ($\phi=\phi_n$) can be obtained by their (G^*, K^*) real and imaginary parts separately (Eq. (2.6e)). So, these parts are to be recombined for the final solution (Eq. (2.6f), $j=\sqrt{-1}$). A detailed description of this methodology is available in (MathWorks Inc., 2020).

$$f_v=\left[(f_1^*)_R \quad (f_1^*)_I \quad (f_2^*)_R \quad (f_2^*)_I\right]^{\mathrm{T}}$$

$$f_1^*=f_G^*\left(G_d,K_d,G^*(\omega),K^*(\omega)\right)\frac{G^*(\omega)}{1-\phi/\phi_m},$$

$$f_2^*=f_K^*\left(G_d,K_d,G^*(\omega),K^*(\omega)\right)\frac{K^*(\omega)}{1-\phi/\phi_m} \tag{2.6c}$$

$$y_0=\left[(G_m^*)_R \quad (G_m^*)_I \quad (K_m^*)_R \quad (K_m^*)_I\right] \text{ for } \phi=0 \tag{2.6d}$$

$$y_n=\left[(G^*)_R \quad (G^*)_I \quad (K^*)_R \quad (K^*)_I\right] \text{ for } \phi=\phi_n \tag{2.6e}$$

$$G^*=(G^*)_R+j(G^*)_I,\ K^*=(K^*)_R+j(K^*)_I \text{ for } \phi=\phi_n \tag{2.6f}$$

It should be noted here that the value of the maximum packing volume fraction (ϕ_m) is usually dependent on the type of packing arrangement of particles within the domain of the matrix phase. For instance, the value of ϕ_m is 0.637 for the random close packing (RCP) of monosized spherical particles, while it becomes as 0.74 for the hexagonal close packing (HCP) of uniform sphere particles. However, it is unlikely that the microspheres would be arranged in a regular periodic array, and thus RCP provides a more appropriate estimate of ϕ_m (Pal, 2005; Porfiri and Gupta, 2009). So, presently the value of ϕ_m is taken as 0.637 following RCP. Besides the mechanical properties of the VEPC, its effective mass density (ρ) for a specified volume fraction (ϕ) of inclusion is presently estimated according to the rule of mixture as illustrated in Eq. (2.7) where ρ_d and ρ_m denote mass density of inclusion and matrix phase, respectively.

$$\rho = \rho_d \phi + \rho_m (1-\phi) \tag{2.7}$$

Apart from the aforesaid macroscopically homogeneous isotropic properties of VEPC at the core of the sandwich beam, the face layers are considered to be made of a conventional elastic isotropic material. So, the constitutive relations for a component layer in the sandwich beam can be written under the plane stress assumption as,

$$\boldsymbol{\sigma}^k = \boldsymbol{C}^k(\omega)\boldsymbol{\varepsilon}, \quad k = 1,2,3 \tag{2.8}$$

$$\boldsymbol{C}^k(\omega) = \frac{E^k(\omega)}{1-\left(\nu^k(\omega)\right)^2}\begin{bmatrix} 1 & \nu^k(\omega) & 0 \\ \nu^k(\omega) & 1 & 0 \\ 0 & 0 & \left(1-\nu^k(\omega)\right)/2 \end{bmatrix} \tag{2.9}$$

where, k represents the bottom face layer, VEPC layer and top face layer as per its value as 1, 2 and 3, respectively; $E^k(\omega)$ and $\nu^k(\omega)$ denote Young's modulus and Poisson's ratio, respectively for the material of k^{th} layer. It should be noted here that the stiffness matrix $(\boldsymbol{C}^k(\omega))$ is a frequency-dependent complex quantity for the VEPC layer $(k=2)$ whereas similar matrix for the face layers ($k=1,3$) is a frequency-independent real quantity. Here, the material properties of VEPC layer $(k=2)$ like Young's modulus $(E^k(\omega))$ and Poisson's ratio $(\nu^k(\omega))$ can

be obtained from Eq. (2.3c), where the effective bulk ($K^k(\omega)$) and shear ($G^k(\omega)$) moduli of the same composite (VEPC) layer can be computed through the aforesaid solution of nonlinear coupled differential equations (Eqs. (2.6a)-(2.6b)).

2.2.2 Finite element (FE) model of the sandwich beam

For vibration of the sandwich beam under the uniformly distributed transverse harmonic load ($p(t)$) at its top surface ($z=h$), the first variations of total potential energy (δT_P) and total kinetic energy (δT_K) over the xz-plane (Fig. 2.1(b)) can be written as,

$$\delta T_P = \sum_{k=1}^{3}\left[\int_{A_k}\left\langle(\delta\boldsymbol{\varepsilon})^{\mathrm{T}}\boldsymbol{\sigma}^k\right\rangle dA_k\right] - \int_L\left\langle(\delta w)p(t)\right\rangle_{z=h}dL \tag{2.10a}$$

$$\delta T_K = \sum_{k=1}^{3}\left[\int_{A_k}\left(\{\delta\dot{u}\quad\delta\dot{w}\}\rho^k\{\dot{u}\quad\dot{w}\}^{\mathrm{T}}\right)dA_k\right] \tag{2.10b}$$

where, δ is the operator for the first variation; ρ^k is the mass density for the k^{th} layer within the sandwich beam; A^k is the area for k^{th} material over the xz-plane (Fig. 2.1(b)).

In order to derive the FE model of the sandwich beam based on the plane stress assumption, the xz-plane (Fig. 2.1(b)) is discretized by nine-node isoparametric quadrilateral elements. The edges of a typical element are in parallel to the corresponding edges of the xz-plane. Since the beam is comprised of two different materials, a typical element on the xz-plane is either made of the VEPC for core layer or made of the isotropic material for face layers. Now, the displacement vector ($\boldsymbol{d}$) at a point within a typical element can be written as given in Eq. (2.11) where $\boldsymbol{d}^e$ and $\boldsymbol{N}$ are the elemental nodal displacement vector ($\boldsymbol{d}^e$) and shape function matrix ($\boldsymbol{N}$), respectively.

$$\boldsymbol{d} = \boldsymbol{N}\boldsymbol{d}^e \tag{2.11}$$

The governing equations of motion of the sandwich beam are derived employing extended Hamilton's principle as given in Eq. (2.12). Using Eqs. (2.8), (2.2) and (2.11) in Eqs. (2.10a) and (2.10b), and then substituting the resulting expressions in Eq. (2.12), the elemental FE equations of motion can be obtained as given in Eq. (2.13).

$$\int_{t_1}^{t_2}\left(\delta T_K - \delta T_P\right)dt = 0 \tag{2.12}$$

$$\boldsymbol{M}^e\ddot{\boldsymbol{d}}^e + \boldsymbol{K}^e(\omega)\boldsymbol{d}^e = \boldsymbol{P}_M^e\, p(t)$$

$$\boldsymbol{M}^e = \int_{A_k^e}\left(\boldsymbol{N}^{\mathrm{T}}\rho^k\boldsymbol{N}\right)dA_k^e \ ,$$

$$\boldsymbol{K}^e(\omega) = \int_{A_k^e}\left(\boldsymbol{N}^{\mathrm{T}}\boldsymbol{L}^{\mathrm{T}}\boldsymbol{C}^k(\omega)\boldsymbol{L}\boldsymbol{N}\right)dA_k^e \ ,$$

$$\boldsymbol{P}_M^e = \int_{L^e}\left(\boldsymbol{N}^{\mathrm{T}}\{0 \quad 1\}^{\mathrm{T}}\right)_{z=h} dL^e \tag{2.13}$$

In Eq. (2.13), $\boldsymbol{M}^e$, $\boldsymbol{K}^e$ and $\boldsymbol{P}_M^e$ are the elemental mass matrix, stiffness matrix and nodal load coefficient vector, respectively; A_k^e is the area of an element made of k^{th} material; L^e is the elemental length over the top edge ($z = h$) of the xz-plane (Fig. 2.1(b)). It may be noted here that the stiffness matrix ($\boldsymbol{K}^e(\omega)$, Eq. (2.13)) is a frequency-dependent complex quantity since the frequency-dependent material properties of VEPC are presently modelled following the complex stiffness method. However, the assemblage of the elemental equations (Eq. (2.13)) in the global space yields the FE equations of motion of the sandwich beam as,

$$\boldsymbol{M}\ddot{\boldsymbol{X}} + \boldsymbol{K}(\omega)\boldsymbol{X} = \boldsymbol{P}_M\, p(t) \tag{2.14}$$

where, $\boldsymbol{M}$, $\boldsymbol{K}$ and $\boldsymbol{P}_M$ are the global mass matrix, stiffness matrix and nodal load coefficient vector, respectively; $\boldsymbol{X}$ is the global nodal displacement vector.

2.3 Solution and estimation of damping

The uniformly distributed transverse harmonic load is considered in the form as $p(t) = p_0 e^{j\omega t}$ ($j = \sqrt{-1}$). Here, p_0 and ω are the load-amplitude and operating frequency, respectively. For the corresponding linear steady-state vibration of the sandwich beam, the FE equations of motion (Eq. (2.14)) can be reduced as (Meirovitch, 1997),

$$\left(-\omega^2\boldsymbol{M} + \boldsymbol{K}(\omega)\right)\bar{\boldsymbol{X}} = \boldsymbol{P}_M p_0 \tag{2.15}$$

where, $\bar{\boldsymbol{X}}$ is the complex nodal displacement vector and its absolute value represents the nodal displacement-amplitude vector. Since the stiffness matrix ($\boldsymbol{K}(\omega)$) is a complex quantity, Eq. (2.15) can also be written in the following form,

$$\left(-\omega^2\boldsymbol{M}+\boldsymbol{K}^R(\omega)+j\boldsymbol{K}^I(\omega)\right)\bar{\boldsymbol{X}}=\boldsymbol{P}_M p_0 \tag{2.16}$$

Now, for free vibration ($p_0=0$) of the sandwich beam, Eq. (2.16) can be written as

$$\left(\boldsymbol{K}^R(\omega)+j\boldsymbol{K}^I(\omega)\right)\boldsymbol{\psi}_i=\omega_i^2\boldsymbol{M}\boldsymbol{\psi}_i \tag{2.17}$$

where, $\boldsymbol{\psi}_i$ and ω_i are the complex eigenvector and natural frequency, respectively for the i^{th} mode of vibration of the sandwich beam. The complex natural frequency (ω_i) can be expressed in terms of the natural frequency $\left(\omega_i^o\right)$ and the modal loss factor $\left(\eta_i\right)$ for the i^{th} mode of vibration as (Hu et al., 2008; Jin et al., 2015),

$$\left(\omega_i\right)^2=\left(\omega_i^o\right)^2\langle 1+j\eta_i\rangle \tag{2.18}$$

Since the stiffness matrix ($\boldsymbol{K}(\omega)$) is a function of the operating frequency (ω), Eq. (2.17) is presently solved using direct iteration method to obtain the natural frequency (ω_i^o) and modal loss factor (η_i) for the i^{th} mode of vibration of the sandwich beam. This solution method is implemented by expressing Eq. (2.17) in the following form,

$$\left\langle \boldsymbol{K}^R(\omega_i^{prev})+j\boldsymbol{K}^I(\omega_i^{prev})\right\rangle\boldsymbol{\psi}_i=(\omega_i^{curr})^2\boldsymbol{M}\boldsymbol{\psi}_i \tag{2.19}$$

where, the superscripts *prev* and *curr* indicate the values of ω_i corresponding to the previous and current iterations, respectively. The iteration starts with a frequency (ω_i^{prev}) that is the natural frequency of the beam without the VEPC core. In every iteration, the frequency-dependent properties of the VEPC are computed at the frequency ω_i^{prev} obtained from the previous iteration, and a complex linear eigenvalue problem is solved for ω_i^{curr}. If the value of ω_i^{curr} becomes satisfactory with the value of ω_i^{prev} according to convergence criteria, the iteration is terminated with the solution as, $\omega_i^{curr}=\omega_i^{prev}=\omega_i$.

2.4 Numerical results and discussion

In this section, first, the frequency-dependent effective material properties of the VEPC are studied for the variation of volume fraction of inclusion. Next, the effectiveness of this VEPC as a material for the damping layer in the CLD treatment is investigated through the evaluation of modal loss factor and frequency responses of the sandwich beam. Subsequently, an optimal partial CLD treatment of the sandwich beam is presented using the VEPC patches at the core.

The length (L), width (b) and thickness (h_f) of the face layers of the sandwich beam are taken as 0.4 m, 2.5 mm and 2.5 mm, respectively. Unless otherwise mentioned, the thickness (h_c) of the viscoelastic or VEPC core is considered as 5 mm. The ends of the sandwich beam are considered either as simply-supported ends ($u=0$ at $x=0$ and $z=0$; $w=0$ at $x=0$, L and $z=0$ to h) or as fully clamped ends ($u=0$, $w=0$ at $x=0$, L and $z=0$ to h). The face layers are considered to be made of Aluminium ($E=70$ GPa, $\nu=0.3$, $\rho=2700$ kg/m^3). The material constants of graphite particles are $E_d=250$ GPa, $\nu_d=0.3$, $\rho_d=$ 1400 kg/m^3 (Jones, 1998). The properties of Butyl rubber usually vary with the operating temperature and frequency (Jones, 2001). However, since the sandwich beam presently operates at the room temperature (32^o C), the frequency-dependent properties of Butyl rubber are taken from (Jones, 2001) at the same temperature (32^o C). The values of Poisson's ratio and mass density of Butyl rubber are taken as 0.49 and 920 kg/m^3, respectively.

For the computation of effective properties of the VEPC, Eqs. (2.6a)-(2.6b) are solved using MATLAB function ode45 (MathWorks Inc., 2020). In order to verify this solution, the reference experimental and finite element results (Marra et al., 1999) are taken for the effective storage and loss moduli of a VEPC. This VEPC (Marra et al., 1999) is comprised of a soft viscoelastic (P(VDF-TrFE)) matrix and elastic spherical particles (Ca-modified $PbTiO_3$). Figure 2.2 illustrates these reference results while similar results obtained through the present solution of Eqs. (2.6a)-(2.6b) are also presented in the same figure (Fig. 2.2). It may be observed from Fig. 2.2 that the presently computed results are in close agreement with the reference experimental results (Marra et al., 1999) up to a volume fraction (ϕ) of inclusion as 0.5. It may be noted here that the

formulation of the analytical expressions (Eqs. (2.6a)-(2.6b)) is based on the inclusion of undeformed elastic solid particles. In practice, a high volume fraction of particles may cause particle clustering as well as deformation of particles. Therefore, these analytical expressions are expected to provide a good estimation of effective properties at a low or a moderate volume fraction of inclusion as the same observation is obtained through the verification study (Fig. 2.2) with reference to the experimental results (Marra et al., 1999). However, based on this verification study, the analytical expressions (Eqs. (2.6a)-(2.6b)) are presently utilized to determine the effective moduli of VEPC for the volume fraction (ϕ) of inclusion up to 0.5.

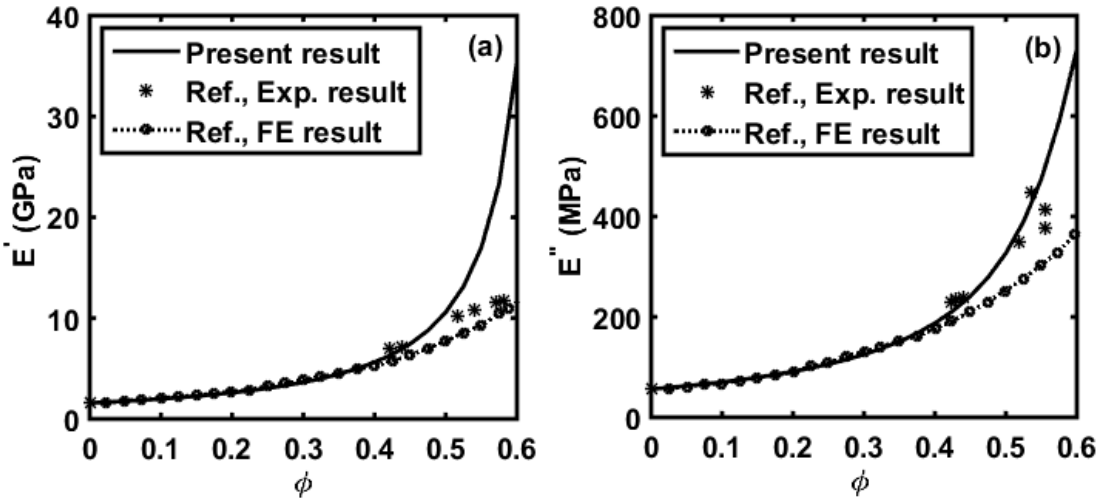

Fig. 2.2 Verification of the present solutions for effective (a) storage modulus (E') and (b) loss modulus (E'') of VEPC (Ref. Marra et al., 1999).

In order to study the frequency-dependent effective properties of the present VEPC, the properties of Butyl rubber are taken at some frequencies within a frequency range of interest. The effective material constants of the VEPC at the same frequencies are computed by solving Eqs. (2.6a)-(2.6b). Subsequently, the computed values of every material constant are fitted through a polynomial curve for expressing the functional variation of that effective material constant with frequency. These results are illustrated in Figs. 2.3-2.4 for different values of the volume fraction (ϕ) of inclusion. It may be observed from Figs. 2.3(a)-2.3(b) that the effective storage modulus (E' or G') of the VEPC increases with the increasing frequency for any value of the volume fraction (ϕ) of inclusion. It may be due to the fact that the storage modulus of the

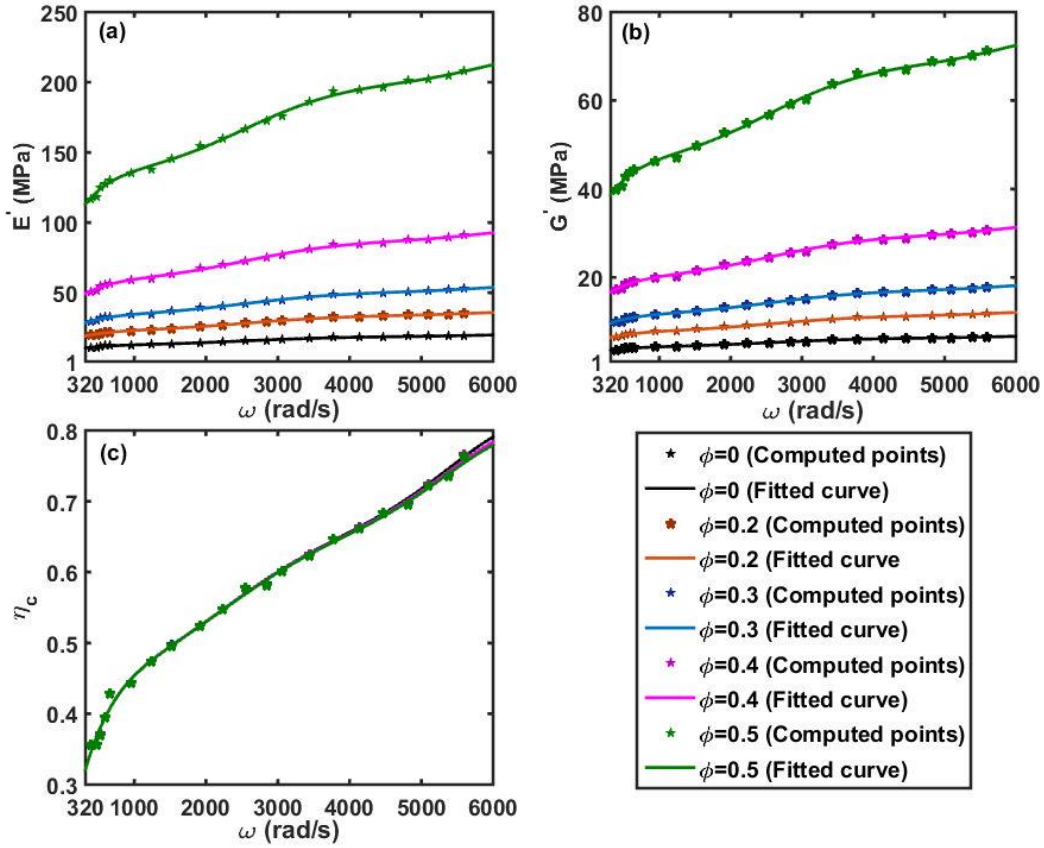

Fig. 2.3 Variations of effective properties of the VEPC with frequency for different volume fractions (ϕ) of inclusion; (a) storage Young's modulus (E'), (b) storage shear modulus (G') and (c) loss factor (η_c).

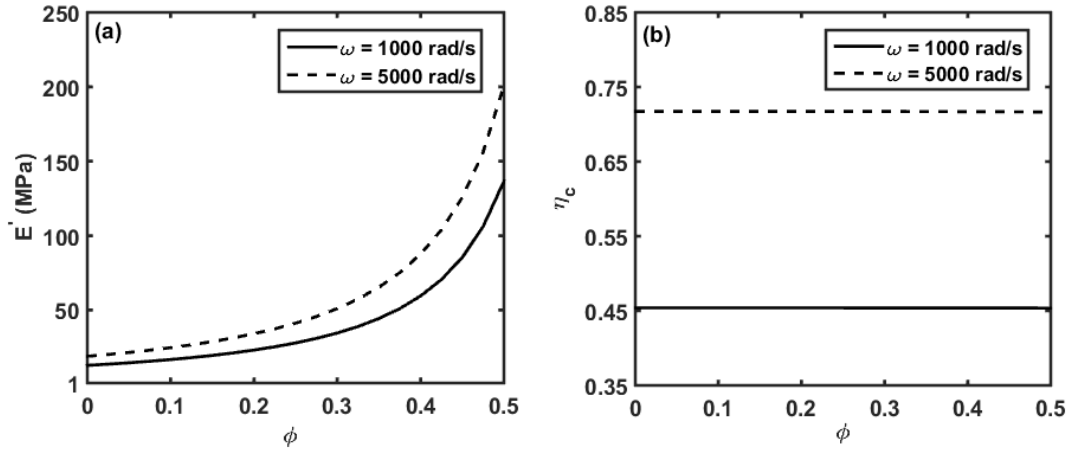

Fig. 2.4 Variations of (a) storage Young's modulus (E') and (b) loss factor (η_c) of the VEPC with the volume fraction (ϕ) of inclusion at two different frequencies.

viscoelastic matrix increases with the increasing frequency. In parallel, as it is illustrated in Fig. 2.3(c), the effective loss factor (η_c) of the VEPC also increases with the increasing frequency mainly because of the corresponding increase of loss factor of the viscoelastic matrix. However, it is important to observe from Fig. 2.3 that the effective storage modulus is significantly dependent on the volume fraction (ϕ) of inclusion, whereas the effective loss factor (η_c) is not that much sensitive to the same parameter (ϕ). In order to corroborate it clearly, the variations of the effective storage modulus (E') and loss factor (η_c) with the volume fraction (ϕ) of inclusion are illustrated in Figs. 2.4(a) and 2.4(b), respectively for two different frequencies. For any frequency, the results in Figs. 2.4(a)-2.4(b) indicate that the effective storage modulus (E') of the VEPC increases steeply after a certain value of the increasing volume fraction (ϕ) of inclusion (Fig. 2.4(a)). In parallel, the effective loss factor (η_c) of the same VEPC slowly decreases with the increasing volume fraction (ϕ) of inclusion (Fig. 2.4(b)). Now, recalling the theory of linear viscoelasticity, the stored energy in a viscoelastic medium is measured through its storage modulus while the dissipated-energy from the same viscoelastic medium is quantified as the stored energy multiplied by the loss factor of that medium. So, from the results described above (Figs. 2.4(a)-2.4(b)), it is not clear that the damping characteristics of the CLD treatment will improve for the inclusion of graphite particles within the constrained viscoelastic layer. Therefore, further analysis of damping in the sandwich beam (Fig. 2.1) is carried out in the next section.

2.4.1 Analysis of damping in the sandwich beam with VEPC core

The sandwich beam with a viscoelastic core is a usual structural configuration of beam elements for their CLD treatment. However, presently the graphite particles are incorporated dispersedly within the viscoelastic core (VEPC core), and the corresponding change in the passive damping characteristics of the sandwich beam is studied by evaluating the modal loss factor, as well as the frequency responses, of the sandwich beam using its presently derived FE model. For the verification of this FE model and the corresponding solution of Eq. (2.19), the reference results are taken from (Fasana et al., 1997) for natural frequency (f_n) and modal loss factor (η) of a simply-supported/clamped-free

sandwich beam with the viscoelastic core. Table 2.1 shows these reference results. Similar results obtained through the present FE formulation are also furnished in the same table. It may be observed from Table 2.1 that the present results are in good agreement with the similar results available in (Fasana et al., 1997) thus verifying the accuracy of the present FE model of the sandwich beam.

Table 2.1 Verification of the present FE model of a sandwich beam (η_c : loss factor for the material of viscoelastic core).

Bending mode	Simply-supported sandwich beam				Clamped-free sandwich beam			
	Present		Ref. (Fasana et al., 1997)		Present		Ref. (Fasana et al., 1997)	
	f_n (Hz)	η/η_c (%)	f_n (Hz)	η/η_c (%)	f_n (Hz)	η/η_c (%)	f_n (Hz)	η/η_c (%)
1	68.85	1.92	68.85	1.92	24.67	0.84	24.7	0.85
2	268.38	6.02	268.38	6.02	151.20	4.47	151	4.51
3	584.62	9.60	584.62	9.60	411.63	7.90	412	7.96
4	1008.6	11.5	1008.6	11.5	783.81	10.35	784	10.4

Table 2.2 FE mesh convergence study for the sandwich beam with VEPC core ($\phi = 0.2$, ω_n: fundamental natural frequency, η : modal loss factor).

No. of elements	Fully clamped sandwich beam		Simply-supported sandwich beam	
	ω_n (rad/s)	η	ω_n (rad/s)	η
112	714.750	0.2343	499.177	0.2459
330	714.461	0.2343	499.176	0.2459
550	714.205	0.2343	499.176	0.2459
760	714.204	0.2343	499.176	0.2459

The FE mesh is generated by dividing the horizontal and vertical spans of the xz-section (Fig. 2.1(b)) of the sandwich beam in such a manner that every element is in the shape of a rectangle with its edges in parallel to the sides of the xz-section. Also, a typical element is made of one of the phase materials within the section. Using this FE mesh, the numerical results are evaluated after an FE mesh convergence study, where the fundamental natural frequency (ω_n) and the corresponding modal loss factor (η) are evaluated by increasing the number of elements. These results are illustrated in Table 2.2. On the basis of these results

(Table 2.2), the FE mesh of a typical xz -section of the sandwich beam is decided for evaluation of the numerical results.

For the present sandwich beam with the VEPC core, Table 2.3 and Figs. 2.5(a)-2.5(b) illustrate the variations of fundamental natural frequency and modal loss factor with the volume fraction (ϕ) of inclusion in the VEPC core for the simply-supported or the fully clamped boundary conditions. It may be observed from Fig. 2.5(b) and Table 2.3 that the modal loss factor (η) first increases and then decreases as the volume fraction (ϕ) of inclusion

Table 2.3 Variations of the fundamental natural frequency (ω_n) and modal loss factor (η) of the sandwich beam with the volume fraction (ϕ) of inclusion.

Volume fraction	Fully clamped sandwich beam		Simply-supported sandwich beam	
(ϕ)	ω_n (rad/s)	η	ω_n (rad/s)	η
0	616.742	0.1810	406.852	0.2327
0.1	655.707	0.2060	446.008	0.2421
0.2	714.204	0.2343	499.176	0.2459
0.3	807.183	0.2638	573.104	0.2380
0.4	968.283	0.2871	677.124	0.2068
0.5	1288.58	0.2758	817.215	0.1358

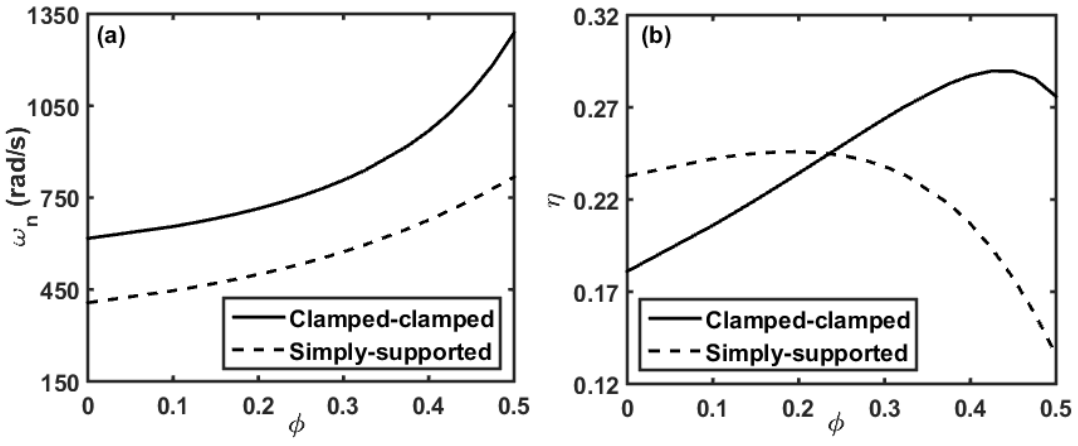

Fig. 2.5 Variations of the (a) fundamental natural frequency (ω_n) and (b) modal loss factor (η) of the sandwich beam with the volume fraction (ϕ) of inclusion in the VEPC core.

increases from its (ϕ) zero-value ($\phi=0$). The zero-value of the volume fraction (ϕ) of inclusion indicates pure viscoelastic material (VEM). So, the damping in

the sandwich beam increases due to the inclusion of graphite particles within the viscoelastic core. However, this advantage can be achieved up to a certain value of the volume fraction (ϕ) of inclusion where the optimal value of ϕ arises for the maximum value of the modal loss factor (η). In fact, the variation of damping (η) in the sandwich beam for an increase in the volume fraction (ϕ) of inclusion is mainly governed by the corresponding rate of increase in the effective storage modulus and the rate of decrease in the effective loss factor (η_c) of the VEPC (Fig. 2.4). The combined effect of these two factors yields an optimal value of the volume fraction (ϕ) of inclusion of graphite particles for the maximum damping (η) in the sandwich beam. It may also be observed from Fig. 2.5(b) that the optimal volume fraction (ϕ) of inclusion and the corresponding maximum damping or modal loss factor (η) are dependent on the boundary conditions over the ends of the sandwich beam.

In parallel to the variation of damping or modal loss factor, the natural frequency of the sandwich beam increases as the volume fraction (ϕ) of inclusion increases (Fig. 2.5(a), Table 2.3). However, the optimal volume fraction (ϕ) of inclusion would be the primary concern in the design of the VEPC core, and the change in the natural frequency does not appear remarkably till that (optimal) volume fraction of inclusion (Figs. 2.5(a)-2.5(b)).

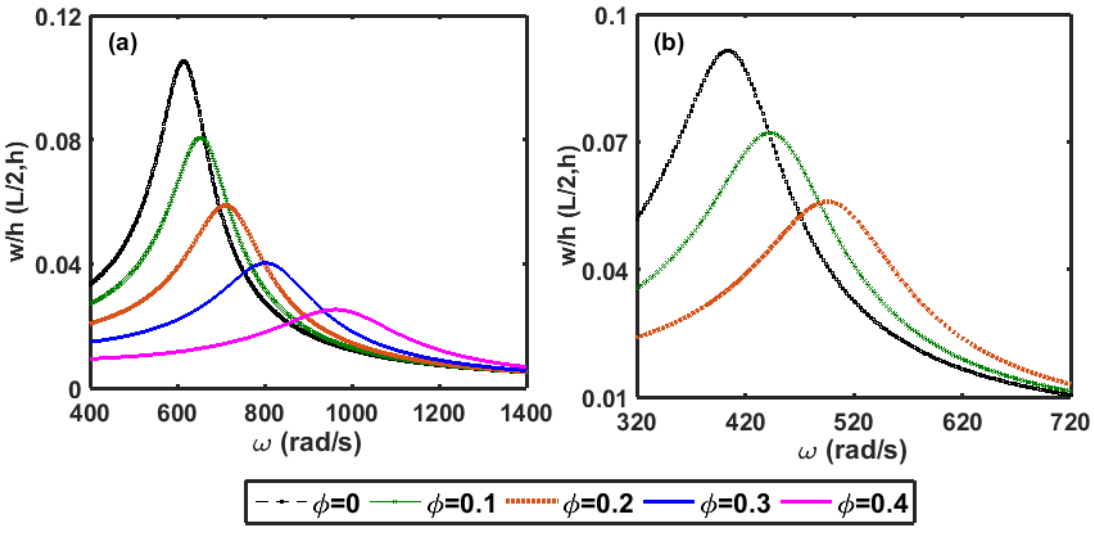

Fig. 2.6 Frequency responses of the (a) fully clamped or (b) simply-supported sandwich beam around its fundamental natural frequency.

The primary concern in the incorporation of damping within a vibrating system is to attenuate the vibration-amplitude at resonance. Accordingly, the usefulness of the aforesaid improved damping in the sandwich beam through the design of the VEPC core is corroborated by evaluating the frequency responses of the fully clamped/simply-supported sandwich beam. These results are illustrated in Figs. 2.6(a)-2.6(b), where the variation of transverse displacement-amplitude (w) at the middle point ($L/2, h$) over the top surface of the sandwich beam is plotted within a frequency range around the fundamental natural frequency. The frequency responses are evaluated for different values of the volume fraction (ϕ) of inclusion of graphite particles within the viscoelastic core while the amplitude (p_0) of the uniformly distributed transverse harmonic load is considered as 1000 N/m^2 or 500 N/m^2 for the fully clamped or the simply-supported sandwich beam. It can be observed from Figs. 2.6(a)-2.6(b) that the attenuation of the resonant displacement-amplitude of the sandwich beam increases significantly for an increase in the volume fraction (ϕ) of inclusion. However, from the results in Figs. 2.5(a)-2.5(b) and 2.6(a)-2.6(b), it may be concluded that the inclusion of dispersed graphite particles in the viscoelastic core of a sandwich beam yields significantly improved passive damping in that beam. But, there is a limiting value of the volume fraction of inclusion for achieving maximum augmentation of passive damping.

The energy-dissipation capability of the constrained VEPC layer mainly depends on its geometrical properties and volume fraction (ϕ) of inclusion. Presently, the in-plane dimensions, namely length (L) and width (b), of the VEPC layer are considered as equal to that for the overall sandwich beam. So, the remaining parameters, namely the volume fraction (ϕ) of inclusion and core-thickness (h_c), are to be taken with their appropriate values for effective utilization of the VEPC layer. It is presently carried out in an optimal manner by taking these parameters (ϕ, h_c) within the bounds as $0 \le \phi \le 0.5$ and 0.5 mm $\le h_c \le$ 5 mm.

Within these bounds of the parameters (ϕ, h_c), the contour of modal loss factor (η) at the fundamental bending mode of vibration of the sandwich beam is evaluated as shown in Figs. 2.7(a)-2.7(b) for two different boundary conditions of the sandwich beam. It may be observed from these figures that the optimal

value (point S or T) of the volume fraction (ϕ) appears as 0.4 or 0.2 for the fully clamped or the simply-supported sandwich beam. In parallel, the optimal value of thickness (h_c) of the VEPC layer does not appear within the specified bounds (0.5 mm $\leq h_c \leq$ 5 mm). However, the variation of modal loss factor (η) with the core-thickness (h_c) is illustrated in Figs. 2.8(a)-2.8(b) where the volume fraction (ϕ) of inclusion is taken with its optimal value.

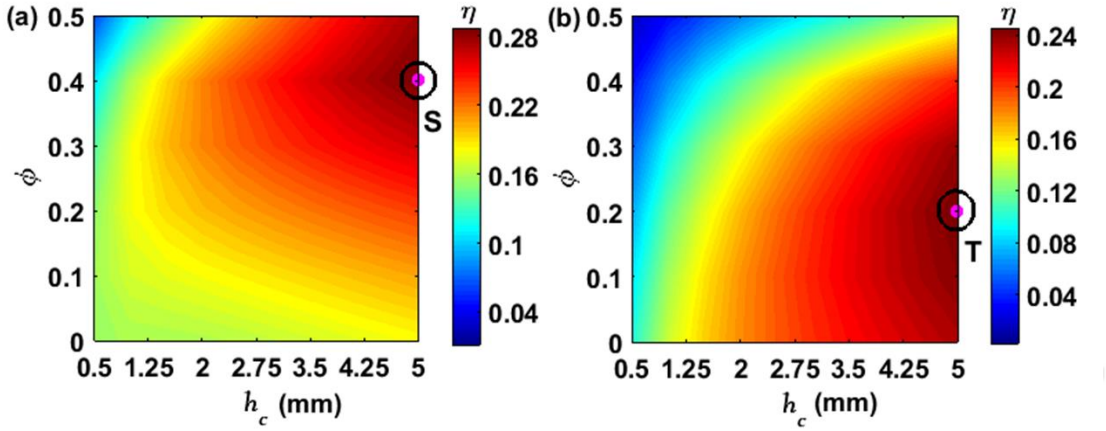

Fig. 2.7 Contour plot for the variation of modal loss factor (η) corresponding to the fundamental bending mode of vibration of (a) fully clamped or (b) simply-supported sandwich beam within the two-dimensional domain of core-thickness (h_c) and volume fraction (ϕ) of inclusion.

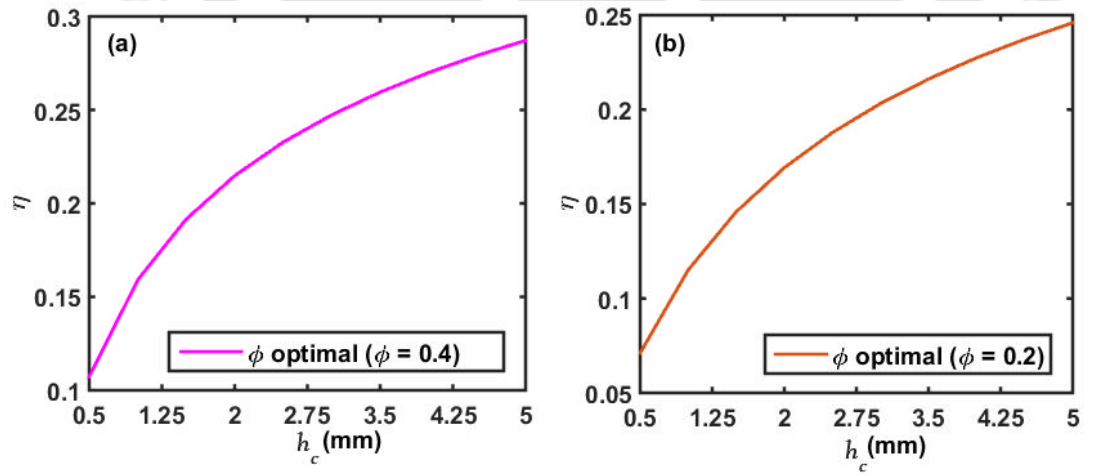

Fig. 2.8 Variation of modal loss factor (η) corresponding to the fundamental bending mode of vibration of the sandwich beam with the core-thickness (h_c); (a) fully clamped sandwich beam with the optimal value of ϕ as 0.4, (b) simply-supported sandwich beam with the optimal value of ϕ as 0.2.

It is clear from these results (Figs. 2.8(a)-2.8(b)) that the damping in the sandwich beam increases as the thickness (h_c) of VEPC layer increases while the rate of increase in the modal loss factor (η) decreases at high value of the core-thickness (h_c). So, the thickness (h_c) of the VEPC layer becomes a less sensitive parameter to the passive damping in the sandwich beam when it (h_c) reaches to a high value. However, for further results, the thickness of the VEPC layer at the core of the sandwich beam is considered as 5 mm, and the same composite layer is taken with the aforesaid optimal value of the volume fraction of inclusion.

2.4.2 Partial CLD treatment of sandwich beam using VEPC

In this section, the partial CLD treatment of the sandwich beam is presented using VEPC patches at the core. The primary objective of the partial CLD treatment is to achieve the maximum passive damping in a structure using the minimum mass/weight of the damping arrangement. Based on this objective, different types of configurations of the partial CLD treatment are addressed in the literature (Dewa et al., 1991; Grewal et al., 2013; Kung and Singh, 1998; Madeira et al., 2015; Marcelin et al., 1992). Presently, one of these configurations of the partial CLD treatment is followed where the patches of the viscoelastic damping material are used optimally according to the objective mentioned above. However, the main motive is to investigate the improvement of passive damping in the partial CLD treatment of the sandwich beam with respect to the increased weight of the overall beam when the graphite particles are incorporated dispersedly within the viscoelastic patches at the core.

The core of the sandwich beam is considered to be made of foam ($E = 35.5$ MPa, $G = 12.76$ MPa, $\rho = 32$ kg/m^3), and the VEPC patches are inserted within the core optimally based on the aforesaid objective of the partial CLD treatment. Here, the thickness (h_c) and width (b) of the VEPC patches are considered as equal to that for the overall beam, while the length (l_p) and locations of the VEPC patches are decided through the following optimization procedure.

First, a VEPC patch with a small length (10 mm) is taken. The thickness (h_c) and width (b) of the VEPC patch are equal to that for the core. This VEPC patch is located at different points over the length of the beam. At every location

of the VEPC patch, the rest of the volume of the core is filled up by foam, and the corresponding value of the modal loss factor (η) is computed for the fundamental mode of vibration of the sandwich beam. Next, the computed value of the modal loss factor (η) corresponding to a location of the small VEPC patch is plotted against the x-coordinate of the middle point of the VEPC patch at that location. This plot is illustrated in Figs. 2.9(a)-2.9(b) for two different boundary

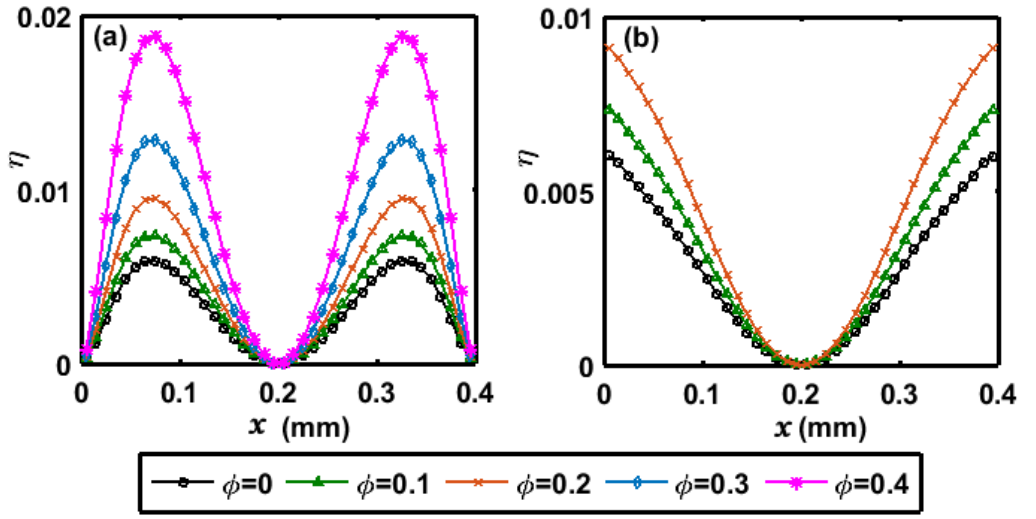

Fig. 2.9 Variation of modal loss factor (η) corresponding to the fundamental mode of vibration of the sandwich beam for different locations of the small VEPC patch within the length (L=0.4 m) of the beam; (a) fully clamped or (b) simply-supported sandwich beam.

conditions of the sandwich beam. A curve in these figures is evaluated for a specified volume fraction (ϕ) of inclusion in the VEPC patch. Now, the volumes of the small VEPC patch and foam at the core remain constant for any location of the VEPC patch within the length of the sandwich beam. Therefore, a point over a curve in Figs. 2.9(a)-2.9(b) infers the importance of the VEPC material at that point for attenuation of the fundamental mode of vibration of the sandwich beam. Accordingly, the location or x-coordinate corresponding to the maximum value of modal loss factor (η) over a curve would be the optimal location of the VEPC patch within the length of the beam. It can be observed from the curves in Figs. 2.9(a)-2.9(b) that the volume fraction (ϕ) of inclusion does not have much effect on the optimal locations of the VEPC patch over the length of the beam. So, the VEPC patch can be taken with the aforesaid optimal volume fraction of inclusion while its optimal locations appear as $x=0$ and $x=0.4$ m (Fig. 2.9(b))

for the simply-supported sandwich beam, and $x = 0.075$ m and $x = 0.325$ m (Fig. 2.9(a)) for the fully clamped sandwich beam. Presently, two VEPC patches are taken corresponding to the two optimal locations.

After deciding the optimal locations of the VEPC patches, their optimal length is determined by evaluating the variations of modal loss factor and weight of the sandwich beam for a step-wise increment of length (l_p) of the VEPC patches. In every step of increment of length (l_p) of the VEPC patches, the middle point of a patch is kept as coincident with the corresponding optimal location. If it becomes difficult to keep the middle point of a patch at the corresponding optimal location, then the minimum distance between the same points is maintained. For instance, let the lengths of a VEPC patch in two

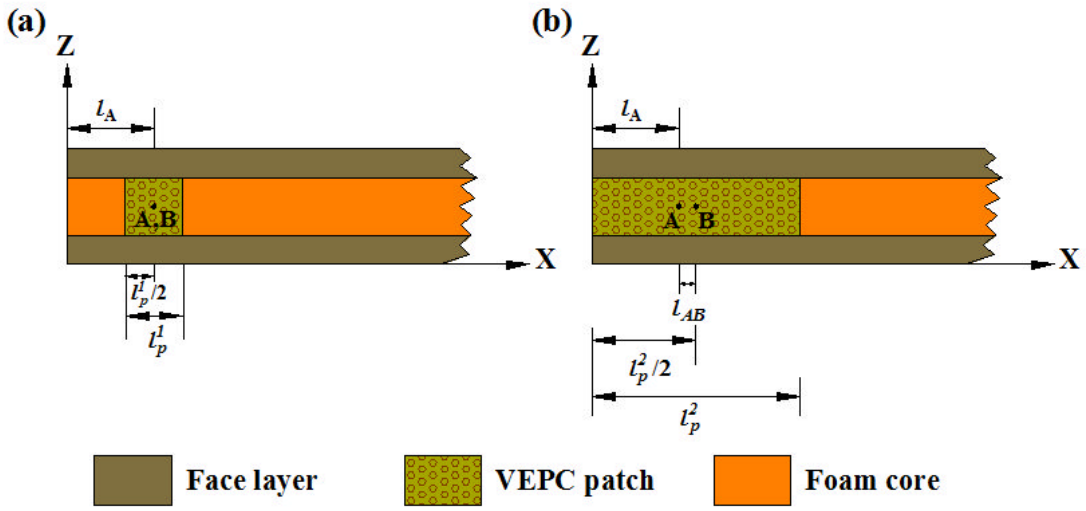

Fig. 2.10. Schematic diagram for the location of the VEPC patch following its optimal location while the length (l_p) of the VEPC patch in incremented from l_p^1 to l_p^2 ($l_p^2 > l_p^1$); (a) $l_p = l_p^1$ and (b) $l_p = l_p^2$.

consecutive steps of increment are l_p^1 and l_p^2 ($l_p^2 > l_p^1$) as shown in Figs. 2.10(a)-2.10(b), where the optimal location and the middle point of the VEPC patch are denoted by the points A and B, respectively. Now, for $l_p = l_p^1$ (Fig. 2.10(a)), half of the length ($l_p^1/2$) of the patch does not exceed the available space (l_A) so that the middle point (B) of the VEPC patch is kept as coincident with the corresponding optimal location (point A). On the next step of increment of

length ($l_p = l_p^2$) (Fig. 2.10(b)), half of the length ($l_p^2/2$) of the VEPC patch becomes greater than the available space ($(l_p^2/2) > l_A$). So, the VEPC patch is optimally located by keeping its middle point (B) at the minimum distant (l_{AB}) from the corresponding optimal location (A).

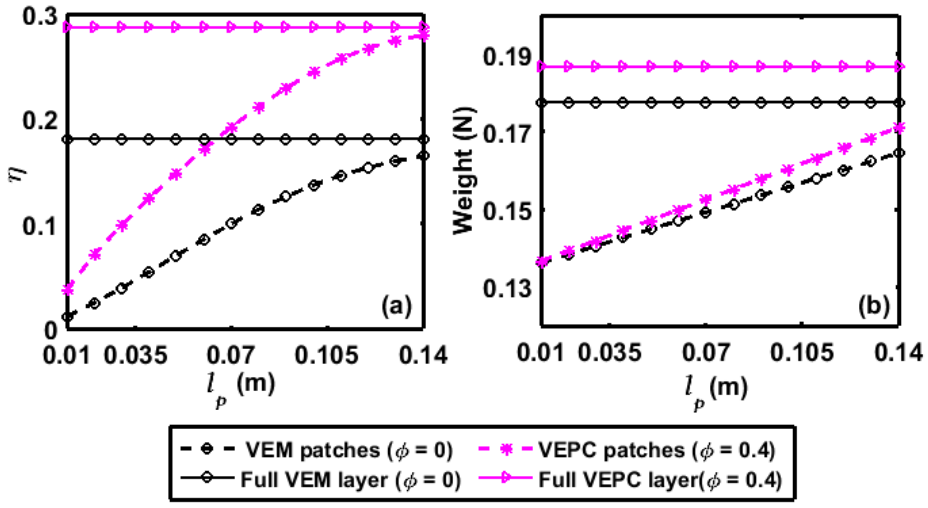

Fig. 2.11 Variations of (a) modal loss factor (η) at the fundamental mode of vibration and (b) weight of the fully clamped sandwich beam with the length (l_p) of VEPC/VEM patches at the core while the patches are located optimally.

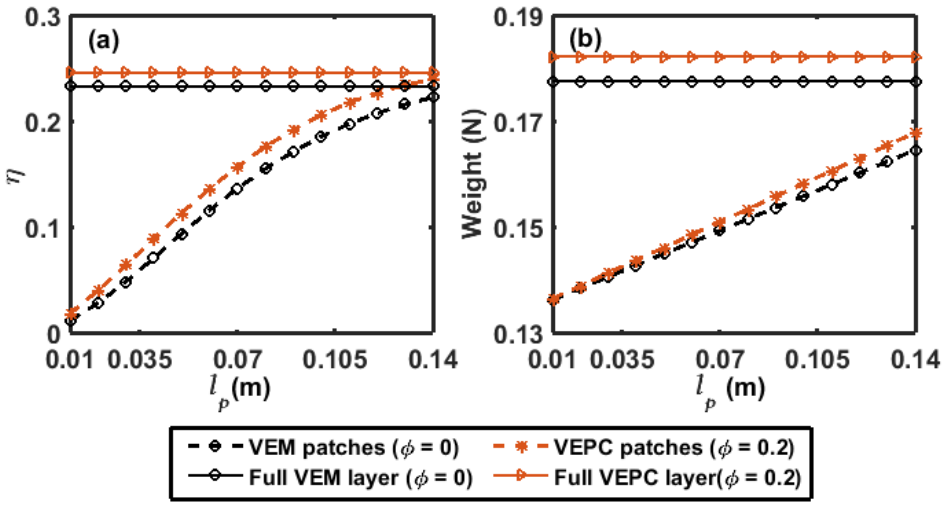

Fig. 2.12. Variations of (a) modal loss factor (η) at the fundamental mode of vibration and (b) weight of the simply-supported sandwich beam with the length (l_p) of VEPC/VEM patches at the core while the patches are located optimally.

Figures 2.11 and 2.12 illustrate the variations of modal loss factor and weight of the sandwich beam for the step-wise increment of length (l_p) of the two VEPC patches that are located following the aforesaid optimal locations over the length of the simply-supported/fully clamped beam. In each of these figures (Figs. 2.11 and 2.12), two solid lines are also drawn for indicating the reference results for modal loss factor and weight of the sandwich beam when the volume of the core is filled up by VEPC or pure viscoelastic material (VEM). It may be observed from Fig. 2.11(a) that the VEPC patches with a length (l_p) of 0.14 m provide almost the same damping as that arises by the use of the VEPC throughout the core, while the weight of the fully clamped sandwich beam decreases significantly (Fig. 2.11(b)). Similar observations are also obtained for the simply-supported sandwich beam (Figs. 2.12(a)-(b)). However, it is important to observe from these results (Figs. 2.11-2.12) that the advantages mentioned above in the partial CLD treatment appear for both the VEPC and monolithic viscoelastic material (VEM). But, the damping in the sandwich beam increases significantly for the use of the present VEPC instead of the monolithic VEM.

According to these results (Figs. 2.11-2.12), the optimal size and locations of VEPC or VEM patches are illustrated in Table 2.4 by specifying x-coordinates of left (x_L) and right (x_R) ends of every patch. Using this optimal configuration of VEPC or VEM patches within the core of foam, the frequency responses of the sandwich beam around its fundamental natural frequency are evaluated as presented in Figs. 2.13(a)-2.13(b). Similar responses of the VEPC or VEM layer that fully covers the core of the sandwich beam are also plotted in the same figures. It may be observed from these results (Figs. 2.13(a)-2.13(b)) that the optimal arrangement of VEPC or VEM patches within the core provides almost the same attenuation of the resonant displacement-amplitude as that appears for the full VEPC or VEM layer within the core of the sandwich beam.

Table 2.4 Optimal size and locations of VEPC or VEM patches at the core of the sandwich beam.

VEPC/VEM patches	Fully clamped sandwich beam		Simply-supported sandwich beam	
	x_L (m)	x_R (m)	x_L (m)	x_R (m)
Patch 1	0.005	0.145	0	0.14
Patch 2	0.255	0.395	0.26	0.4

But, the advantage of reduced weight (Figs. 2.11(b) and 2.12(b)) arises for the use of the damping material (VEPC or VEM) in the form of the patch instead of the form of the layer. More importantly, the VEPC patches provide significantly higher attenuation of the resonant displacement-amplitude than that for the VEM patches (Figs. 2.13(a)-2.13(b)) while there is a minimal difference between the corresponding weights of the sandwich beam (Figs. 2.11(b) and 2.12(b)). According to these observations, the present VEPC is a potential damping material for attenuation of vibration of sandwich beams.

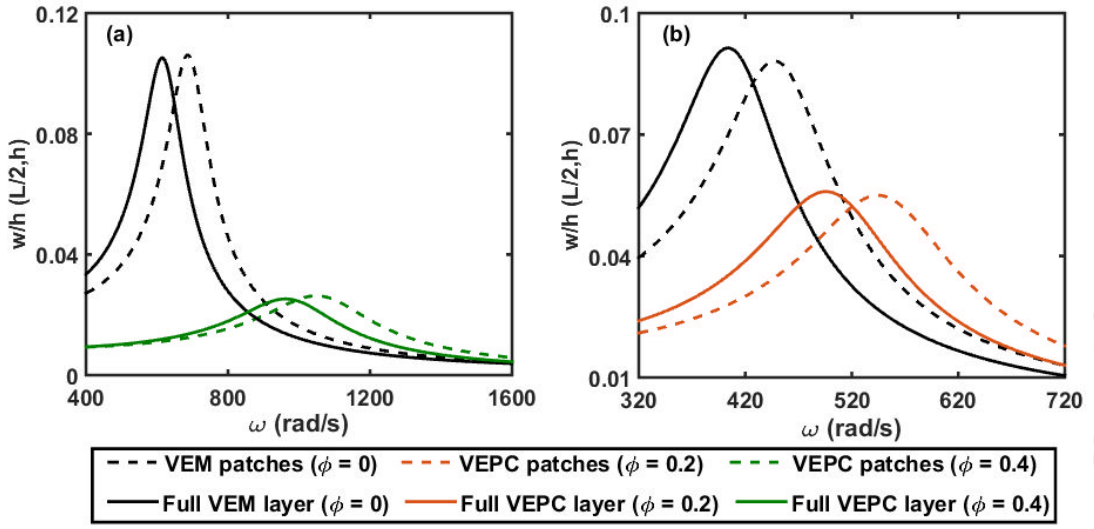

Fig. 2.13 Frequency responses of the (a) fully clamped or (b) simply-supported sandwich beam around its fundamental natural frequency either using the optimal configuration of the VEPC/VEM patches or using the full VEPC/VEM layer at the core.

2.5 Summary

The micro-sized graphite particles are dispersedly incorporated within the viscoelastic core of a fully clamped/simply-supported sandwich beam, and the damping characteristics of the sandwich beam are investigated corresponding to its fundamental bending mode of vibration. The effective properties of the VEPC core are computed using a differential scheme in conjunction with the elastic-viscoelastic correspondence principle. It is observed that the effective storage modulus of the VEPC increases for an increase in the volume fraction of inclusion of graphite particles while the effective material loss factor of the same VEPC decreases. These characteristics of the VEPC core yield improved passive damping in the sandwich beam. However, the passive damping in the sandwich

beam increases up to a certain value of the increasing volume fraction of inclusion, where the optimal value of the volume fraction of inclusion arises for the maximum passive damping in the sandwich beam. The subsequent study on the optimal partial CLD treatment of the sandwich beam reveals that the optimal size and locations of the patches of viscoelastic material do not change for the inclusion of graphite particles. Also, a minimal change of weight of the sandwich beam arises for the inclusion, while the same inclusion causes a significantly improved passive damping in the sandwich beam.

Chapter 3

Passive control of parametric instability of sandwich beams using viscoelastic particulate composite (VEPC) damping layers

3.1 Introduction

Flexible structural elements in engineering systems usually operate under various dynamic forces, where the dynamic instability through the parametric resonance is a common phenomenon for the commencement or enhancement of vibration of the structural elements. Generally, this kind of dynamic instability is called parametric instability, and it appears with three types, namely primary, secondary and combinatory parametric instabilities depending on the operating frequency range (Nayfeh and Mook, 1995). However, among these different parametric instabilities, the critical one is the principal primary parametric instability (Bolotin, 1964), and it is usually characterized by the instability width and the origin of instability of an instability region (Fig. 3.1) in the two-dimensional domain of frequency (ω) and amplitude (λ) of the applied dynamic force (Sankar et al., 2016).

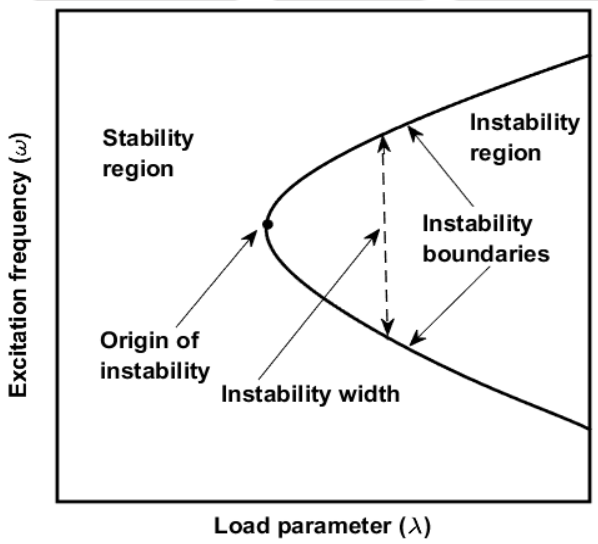

Fig. 3.1 A typical parametric instability region in the two-dimensional domain of frequency (ω) and load-amplitude (λ) of excitation.

A great deal of research on the parametric instability of various structures has been reported in the literature (Dey and Singha, 2006; Ke et al., 2013; Langthjem and Sugiyama, 2000; Mohanty et al., 2012), where it is revealed that the parametric instability may lead to the failure and/or improper functionality of structural elements during operation. So, a good number of studies on the control of parametric instability have also been reported by many researchers. In this line, the application of the CLD treatment is addressed in a good number of studies, as a corresponding review is presented in section (1.3.2.3). Through these available studies, it is revealed that the CLD treatment possesses significant passive damping capability to control the parametric instability of thin-walled flexible structures. Motivating by this observation, the study in this chapter is carried out for further development of CLD treatment in the control of parametric instability of flexible structures.

In the conventional CLD treatment, a soft viscoelastic damping layer is constrained between two stiff layers in the form of a laminate (Fig. 1.8). As the laminate undergoes bending mode of vibration, the viscoelastic damping in the structure arises mainly through the transverse shear deformation of the constrained viscoelastic layer. This passive damping is utilized in the aforesaid studies (section (1.3.2.3)) to stabilize the laminated structure by reducing the parametric instability region. This reduction of the parametric instability region occurs through a decrease in the width of instability region and a shift of the origin of instability towards a high amplitude of the applied dynamic force. Apart from these two aspects of controlling the parametric instability region, another potential way is to shift the instability region out of the frequency range of operation. It indicates a shift of the natural frequency (ω_n) of the laminated structure since the origin of instability region appears at an operating frequency (ω) that is equal to $2\omega_n / q$ ($q = 1, 2, 3, ...$) (Bolotin, 1964). However, for this additional functionality of the CLD treatment, it would be capable of regulating the stiffness of the laminated structure besides its sufficient passive damping capability. A study in this direction, particularly for enhanced functionality of the CLD treatment in the control of parametric instability, is not yet reported in the literature to the best knowledge of this researcher. However, it is attempted in this

chapter by means of incorporating the inclusion of graphite particles within the constrained viscoelastic damping layer in the CLD treatment.

The stiffness of this VEPC damping layer can be tuned by varying the volume fraction of inclusion (VFI) so that the desired natural frequency of the laminated structure or frequency-shift of the instability region may be achieved. In parallel to this potential advantage, the study in the previous chapter shows improved passive damping or energy-dissipation capability of the CLD treatment due to the inclusion in the constrained viscoelastic damping layer. So, the instability region is expected to reduce due to the improved damping besides the potential advantage of a frequency-shift of the same instability region due to the inclusion of graphite particles. A detailed investigation on these issues is performed here towards the development of the CLD treatment for improved passive control of parametric instability of flexible structures. The overall study is performed considering beam elements that usually undergo parametric instability during operation under the dynamic axial compressive load. The CLD arrangement is made through the layered beam elements having single or multiple constrained VEPC damping layers, and the characteristics of the principal primary parametric instability region are mainly investigated by varying the volume fraction of inclusion in the VEPC layers.

In section 3.2, the geometric configurations of the layered beams with the constrained VEPC layers are first described. Next, in section 3.3, an FE model of the layered beams under the dynamic axial compressive load is derived, and the method of solution is furnished for evaluation of the parametric instability region, modal damping and critical buckling load. Subsequently, the numerical results are presented in section 3.4, where, first, the dynamic characteristics of the layered beams under an axial compressive load are analyzed particularly for the inclusion of graphite particles in the constrained viscoelastic layers. Next, the effects of the inclusion on the static/dynamic stability of the layered beams are investigated. Finally, the overall study on this chapter is summarized in section 3.5.

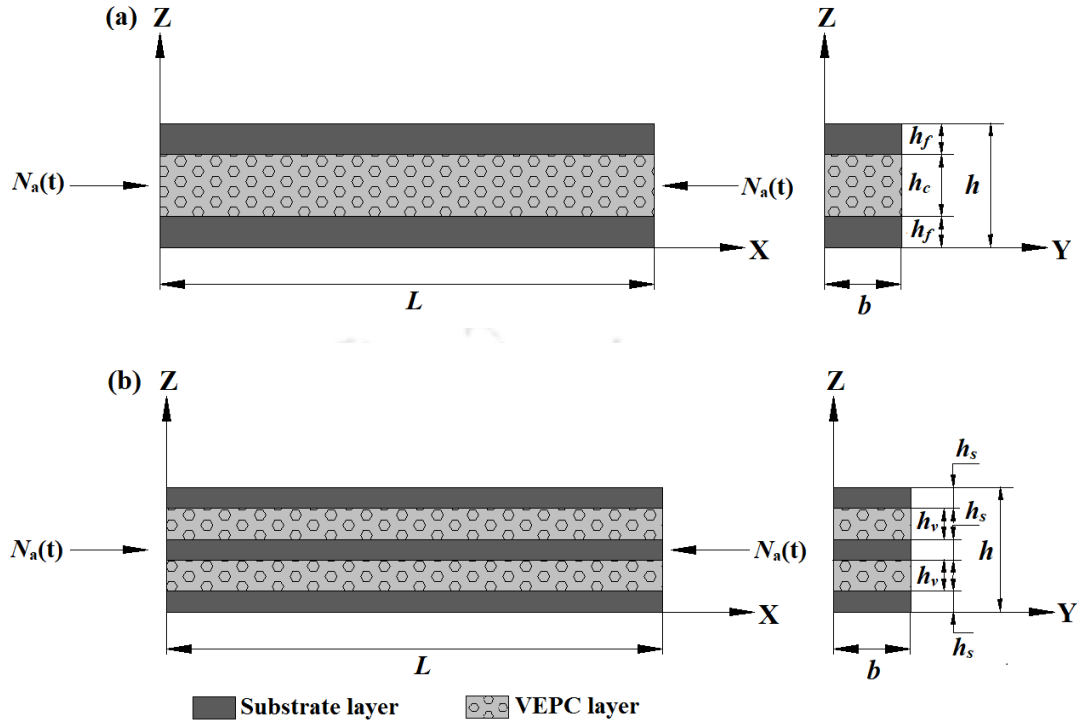

Fig. 3.2 Schematic diagrams of (a) three-layered and (b) five-layered beams with constrained VEPC layers.

3.2 Layered beams with constrained VEPC layers

The CLD treatment is usually comprised of one viscoelastic damping layer. However, the same damping treatment may also be comprised of multiple viscoelastic layers for its enhanced damping effectiveness (Alam and Asnani, 1984a, 1984b; Suzuki et al., 2003). This observation is reported in the literature for the CLD treatment using monolithic viscoelastic layers. But the same observation may not hold for the present CLD treatment using the VEPC damping layers. Therefore, the present study for the CLD treatment of parametric instability of beam elements is performed considering two different layered beams, as shown in Figs. 3.2(a)-3.2(b). The first one (Fig. 3.2(a)) is a sandwich beam having the VEPC core and identical face/substrate layers. The next one (Fig. 3.2(b)) is a multi-layered beam having two identical VEPC layers that are constrained by three uniform substrate layers. The VEPC core layer in the sandwich beam (Fig. 3.2(a)) is divided through its middle surface to obtain two identical VEPC layers in forming the multi-layered beam (Fig. 3.2(b)) ($h_v = h_c/2$).

Also, the total thickness of the substrate layers remains the same ($h_s = 2h_f/3$) for both the layered beams.

3.3 Mathematical formulation

The stability analysis in the FE framework usually involves a high computational cost, and this difficulty may appear severely for a large number of nodal degrees of freedom in the FE model. However, for achieving reduced computational cost, the equivalent single layer (ESL) and layer-wise (LW) theories are recommended for mathematical modelling and analysis of layered structures (Filippi and Carrera, 2016; Reddy, 2003). Of these, theories based on the ESL approach may not be able to correctly predict the dynamic characteristics of layered viscoelastic structures, whereas LW zigzag theories provide high level accuracy (Filippi and Carrera, 2017). Moreover, in the LW approach, the displacement field in each subdomain of the mathematical/physical layer can be defined independently, and it provides a trade-off between computational cost and accuracy (Filippi and Carrera, 2016). Presently, LW theory is employed where the cross-section of a layered beam is divided into a number of subdomains that are the physical layers. In every layer, the in-plane displacement component is taken through Taylor expansion in the thickness coordinate as follows,

$$u^k(x,z,t) = u_0(x,t) + z_i^k \alpha_i(x,t) + \left(z_i^k\right)^2 \beta_i(x,t) + \left(z_i^k\right)^3 \gamma_i(x,t),$$

$$w^k(x,z,t) = w_0(x,t)$$

$$\alpha_k = \left.\frac{\partial u^k}{\partial z}\right|_{z_R^k}, \quad \beta_k = \left.\frac{1}{2!}\frac{\partial^2 u^k}{\partial z^2}\right|_{z_R^k}, \quad \gamma_k = \left.\frac{1}{3!}\frac{\partial^3 u^k}{\partial z^3}\right|_{z_R^k} \tag{3.1}$$

where, the superscript (k) / subscript (i) indicates a layer in the layered beams starting from its (k/i) value as 1 for the bottom-most layer; a repeated index within a term implies summation over the range of that index; u^k and w^k are the displacements at any point in the k^{th} layer along the x and z directions, respectively, while u_0 and w_0 denote the same at any point on the reference plane ($z = 0$). The different thickness coordinates (z_i^k) are given in Eq. (3.2) where the

thickness of the k^{th} layer and the total number of layers in a layered beam are denoted by h_k and N_L, respectively.

$$z_R^k = 0, h_1, (h_1+h_2), ..., \left(h_1+h_2+....+h_{(N_L-1)}\right) \text{ for } k = 1,2,3,....,(N_L-1)$$

$$z_1^k = z \text{ or } h_1 \text{ for } k=1 \text{ or } k>1$$

$$z_2^k = 0 \text{ or } (z-h_1) \text{ or } h_2 \text{ for } k<2 \text{ or } k=2 \text{ or } k>2$$

$$z_3^k = 0 \text{ or } \left(z-h_1-h_2\right) \text{ or } h_3 \text{ for } k<3 \text{ or } k=3 \text{ or } k>3$$

.

.

$$z_{(N_L-1)}^k = 0 \text{ or } \left(z-h_1-h_2-h_3-.....-h_{(N_L-2)}\right) \text{ or } h_{(N_L-1)} \text{ for } k<(N_L-1)$$

$$\text{or } k=(N_L-1) \text{ or } k>(N_L-1)$$

$$z_{N_L}^k = 0 \text{ or } \left(z-h_1-h_2-h_3-.....-h_{(N_L-1)}\right) \text{ for } k<N_L \text{ or } k=N_L \tag{3.2}$$

The displacement components (u^k, w^k) at any point within the k^{th} layer can be written as,

$$\boldsymbol{d}^k = \left(\boldsymbol{d}_t + \boldsymbol{Z}_r^k \boldsymbol{d}_r\right) \tag{3.3a}$$

$$\boldsymbol{d}^k = \left\{u^k \quad w^k\right\}^{\mathrm{T}}, \ \boldsymbol{d}_t = \left\{u_0 \quad w_0\right\}^{\mathrm{T}},$$

$$\boldsymbol{d}_r = \left\{\alpha_1 \quad \beta_1 \quad \gamma_1 \quad \alpha_2 \quad \beta_2 \quad \gamma_2 \quad .... \quad .... \quad .... \quad \alpha_{N_L} \quad \beta_{N_L} \quad \gamma_{N_L}\right\}^{\mathrm{T}}$$

$$\boldsymbol{Z}_r^k = \left[\boldsymbol{Z}_1^k \quad \boldsymbol{Z}_2^k \quad .... \quad .... \quad .... \quad \boldsymbol{Z}_{N_L}^k\right], \ \boldsymbol{Z}_i^k = \begin{bmatrix} z_i^k & \left(z_i^k\right)^2 & \left(z_i^k\right)^3 \\ 0 & 0 & 0 \end{bmatrix} \tag{3.3b}$$

The displacement components in Eqs. (3.3a)-(3.3b) can also be written in terms of the generalized displacement vector ($\boldsymbol{d}$) and transformation matrices ($\boldsymbol{T}_t$, $\boldsymbol{T}_r$) as follows,

$$\boldsymbol{d}^k = \left(\boldsymbol{T}_t + \boldsymbol{Z}_r^k \boldsymbol{T}_r\right)\boldsymbol{d} \tag{3.4a}$$

$$\boldsymbol{d}=\left\{u_0 \quad w_0 \quad \alpha_1 \quad \beta_1 \quad \gamma_1 \quad \alpha_2 \quad \beta_2 \quad \gamma_2 \quad .... \quad .... \quad .... \quad \alpha_{N_L} \quad \beta_{N_L} \quad \gamma_{N_L}\right\}^{\mathrm{T}}$$

$$\boldsymbol{T}_t=\left[\boldsymbol{I}_{(2\times 2)} \quad \boldsymbol{O}_{(2\times 3N_L)}\right],\ \boldsymbol{T}_r=\left[\boldsymbol{O}_{(3N_L\times 2)} \quad \boldsymbol{I}_{(3N_L\times 3N_L)}\right] \tag{3.4b}$$

where, $\boldsymbol{I}$ and $\boldsymbol{O}$ denote the identity matrix and null matrix, respectively, and the subscript $(m\times n)$ indicates the size of a matrix. The state of strain and the state of stress at any point within a layer (k) can be written as,

$$\varepsilon_b^k=\varepsilon_x^k,\ \varepsilon_s^k=\varepsilon_{xz}^k \tag{3.5a}$$

$$\sigma_b^k=\sigma_x^k,\ \sigma_s^k=\sigma_{xz}^k \tag{3.5b}$$

where, ε_x^k and σ_x^k are the normal strain and normal stress, respectively, along the x direction within the k^{th} layer; ε_{xz}^k and σ_{xz}^k are the shear strain and shear stress, respectively, over the xz-plane of the k^{th} layer. The strain-displacement relations for the k^{th} layer can be expressed as,

$$\varepsilon_b^k=\left(\varepsilon_{b0}+\boldsymbol{Z}_b^k\boldsymbol{\kappa}_b\right),\ \varepsilon_s^k=\left(\varepsilon_{s0}+\boldsymbol{Z}_s^k\boldsymbol{\kappa}_s\right)$$

$$\varepsilon_{b0}=\frac{\partial u_0}{\partial x},\ \varepsilon_{s0}=\frac{\partial w_0}{\partial x},$$

$$\boldsymbol{k}_b=\left\{\boldsymbol{k}_b^1 \quad \boldsymbol{k}_b^2 \quad .... \quad .... \quad .... \quad \boldsymbol{k}_b^{N_L}\right\}^{\mathrm{T}},$$

$$\boldsymbol{k}_s=\left\{\boldsymbol{k}_s^1 \quad \boldsymbol{k}_s^2 \quad .... \quad .... \quad .... \quad \boldsymbol{k}_s^{N_L}\right\}^{\mathrm{T}},$$

$$\boldsymbol{k}_b^i=\left\{\frac{\partial\alpha_i}{\partial x} \quad \frac{\partial\beta_i}{\partial x} \quad \frac{\partial\gamma_i}{\partial x}\right\},\ \boldsymbol{k}_s^i=\left\{\alpha_i \quad \beta_i \quad \gamma_i\right\},$$

$$\boldsymbol{Z}_b^k=\left\{\boldsymbol{Z}_{b1}^k \quad \boldsymbol{Z}_{b2}^k \quad .... \quad .... \quad .... \quad \boldsymbol{Z}_{bN_L}^k\right\},$$

$$\boldsymbol{Z}_{bi}^k=\left\{z_i^k \quad \left(z_i^k\right)^2 \quad \left(z_i^k\right)^3\right\},\ \boldsymbol{Z}_s^k=\frac{\partial}{\partial z}\left(\boldsymbol{Z}_b^k\right) \tag{3.6}$$

All layers in the beams (Figs. 3.2(a) and 3.2(b)) are made of isotropic materials. So, according to the state of stress and state of strain (Eqs. (3.5a) and (3.5b)), the constitutive relations for a layer (k) in the layered beams can be written as,

$$\sigma_b^k = C_b^k(\omega)\,\varepsilon_b^k,$$

$$\sigma_s^k = C_s^k(\omega)\,\varepsilon_s^k,\ k = 1,2,3,\ldots..,N_L$$

$$C_b^k(\omega) = E^k(\omega),\ C_s^k(\omega) = G^k(\omega) \tag{3.7}$$

where, the moduli ($E^k(\omega)$, $G^k(\omega)$) for the substrate layers are real quantities and independent of the operating frequency (ω). However, the same moduli for the VEPC layers are the frequency-dependent complex quantities since the VEPC layers are modelled using complex stiffness method and the layered beams are considered to operate at a constant temperature. These moduli ($E^k(\omega)$, $G^k(\omega)$) of the VEPC layers can be obtained by the solution of Eqs. (2.6a)-(2.6b), as the corresponding method of solution is described in section 2.2.1.

3.3.1 Finite element formulation

The first variations of the strain energy (δT_P) and kinetic energy (δT_K) of a layered beam at an instant of time (t) can be written as given in Eqs. (3.8) and (3.9), where ρ^k is the mass density of the k^{th} layer.

$$\delta T_P = \int_0^L \left[\sum_{k=1}^{N_L} \int_{h_k}^{h_{k+1}} \left\langle (\delta\varepsilon_b^k)\sigma_b^k + (\delta\varepsilon_s^k)\sigma_s^k \right\rangle dz \right] dx \tag{3.8}$$

$$\delta T_K = \int_0^L \left[\sum_{k=1}^{N_L} \int_{h_k}^{h_{k+1}} \left\langle \left\{ \delta\dot{u}^k \quad \delta\dot{w}^k \right\} \rho^k \left\{ \dot{u}^k \quad \dot{w}^k \right\}^{\mathrm{T}} \right\rangle dz \right] dx \tag{3.9}$$

For the applied axial compressive load ($N_a(t)$), the first variation of the external work done (δW) at an instant of time (t) can be written as,

$$\delta W = \int_0^L \left\langle \frac{N_a}{b} \frac{\partial w_0}{\partial x} \frac{\partial(\delta w_0)}{\partial x} \right\rangle dx = \int_0^L \frac{N_a}{b} \left\langle \left(\frac{\partial(\delta \boldsymbol{d})}{\partial x} \right)^{\mathrm{T}} \boldsymbol{T}_t^{\mathrm{T}} \begin{bmatrix} 0 & 0 \\ 0 & 1 \end{bmatrix} \boldsymbol{T}_t \frac{\partial \boldsymbol{d}}{\partial x} \right\rangle dx \tag{3.10}$$

For deriving the FE equations of motion, the length of the layered beams is discretized by 3-node isoparametric bar elements. The generalized displacement vector ($\boldsymbol{d}$, Eq. (3.4)) at any point within a typical element can be expressed in

terms of the shape function matrix ($\boldsymbol{N}$) and the elemental nodal displacement vector ($\boldsymbol{d}^e$) similar to Eq. (2.11).

$$\boldsymbol{d} = \boldsymbol{N}\boldsymbol{d}^e \tag{2.11}$$

Using Eq. (2.11), the generalized strain vectors (Eq. (3.6)) at any point within a typical element can be written as,

$$\begin{gathered}\varepsilon_{b0} = \boldsymbol{B}_{b0}\boldsymbol{d}^e\ ,\ \boldsymbol{\kappa}_b = \boldsymbol{B}_{b\kappa}\boldsymbol{d}^e\ ,\ \varepsilon_{s0} = \boldsymbol{B}_{s0}\boldsymbol{d}^e\ ,\ \boldsymbol{\kappa}_s = \boldsymbol{B}_{s\kappa}\boldsymbol{d}^e\ ,\\ \boldsymbol{B}_{b0} = L_{b0}\boldsymbol{T}_t\boldsymbol{N}\ ,\ \boldsymbol{B}_{b\kappa} = \boldsymbol{L}_{b\kappa}\boldsymbol{T}_r\boldsymbol{N}\ ,\ \boldsymbol{B}_{s0} = L_{s0}\boldsymbol{T}_t\boldsymbol{N}\ ,\ \boldsymbol{B}_{s\kappa} = \boldsymbol{L}_{s\kappa}\boldsymbol{T}_r\boldsymbol{N}\ ,\end{gathered} \tag{3.11a}$$

$$L_{b0} = \partial/\partial x\ ,\ \boldsymbol{L}_{b\kappa} = \boldsymbol{I}_{(3N_L\times 3N_L)}\otimes\left(\partial/\partial x\right),\ L_{s0} = \partial/\partial x\ ,\ \boldsymbol{L}_{s\kappa} = \boldsymbol{I}_{(3N_L\times 3N_L)} \tag{3.11b}$$

where, $\otimes$ represents Kronecker product and $\boldsymbol{I}$ is the unit matrix. Using Eqs. (3.4), (3.6), (3.7), (2.11) and (3.11) in Eqs. (3.8), (3.9) and (3.10), the internal energy (δT_P), kinetic energy (δT_K) and external work done (δW) can be obtained for a typical element. Subsequently, employing extended Hamilton's principle (Eq. (3.12)), the elemental equations of motion can be obtained, as given in Eqs. (3.13) and (3.14).

$$\int_{t_1}^{t_2}\left(\delta T_K - \delta T_P + \delta W\right)dt = 0 \tag{3.12}$$

$$\boldsymbol{M}^e\ddot{\boldsymbol{d}}^e + \left(\boldsymbol{K}_b^e(\omega) + \boldsymbol{K}_s^e(\omega) - N_a(t)\,\boldsymbol{K}_g^e\right)\boldsymbol{d}^e = 0 \tag{3.13}$$

$$\boldsymbol{K}_b^e(\omega) = \int_{L^e}\left[\left(\boldsymbol{B}_{b0}\right)^{\mathrm{T}}\left\langle A_b(\omega)\,\boldsymbol{B}_{b0} + \boldsymbol{B}_{b1}(\omega)\,\boldsymbol{B}_{b\kappa}\right\rangle + \left(\boldsymbol{B}_{b\kappa}\right)^{\mathrm{T}}\left\langle \boldsymbol{B}_{b2}(\omega)\,\boldsymbol{B}_{b0} + \boldsymbol{D}_b(\omega)\,\boldsymbol{B}_{b\kappa}\right\rangle\right]dL^e\ ,$$

$$\boldsymbol{K}_s^e(\omega) = \int_{L^e}\left[\left(\boldsymbol{B}_{s0}\right)^{\mathrm{T}}\left\langle A_s(\omega)\,\boldsymbol{B}_{s0} + \boldsymbol{B}_{s1}(\omega)\,\boldsymbol{B}_{s\kappa}\right\rangle + \left(\boldsymbol{B}_{s\kappa}\right)^{\mathrm{T}}\left\langle \boldsymbol{B}_{s2}(\omega)\,\boldsymbol{B}_{s0} + \boldsymbol{D}_s(\omega)\,\boldsymbol{B}_{s\kappa}\right\rangle\right]dL^e\ ,$$

$$\boldsymbol{M}^e = \int_{L^e}\left[\boldsymbol{N}^{\mathrm{T}}\left\langle\left(\boldsymbol{T}_t\right)^{\mathrm{T}} m_1\boldsymbol{T}_t + \left(\boldsymbol{T}_t\right)^{\mathrm{T}}\boldsymbol{m}_2\boldsymbol{T}_r + \left(\boldsymbol{T}_r\right)^{\mathrm{T}}\boldsymbol{m}_3\boldsymbol{T}_t + \left(\boldsymbol{T}_r\right)^{\mathrm{T}}\boldsymbol{m}_4\boldsymbol{T}_r\right\rangle\boldsymbol{N}\right]dL^e\ ,$$

$$\boldsymbol{K}_g^e = \frac{1}{b}\int_{L^e}\left\langle\left(\boldsymbol{B}_{b0}\right)^{\mathrm{T}}\begin{bmatrix}0 & 0\\ 0 & 1\end{bmatrix}\boldsymbol{B}_{b0}\right\rangle dL^e \tag{3.14}$$

where, L^e is the elemental length and the other quantities are as follows,

$$A_b(\omega) = \sum_{k=1}^{N_L}\int_{h_k}^{h_{k+1}} C_b^k(\omega)\,dz\ ,\ \boldsymbol{B}_{b1}(\omega) = \sum_{k=1}^{N_L}\int_{h_k}^{h_{k+1}} C_b^k(\omega)\,\boldsymbol{Z}_b^k\,dz\ ,$$

$$\boldsymbol{B}_{b2}(\omega)=\sum_{k=1}^{N_L}\int_{h_k}^{h_{k+1}}\left(\boldsymbol{Z}_b^k\right)^{\mathrm{T}}C_b^k(\omega)\,dz\,,\ \boldsymbol{D}_b(\omega)=\sum_{k=1}^{N_L}\int_{h_k}^{h_{k+1}}\left(\boldsymbol{Z}_b^k\right)^{\mathrm{T}}C_b^k(\omega)\,\boldsymbol{Z}_b^k\,dz\,,$$

$$A_s(\omega)=\sum_{k=1}^{N_L}\int_{h_k}^{h_{k+1}}C_s^k(\omega)\,dz\,,\ \boldsymbol{B}_{s1}(\omega)=\sum_{k=1}^{N_L}\int_{h_k}^{h_{k+1}}C_s^k(\omega)\,\boldsymbol{Z}_s^k\,dz\,,$$

$$\boldsymbol{B}_{s2}(\omega)=\sum_{k=1}^{N_L}\int_{h_k}^{h_{k+1}}\left(\boldsymbol{Z}_s^k\right)^{\mathrm{T}}C_s^k(\omega)\,dz\,,\ \boldsymbol{D}_s(\omega)=\sum_{k=1}^{N_L}\int_{h_k}^{h_{k+1}}\left(\boldsymbol{Z}_s^k\right)^{\mathrm{T}}C_s^k(\omega)\,\boldsymbol{Z}_s^k\,dz\,,$$

$$m_1=\sum_{k=1}^{N_L}\int_{h_k}^{h_{k+1}}\rho^k dz\ \boldsymbol{m}_2=\sum_{k=1}^{N_L}\int_{h_k}^{h_{k+1}}\rho^k\boldsymbol{Z}_r^k dz\,,$$

$$\boldsymbol{m}_3=\sum_{k=1}^{N_L}\int_{h_k}^{h_{k+1}}\left(\boldsymbol{Z}_r^k\right)^{\mathrm{T}}\rho^k dz\,,\boldsymbol{m}_4=\sum_{k=1}^{N_L}\int_{h_k}^{h_{k+1}}\left(\boldsymbol{Z}_r^k\right)^{\mathrm{T}}\rho^k\boldsymbol{Z}_r^k dz \tag{3.15}$$

Assembling the elemental equations (Eqs. (3.13)), the following global FE equations of motion of the layered beams can be obtained,

$$\boldsymbol{M}\ddot{\boldsymbol{X}}+\left\langle\boldsymbol{K}(\omega)-N_a(t)\,\boldsymbol{K}_g\right\rangle\boldsymbol{X}=0\,,\ \boldsymbol{K}(\omega)=\left\langle\boldsymbol{K}_b(\omega)+\boldsymbol{K}_s(\omega)\right\rangle \tag{3.16}$$

where, $\boldsymbol{M}$ is the global mass matrix; $\boldsymbol{K}_b(\omega)$ and $\boldsymbol{K}_s(\omega)$ are the bending and transverse shear counterparts of the global stiffness matrix $\boldsymbol{K}(\omega)$; $\boldsymbol{K}_g$ is the global geometric stiffness matrix; $\boldsymbol{X}$ is the global nodal displacement vector. Since the VEPC is presently modelled using the complex stiffness method, Eq. (3.16) can be written as,

$$\boldsymbol{M}\ddot{\boldsymbol{X}}+\left\langle\boldsymbol{K}^R(\omega)+j\boldsymbol{K}^I(\omega)-N_a(t)\,\boldsymbol{K}_g\right\rangle\boldsymbol{X}=0\,,\ j=\sqrt{-1} \tag{3.17}$$

where, the superscripts R and I indicate real and imaginary counterparts of a complex quantity, respectively. The periodically varying axial compressive load ($N_a(t)$) is considered in the following form (Bolotin, 1964),

$$N_a(t)=N_0\left(1+\lambda\cos\omega t\right) \tag{3.18}$$

where, N_0 is the static axial compressive load and λ is the dynamic load parameter. According to this form of the axial compressive load, Eq. (3.17) can be modified as,

$$\boldsymbol{M}\ddot{\boldsymbol{X}}+\left\langle\boldsymbol{K}^R(\omega)+j\boldsymbol{K}^I(\omega)-N_0(1+\lambda\cos\omega t)\boldsymbol{K}_g\right\rangle\boldsymbol{X}=0 \tag{3.19}$$

3.3.2 Formulation for the parametric instability analysis

The dynamic instability of the layered beams appears through the parametric resonance where the excitation frequency (ω) is equal to $2\omega_n / q$ ($q = 1,2,3,....$) (Bolotin, 1964). Here, the natural frequency (ω_n) of a layered beam corresponding to its static equilibrium under the static axial compressive load (N_0) can be evaluated by forming an eigenvalue problem from Eq. (3.19) as follows,

$$\left\langle \boldsymbol{K}^R(\omega_i) + j\boldsymbol{K}^I(\omega_i) - N_0\boldsymbol{K}_g \right\rangle \boldsymbol{\psi}_i = \omega_i^2 \boldsymbol{M}\boldsymbol{\psi}_i \tag{3.20}$$

where, $\boldsymbol{\psi}_i$ and ω_i are the complex eigenvector and natural frequency, respectively for the i^{th} mode of vibration of the layered beam. It may be noted here that a similar equation (Eq. (2.17)) also appeared in the previous chapter, and the same procedure of solution is applied here for the solution of Eq. (3.20) in the evaluation of the complex natural frequency. Subsequently, Eq. (2.18) is utilized for computation of the natural frequency and the modal loss factor of the layered beams.

However, it is important to note from Eq, (3.20) that the stiffness of the layered beam decreases for an increase in the static axial compressive load (N_0). So, the natural frequency of the layered beam decreases and even approaches to zero-value for the increasing static axial compressive load (N_0). The zero-value of the natural frequency implies the instability of the layered beam due to divergence, and thus the corresponding static axial compressive load (N_0) can be marked as the critical bucking load (N_{cr}) (Deng et al., 2017; Gu et al., 2017 Paidoussis, 1998). According to this characteristic, the critical buckling (N_{cr}) load is presently computed, and the parametric instability of the layered beams is analyzed at their pre-buckled equilibrium state by assigning the static axial compressive load (N_0) as less than the critical buckling load (N_{cr}).

The parametric instability of a layered beam at its pre-buckled equilibrium state arises due to the dynamic counterpart ($N_0 \lambda \cos\omega t$) of the applied axial compressive load (Eq. (3.18)). The corresponding instability region is presently evaluated by implementing Bolotin's method (Bolotin, 1964). According to this

method, the periodic displacement ($\boldsymbol{X}(t)$) of a layered beam during its vibration through parametric resonance can be assumed as (Paidoussis, 1998),

$$\boldsymbol{X}(t) = \sum_{n=1,3,5..}^{N_F} \left\langle \boldsymbol{c}_n e^{jn\omega t/2} + \boldsymbol{c}_{-n} e^{-jn\omega t/2} \right\rangle \tag{3.21}$$

where, $\boldsymbol{c}_n$ and $\boldsymbol{c}_{-n}$ are the complex amplitude vectors and N_F indicates the number of terms in the complex Fourier series. Substituting this assumed solution (Eq. (3.21)) in the finite element equations of motion (Eq. (3.19) or Eq. (3.22)), a set of algebraic equations can be obtained by taking the coefficients of the terms $e^{jn\omega t/2}$ and $e^{-jn\omega t/2}$ as equal to zero. For instance, Eq. (3.23) illustrates the obtained algebraic equations for the consideration of $N_F = 3$ in the solution (Eq. (3.21)) where $\boldsymbol{0}$ is the null matrix.

$$\boldsymbol{M}\ddot{\boldsymbol{X}} + \left[\boldsymbol{K}^R(\omega) + j\boldsymbol{K}^I(\omega) - N_0 \left\langle 1 + \lambda \left(\frac{e^{j\omega t} + e^{-j\omega t}}{2} \right) \right\rangle \boldsymbol{K}_g \right] \boldsymbol{X} = 0 \tag{3.22}$$

$$\begin{bmatrix} \boldsymbol{S}_{11} & \boldsymbol{S}_{12} & \boldsymbol{S}_{13} & \boldsymbol{0} \\ \boldsymbol{S}_{21} & \boldsymbol{S}_{22} & \boldsymbol{0} & \boldsymbol{S}_{24} \\ \boldsymbol{S}_{31} & \boldsymbol{0} & \boldsymbol{S}_{33} & \boldsymbol{0} \\ \boldsymbol{0} & \boldsymbol{S}_{42} & \boldsymbol{0} & \boldsymbol{S}_{44} \end{bmatrix} \begin{Bmatrix} \boldsymbol{c}_1 \\ \boldsymbol{c}_{-1} \\ \boldsymbol{c}_3 \\ \boldsymbol{c}_{-3} \end{Bmatrix} = \boldsymbol{0}$$

$$\boldsymbol{S}_{11} = \left(-\frac{1}{4}\omega^2 \boldsymbol{M} + \boldsymbol{K}(\omega) - N_0 \boldsymbol{K}_g \right),\ \boldsymbol{S}_{12} = \left(-\frac{\lambda}{2} N_0 \boldsymbol{K}_g \right),\ \boldsymbol{S}_{13} = \boldsymbol{S}_{12},\ \boldsymbol{S}_{21} = \boldsymbol{S}_{12},\ \boldsymbol{S}_{22} = \boldsymbol{S}_{11},$$

$$\boldsymbol{S}_{24} = \boldsymbol{S}_{12},\ \boldsymbol{S}_{31} = \boldsymbol{S}_{12},\ \boldsymbol{S}_{33} = \left(-\frac{9}{4}\omega^2 \boldsymbol{M} + \boldsymbol{K}(\omega) - N_0 \boldsymbol{K}_g \right),\ \boldsymbol{S}_{42} = \boldsymbol{S}_{12},\ \boldsymbol{S}_{44} = \boldsymbol{S}_{33} \tag{3.23}$$

It may be noted here that an appropriate number (N_F) of harmonic terms in the assumed solution (Eq. (3.21)) is to be considered for sufficient numerical accuracy in the result. However, the homogeneous algebraic equations similar to Eq. (3.23) provide a characteristic equation in terms of the excitation frequency (ω) and dynamic load parameter (λ). The solutions (λ, ω) of this characteristic equation constitute the boundary of the parametric instability region. Presently, the parametric instability of the layered beams is studied corresponding to the principal primary parametric resonance that occurs at the excitation frequency $2\omega_1$ where ω_1 is the fundamental natural frequency. Therefore, the excitation

frequency (ω) is varied around $2\omega_1$, and the corresponding variation of the dynamic load parameter (λ) is computed by the solution of the characteristic equation using MATLAB function '*solve*'. Here, for every excitation frequency, the frequency-dependent material properties of VEPC layers are first computed by solving Eqs. (2.6a)-(2.6b), and then the characteristic equation is formed for the solution of the load parameter (λ) at that excitation frequency (ω). The plot of these solutions (λ, ω) yields the boundary of the principal primary parametric instability region in the two-dimensional domain of ω and λ.

For the finite element discretization, a large number (N) of nodal degrees of freedom may appear, and it usually involves a high computational time in the solution of the characteristic equation. In this concern, a reduced-order model of the system (Eq. (3.22)) can be derived without the loss of sufficient numerical accuracy in the results, and it essentially reduces the computational time. For derivation of this reduced-order model, the basis vectors may be chosen from the eigenmodes ($\boldsymbol{\psi}_i$), and a modal matrix ($\boldsymbol{\psi}$) can be formed with a suitable number of eigenmodes ($\boldsymbol{\psi}_i$, $i=1,2,3,.....q$, $q \le N$) for the transformation (Eq. (3.24)) from the nodal ($\boldsymbol{X}$) to the modal ($\boldsymbol{X}^r$) coordinates. Using this coordinate transformation, the governing equation of motion (Eq. (3.22)) can be expressed in terms of a small number (q) of modal coordinates ($\boldsymbol{X}^r$) instead of a large number (N) of nodal coordinates ($\boldsymbol{X}$), as given in Eq. (3.25). The corresponding solution can be assumed similar to Eq. (3.21), as given through Eq. (3.26). Introducing Eq. (3.26) in Eq. (3.25), the characteristic equation can be obtained in the similar form as that appears in Eq. (3.23), where the size of the matrices ($\boldsymbol{S}_{ij}$) reduces to ($q \times q$) from ($N \times N$). Here, the reduction in the size of the matrices ($\boldsymbol{S}_{ij}$) essentially provides the advantage of the reduced computational time; however, the number (q) of eigenmodes is to be chosen appropriately through a convergence study for achieving sufficient numerical accuracy in the results.

$$\boldsymbol{X} = \boldsymbol{\psi}\boldsymbol{X}^r, \ \boldsymbol{\psi} = \begin{bmatrix} \boldsymbol{\psi}_1 & \boldsymbol{\psi}_2 & \boldsymbol{\psi}_3 & \dots & \dots & \boldsymbol{\psi}_q \end{bmatrix} \tag{3.24}$$

$$\boldsymbol{M}^r \ddot{\boldsymbol{X}}^r + \left[\boldsymbol{K}^r(\omega) - N_0 \left\langle 1 + \lambda \left(\frac{e^{j\omega t} + e^{-j\omega t}}{2} \right) \right\rangle \boldsymbol{K}_g^r \right] \boldsymbol{X}^r = 0 \,,$$

$$\boldsymbol{M}^r = \left(\boldsymbol{\psi}^T \boldsymbol{M} \boldsymbol{\psi} \right), \; \boldsymbol{K}^r = \left(\boldsymbol{\psi}^T \boldsymbol{K} \boldsymbol{\psi} \right), \; \boldsymbol{K}_g^r = \left(\boldsymbol{\psi}^T \boldsymbol{K}_g \boldsymbol{\psi} \right) \tag{3.25}$$

$$\boldsymbol{X}^r(t) = \sum_{n=1,3,5..}^{N_F} \left\langle \boldsymbol{c}_n^r \, e^{jn\omega t/2} + \boldsymbol{c}_{-n}^r \, e^{-jn\omega t/2} \right\rangle \tag{3.26}$$

3.4 Numerical results and discussion

In this section, the usefulness of the VEPC damping layer for CLD treatment of parametric instability of the layered beams is investigated by evaluating the numerical results. For simplicity in the presentation of numerical results, the sandwich beam (Fig. 3.2(a)) is denoted by three-layered beam while the second one (Fig. 3.2(b)) is indicated by five-layered beam. The ends of any of these beams are taken as clamped ends. The geometrical properties of these layered beams are taken as, L = 0.6 m, b = 2.5 mm, h_f = 3 mm, h_c = 6 mm, h_s = 2 mm, h_v = 3 mm. The substrate layers are considered to be made of Aluminium (E = 70 GPa, ν = 0.3, ρ = 2700 kg/m^3). The VEPC damping layer is taken as that is considered for the analysis in Chapter 2. However, it is observed from the results in Figs. (2.3) and (2.4) that the effective storage Young's modulus of the VEPC significantly increases with the increasing VFI (ϕ) for any frequency (ω) especially when the VFI (ϕ) increases beyond its value as 0.3. At the same time, the effective loss factor of the VEPC decreases slowly with the increase in the VFI (ϕ) at any operating frequency (ω). The effects of these material characteristics of the VEPC damping layer on the static stability and parametric instability of the layered beams are investigated in the following sections.

3.4.1 Effect of the inclusion on the static stability of the layered beams

The results in Fig. 2.4 show a significant increase in the effective stiffness of the viscoelastic layers due to the inclusion of graphite particles. The corresponding effect on the buckling instability of the layered beams is investigated in this section by computing the critical buckling load (N_{cr}) at the fundamental buckling

mode of the layered beams. The critical buckling load (N_{cr}) is computed following the procedure, as mentioned in section 3.3.2. According to this procedure, the static axial compressive load (N_0) is incremented in small steps from its zero-value, and the eigenvalue problem (Eq. (3.20)) is solved to obtain the natural frequency and modal loss factor in every incremental load step. Once the natural frequency becomes very close to zero-value, the corresponding static axial compressive load (N_0) is identified as the critical buckling load (N_{cr}). It may be noted here that this solution procedure not only provides the critical buckling load (N_{cr}) but also yields the natural frequency and modal loss factor at different values of the static axial compressive load.

For verification of these solutions using the aforesaid FE formulation for layered beams, reference results are not available in the literature for the natural frequency and loss factor of a beam under the static axial compressive load. So, presently this verification is performed by taking the reference results (Daya and Potier-Ferry, 2001) for the natural frequency and loss factor of a clamped-free sandwich beam without axial compressive load ($N_0 = 0$). These reference results are illustrated in Table 3.1, together with the presently computed results for the same sandwich beam. Table 3.1 shows a good agreement of the present results with similar reference results (Daya and Potier-Ferry, 2001), thus verifying the present FE formulation and solution for computation of natural frequency and modal loss factor of the layered beams.

In order to achieve sufficient numerical accuracy in the present FE results, FE mesh-convergence study is performed where the fundamental natural frequency (ω_n) and the corresponding modal loss factor (η) of the three/five-layered beam are computed by increasing the number of elements. The corresponding results are illustrated in Table 3.2. Table 3.2 indicates the minimum number of elements in the FE mesh of a layered beam for sufficient accuracy in the numerical results. So, the FE mesh of the layered beams is decided following this study for evaluation of further numerical results.

Table 3.1 Verification of the present FE formulation and solution for computation of natural frequency (f_n) and modal loss factor (η) of layered beams with constrained viscoelastic layers (η_c is the loss factor of the viscoelastic layer).

η_c	Present		Ref. (Daya and Potier-Ferry, 2001)	
	f_n (Hz)	η/η_c	f_n (Hz)	η/η_c
0.1	64.121	0.2814	64.2	0.281
0.3	64.473	0.2723	64.5	0.272
0.6	65.530	0.2460	65.6	0.246

Table 3.2 FE mesh convergence study for three/five-layered beam with VEPC layers ($\phi =$ 0.2 (VFI), ω_n : fundamental natural frequency, η : modal loss factor).

No. of elements	Three-layered beam		Five-layered beam	
	ω_n (rad/s)	η	ω_n (rad/s)	η
50	423.2107	0.2133	408.6407	0.2464
100	423.2106	0.2133	408.6406	0.2464
250	423.2106	0.2133	408.6406	0.2464
500	423.2106	0.2133	408.6406	0.2464

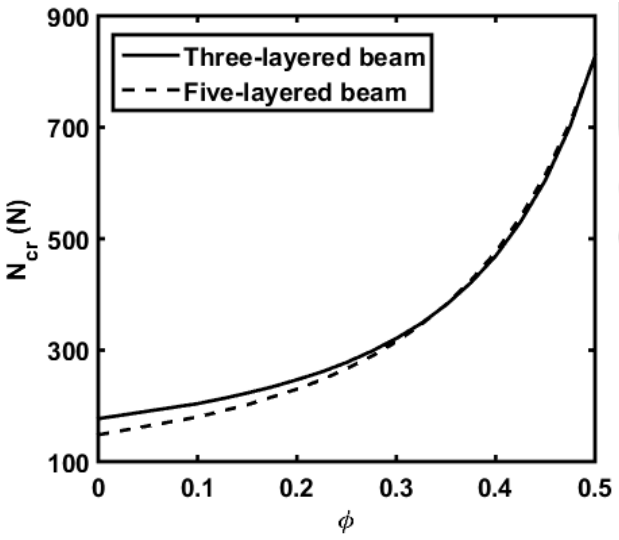

Fig. 3.3 Variation of the critical buckling load (N_{cr}) with the VFI (ϕ).

However, according to the aforesaid solution procedure, the critical buckling loads (N_{cr}) for the layered beams are computed for different values of the VFI (ϕ) as illustrated in Fig. 3.3. For any value of the VFI (ϕ), it may be observed from Fig. 3.3 that the critical buckling load remains almost the same for both the three-layered and five-layered beams. However, it is important to notice from the same figure (Fig. 3.3) that the critical buckling load significantly increases with the increase in the VFI (ϕ) especially when the VFI (ϕ) increases beyond its value as 0.3. Therefore, the static stability of the layered beams under the static axial compressive load (N_0) improves significantly due to the inclusion of graphite particles within the constrained viscoelastic layers.

Besides this advantage, the other effects of the inclusion of graphite particles on the CLD treatment of parametric instability of the layered beams are investigated in the subsequent sections. However, this investigation is carried out in the subsequent sections mainly by varying the VFI (ϕ) where the pre-buckled equilibrium state of the layered beams is considered by taking the static axial compressive load (N_0) as less than the critical buckling load (N_{cr}). Now, as it is observed from Fig. 3.3, the critical buckling load (N_{cr}) significantly varies with the VFI (ϕ). So, the static axial compressive load (N_0) at a VFI (ϕ) is presently taken with reference to the critical buckling load (N_{cr}) at the same VFI (ϕ) by specifying a static load parameter (r_p) as, $r_p = (N_0 / N_{cr})$. It may be noted here that a value of r_p as less than 1 indicates the pre-buckled equilibrium state of the layered beams.

3.4.2 Passive damping and natural frequency of the layered beams

In the CLD treatment of parametric instability, the objective is to reduce the instability region so that it appears minimally within the operating ranges of frequency (ω) and dynamic load parameter (λ). Presently, it is attempted through a frequency-shift in the natural frequency and also the improved passive damping in the CLD treatment by means of incorporating the inclusion of graphite particles in the constrained viscoelastic layers. So, initially, an assessment is made for the

variations of the natural frequency and modal loss factor of the layered beams with the VFI (ϕ) in the presence of an axial compressive load. Here, the free vibration of the layered beams corresponding to the fundamental bending mode of vibration at the pre-buckled equilibrium state ($r_p < 1$) is considered.

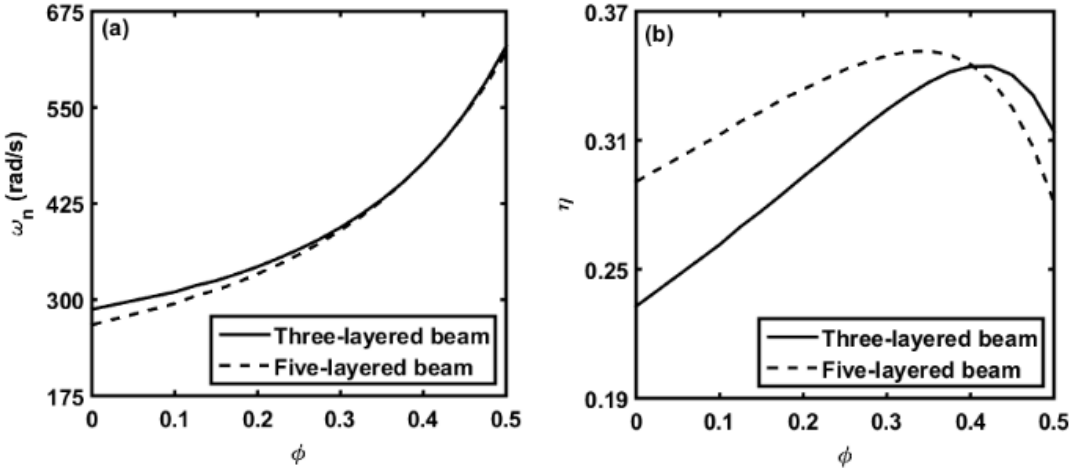

Fig. 3.4 (a) Fundamental natural frequency (ω_n) and (b) modal loss factor (η) of the layered beams for different values of VFI (ϕ) ($r_p = 0.4$).

Figure 3.4 illustrates the variations of the natural frequency and modal loss factor of the layered beams with the VFI (ϕ) where the static load parameter (r_p) is taken as 0.4. It may be observed from Fig. 3.4(a) that the natural frequency of the layered beams significantly increases with the increasing VFI (ϕ). It may be due to the fact that the effective stiffness of the constrained VEPC layers increases for the increase in the VFI (ϕ) (Fig. 2.4). Besides this variation of the natural frequency, Fig. 3.4(b) shows that the modal loss factor (η) in the layered beams increases with the increase in the VFI (ϕ). But, it occurs up to a certain value of the increasing VFI (ϕ) where maximum damping in the layered beams arises. So, similar to the previous result (Fig. 2.5) for the sandwich beam with no axial load, an optimal value of VFI (ϕ) arises for maximum damping in a layered beam under the axial load. It may also be observed from Fig. 3.4(b) that the damping (η) is significantly more in the five-layered beam than that in the three-layered beam when the monolithic viscoelastic layers ($\phi = 0$) are used. However, this difference

reduces as the graphite particles are incorporated within the constrained viscoelastic damping layers.

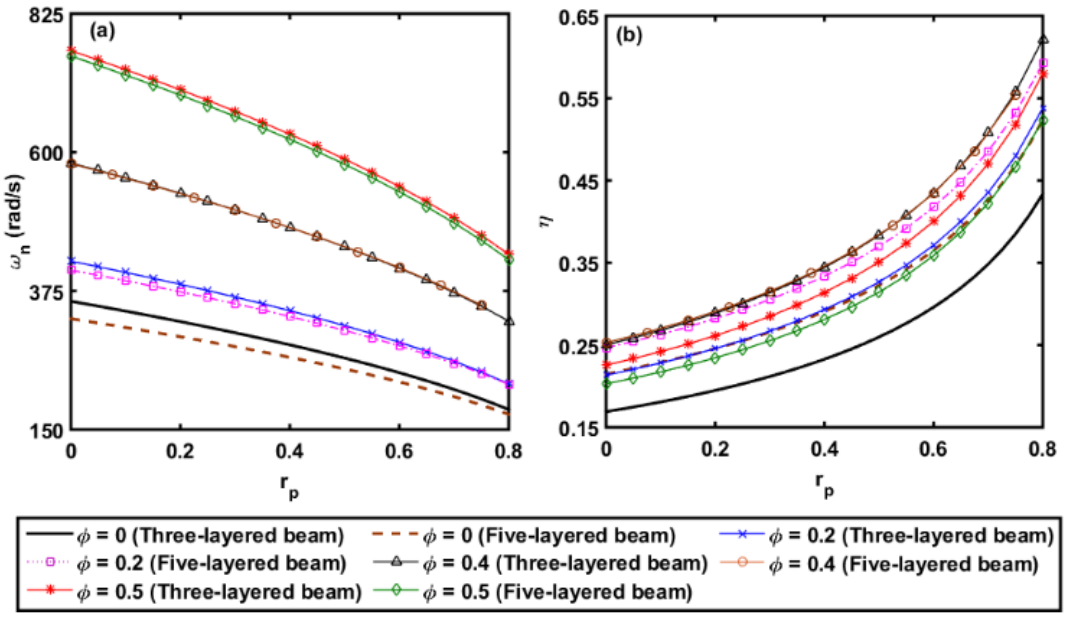

Fig. 3.5 (a) Fundamental natural frequency (ω_n) and (b) modal loss factor (η) of the layered beams for different values of the static load parameter (r_p) and VFI (ϕ).

The results in Figs. 3.4(a) and 3.4(b) are evaluated considering a constant value of the static load parameter ($r_p = 0.4$). However, for the variation of the same parameter (r_p), the corresponding changes in the natural frequency and modal loss factor are illustrated in Figs. 3.5(a) and 3.5(b), respectively, for different values of the VFI (ϕ). For any value of the VFI (ϕ), it may be observed from Fig. 3.5(a) that the natural frequency (ω_n) decreases with an increase in the static axial compressive load since this axial load imposes negative stiffness. In parallel, Fig. 3.5(b) shows that the modal damping (η) in the layered beams increases with the increasing static axial compressive load for any value of VFI (ϕ).

The aforesaid characteristics of the layered beams are further clarified through the results in Tables 3.3, 3.4 and 3.5 for a clear understanding about the influence of VFI (ϕ) and static axial compressive load (N_0) on the first natural frequency (ω_n) and the corresponding modal loss factor (η). For zero-value of the

static axial compressive load (N_0), it is clear from the results in Table 3.3 that the natural frequency of the layered beams increases when the monolithic viscoelastic layers ($\phi = 0$) are replaced by the present VEPC layers ($\phi \neq 0$), while there is an optimal value of the VFI (ϕ) for the maximum increase in the modal loss factor (η). Now, if the static axial compressive load is applied ($N_0 \neq 0$), then Table 3.4 shows similar variation of the natural frequency or the modal loss factor with VFI (ϕ) as that appears in the previous case (Table 3.3) for the zero-value of the static axial compressive load. However, for a specified value of the VFI (ϕ), the static axial compressive load (N_0) causes a significant decrease in the natural frequency and an increase in the modal loss factor (Tables 3.3 and 3.4). Further, if the static axial compressive load (N_0) increases with a specified value of VFI (ϕ), then the natural frequency continues to decrease while the modal loss factor increases significantly (Table 3.5).

These results imply that the damping effectiveness of the CLD treatment can significantly be improved by the inclusion of graphite particles in the constrained viscoelastic layers where the maximum improvement of damping is limited to a certain value of the VFI (ϕ). In parallel, the natural frequency of the structures can also be tuned by varying the volume fraction (ϕ) of the inclusion for any value of the static axial compressive load. The usefulness of these characteristics of the present CLD treatment in control of parametric instability of the layered beams is investigated in the next section.

Table 3.3 Variations of the first natural frequency (ω_n) and the corresponding modal loss factor (η) of a layered-beam with VFI (ϕ) for zero-value of the static axial compressive load (N_0 = 0).

VFI (ϕ)	Three-layered beam		Five-layered beam	
	ω_n	η	ω_n	η
0	358.17	0.1689	329.86	0.2146
0.1	384.55	0.1901	362.70	0.2309
0.2	423.21	0.2133	408.64	0.2464
0.3	482.93	0.2362	476.11	0.2573
0.4	582.39	0.2502	581.55	0.2527
0.5	765.02	0.2256	756.23	0.2028

Table 3.4 Variations of the first natural frequency (ω_n) and the corresponding modal loss factor (η) of a layered-beam with VFI (ϕ) for a specified static axial compressive load (N_0 = 50 N).

VFI (ϕ)	Three-layered beam		Five-layered beam	
	ω_n	η	ω_n	η
0	310.33	0.2085	278.15	0.2746
0.1	341.31	0.2271	317.59	0.2807
0.2	385.23	0.2462	370.24	0.2858
0.3	450.92	0.2630	444.51	0.2861
0.4	556.99	0.2691	556.74	0.2711
0.5	746.53	0.2351	737.76	0.2113

Table 3.5 Variations of the first natural frequency (ω_n) and the corresponding modal loss factor (η) of a layered-beam with the static axial compressive load (N_0) for a specified VFI (ϕ = 0.3).

N_0	Three-layered beam		Five-layered beam	
	ω_n	η	ω_n	η
50	450.92	0.2630	444.51	0.2861
100	415.70	0.2984	409.74	0.3241
150	376.08	0.34775	370.59	0.3772

3.4.3 CLD treatment of parametric instability

The effectiveness of the present CLD treatment in control of parametric instability is investigated in this section considering the principal primary parametric instability of the layered beams at the pre-buckled equilibrium state. The corresponding parametric instability region is evaluated following the solution procedure, as described in section 3.3.2. However, in this solution procedure, the number (q) of eigenmodes (ψ_i , $i = 1,2,3,.....q$) and the number (N_F , Eq. (3.21)) of harmonic terms are to be considered appropriately for achieving sufficient numerical accuracy in the results. A convergence study is carried out in this concern where the number of eigenmodes is increased in steps starting from the first eigenmode. For each of these steps, the parametric instability region is evaluated by increasing the number (N_F) of harmonic terms. It is observed that the first five eigenmodes are sufficient in combination with the first three ($N_F = 3$) harmonic terms to obtain sufficient numerical accuracy in the estimation of the

instability region. Figure 3.6 illustrates these results for the consideration of the first five eigenmodes, where it can be observed that the minimum number of harmonic terms for sufficient numerical accuracy in the result appears as $N_F = 3$, and the same is considered for evaluation of further numerical results.

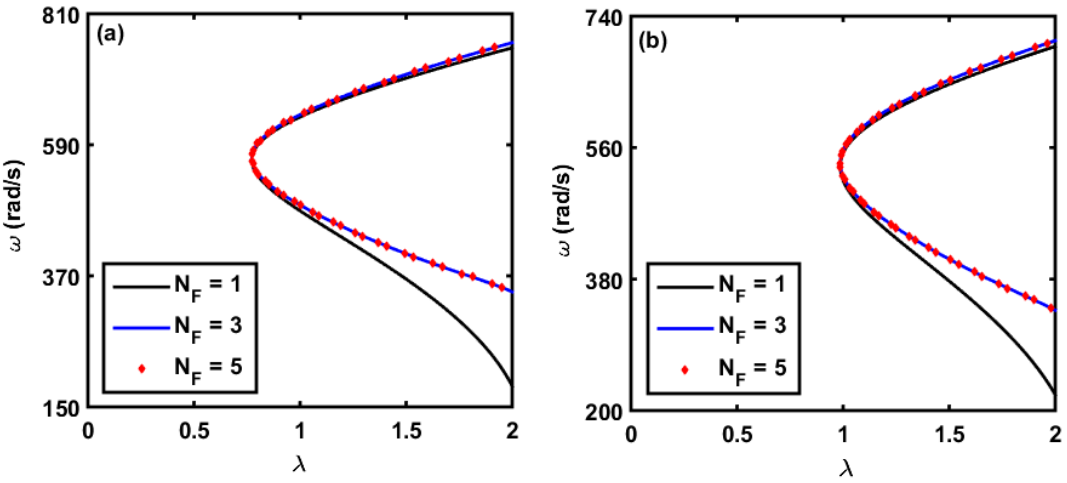

Fig. 3.6 Convergence study for appropriate number of harmonic terms in the assumed solution (Eq. (3.21)) in evaluation of the principal primary parametric instability region; (a) three-layered and (b) five-layered beams ($\phi = 0.1$, $r_p = 0.5$).

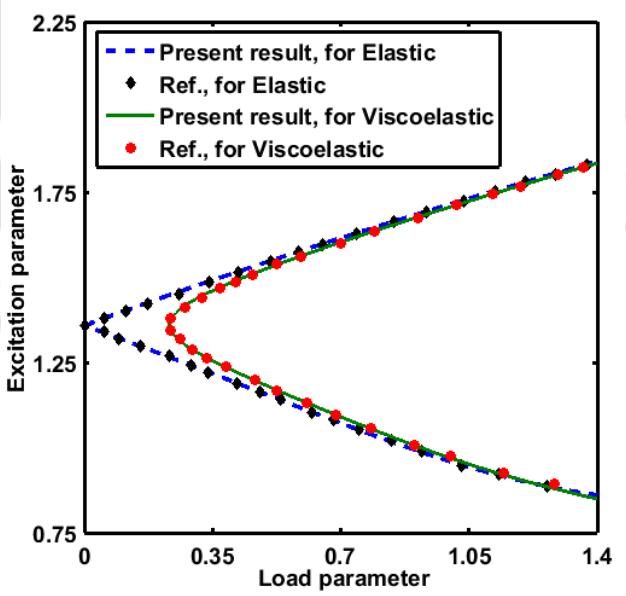

Fig. 3.7 Verification of the present FE formulation for evaluation of the principal primary parametric instability region (Ref. Shih and Yeh, 2005).

Besides this convergence study, the accuracy of the present FE formulation is also verified by taking the reference results (Shih and Yeh, 2005) for the principal primary parametric instability region of a simply-supported viscoelastic beam. These reference results are illustrated in Fig. 3.7, along with the presently computed FE results for the same viscoelastic beam. It may be observed from Fig. 3.7 that the present results are in good agreement with the similar reference results (Shih and Yeh, 2005), and this comparison study verifies the accuracy of the present FE formulation.

Figure 3.8 illustrates the principal primary parametric instability regions for different volume fractions (ϕ) of the inclusion of graphite particles in the constrained viscoelastic layers of the layered beams. For better clarification of these results, the corresponding variations of the dynamic load parameter (λ_0) and frequency (ω_0) at the origin of instability are illustrated in Figs. 3.9(a) and 3.9(b), respectively. The variation of the width (w_I) of instability region is also illustrated in Fig. 3.9(c). For these results (Figs. 3.8 and 3.9), the static load

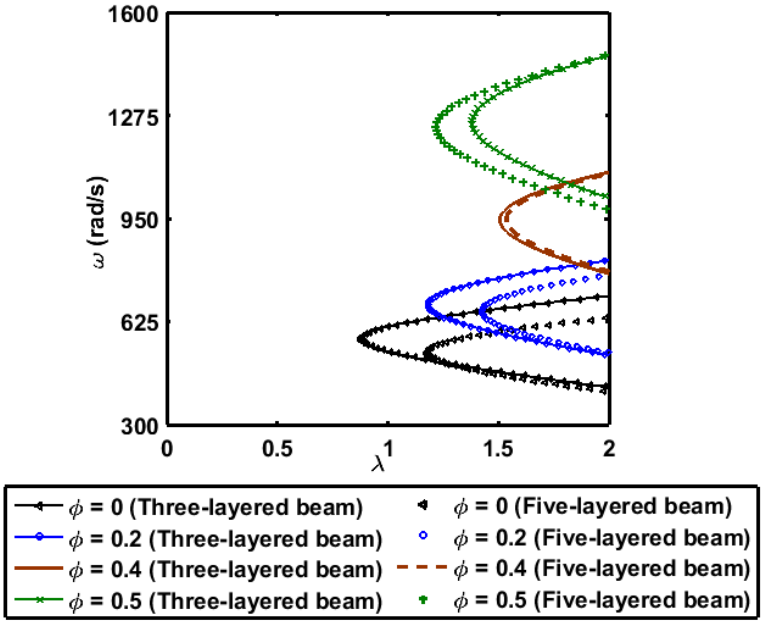

Fig. 3.8 Principal primary parametric instability regions for different values of VFI (ϕ) ($r_p = 0.4$).

parameter (r_p) is taken with a value as 0.4, and the width (w_I) of instability region is measured at $\lambda = 2$.

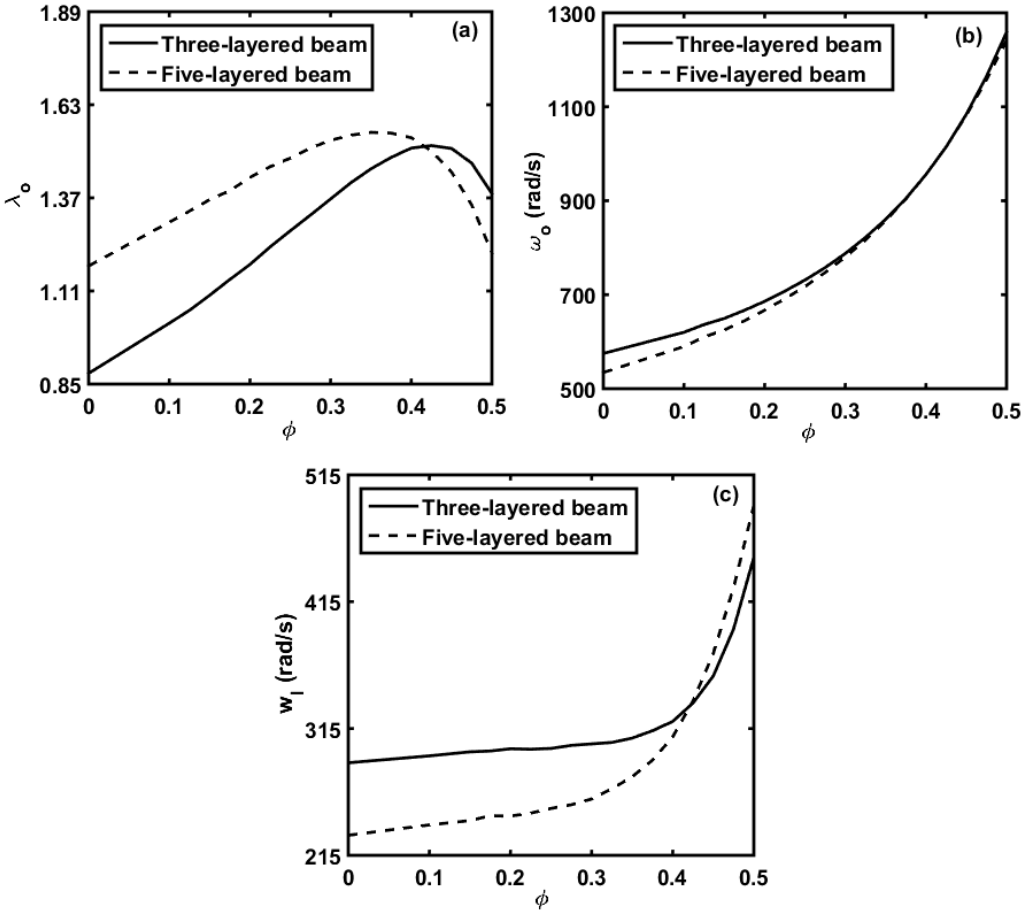

Fig. 3.9 Variations of (a) load parameter (λ_o) at the origin of instability, (b) frequency (ω_o) at the origin of instability and (c) width (w_I, $\lambda = 2$) of instability region with the VFI (ϕ) (r_p = 0.4).

It may be observed from Figs. 3.8 and 3.9(b) that the instability region significantly shifts towards a high frequency for an increase in the VFI (ϕ). It appears following the variation of the natural frequency with VFI (ϕ) (Fig. 3.4(a)) since the frequency (ω_o) at the origin of the principal primary parametric instability region is twice of the natural frequency. From these results, it is clear that the volume fraction (ϕ) of inclusion in the VEPC layers may be used as a

tuning parameter for a frequency-shift of the instability region particularly for reducing its appearance within a frequency range of interest. However, it may also be observed from Figs. 3.8 and 3.9(a) that the instability region significantly reduces towards a high value of the dynamic load parameter (λ) when the VFI (ϕ) increases. Here, the change in the dynamic load parameter (λ_o) at the origin of the instability region appears following the variation of the modal damping (Fig. 3.4(b)). Therefore, the reduction of the instability region towards a high value of the dynamic load parameter (λ) is mainly governed by modal damping. So, the maximum reduction of the instability region in the direction of the dynamic load parameter appears corresponding to the maximum damping at the optimal value of the VFI (ϕ). In parallel, Fig. 3.9(c) shows that the width (w_I) of the instability region does not vary significantly up to the optimal value of the VFI (ϕ).

Therefore, the maximum reduction of the instability region can be achieved up to the optimal value of the VFI (ϕ). Also, for the optimal value of the VFI (ϕ), the instability region remains almost the same for both the three-layered and five-layered beams (Fig. 3.8). However, if it is required to regulate the VFI (ϕ) from its optimal value, particularly for shifting the instability region aside from the frequency range of interest, then the instability region enlarges from its minimum shape. In this case, the multi-layered beam would be preferred when the VFI (ϕ) is less than its optimal value. Conversely, the sandwich beam may be used if the VFI (ϕ) is greater than its optimal value.

The results in Figs. 3.8 and 3.9 are illustrated considering the constant value of the static load parameter (r_p) as 0.4. However, for different values of the static load parameter (r_p), the corresponding variation of the instability region is illustrated in Fig. 3.10. For any value of the VFI (ϕ), it may be observed from Fig. 3.10 that the instability region moves towards a low frequency as the static load parameter (r_p) increases since the natural frequency decreases (Fig. 3.5(a)). However, it may also be observed from the same figure (Fig. 3.10) that the instability region decreases with the increasing VFI (ϕ) at a greater rate when the static load parameter (r_p) decreases.

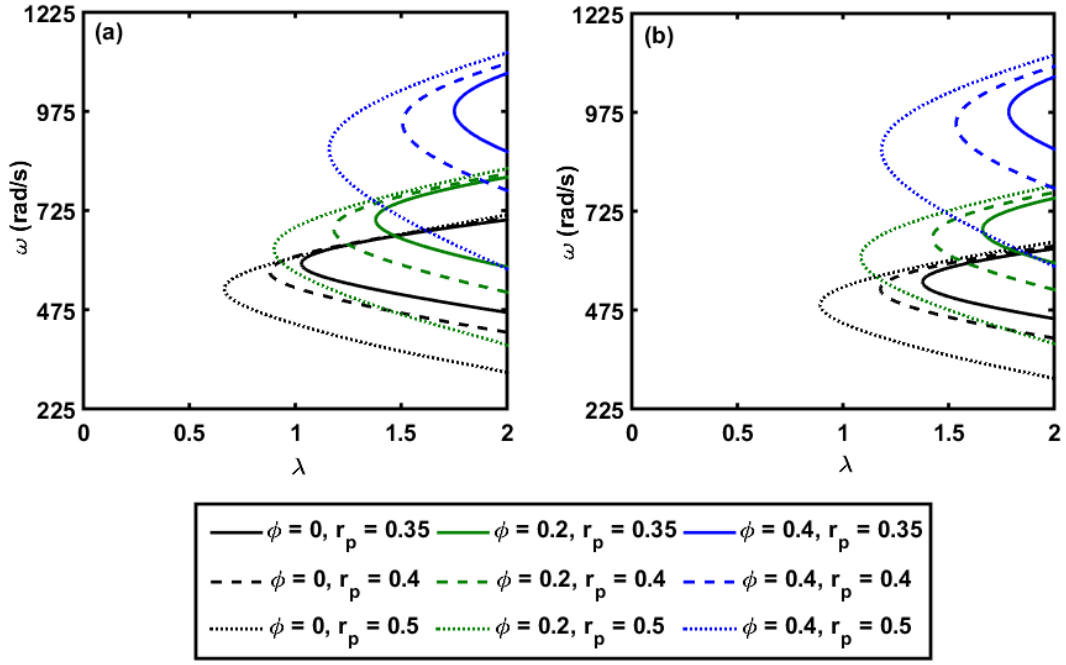

Fig. 3.10 Variation of the principal primary parametric instability region with the static load parameter (r_p) for different values of the VFI (ϕ); (a) three-layered and (b) five-layered beams.

From the results in Figs. 3.8, 3.9, and 3.10, it may be concluded that the effectiveness of the CLD treatment in control of parametric instability can significantly be improved by using the present VEPC layers instead of the conventional monolithic viscoelastic layers. The VEPC layer not only provides the advantage of the reduced instability region but also allows to tailor its effective material properties for shifting the instability region aside from the frequency range of interest. So, the present VEPC layer seems to be a potential passive damping layer for augmented CLD treatment of parametric instability of thin-walled flexible structures.

3.5 Summary

Constrained layer damping (CLD) treatment of parametric instability of layered beams is investigated by incorporating the inclusion of graphite particles within the constrained viscoelastic layers. Two different layered beams are considered for the CLD treatment using single or multiple VEPC damping layers. The first

one is a three-layered beam having one VEPC damping layer between two identical substrate layers. The second one is a five-layered beam where two identical VEPC damping layers are constrained by three uniform substrate layers. However, the influence of the material characteristics of the VEPC layer on the static stability, constrained layer damping, and parametric instability of the layered beams is analyzed by deriving a FE model for the layered beams based on the layer-wise deformation theory. This analysis reveals the following observations.

(a) The static stability of the layered beams under the axial compressive load improves significantly due to the inclusion of graphite particles.

(b) The improved constrained layer damping in the layered beams causes a significant decrease in the parametric instability region. The maximum reduction of the instability region appears corresponding to the maximum damping in the layered beams at the optimal value of the VFI.

(c) The five-layered beam is more stable than the three-layered beam when the VFI is lesser than its optimal value. The reverse holds as the value of the VFI is greater than its optimal value. However, both the layered beams exhibit almost the same parametric instability characteristics for the optimal value of the VFI.

(d) Besides the improved passive damping, the natural frequency of the layered beams can also be regulated by tuning the volume fraction of inclusion in the constrained VEPC layers. These characteristics not only provide the advantage of an augmented reduction of the instability region but also yield a provision of shifting the instability region aside from the frequency range of interest. Therefore, the appearance of the instability region within the operating ranges of frequency and dynamic load parameter can be reduced significantly for improved dynamic stability of structures.

Chapter 4

Active constrained layer damping treatment using the inclusion of graphite particles within the viscoelastic damping layer

4.1 Introduction

The performance of a VEPC damping layer in the CLD treatment is studied in the previous two chapters, and it is found that the damping in the CLD treatment significantly improves when the monolithic viscoelastic damping layer is replaced by the VEPC layer. In this chapter, the fruitfulness of this VEPC layer in the ACLD treatment is investigated. The conventional ACLD treatment is comprised of a monolithic viscoelastic damping layer that is constrained by a piezoelectric actuator layer. Here, the primary function of the actuation force in the piezoelectric actuator layer is to enhance the transverse shear deformation of the constrained viscoelastic layer so that the hybrid active-passive damping in the ACLD treatment improves (Baz, 2019). The other function of the same actuation force is to actuate the substrate structure directly. But, it does not appear effectively since the actuation force cannot transfer from the actuator layer to the substrate structure properly due to a very low stiffness of the intermediate viscoelastic layer. Here, a viscoelastic layer with a high stiffness may be used for fruitful appearance of the secondary function of the actuator layer. But, the increased stiffness of the viscoelastic layer usually yields a decrease in its material loss factor, and it causes a significant reduction in the overall active-passive damping performance of the ACLD treatment. So, a soft viscoelastic layer with high material loss factor is usually recommended for the ACLD treatment. It basically implies improper utilisation of the actuation force in the piezoelectric actuator layer. This shortcoming was reported by Liao and Wang (1996), where they introduced the edge-elements for improved transfer of the actuation force in the ACLD treatment.

However, this shortcoming can also be mitigated by the use of the present VEPC as a material for the constrained damping layer in the ACLD arrangement. The inclusion of graphite particles improves the stiffness of the actively constrained VEPC damping layer, and thus the augmented transfer of actuation

force from the piezoelectric actuator layer to substrate structure would appear. This improved transfer of actuation force is expected to provide an enhanced active counterpart of the total active-passive damping in the ACLD treatment. Besides this potential advantage, the passive damping capability of the VEPC layer also improves due to the inclusion as it is observed from the studies in the previous two chapters. So, both the active and passive counterparts of the total active-passive damping are expected to increase towards an augmented ACLD treatment. A detailed study on this issue is performed in this chapter, considering the VEPC damping layer in the conventional arrangement of ACLD treatment for control of plate vibration.

In the following sections, first, an FE model of a substrate plate integrated with an ACLD layer is derived based on the layer-wise deformation theory, where the damping layer is made of VEPC and the piezoelectric constraining layer is activated by supplying the external electrical voltage according to the velocity feedback control law. Next, the numerical results for the modal loss factor, and frequency responses of the ACLD treated plate are presented to analyse the active-passive damping mainly by varying the volume fraction of inclusion of graphite particles in the actively constrained VEPC layer. This analysis explores the change of active-passive damping in terms of its active and passive counterparts when the inclusion of graphite particles is incorporated in the viscoelastic damping layer. Finally, the observations from this study are summarized.

4.2 Mathematical formulation

Figure 4.1 shows a substrate plate integrated with a VEPC layer that is constrained by a piezoelectric actuator layer. The length, width and thickness of the substrate plate are denoted by a, b and h, respectively. The thicknesses of the constrained viscoelastic layer and the constraining piezoelectric layer are denoted by h_v and h_c, respectively. The middle plane of the substrate plate is taken as the reference plane, and the same plane is also taken as the xy plane of the reference Cartesian coordinate system (xyz), as shown in Fig. 4.1. The kinematics of deformation of this layered plate is presently defined following the

layer-wise (LW) theory, where the displacement field in each layer can be taken according to the first-order shear deformation theory (FSDT) since the layers in the laminated plate are of small thickness (Cupiał and Niziół, 1995). However, the FSDT is usually employed for defining the deformation characteristics of a thin layer where the transverse shear strain appears with a very small value compared to the in-plane strain components in that layer. Otherwise, the third-order shear deformation theory (TSDT) is recommended for better results (Reddy, 2003). Now, as per the working principle of ACLD treatment in the layered arrangement, the viscoelastic layer undergoes significant transverse

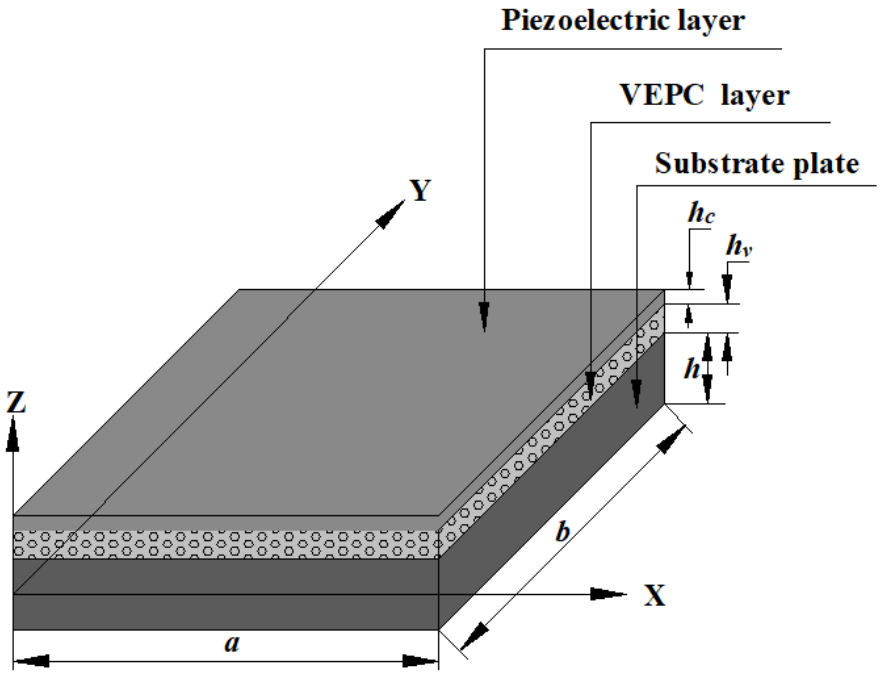

Fig. 4.1 Schematic diagram of a substrate plate integrated with an actively constrained VEPC layer.

shear strain even though it is a thin layer. So, presently the deformation of the constrained viscoelastic layer is modelled using TSDT while the FSDT is retained for other two layers. Accordingly, the displacement components u^k, v^k and w^k at any point of the layered plate along the x, y and z directions, respectively can be written following the Taylor series expansion with respect to the thickness coordinate as,

$$u^k = u_0 + \boldsymbol{z}^k \boldsymbol{\phi}_x \,,\; v^k = v_0 + \boldsymbol{z}^k \boldsymbol{\phi}_y \,,\; w^k = w_0$$

$$\boldsymbol{\phi}_x = \left\{ \phi_x^1 \quad \phi_x^2 \quad \phi_x^3 \quad \beta_x^2 \quad \gamma_x^2 \right\}^{\mathrm{T}},$$

$$\boldsymbol{\phi}_y = \left\{ \phi_y^1 \quad \phi_y^2 \quad \phi_y^3 \quad \beta_y^2 \quad \gamma_y^2 \right\}^{\mathrm{T}},$$

$$\phi_x^k = \left.\frac{\partial u^k}{\partial z}\right|_{z_R^k}, \quad \phi_y^k = \left.\frac{\partial v^k}{\partial z}\right|_{z_R^k} \quad \text{for } k = 1,2,3$$

$$\beta_x^k = \left.\frac{1}{2!}\frac{\partial^2 u^k}{\partial z^2}\right|_{z_R^k}, \quad \beta_y^k = \left.\frac{1}{2!}\frac{\partial^2 v^k}{\partial z^2}\right|_{z_R^k} \quad \text{for } k = 2$$

$$\gamma_x^k = \left.\frac{1}{3!}\frac{\partial^3 u^k}{\partial z^3}\right|_{z_R^k}, \quad \gamma_y^k = \left.\frac{1}{3!}\frac{\partial^3 v^k}{\partial z^3}\right|_{z_R^k} \quad \text{for } k = 2 \qquad (4.1a)$$

In Eq. (4.1a), the superscript k indicates the substrate plate, constrained damping layer and piezoelectric constraining layer as per its values as 1, 2 and 3, respectively; u_0, v_0 and w_0 are the displacements at any point on the middle plane of the substrate plate along the x, y and z directions, respectively. The different thickness coordinates appearing in Eq. (4.1a) are given in Eq. (4.1b).

$$z_R^k = 0, h/2, (h/2 + h_v) \;\text{ for }\; k = 1,2,3$$

$$\boldsymbol{z}^1 = \left\{ z \quad 0 \quad 0 \quad 0 \quad 0 \right\} \;\text{ for }\; k = 1$$

$$\boldsymbol{z}^2 = \left\{ h/2 \quad (z - h/2) \quad 0 \quad (z - h/2)^2 \quad (z - h/2)^3 \right\} \;\text{ for }\; k = 2$$

$$\boldsymbol{z}^3 = \left\{ h/2 \quad h_v \quad (z - h/2 - h_v) \quad h_v{}^2 \quad h_v{}^3 \right\} \;\text{ for }\; k = 3 \qquad (4.1b)$$

The displacement components (u^k, v^k, w^k) at any point within the k^{th} layer can be expressed as,

$$\boldsymbol{d}^k = \left(\boldsymbol{T}_t + \boldsymbol{Z}_r^k \boldsymbol{T}_r \right) \boldsymbol{d} \,,\; \boldsymbol{d}^k = \left\{ u^k \quad v^k \quad w^k \right\}^{\mathrm{T}}$$

$$\boldsymbol{d} = \left\{ u_0 \quad v_0 \quad w_0 \quad \phi_x^1 \quad \phi_x^2 \quad \phi_x^3 \quad \beta_x^2 \quad \gamma_x^2 \quad \phi_y^1 \quad \phi_y^2 \quad \phi_y^3 \quad \beta_y^2 \quad \gamma_y^2 \right\}^{\mathrm{T}}$$

$$\boldsymbol{Z}_r^k = \begin{bmatrix} \boldsymbol{z}^k & \boldsymbol{0} & \boldsymbol{0} \\ \boldsymbol{0} & \boldsymbol{z}^k & \boldsymbol{0} \end{bmatrix}^{\mathrm{T}}$$

$$\boldsymbol{T}_t = \left[\boldsymbol{I}_{3\times 3} \quad \boldsymbol{O}_{3\times 10}\right], \quad \boldsymbol{T}_r = \left[\boldsymbol{O}_{10\times 3} \quad \boldsymbol{I}_{10\times 10}\right] \tag{4.2}$$

where, $\mathbf{0}$ represents the null vector; $\boldsymbol{T}_t$ and $\boldsymbol{T}_r$ are the transformation matrices. The state of strain and the state of stress at any point within a layer (k) of the laminated plate can be written as,

$$\boldsymbol{\varepsilon}_b^k = \left\{\varepsilon_x^k \quad \varepsilon_y^k \quad \varepsilon_{xy}^k\right\}^{\mathrm{T}},$$

$$\boldsymbol{\varepsilon}_s^k = \left\{\varepsilon_{xz}^k \quad \varepsilon_{yz}^k\right\}^{\mathrm{T}} \tag{4.3a}$$

$$\boldsymbol{\sigma}_b^k = \left\{\sigma_x^k \quad \sigma_y^k \quad \sigma_{xy}^k\right\}^{\mathrm{T}},$$

$$\boldsymbol{\sigma}_s^k = \left\{\sigma_{xz}^k \quad \sigma_{yz}^k\right\}^{\mathrm{T}} \tag{4.3b}$$

where, the symbols ε and σ represent strain and stress components, respectively; the subscripts x and y indicate the normal stress or strain along the x and y directions, respectively; the subscripts xy, xz and yz denote the shear strain or stress on the xy, xz and yz planes, respectively. The strain-displacement relations for the k^{th} layer can be written as given in Eq. (4.4), where $\otimes$ represents the Kronecker product.

$$\boldsymbol{\varepsilon}_b^k = \left(\boldsymbol{\varepsilon}_{b0} + \boldsymbol{Z}_b^k \boldsymbol{\kappa}_b\right),$$

$$\boldsymbol{\varepsilon}_s^k = \left(\boldsymbol{\varepsilon}_{s0} + \boldsymbol{Z}_s^k \boldsymbol{\kappa}_s\right)$$

$$\boldsymbol{\varepsilon}_{b0} = \begin{Bmatrix} \dfrac{\partial u_0}{\partial x} \\ \dfrac{\partial v_0}{\partial y} \\ \dfrac{\partial u_0}{\partial y} + \dfrac{\partial v_0}{\partial x} \end{Bmatrix}, \quad \boldsymbol{\kappa}_b = \begin{Bmatrix} \dfrac{\partial \boldsymbol{\phi}_x}{\partial x} \\ \dfrac{\partial \boldsymbol{\phi}_y}{\partial y} \\ \dfrac{\partial \boldsymbol{\phi}_x}{\partial y} + \dfrac{\partial \boldsymbol{\phi}_y}{\partial x} \end{Bmatrix},$$

$$\boldsymbol{\varepsilon}_{s0} = \begin{Bmatrix} \dfrac{\partial w_0}{\partial x} \\ \dfrac{\partial w_0}{\partial y} \end{Bmatrix}, \quad \boldsymbol{\kappa}_s = \begin{Bmatrix} \boldsymbol{\phi}_x \\ \boldsymbol{\phi}_y \end{Bmatrix},$$

$$\boldsymbol{Z}_b^k = \boldsymbol{I}_{3\times3} \otimes \boldsymbol{z}^k \,,\ \boldsymbol{Z}_s^k = \boldsymbol{I}_{2\times2} \otimes \left(\partial \boldsymbol{z}^k / \partial z\right) \tag{4.4}$$

The piezoelectric constraining layer is transversely poled, and its constitutive relations can be written, as given in Eq. (4.5) (Cady, 1946),

$$\boldsymbol{\sigma} = \boldsymbol{C}\boldsymbol{\varepsilon} - \boldsymbol{e}\boldsymbol{E} \,,\ \boldsymbol{D} = \boldsymbol{e}^{\mathrm{T}}\boldsymbol{\varepsilon} + \in \boldsymbol{E}$$

$$\boldsymbol{E} = \begin{Bmatrix} E_x & E_y & E_z \end{Bmatrix}^{\mathrm{T}} ,\ \boldsymbol{D} = \begin{Bmatrix} D_x & D_y & D_z \end{Bmatrix}^{\mathrm{T}} \tag{4.5a}$$

$$\boldsymbol{C} = \begin{bmatrix} C_{11} & C_{12} & C_{13} & 0 & 0 & 0 \\ C_{12} & C_{22} & C_{23} & 0 & 0 & 0 \\ C_{13} & C_{23} & C_{33} & 0 & 0 & 0 \\ 0 & 0 & 0 & C_{44} & 0 & 0 \\ 0 & 0 & 0 & 0 & C_{55} & 0 \\ 0 & 0 & 0 & 0 & 0 & C_{66} \end{bmatrix},$$

$$\boldsymbol{e} = \begin{bmatrix} 0 & 0 & e_{31} \\ 0 & 0 & e_{32} \\ 0 & 0 & e_{33} \\ 0 & e_{24} & 0 \\ e_{15} & 0 & 0 \\ 0 & 0 & 0 \end{bmatrix},\ \in = \begin{bmatrix} \in_{11} & 0 & 0 \\ 0 & \in_{22} & 0 \\ 0 & 0 & \in_{33} \end{bmatrix} \tag{4.5b}$$

where, E_x / D_x, E_y / D_y and E_z / D_z are the electric field/electric displacement components along the x, y and z directions, respectively; the symbols $\boldsymbol{\sigma}$ and $\boldsymbol{\varepsilon}$ stand for the stress and strain vectors, respectively; C_{ij} are the stiffness coefficients at the constant electric field; e_{ij} are the piezoelectric coefficients at the constant electric field or constant strain; $\in_{ij}$ are the electrical permittivity coefficients at the constant strain. However, in the present ACLD treated plate, the piezoelectric actuator layer is activated by supplying the external voltage (V) across its top and bottom fully electrode surfaces. Since it is a very thin active constraining layer, the electric field components can be assumed as, $E_z = -V / h_c$, $E_x \approx 0$ and $E_y \approx 0$. With this assumption and the aforesaid state of stress/strain at a point in the piezoelectric constraining layer, its constitutive relations (Eq. (4.5)) can be reduced as,

$$\boldsymbol{\sigma}_b^k = \boldsymbol{C}_b^k \boldsymbol{\varepsilon}_b^k - \boldsymbol{e}_b^k E_z\,,\ \boldsymbol{\sigma}_s^k = \boldsymbol{C}_s^k \boldsymbol{\varepsilon}_s^k$$

$$D_z^k = \left(\boldsymbol{e}_b^k\right)^{\mathrm{T}} \boldsymbol{\varepsilon}_b^k + \epsilon_{33}^k E_z\,,\ k = 3$$

$$\boldsymbol{C}_b^k = \begin{bmatrix} \bar{C}_{11}^k & \bar{C}_{12}^k & 0 \\ \bar{C}_{12}^k & \bar{C}_{22}^k & 0 \\ 0 & 0 & C_{66}^k \end{bmatrix},\ \boldsymbol{C}_s^k = \begin{bmatrix} C_{55}^k & 0 \\ 0 & C_{44}^k \end{bmatrix},\ \boldsymbol{e}_b^k = \begin{Bmatrix} \bar{e}_{31}^k & \bar{e}_{32}^k & 0 \end{Bmatrix}^{\mathrm{T}},$$

$$\bar{C}_{11}^k = \left\langle C_{11}^k - \left(C_{13}^k\right)^2 \Big/ C_{33}^k \right\rangle,\ \bar{C}_{22}^k = \left\langle C_{22}^k - \left(C_{23}^k\right)^2 \Big/ C_{33}^k \right\rangle,\ \bar{C}_{12}^k = \left\langle C_{12}^k - C_{13}^k C_{23}^k / C_{33}^k \right\rangle,$$

$$\bar{e}_{31}^k = \left\langle e_{31}^k - C_{13}^k e_{33}^k / C_{33}^k \right\rangle,\ \bar{e}_{32}^k = \left\langle e_{32}^k - C_{23}^k e_{33}^k / C_{33}^k \right\rangle \tag{4.6}$$

The substrate plate is considered to be made of an elastic isotropic material. The VEPC is also a macroscopically homogeneous isotropic material, and its effective properties can be determined following the same procedure as given in section 2.2.1. So, the constitutive relations for these materials can be written as,

$$\boldsymbol{\sigma}_b^k = \boldsymbol{C}_b^k \boldsymbol{\varepsilon}_b^k\,,\ \boldsymbol{\sigma}_s^k = \boldsymbol{C}_s^k \boldsymbol{\varepsilon}_s^k$$

$$\boldsymbol{C}_b^k = \frac{E^k}{1-\left(\nu^k\right)^2} \begin{bmatrix} 1 & \nu^k & 0 \\ \nu^k & 1 & 0 \\ 0 & 0 & \left(1-\nu^k\right)/2 \end{bmatrix},\ \boldsymbol{C}_s^k = \frac{E^k}{2\left(1+\nu^k\right)} \begin{bmatrix} 1 & 0 \\ 0 & 1 \end{bmatrix},\ k = 1,2 \tag{4.7}$$

In Eq. (4.7), E^k and ν^k are the Young's modulus and Poisson's ration for the k^{th} layer $(k = 1,2)$. Here, the stiffness matrices $(\boldsymbol{C}_b^k, \boldsymbol{C}_s^k)$ are the complex quantities only for the VEPC layer $(k = 2)$ since this viscoelastic layer is presently modelled using complex stiffness method. Further, these stiffness matrices for the VEPC layer are the frequency dependent quantities since the overall plate (Fig. 4.1) is considered to operate at a constant temperature.

For deriving the FE model of the overall plate, the rectangular reference plane i.e. the middle plane $(z = 0)$ of the substrate plate is discretized using nine-node quadrilateral isoparametric elements. Every element is in the shape of the rectangle with the edges in parallel to the in-plane axial directions. However, the

displacement vector ($\boldsymbol{d}^k$) and the strain vectors ($\boldsymbol{\varepsilon}_{b0}$, $\boldsymbol{\kappa}_b$, $\boldsymbol{\varepsilon}_{s0}$, $\boldsymbol{\kappa}_s$) at any point within a typical element can be expressed in terms of the shape function matrix ($\boldsymbol{N}$) and the elemental nodal displacement vector ($\boldsymbol{d}^e$), as given in Eqs. (4.8), (3.11a) and (4.9).

$$\boldsymbol{d}^k = \left(\boldsymbol{T}_t + \boldsymbol{Z}_r^k \boldsymbol{T}_r\right) \boldsymbol{N} \boldsymbol{d}^e \tag{4.8}$$

$$\begin{aligned}
&\boldsymbol{\varepsilon}_{b0} = \boldsymbol{B}_{b0}\boldsymbol{d}^e\,,\ \boldsymbol{\kappa}_b = \boldsymbol{B}_{b\kappa}\boldsymbol{d}^e\,,\\
&\boldsymbol{\varepsilon}_{s0} = \boldsymbol{B}_{s0}\boldsymbol{d}^e\,,\ \boldsymbol{\kappa}_s = \boldsymbol{B}_{s\kappa}\boldsymbol{d}^e\,,\\
&\boldsymbol{B}_{b0} = \boldsymbol{L}_{b0}\boldsymbol{T}_t\boldsymbol{N}\,,\ \boldsymbol{B}_{b\kappa} = \boldsymbol{L}_{b\kappa}\boldsymbol{T}_r\boldsymbol{N}\,,\\
&\boldsymbol{B}_{s0} = \boldsymbol{L}_{s0}\boldsymbol{T}_t\boldsymbol{N}\,,\ \boldsymbol{B}_{s\kappa} = \boldsymbol{L}_{s\kappa}\boldsymbol{T}_r\boldsymbol{N}
\end{aligned} \tag{3.11a}$$

$$\boldsymbol{L}_{b0} = \begin{bmatrix} \partial/\partial x & 0 & 0 \\ 0 & \partial/\partial x & 0 \\ \partial/\partial y & \partial/\partial x & 0 \end{bmatrix},\ \boldsymbol{L}_{s0} = \begin{bmatrix} 0 & 0 & \partial/\partial x \\ 0 & 0 & \partial/\partial y \end{bmatrix},$$

$$\boldsymbol{L}_{b\kappa} = \begin{bmatrix} 0 & 0 & 0 & \partial/\partial x & \partial/\partial x & \partial/\partial x & \partial/\partial x & \partial/\partial x & 0 & 0 & 0 & 0 & 0 \\ 0 & 0 & 0 & 0 & 0 & 0 & 0 & 0 & \partial/\partial y & \partial/\partial y & \partial/\partial y & \partial/\partial y & \partial/\partial y \\ 0 & 0 & 0 & \partial/\partial y & \partial/\partial y & \partial/\partial y & \partial/\partial y & \partial/\partial y & \partial/\partial x & \partial/\partial x & \partial/\partial x & \partial/\partial x & \partial/\partial x \end{bmatrix},$$

$$\boldsymbol{L}_{s\kappa} = \begin{bmatrix} 0 & 0 & 0 & 1 & 1 & 1 & 1 & 1 & 0 & 0 & 0 & 0 & 0 \\ 0 & 0 & 0 & 0 & 0 & 0 & 0 & 0 & 1 & 1 & 1 & 1 & 1 \end{bmatrix} \tag{4.9}$$

The overall plate is considered to vibrate under a transverse harmonic point-load ($p(t)$) at the middle point ($a/2, b/2, -h/2$) of the bottom plate-surface. The corresponding governing equation of motion is derived employing extended Hamilton's principle (Eq. (2.12)), where the first variations of the total potential energy (δT_p) and the total kinetic energy (δT_k) of the overall plate at an instant of time (t) can be written by Eqs. (4.10) and (4.11), respectively.

$$\int_{t_1}^{t_2} \left(\delta T_K - \delta T_P\right) dt = 0 \tag{2.12}$$

$$\delta T_p = \int_0^a \int_0^b \left[\sum_{k=1}^{3} \int_{h_k}^{h_{k+1}} \left\langle (\delta \boldsymbol{\varepsilon}_b^k)^{\mathrm{T}} \boldsymbol{\sigma}_b^k + (\delta \boldsymbol{\varepsilon}_s^k)^{\mathrm{T}} \boldsymbol{\sigma}_s^k \right\rangle dz - \int_{h_k}^{h_{k+1}} \left(\delta E_z\right)^{\mathrm{T}} D_z^k \Big|_{k=3} dz \right] dy dx - \left\langle \delta w_0\, p(t) \right\rangle_{\left(\frac{a}{2}, \frac{b}{2}, -\frac{h}{2}\right)} \tag{4.10}$$

$$\delta T_K = \int_0^a \int_0^b \left[\sum_{k=1}^{3} \int_{h_k}^{h_{k+1}} \left\langle \left\{ \delta(\dot{u}^k) \quad \delta(\dot{v}^k) \quad \delta(\dot{w}^k) \right\} \rho^k \left\{ (\dot{u}^k) \quad (\dot{v}^k) \quad (\dot{w}^k) \right\}^{\mathrm{T}} \right\rangle dz \right] dydx \tag{4.11}$$

In Eqs. (4.10) and (4.11), ρ^k is the mass density of k^{th} layer; h^k and h^{k+1} represent the z coordinates of the bottom and top surfaces of k^{th} layer, respectively. Using Eqs. (4.6), (4.7), (4.8) and (4.9) in Eqs. (2.12), (4.10) and (4.11), the elemental equation of motion can be obtained as given in Eqs. (4.12) and (4.13).

$$\boldsymbol{M}^e \ddot{\boldsymbol{d}}^e + \left(\boldsymbol{K}_b^e(\omega) + \boldsymbol{K}_s^e(\omega) \right) \boldsymbol{d}^e = \boldsymbol{P}_E^e V + \boldsymbol{P}_M^e p(t) \tag{4.12}$$

$$\boldsymbol{K}_b^e(\omega) = \int_{A^e} \left\langle (\boldsymbol{B}_{b0})^{\mathrm{T}} \left(\boldsymbol{A}_b(\omega)\boldsymbol{B}_{b0} + \boldsymbol{B}_{L1}(\omega)\boldsymbol{B}_{b\kappa} \right) + (\boldsymbol{B}_{b\kappa})^{\mathrm{T}} \left(\boldsymbol{B}_{L2}(\omega)\boldsymbol{B}_{b0} + \boldsymbol{D}_b(\omega)\boldsymbol{B}_{b\kappa} \right) \right\rangle dA^e ,$$

$$\boldsymbol{K}_s^e(\omega) = \boldsymbol{K}_{sp}^e + \boldsymbol{K}_v^e(\omega) ,$$

$$\boldsymbol{K}_{sp}^e = \int_{A^e} \left\langle (\boldsymbol{B}_{s0})^{\mathrm{T}} \left(\boldsymbol{A}_{sp}\boldsymbol{B}_{s0} + \boldsymbol{B}_{sp1}\boldsymbol{B}_{s\kappa} \right) + (\boldsymbol{B}_{s\kappa})^{\mathrm{T}} \left(\boldsymbol{B}_{sp2}\boldsymbol{B}_{s0} + \boldsymbol{D}_{sp}\boldsymbol{B}_{s\kappa} \right) \right\rangle dA^e ,$$

$$\boldsymbol{K}_v^e(\omega) = \int_{A^e} \left\langle (\boldsymbol{B}_{s0})^{\mathrm{T}} \left(\boldsymbol{A}_v(\omega)\boldsymbol{B}_{s0} + \boldsymbol{B}_{v1}(\omega)\boldsymbol{B}_{s\kappa} \right) + (\boldsymbol{B}_{s\kappa})^{\mathrm{T}} \left(\boldsymbol{B}_{v2}(\omega)\boldsymbol{B}_{s0} + \boldsymbol{D}_v(\omega)\boldsymbol{B}_{s\kappa} \right) \right\rangle dA^e ,$$

$$\boldsymbol{P}_E^e = \int_{A^e} \left\langle (\boldsymbol{B}_{b0})^{\mathrm{T}} \boldsymbol{A}_{be} + (\boldsymbol{B}_{b\kappa})^{\mathrm{T}} \boldsymbol{B}_{be} \right\rangle dA^e ,$$

$$\boldsymbol{P}_M^e = \left\langle (\boldsymbol{T}_t)^{\mathrm{T}} \{0 \quad 0 \quad 1\}^{\mathrm{T}} \right\rangle_{\frac{a}{2},\frac{b}{2},-\frac{h}{2}} ,$$

$$\boldsymbol{M}^e = \int_{A^e} (\boldsymbol{N})^{\mathrm{T}} \left\langle (\boldsymbol{T})_t^{\mathrm{T}} \left(\boldsymbol{m}_1\boldsymbol{T}_t + \boldsymbol{m}_2\boldsymbol{T}_r \right) + (\boldsymbol{T}_r)^{\mathrm{T}} \left(\boldsymbol{m}_3\boldsymbol{T}_t + \boldsymbol{m}_4\boldsymbol{T}_r \right) \right\rangle \boldsymbol{N} \; dA^e \tag{4.13}$$

In Eqs. (4.12) and (4.13), A^e is the elemental area and the other matrices are given in Eq. (4.14).

$$\boldsymbol{A}_b(\omega) = \sum_{k=1}^{3} \int_{h_k}^{h_{k+1}} \boldsymbol{C}_b^k(\omega) dz , \; \boldsymbol{B}_{L1}(\omega) = \sum_{k=1}^{3} \int_{h_k}^{h_{k+1}} \boldsymbol{C}_b^k(\omega) \boldsymbol{Z}_b^k dz \; ,$$

$$\boldsymbol{B}_{L2}(\omega) = \sum_{k=1}^{3} \int_{h_k}^{h_{k+1}} \left(\boldsymbol{Z}_b^k \right)^{\mathrm{T}} \boldsymbol{C}_b^k(\omega) dz , \; \boldsymbol{D}_b(\omega) = \sum_{k=1}^{3} \int_{h_k}^{h_{k+1}} \left(\boldsymbol{Z}_b^k \right)^{\mathrm{T}} \boldsymbol{C}_b^k(\omega) \boldsymbol{Z}_b^k dz ,$$

$$\boldsymbol{A}_{sp}=\sum_{\substack{k=1\\k\neq 2}}^{3}\int_{h_k}^{h_{k+1}}\boldsymbol{C}_s^k\,dz\,,\ \boldsymbol{B}_{sp1}=\sum_{\substack{k=1\\k\neq 2}}^{3}\int_{h_k}^{h_{k+1}}\boldsymbol{C}_s^k\boldsymbol{Z}_s^k\,dz\ ,$$

$$\boldsymbol{B}_{sp2}=\sum_{\substack{k=1\\k\neq 2}}^{3}\int_{h_k}^{h_{k+1}}\left(\boldsymbol{Z}_s^k\right)^{\mathrm{T}}\boldsymbol{C}_s^k\,dz\,,\ \boldsymbol{D}_{sp}=\sum_{\substack{k=1\\k\neq 2}}^{3}\int_{h_k}^{h_{k+1}}\left(\boldsymbol{Z}_s^k\right)^{\mathrm{T}}\boldsymbol{C}_s^k\boldsymbol{Z}_s^k\,dz\,,$$

$$\boldsymbol{A}_v(\omega)=\int_{h_k}^{h_{k+1}}\boldsymbol{C}_s^k(\omega)dz\Big|_{k=2}\,,\ \boldsymbol{B}_{v1}(\omega)=\int_{h_k}^{h_{k+1}}\boldsymbol{C}_s^k(\omega)\boldsymbol{Z}_s^k\,dz\Big|_{k=2}\,,$$

$$\boldsymbol{B}_{v2}(\omega)=\int_{h_k}^{h_{k+1}}\left(\boldsymbol{Z}_s^k\right)^{\mathrm{T}}\boldsymbol{C}_s^k(\omega)\Big|_{k=2}\,,\ \boldsymbol{D}_v(\omega)=\int_{h_k}^{h_{k+1}}\left(\boldsymbol{Z}_s^k\right)^{\mathrm{T}}\boldsymbol{C}_s^k(\omega)\boldsymbol{Z}_s^k\Big|_{k=2}\,,$$

$$\boldsymbol{m}_1=\sum_{k=1}^{3}\int_{h_k}^{h_{k+1}}\rho^k\,dz\,,\ \boldsymbol{m}_2=\sum_{k=1}^{3}\int_{h_k}^{h_{k+1}}\rho^k\boldsymbol{Z}_r^k\,dz\,,$$

$$\boldsymbol{m}_3=\sum_{k=1}^{3}\int_{h_k}^{h_{k+1}}\left(\boldsymbol{Z}_r^k\right)^{\mathrm{T}}\rho^k\,dz\,,\ \boldsymbol{m}_4=\sum_{k=1}^{3}\int_{h_k}^{h_{k+1}}\left(\boldsymbol{Z}_r^k\right)^{\mathrm{T}}\rho^k\boldsymbol{Z}_r^k\,dz\,,$$

$$\boldsymbol{A}_{be}=\int_{h_k}^{h_{k+1}}\boldsymbol{e}_b^k\left(-1/h_c\right)dz\Big|_{k=3}\,,\ \boldsymbol{B}_{be}=\int_{h_k}^{h_{k+1}}\left(\boldsymbol{Z}_b^k\right)^{\mathrm{T}}\boldsymbol{e}_b^k\left(-1/h_c\right)dz\Big|_{k=3}\qquad(4.14)$$

Assembling the elemental equations (Eq. (4.12)), the following global equation of motion of the overall plate can be obtained,

$$\boldsymbol{M}\ddot{\boldsymbol{X}}+\boldsymbol{K}(\omega)\,\boldsymbol{X}=\boldsymbol{P}_E\,V+\boldsymbol{P}_M\,p(t)\,,$$
$$\boldsymbol{K}(\omega)=\boldsymbol{K}_b(\omega)+\boldsymbol{K}_s(\omega)\qquad(4.15)$$

where, $\boldsymbol{M}$ is the global mass matrix; $\boldsymbol{K}_b(\omega)$ and $\boldsymbol{K}_s(\omega)$ are the bending and transverse shear counterparts of the global stiffness matrix $\boldsymbol{K}(\omega)$; $\boldsymbol{P}_E$ and $\boldsymbol{P}_M$ are the global nodal electro-elastic and load coefficient vectors, respectively; $\boldsymbol{X}$ is the global nodal displacement vector.

The piezoelectric constraining layer is activated according to the velocity feedback control strategy as,

$$V=-k_d\dot{w}_s\qquad(4.16)$$

where, $\dot{w}_s$ is the transverse velocity sensed at the middle point on the top surface of the overall plate and k_d is the velocity-feedback control gain. Now, $\dot{w}_s$ can be expressed in terms of $\dot{\boldsymbol{X}}$ through a transformation row matrix ($\boldsymbol{N}_T$) according to Eq. (4.17), and then the governing equation of motion (Eq. (4.15)) can be expressed in the form as given in Eqs. (4.18a)-(4.18b).

$$\dot{w}_s = \boldsymbol{N}_T \dot{\boldsymbol{X}} \tag{4.17}$$

$$\boldsymbol{M}\ddot{\boldsymbol{X}} + \boldsymbol{C}\dot{\boldsymbol{X}} + \boldsymbol{K}(\omega)\boldsymbol{X} = \boldsymbol{P}_M p(t) \tag{4.18a}$$

$$\boldsymbol{C} = \boldsymbol{P}_E k_d \boldsymbol{N}_T \tag{4.18b}$$

4.3 Numerical results and discussion

The present investigation on the active-passive damping characteristics of the actively constrained VEPC layer is carried out by evaluating the modal loss factor (η) and frequency responses of the overall plate (Fig. 4.1). The geometrical properties of the overall plate are taken as $a = 0.4$ m, $b = 0.3$ m, $h = 5$ mm and $h_c = 0.5$ mm. Unless otherwise mentioned, the thickness of the VEPC layer is taken as $h_v = 2.5$ mm. The edges of the substrate plate are considered as the clamped edges ($u_0 = 0$, $v_0 = 0$, $w_0 = 0$, $\phi_x^1 = 0$, $\phi_y^1 = 0$ at $x = 0, a$ and $y = 0, b$), while the frequency responses and modal loss factor (η) of the overall plate are evaluated corresponding to the fundamental bending mode of vibration.

The substrate plate is considered to be made of Aluminium ($E = 69$ GPa, $\nu = 0.3$, $\rho = 2740$ kg/m^3) while the piezoelectric layer is made of PZT-5H (Erturk and Inman, 2011) having the properties as $C_{11} = 127$ GPa, $C_{12} = 80.21$ GPa, $C_{13} = 84.67$ GPa, $C_{33} = 117.84$ GPa, $C_{44} = 22.99$ GPa, $C_{66} = 23.47$ GPa, $\rho =$ 7500 kg/m^3, $e_{31} =$ -6.6228 C/m^2, $e_{33} = 23.24$ C/m^2, $e_{24} =$ 17.03 C/m^2. The VEPC damping layer is considered to be made of Butyl rubber matrix and graphite particles. The frequency-dependent effective properties of this VEPC layer at the room temperature (32^o) are evaluated and presented in Chapter 2, where the variations of the effective moduli and material loss factor of VEPC are illustrated either with frequency (Fig. 2.3) or with volume faction (ϕ) of inclusion (Fig. 2.4).

However, the damping characteristics of the ACLD treatment are analysed by evaluating the modal loss factor (η) and frequency responses of the overall plate (Fig. 4.1). Here, the modal loss factor is evaluated through the steady-state free vibration ($p(t)=0$) of the overall plate, where Eq. (4.18) can be written in the form of Eq. (2.17), as given in Eq. (4.19).

$$\left(\boldsymbol{K}^R(\omega_i)+j\left\langle \boldsymbol{K}^I(\omega_i)+\omega_i\boldsymbol{C}\right\rangle\right)\boldsymbol{\psi}_i=\omega^2\boldsymbol{M}\boldsymbol{\psi}_i \tag{4.19}$$

This complex quadratic eigenvalue problem is solved following the same procedure as described in section 2.3 to obtain the complex natural frequency (ω_i) of the overall plate. Subsequently, the natural frequency (ω_i^0) and modal loss factor (η_i) for the i^{th} mode of vibration of the overall plate can be obtained from Eq. (2.18).

$$\left(\omega_i\right)^2=\left(\omega_i^o\right)^2\left\langle 1+j\eta_i\right\rangle \tag{2.18}$$

It may be noted here that the damping (η_i) in the ACLD treatment arises due to the active action only when $\eta_c=0$ and $k_d\neq 0$. In parallel, the damping (η_i) in the ACLD treatment appears due to the passive action only when $k_d=0$ and $\eta_c\neq 0$. For nonzero values of η_c and k_d, the damping (η_i) arises due to both the active and passive actions in the ACLD treatment. However, besides the modal loss factor, the frequency responses of the overall plate around the fundamental natural frequency are evaluated for the transverse harmonic point-load in the form as $p(t)=p_0e^{j\omega t}$, where p_0 is the load-amplitude. For the corresponding linear steady-state vibration of the overall plate, the FE equations of motion (Eq. (4.18)) can be written in the following form (Meirovitch, 1997),

$$\left(-\omega^2\boldsymbol{M}+j\omega\boldsymbol{C}+\boldsymbol{K}(\omega)\right)\bar{\boldsymbol{X}}=\boldsymbol{P}_M p_0 \tag{4.20}$$

where, $\bar{\boldsymbol{X}}$ is the complex nodal displacement vector and its absolute value represents the nodal displacement-amplitude vector. From this solution, the maximum transverse displacement-amplitude ($W_{\max}/h$) at every operating frequency is plotted in the presentation of frequency responses.

For verification of the present FE model in the computation of modal loss factor, the passively ($V = 0$) constrained damping layer is considered to be made of monolithic viscoelastic material, and the natural frequencies, as well as modal loss factors, of this plate, are computed. These results are illustrated in Table 4.1 together with similar results for an identical plate analysed in (Cupiał and Nizioł, 1995). This comparison (Table 4.1) verifies the present FE formulation for computation of the modal loss factor of a plate integrated with a constrained viscoelastic layer.

Table 4.1 Verification of the present FE formulation for computation of natural frequencies ($\omega_{m,n}$) and modal loss factors ($\eta_{m,n}$) of a plate integrated with a constrained viscoelastic layer (m and n are the bending mode numbers along the x and y directions, respectively).

Bending modes (m,n)	Ref. (Cupiał and Nizioł, 1995)		Present FE results	
	$\omega_{m,n}$ (Hz)	$\eta_{m,n}$	$\omega_{m,n}$ (Hz)	$\eta_{m,n}$
(1,1)	60.3	0.190	60.235	0.1901
(1,2)	115.4	0.203	115.224	0.2034
(2,1)	130.6	0.199	130.427	0.1992
(2,2)	178.7	0.181	178.463	0.1806

Table 4.2 Verification of the present FE formulation for modelling the electro-elastic coupling in the piezoelectric layer.

Applied voltage (volt)	Maximum transverse deflection (μm)	
	ANSYS	Present FEM
100	0.217	0.204
200	0.434	0.409
500	1.090	1.023

For further verification of the present FE formulation in modelling the electro-elastic coupling within the piezoelectric layer, the viscoelastic layer is taken with a negligibly small thickness ($h_v \approx 0$). The maximum transverse deflection of this plate is computed for the externally applied voltage across the thickness of the piezoelectric layer. Similar results are also evaluated from the ANSYS model of the same plate, and it is observed that the present results are very close to the results obtained from the ANSYS model of the plate (Table 4.2).

This comparison verifies the present FE formulation for handling the electro-elastic coupling in the piezoelectric layer.

In order to achieve sufficient numerical accuracy in the present FE results, FE mesh-convergence study is performed where the fundamental natural frequency (ω_n), modal loss factor (η) and controlled resonant transverse displacement-amplitude (W_f at ω_n) of the overall plate are computed by increasing the number of elements. The corresponding results are illustrated in Table 4.3, where the requirement of the minimum number of elements in the FE mesh for sufficient accuracy in the numerical results can be observed. Following this study, the FE mesh of the overall layered beam is taken for evaluation of further numerical results.

Table 4.3 FE mesh convergence study for the plate with actively constrained VEPC layer (ϕ = 0.2, p_0 = 40 N, k_d = 100, ω_n: fundamental natural frequency, η: modal loss factor, W_f: maximum transverse displacement-amplitude at resonant frequency).

No. of elements	ω_n (rad/s)	η	W_f/h
64	2155.50	0.0885	0.04776
144	2155.14	0.0885	0.04772
324	2155.08	0.0885	0.04772
506	2155.08	0.0885	0.04772

Figures 4.2 and 4.3(a) illustrate the frequency responses of the overall plate for different values of VFI (ϕ) when the piezoelectric layer is either deactivated ($k_d = 0$) or activated ($k_d \neq 0$), respectively. Figure 4.3(b) shows the variations of the required control voltage corresponding to the frequency responses in Fig. 4.3(a). Figures 4.2 and 4.3(a) show that the attenuation of the resonant displacement-amplitude through the passive ($k_d = 0$) or the active-passive ($k_d \neq 0$) damping in the overall plate increases significantly due to the inclusion of graphite particles in the viscoelastic layer. Also, the required control voltage for the active-passive damping decreases due to the inclusion in the viscoelastic layer (Fig. 4.3(b)).

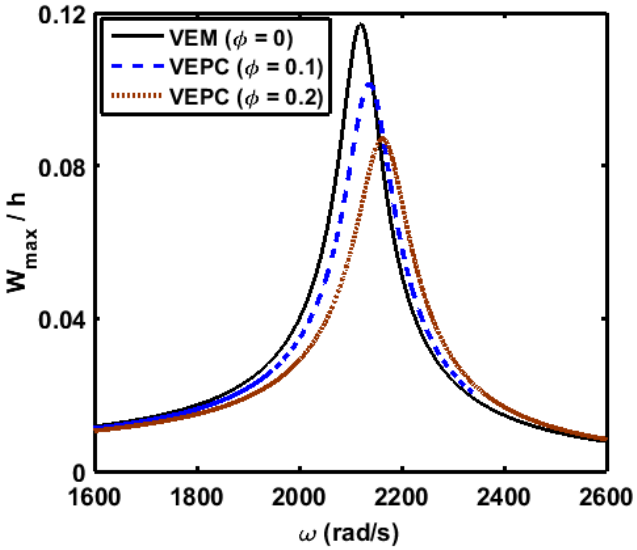

Fig. 4.2 Frequency response of the overall plate for different VFI (ϕ) of graphite particles ($k_d = 0$, $p_0 =$ 40 N, VEM: monlithic viscoelastic material).

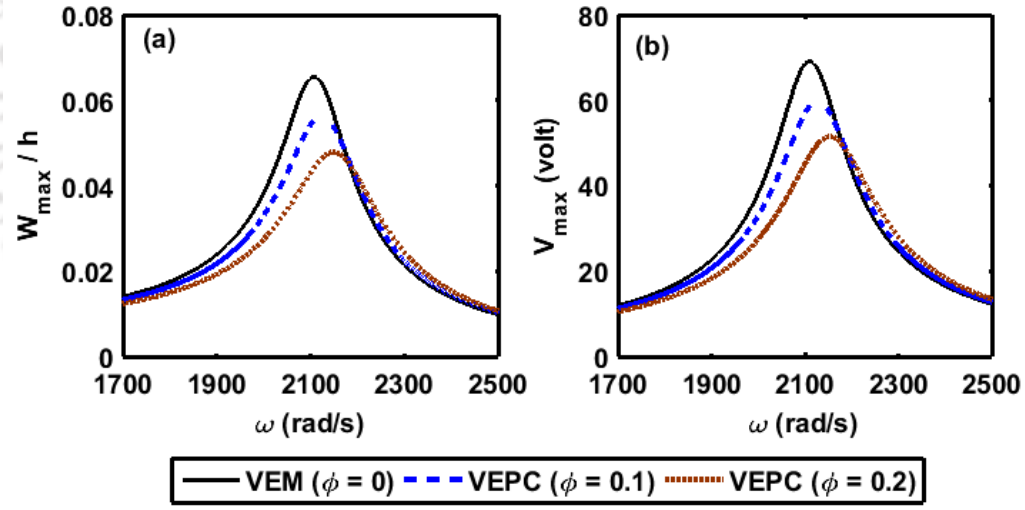

Fig. 4.3(a) Frequency responses of the overall plate and (b) the corresponding variations of the control voltage for different VFI (ϕ) of graphite particles ($k_d = 100$, $p_0 =$40 N, VEM: monlithic viscoelastic material).

However, for investigating the effect of the inclusion on the active ($\eta_c = 0$, $k_d \neq 0$), passive ($\eta_c \neq 0$, $k_d = 0$) and active-passive ($\eta_c \neq 0$, $k_d \neq 0$) damping in the ACLD treatment, the corresponding variations of damping (η) with VFI (ϕ) are presented in Fig. 4.4(a). It may be observed from Fig. 4.4(a) that the active

damping ($\eta_c = 0$, $k_d \neq 0$) first increases and then decreases after a certain value of the increasing VFI (ϕ). In fact, the increased stiffness of the viscoelastic layer due to the inclusion results in an improved transfer of active action from the piezoelectric layer to the substrate plate. Concurrently, the enhanced stiffness of the viscoelastic layer not only causes increased flexural rigidity of the overall plate but also affects the actuating moment in the active action through the reduced distance of the actuator layer from the neutral plane of bending deformation. The combined effect of these facts results in an optimal value of VFI (ϕ) for the maximum active damping.

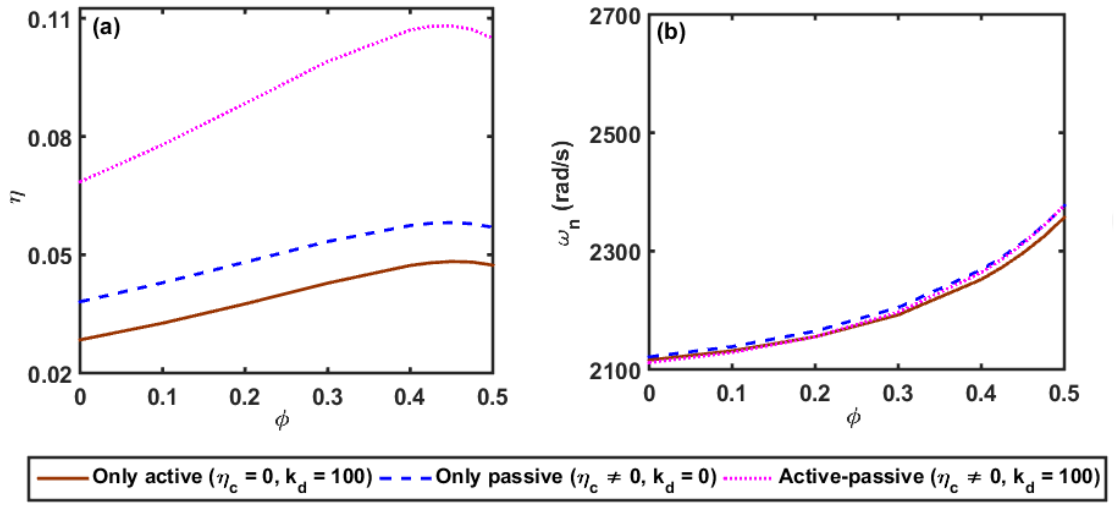

Fig. 4.4 Variations of (a) modal loss factor (η) and (b) natural frequency (ω_n) with the VFI (ϕ) for active ($\eta_c = 0, k_d \neq 0$), passive ($\eta_c \neq 0, k_d = 0$) and active-passive ($\eta_c \neq 0, k_d \neq 0$) damping in the ACLD treatment.

Similar to the active damping ($\eta_c = 0$, $k_d \neq 0$), the passive damping ($\eta_c \neq 0$, $k_d = 0$) in the overall plate also increases with the increasing VFI (ϕ) and the maximum passive damping appears at a certain value of ϕ (Fig. 4.4(a)). Here, the stored energy in the damping layer increases with the increase in VFI (ϕ) but the corresponding decrease of η_c (Fig. 2.4) causes an optimal value of VFI (ϕ) for the maximum passive damping. However, the active and passive damping appear with their maximum values almost at the same value of VFI (ϕ), and it results in significantly improved active-passive damping in the overall plate (Fig.

4.4(a)). Besides the improved active-passive damping, the inclusion of graphite particles causes the increased natural frequency of the overall plate (Fig. 4.4(b)). However, this increment of natural frequency may not appear remarkably at the optimal value of VFI (ϕ) where active-passive damping appears with its maximum value.

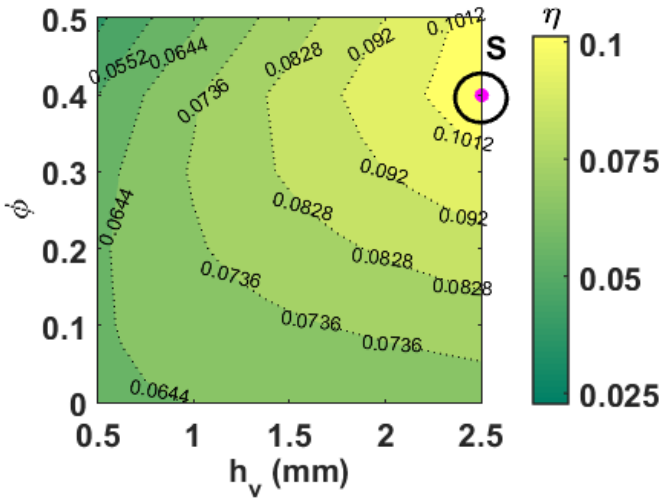

Fig. 4.5 Variation of the modal loss factor (η) within the two-dimensional domain of VFI (ϕ) and thickness (h_v) of VEPC layer ($k_d = 100$).

In order to investigate the combined effect of the VFI (ϕ) and thickness (h_v) of VEPC layer on the damping capability of the ACLD treatment, the variation of active-passive damping (η) over the two-dimensional domain of h_v and ϕ is evaluated as shown in Fig. 4.5. Figure 4.5 shows that the active-passive damping in the overall plate continues to increase with the increasing value of h_v for any value of VFI (ϕ). However, the effect of h_v on η appears indicatively within a particular range of VFI (ϕ) where the optimal value of VFI (ϕ) corresponding to the maximum damping (η) arises as 0.4 (point S, Fig. 4.5). From this result, a value of h_v is presently considered as 2.5 mm, and the variation of η with ϕ is evaluated for different values of the control gain (k_d) as shown in Fig. 4.6. Figure 4.6 shows that the optimal value of ϕ remains almost

the same for any value of k_d but the η vs ϕ slope increases significantly for an increase in the value of k_d .

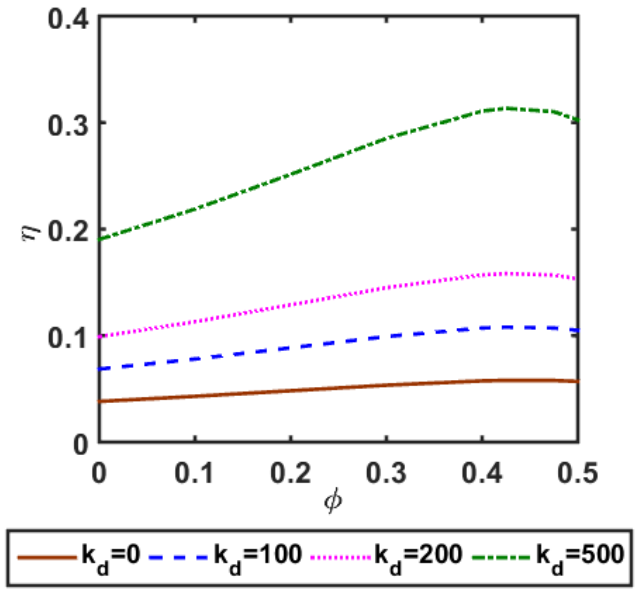

Fig. 4.6 Variation of the modal loss factor (η) with the VFI (ϕ) at different values of the control-gain (k_d) ($h_v = 2.5$ mm).

On the basis of the aforesaid results, the values of ϕ and h_v are taken as 0.4 and 2.5 mm, respectively, and the attenuation of maximum transverse displacement-amplitude ($W_{\max}/h$) around resonant frequency is illustrated in Fig. 4.7(a) for active ($\eta_c = 0, k_d \neq 0$), passive ($\eta_c \neq 0, k_d = 0$) and active-passive ($\eta_c \neq 0, k_d \neq 0$) damping. Similar responses for the monolithic viscoelastic layer ($\phi = 0$) instead of the VEPC layer are also illustrated in the same figure (Fig. 4.7(a)). Figure 4.7(b) shows the variations of the control voltage for the frequency responses in Fig. 4.7(a) corresponding to the nonzero value of the control gain (k_d). For any case of the active, passive and active-passive damping, Figure 4.7(a) shows significantly improved attenuation of the maximum transverse displacement-amplitude ($W_{\max}/h$) around resonant frequency for the use of the present VEPC instead of the monolithic viscoelastic material. Also, the required

control voltage for active or active-passive damping decreases for the use of VEPC instead of monolithic viscoelastic material (Fig. 4.7(b)).

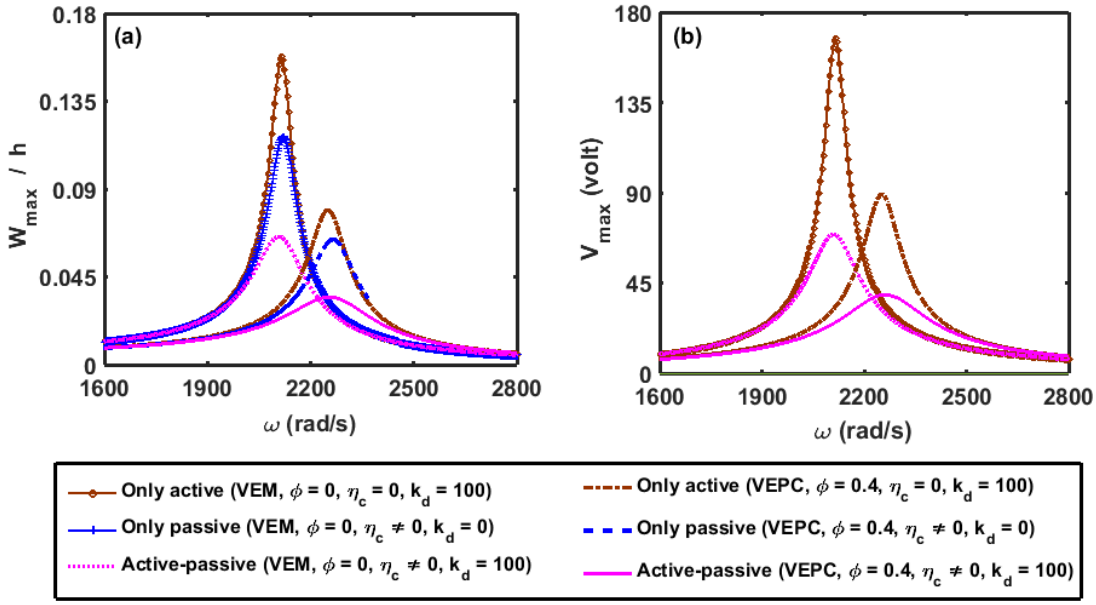

Fig. 4.7(a) Frequency responses of the overall plate and (b) the corresponding variations of control voltage for active, passive and active-passive damping (p_0 = 40 N, VEM: monolithic viscoelastic material).

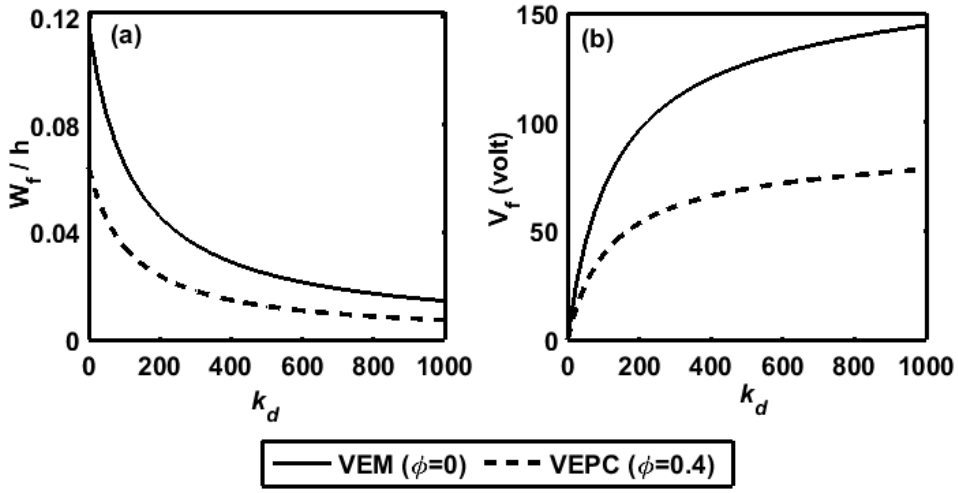

Fig. 4.8 Variations of (a) the resonant displacement-amplitude (W_f/h) and (b) the corresponding control-voltage (V_f) with the control-gain (k_d) (p_0 = 40 N, VEM: monolithic viscoelastic material).

The results in Fig. 4.7 are evaluated at a constant value of k_d. However, for different values of k_d, the corresponding variations of the resonant displacement-amplitude (W_f/h) and control voltage (V_f) are illustrated in Figs. 4.8(a) and 4.8(b), respectively, where the active-passive damping is achieved either through monolithic viscoelastic material or VEPC. For any case of the monolithic viscoelastic material and VEPC, Fig. 4.8(a) shows that a good active-passive damping in the overall plate can be achieved by increasing the value of k_d. But, the superior attenuation of vibration amplitude arises for the VEPC by supplying significantly less control voltage (Fig. 4.8(b)). These results imply the present VEPC as a potential damping material for active-passive damping treatment of structural vibration.

4.4 Summary

In this chapter, the damping characteristics of an actively constrained VEPC layer are investigated by integrating it over the surface of a substrate plate. The VEPC layer is achieved by the inclusion of graphite particles within the butyl rubber matrix, and it is constrained by a piezoelectric actuator layer that is activated by supplying external voltage according to the velocity feedback control law. With this arrangement, a closed-loop FE model of the overall plate is derived, and the active-passive damping characteristics of the actively constrained VEPC layer are studied mainly for the variation of the volume fraction of inclusion of graphite particles.

The analysis reveals that the inclusion of graphite particles in the viscoelastic layer not only causes an augmented transfer of active action from the piezoelectric actuator layer to the substrate plate but also results in enhanced passive damping capability of the constrained viscoelastic layer. As a result, the active-passive damping in the overall plate significantly increases. However, this improvement of active-passive damping can be achieved up to a certain value of the volume fraction of inclusion (VFI), where an optimal VFI arises for the maximum damping. Further study on the active-passive control of frequency responses of the overall plate reveals significantly improved attenuation of resonant displacement-amplitude at the expense of the lesser

control voltage when the conventional monolithic viscoelastic layer is converted to VEPC layer through the optimal VFI of graphite particles. These observations imply the present VEPC as a potential damping material for ACLD treatment of structural vibration.

Chapter 5

Shear actuation-based hybrid active-passive damping in sandwich structures using a graphite particle-filled viscoelastic layer

5.1 Introduction

The concept of sandwich structure is enormously employed for the design of thin-walled structural components in aircraft, spacecraft, ships, railway vehicles, energy absorbent devices, blast protective military equipment, wind energy systems, radiofrequency antenna, biomedical devices, etc. (Birman and Kardomatea, 2018; Herrmann et al., 2005). Generally, the core of a sandwich structure is made of a material with high shear strength and low mass density. So, a sandwich structure possesses the advantage of high bending strength to weight ratio. However, for vibration control of these lightweight thin-walled structures, the application of piezoelectric actuators is extensively addressed in the literature where two kinds of actuators, namely extensional mode and shear mode piezoelectric actuators (Fig. 1.6), are utilised (Li and Yang, 2007; Raja et al., 2004; Thakkar and Ganguli, 2004a; Trindade, 2011; Trindade and Benjeddou, 2008). The extensional mode piezoelectric actuators are usually mounted over the surface of a sandwich structure and provide an extensional actuation force to control the deformation of the overall structure by counteracting the mechanically induced bending stress (Benjeddou et al., 1997; Hwang and Park, 1993; Trinidade, 2007). In contrast, the shear mode piezoelectric actuators are embedded in the core of a sandwich structure so that the transverse shear actuation force in the actuators acts against the similar mechanically induced stress to control the deformation/vibration of the overall structure (Baillargeon and Vel, 2005; Benjeddou and Deu, 2001a; Li and Yang, 2007).

However, if one compares these two kinds of piezoelectric actuators in control of sandwich structures, a shear mode piezoelectric actuator provides many advantages over the extensional mode piezoelectric actuator. Sun and Zhang (1995) reported that the bending stress in the surface-mounted extensional mode piezoelectric actuator is more than that in the shear mode piezoelectric actuator within the core. Also, the inter-laminar stress between the actuator and

host structure is significantly less for the shear mode actuator as compared to that for the extensional mode actuator. The researchers (Sun and Zhang, 1995) also addressed that the extensional mode piezoelectric actuator may provide greater actuation of a sandwich structure than that for the shear mode piezoelectric actuator. But, the required size of the extensional mode piezoelectric actuator is more than that of the shear mode piezoelectric actuator. In another study, Trindade (2007) utilised both the extensional and shear mode piezoelectric actuators to control the vibration of a sandwich beam, and it was observed that the extensional mode piezoelectric actuator provides good control of the low-frequency modes of vibration while the control performance of the shear mode actuator is almost uniform over the wide range of frequency.

The aforesaid observations imply the suitability of the shear mode piezoelectric actuator for control of sandwich structures in comparison to the extensional mode piezoelectric actuator. However, a common shortcoming of both actuators is the incompatibility of their actuation force with the mechanically induced stress, especially for a host structure with high rigidity. Moreover, piezoelectric actuators are usually not suitable for structural vibration control at high-frequency (Azvine et al., 1995). In view of these shortcomings, the utilisation of piezoelectric actuators along with the viscoelastic materials has been addressed by many researchers leading to different hybrid active-passive damping treatment of structural vibration, as a corresponding review is furnished in Chapter 1. However, these hybrid damping treatments are developed utilising the extensional mode piezoelectric actuators. In contrast, there is a little attention paid to the development of similar damping treatment utilising shear mode piezoelectric actuators, although the shear mode piezoelectric actuators are commercially available actuators and provide aforesaid advantages over the extensional mode piezoelectric actuators in control of sandwich structures. In an experimental study (Trindade, 2011) on the use of a shear mode piezoelectric actuator along with a viscoelastic material for control of sandwich beams, it was suggested that the shear mode piezoelectric actuators may be a good choice for active-passive damping. In another study, Batra and Geng (2002) considered two different arrangements for the active-passive damping treatment of a plate. The first one is a sandwich plate where one shear mode piezoelectric actuator layer is covered by two identical viscoelastic layers at the core. In the second one, the host plate is covered by two identical viscoelastic layers that are constrained by the extensional

mode piezoelectric actuator layers. Through these configurations of the hybrid plate, they investigated the effectiveness of the shear mode piezoelectric actuator in comparison to that of the extensional mode piezoelectric actuator for the active-passive damping treatment. It was reported that the shear mode piezoelectric actuator is more effective in damping out the vibration of the hybrid plate than that for the use of the extensional mode piezoelectric actuator (Batra and Geng, 2002). Motivated by this observation and the lack of literature in this field, the study in this chapter focuses on the further development of the shear actuation-based active-passive control of vibration of sandwich structures.

When viscoelastic layers are used along with shear mode piezoelectric actuator layers at the core of a sandwich structure, the main difficulty arises on deciding the appropriate stack of these layers for an effective shear actuation-based active-passive damping. The reason of this difficulty is that both the viscoelastic and piezoelectric actuator layers act for damping through the transverse shear strain. So, their appropriate locations within the stack of layers coincide at a location where the mechanically induced transverse shear strain appears with its maximum value. On having this difficulty, there may be two types of stacking sequences of the actuator and viscoelastic layers at the core of a sandwich structure as shown in Figs. 5.1(a) and 5.1(b). It may be noted here that one (Fig. 5.1(a)) of these stacks of layers was considered in a study reported by Batra and Geng (2002). However, the appropriate one among these two stacking sequences in the core is sorted out at present, and it is the first objective of the study in this chapter.

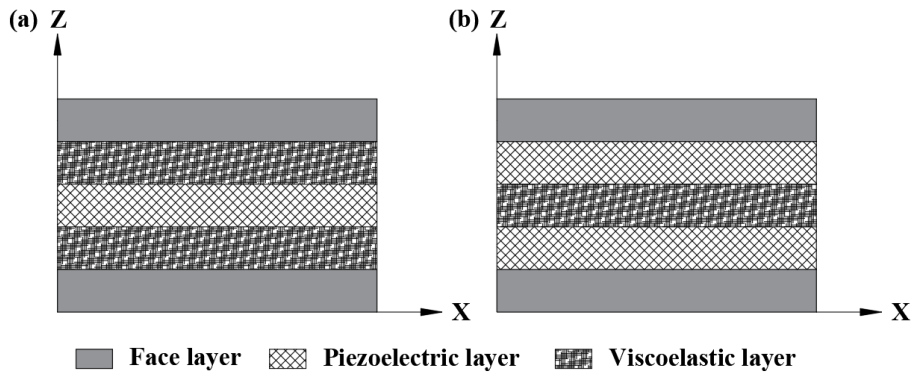

Fig. 5.1 Two different stacking sequences of the shear mode piezoelectric actuator and viscoelastic layers at the core of a sandwich structure; (a) actuator layer is covered by viscoelastic layers; (b) viscoelastic layer is covered by actuator layers.

Apart from the aforesaid concern in deciding the appropriate stack of layers in the core, another shortcoming arises due to the very low stiffness of the viscoelastic damping layer. In the stack of layers, as shown in Fig. 5.1(a), the active action or shear actuation force cannot transfer effectively from the actuator layer to other layers because of the very low stiffness of the adjacent viscoelastic layers. Similarly, for the other stack of layers at the core (Fig. 5.1(b)), the shear actuation force cannot reach effectively to the location of the mechanically induced maximum transverse shear stress around the middle plane of the sandwich structure because of low stiffness of the viscoelastic layer. Therefore, the active action or shear actuation force would be underutilised for both the stacking sequences of layers at the core. To alleviate this shortcoming, the VEPC damping layer can be used, where the increased stiffness in this damping layer due to the inclusion of graphite particles is expected to enhance the transfer of shear actuation force towards an improved shear-based hybrid active-passive damping. A detailed study on this issue is carried out at present, and it is the second objective of the study in this chapter.

On the basis of the aforesaid two objectives, the study in this chapter is performed through the vibration analysis of a sandwich plate-strip where the core is composed according to the two different stacking sequences (Figs. 5.1(a)-5.1(b)) of the actuator and viscoelastic layers. The numerical results mainly illustrate the aspects as (a) the appropriate stacking sequence of the actuator and viscoelastic layers in the core for better damping and (b) the effect of the inclusion on the shear actuation-based active-passive damping characteristics of the sandwich structure. In the following sections, first, in section 5.2, the present arrangement of the viscoelastic/VEPC and shear piezoelectric actuator materials in the core of a sandwich plate-strip is presented. In the next section (section 5.3), a closed-loop three-dimensional (3D) FE model of the plate-strip is developed based on a shear actuation-based active control strategy. Subsequently, in section 5.4, the numerical results are presented to explore the aforesaid aspects in the shear actuation-based active-passive damping. Finally, the overall study in this chapter is summarized in section 5.5.

5.2 Present arrangement of shear actuation-based active-passive damping treatment

Figure 5.2 shows the present sandwich plate strips in the reference Cartesian coordinate (xyz) system. The core is made of a laminate of active and viscoelastic layers in two different stacking sequences (Figs. 5.2(a)-5.2(b)) similar to that as shown in Figs. 5.1(a)-5.1(b). The active layer (Fig. 5.2(a)-5.2(b)) is made of the shear mode piezoelectric actuator, where the actuator is taken in the form of the patch for implementing a shear-based active control strategy, as presented in section 5.4. The identical actuator patches are embedded within the foam layer to form the active composite layer (Fig. 5.3). The length of a patch segment of this composite layer along the x-direction is denoted by L_s while the length of the

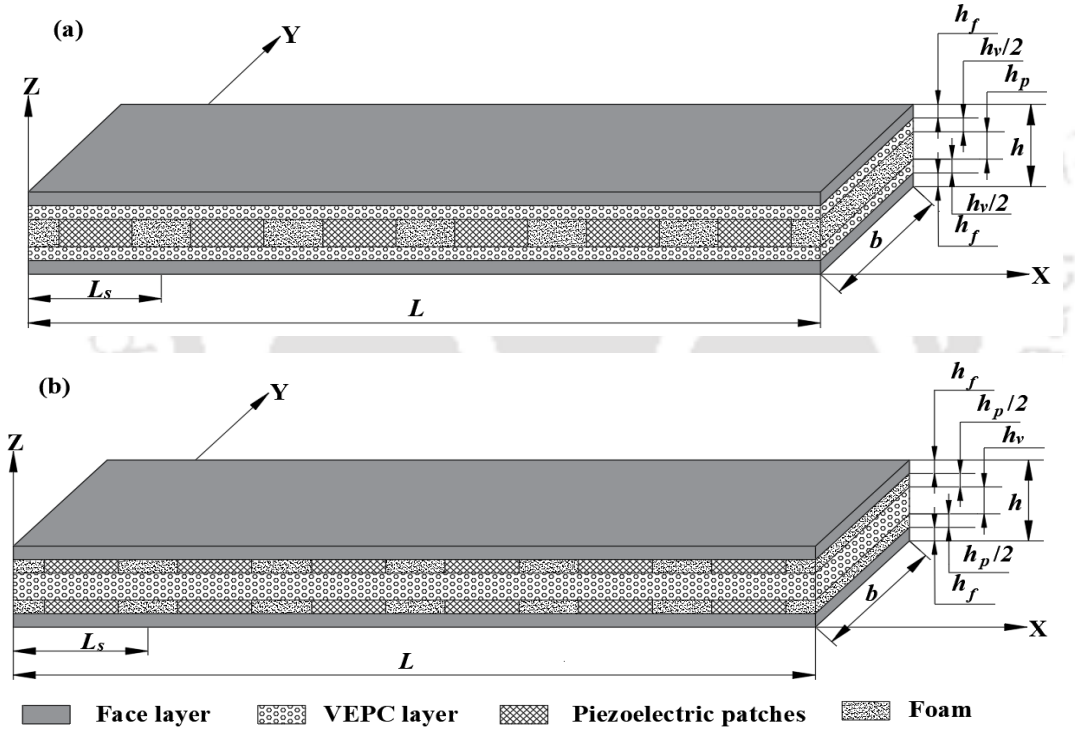

Fig. 5.2 Schematic diagrams of the present sandwich plate strips with two different stacking sequences of active and VEPC layers at the core; (a) Core-config#1 and (b) Core-config#2.

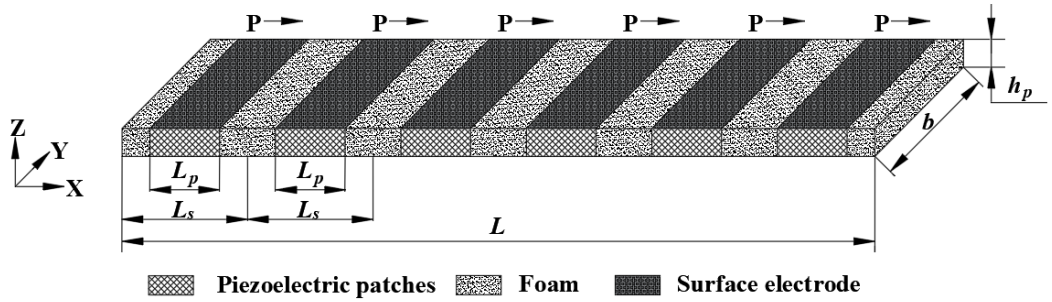

Fig. 5.3 Schematic diagram of the active composite layer made of shear mode piezoelectric actuator patches embedded in the foam layer.

actuator patches in the same direction is designated by L_p. So, the volume fraction of actuator patches in the active composite layer can be denoted by, $v_p = L_p / L_s$. The number of actuator patch segments over the length of the active layer is denoted by n_p. The piezoelectric actuator patches are poled (P) along the x-direction and activated by applying the external voltage across their top and bottom electrode surfaces (Fig. 5.3).

The viscoelastic layer is made of VEPC having the inclusion of graphite particles. The face layers are considered to be made of an isotropic material. The length, width and thickness of the sandwich plate strips are denoted by, L, b and h, respectively. For the sake of simplicity in presenting the results, the plate strips with two different stacking sequences at core are represented by Core-config#1 (Fig. 5.2(a)) and Core-config#2 (Fig. 5.2(b)). The active layer in Core-config#1 (Fig. 5.2(a)) is divided through its middle surface into two identical active layers that are used in Core-config#2 (Fig. 5.2(b)). Similarly, the VEPC layer in Core-config#2 (Fig. 5.2(b)) is divided through its middle surface into two identical VEPC layers to form Core-config#1 (Fig. 5.2(a)). Therefore, the volume of the active or passive VEPC layer remains the same for both the stacking sequences at the core.

5.3 Closed-loop FE model of the sandwich plate-strip

As the plate strips are composed in layered configuration, their mathematical model can be derived using layer-wise (LW) theory where the displacement field is defined independently for every layer, as a similar formulation is presented in the previous chapter. However, the displacement field in a layer within the LW framework is usually defined without satisfying the continuity of the transverse

normal/shear stresses at the inter-laminar surfaces, and it does not produce a significant error in the overall response of a laminate (Reddy, 2003). But, in handling a shear mode actuator layer within a laminate, the continuity of the transverse shear stresses at the inter-layer surface is an essential requirement for accurate modelling of the corresponding transfer of transverse shear actuation force from the actuator layer to other layers in the laminate. So, this continuity condition is to be satisfied while defining a displacement field in a layer within the LW framework. Similar formulation of displacement field in the LW framework is addressed in the available literature (Carrera, 2003; Pandit et al., 2008; Phan-Dao et al., 2016; Tornabene et al., 2015), where it seems a complex formulation because of the satisfaction of continuity of inter-laminar stresses. Alternatively, the same concern can be handled by a simple formulation using 3D finite elements, where all transverse stresses remain continuous at the inter-laminar surfaces and also the complexity in the arrangement of different materials in a laminate can be dealt easily. However, the shortcoming here appears as the high computational cost because of a large number of nodal degrees of freedom in the corresponding 3D finite element model, whereas the main advantage in the LW theory lies in the low computational cost. Having these concerns in the modelling of laminated structures, the present analysis of the layered plate strips is carried out by deriving a 3D FE model.

The state of strain ($\boldsymbol{\varepsilon}$) and the state of stress ($\boldsymbol{\sigma}$) at any point within the sandwich plate-strip can be written as,

$$\boldsymbol{\varepsilon} = \left\{ \varepsilon_x \quad \varepsilon_y \quad \varepsilon_z \quad \gamma_{yz} \quad \gamma_{xz} \quad \gamma_{xy} \right\}^{\mathrm{T}}$$

$$\boldsymbol{\sigma} = \left\{ \sigma_x \quad \sigma_y \quad \sigma_z \quad \tau_{yz} \quad \tau_{xz} \quad \tau_{xy} \right\}^{\mathrm{T}} \tag{5.1}$$

where, ε_x/σ_x, ε_y/σ_y and ε_z/σ_z are the normal strains/stresses along the x, y and z directions, respectively; γ_{yz}/τ_{yz}, γ_{xz}/τ_{xz} and γ_{xy}/τ_{xy} are the shear strains/stresses over the yz, xz and xy planes, respectively. According to the state of strain ($\boldsymbol{\varepsilon}$, Eq. (5.1)), the linear strain-displacement relations can be written in the form similar to Eq. (2.2a), where the displacement vector ($\boldsymbol{d}$) and the operator matrix ($\boldsymbol{L}$) are given in Eq. (5.2).

$$\boldsymbol{\varepsilon} = \boldsymbol{L}\boldsymbol{d} \tag{2.2a}$$

$$\boldsymbol{d} = \{u \quad v \quad w\}^{\mathrm{T}},$$

$$\boldsymbol{L} = \begin{bmatrix} \partial/\partial x & 0 & 0 & 0 & \partial/\partial z & \partial/\partial y \\ 0 & \partial/\partial y & 0 & \partial/\partial z & 0 & \partial/\partial x \\ 0 & 0 & \partial/\partial z & \partial/\partial y & \partial/\partial x & 0 \end{bmatrix}^{\mathrm{T}} \tag{5.2}$$

In Eq. (5.2), u, v and w are the displacements at any point in a plate-strip along the x, y and z directions, respectively. The constitutive relations for the piezoelectric actuator patches can be written in the similar form, as given in Eq. (4.5a); however, the forms of the property matrices ($\boldsymbol{C}$, $\boldsymbol{e}$, $\boldsymbol{\epsilon}$) change due to the alteration of poling direction from thickness (z) to an in-plane (x) direction, as furnished in Eq. (5.3) (Benjeddou, 2007; Benjeddou et al., 1997; Trindade and Benjeddou, 2012).

$$\boldsymbol{\sigma} = \boldsymbol{C}\boldsymbol{\varepsilon} - \boldsymbol{e}\boldsymbol{E}, \quad \boldsymbol{D} = \boldsymbol{e}^{\mathrm{T}}\boldsymbol{\varepsilon} + \boldsymbol{\epsilon}\,\boldsymbol{E}$$

$$\boldsymbol{E} = \{E_x \quad E_y \quad E_z\}^{\mathrm{T}}, \quad \boldsymbol{D} = \{D_x \quad D_y \quad D_z\}^{\mathrm{T}} \tag{4.5a}$$

$$\boldsymbol{C} = \begin{bmatrix} C_{33} & C_{32} & C_{31} & 0 & 0 & 0 \\ C_{23} & C_{22} & C_{21} & 0 & 0 & 0 \\ C_{13} & C_{12} & C_{11} & 0 & 0 & 0 \\ 0 & 0 & 0 & C_{66} & 0 & 0 \\ 0 & 0 & 0 & 0 & C_{55} & 0 \\ 0 & 0 & 0 & 0 & 0 & C_{44} \end{bmatrix},$$

$$\boldsymbol{e} = \begin{bmatrix} e_{33} & 0 & 0 \\ e_{32} & 0 & 0 \\ e_{31} & 0 & 0 \\ 0 & 0 & 0 \\ 0 & 0 & e_{15} \\ 0 & e_{24} & 0 \end{bmatrix}, \quad \boldsymbol{\epsilon} = \begin{bmatrix} \epsilon_{33} & 0 & 0 \\ 0 & \epsilon_{22} & 0 \\ 0 & 0 & \epsilon_{11} \end{bmatrix} \tag{5.3}$$

Here, the shear piezoelectric actuator patches are taken with a very small thickness, and their top and bottom surfaces are fully electrode surfaces (Fig. 5.3). So, it is assumed that, $E_x \approx 0$, $E_y \approx 0$, $E_z = -V/h_a$ where V is the applied voltage across the top and bottom electrode surfaces and h_a is the thickness of the active layer or actuator patch. Accordingly, the constitutive relations (Eqs. (4.5a) and (5.3)) can be reduced as (Benjeddou, 2007; Benjeddou et al., 1997; Trindade and Benjeddou, 2012),

$$\boldsymbol{\sigma}^k = \boldsymbol{C}^k \boldsymbol{\varepsilon} - \boldsymbol{e}^k E_z, \; D_z^k = \left(\boldsymbol{e}^k\right)^{\mathrm{T}} \boldsymbol{\varepsilon} + \in_{11}^k E_z, \; k = 3$$

$$\boldsymbol{C}^k = \begin{bmatrix} C_{33}^k & C_{32}^k & C_{31}^k & 0 & 0 & 0 \\ C_{23}^k & C_{22}^k & C_{21}^k & 0 & 0 & 0 \\ C_{13}^k & C_{12}^k & C_{11}^k & 0 & 0 & 0 \\ 0 & 0 & 0 & C_{66}^k & 0 & 0 \\ 0 & 0 & 0 & 0 & C_{55}^k & 0 \\ 0 & 0 & 0 & 0 & 0 & C_{44}^k \end{bmatrix}, \; \boldsymbol{e}^k = \begin{Bmatrix} 0 \\ 0 \\ 0 \\ 0 \\ e_{15}^k \\ 0 \end{Bmatrix} \tag{5.4}$$

where, the superscript k represents the materials for face layer, foam, actuator patches and VEPC layer as per its value as 1, 2, 3 and 4, respectively. However, the other materials in the sandwich plate strips for the face layer, VEPC layer and foam layer are piezoelectrically inactive isotropic materials, and their constitutive relations can be written, as given in Eq. (5.5) where E^k and ν^k are the Young's modulus and Poisson's ratio, respectively for the k^{th} material.

$$\boldsymbol{\sigma}^k = \boldsymbol{C}^k \boldsymbol{\varepsilon}, \; k = 1, 2, 4$$

$$\boldsymbol{C}^k = \frac{E^k}{\left(1+\nu^k\right)\left(1-2\nu^k\right)} \begin{bmatrix} \left(1-\nu^k\right) & \nu^k & \nu^k & 0 & 0 & 0 \\ \nu^k & \left(1-\nu^k\right) & \nu^k & 0 & 0 & 0 \\ \nu^k & \nu^k & \left(1-\nu^k\right) & 0 & 0 & 0 \\ 0 & 0 & 0 & \left(\frac{1-2\nu^k}{2}\right) & 0 & 0 \\ 0 & 0 & 0 & 0 & \left(\frac{1-2\nu^k}{2}\right) & 0 \\ 0 & 0 & 0 & 0 & 0 & \left(\frac{1-2\nu^k}{2}\right) \end{bmatrix} \tag{5.5}$$

It may be noted here that the stiffness matrix ($\boldsymbol{C}^k$) for the VEPC layer ($k = 4$) is a frequency-dependent complex quantity as it is obtained from the complex material moduli of VEPC through the solution of Eqs. 2.6(a)-2.6(b). Similar stiffness matrix ($\boldsymbol{C}^k$) for the materials of face layer ($k = 1$) and foam ($k = 2$) are frequency-independent real quantity.

The sandwich plate strips are considered to operate under a transverse harmonic point-load ($p(t)$) at the middle point ($L/2, b/2, h$). For the corresponding

vibration, the first variations of the total potential energy (δT_P) and the total kinetic energy (δT_K) of the sandwich plate strips can be written, as given in Eqs. (5.6) and (5.7), respectively, where ρ^k is the mass density and V^k is the volume for the k^{th} material.

$$\delta T_P = \sum_{k=1}^{4}\left[\int_{V_k}\left\langle(\delta\boldsymbol{\varepsilon})^{\mathrm{T}}\boldsymbol{\sigma}^k - (\delta E_z)^{\mathrm{T}} D_z^k\right\rangle dV_k\right] - \left\langle \delta w\, p(t)\right\rangle_{\left(\frac{L}{2},\frac{b}{2},h\right)} \tag{5.6}$$

$$\delta T_K = \sum_{k=1}^{4}\left[\int_{V_k}\left(\{\delta\dot{u} \quad \delta\dot{v} \quad \delta\dot{w}\}\rho^k\{\dot{u} \quad \dot{v} \quad \dot{w}\}^{\mathrm{T}}\right)dV_k\right] \tag{5.7}$$

For deriving the FE model, the domain of a sandwich plate-strip is discretised by 27-node isoparametric elements. The edges of every element are parallel to the axes of the reference coordinate system, and a typical element is made of one of the four component materials ($k = 1,2,3,4$). The displacement ($\boldsymbol{d}$) vector at a point in a typical element can be expressed by the elemental nodal displacement vector ($\boldsymbol{d}^e$) and the shape function matrix ($\boldsymbol{N}$) in the same form, as given in Eq. (2.11).

$$\boldsymbol{d} = \boldsymbol{N}\boldsymbol{d}^e \tag{2.11}$$

Using Eqs. (5.4), (5.5), (2.2a), (5.2) and (2.11) in Eqs. (5.6) and (5.7), and then substituting the resulting expressions in the mathematical expression of extended Hamilton's principle (Eq. (2.12), the FE equations of motion of a typical element can be obtained, as given in Eq. (5.8).

$$\int_{t_1}^{t_2}(\delta T_K - \delta T_P)\,dt = 0 \tag{2.12}$$

$$\boldsymbol{M}^e\ddot{\boldsymbol{d}}^e + \boldsymbol{K}^e(\omega)\,\boldsymbol{d}^e = \boldsymbol{P}_E^e E_z + \boldsymbol{P}_M^e\, p(t)$$

$$\boldsymbol{M}^e = \int_{V_k^e}\left(\boldsymbol{N}^{\mathrm{T}}\rho^k\boldsymbol{N}\right)dV_k^e,\ \ \boldsymbol{K}^e(\omega) = \int_{V_k^e}\left(\boldsymbol{N}^{\mathrm{T}}\boldsymbol{L}^{\mathrm{T}}\boldsymbol{C}^k(\omega)\,\boldsymbol{L}\boldsymbol{N}\right)dV_k^e,$$

$$\boldsymbol{P}_E^{\boldsymbol{e}} = \int_{V_k^e}\left(\boldsymbol{N}^{\mathrm{T}}\boldsymbol{L}^{\mathrm{T}}\boldsymbol{e}^k\right)dV_k^e,\ \ \boldsymbol{P}_M^e = \left\langle \boldsymbol{N}^{\mathrm{T}}\{0 \quad 0 \quad 1\}^{\mathrm{T}}\right\rangle_{x_e,y_e,z_e} \tag{5.8}$$

In Eq. (5.8), V_k^e is the elemental volume within k^{th} material; $\boldsymbol{M}^e$ and $\boldsymbol{K}^e$ are the elemental mass and stiffness matrices, respectively; $\boldsymbol{P}_E^e$ is the elemental nodal

electro-elastic coefficient vector and $\boldsymbol{P}_M^e$ is the elemental nodal load coefficient vector; x_e, y_e and z_e are the coordinates at the applied transverse point-load over the surface of an element. It may be noted here that the elemental stiffness matrix ($\boldsymbol{K}^e(\omega)$) for an element made of VEPC is a frequency-dependent complex quantity whereas similar matrix for an element made of any other material is a constant real quantity. Also, $\boldsymbol{P}_E^e$ is a null vector for the elements made of piezoelectrically inactive materials ($k = 1,2,4$). Now, assembling the elemental equations (Eq. (5.8)), the global equations of motion for the vibration of the sandwich plate strips can be obtained as,

$$\boldsymbol{M}\ddot{\boldsymbol{X}} + \boldsymbol{K}(\omega)\,\boldsymbol{X} = \sum_{s=1}^{n_p}\left(\boldsymbol{P}_E^s\, E_z^s\right) + \boldsymbol{P}_M\, p(t) \tag{5.9}$$

where, $\boldsymbol{M}$ and $\boldsymbol{K}$ are the global mass and stiffness matrices, respectively; $\boldsymbol{P}_M$ is the global nodal load coefficient vector; $\boldsymbol{X}$ is the global nodal displacement vector; n_p is the number of actuator patch segments along the x-direction; $\boldsymbol{P}_E^s$ is the global nodal electro-elastic coefficient vector for the s^{th} actuator patch segment, and it is obtained through the assemblage of elemental nodal electro-elastic coefficient vectors ($\boldsymbol{P}_E^e$) for the elements within the s^{th} actuator patch segment; E_z^s is the applied transverse electric field for the s^{th} actuator patch segment.

According to the poling (P) direction of piezoelectric actuators (Fig. 5.3) and the applied transverse electric field (E_z^s), the actuator patches provide shear actuation force in the xz-plane. This actuation force is utilised to counteract the mechanically induced transverse shear stress (τ_{xz}) for actuation of bending deformation of the sandwich plate-strip. Here, the mechanical stress (τ_{xz}) changes its sign at the antinodes of a bending mode shape of vibration of the plate-strip. Therefore, the sign of the applied electric field (E_z^s) is to be varied over the actuator patch segments for effective actuation of bending deformation of the plate-strip. Now, the locations of the change of sign of the slope of bending of the plate-strip are coincident with that for the mechanical stress (τ_{xz}). So, presently the time-rate of change of the local slope of bending around an actuator patch

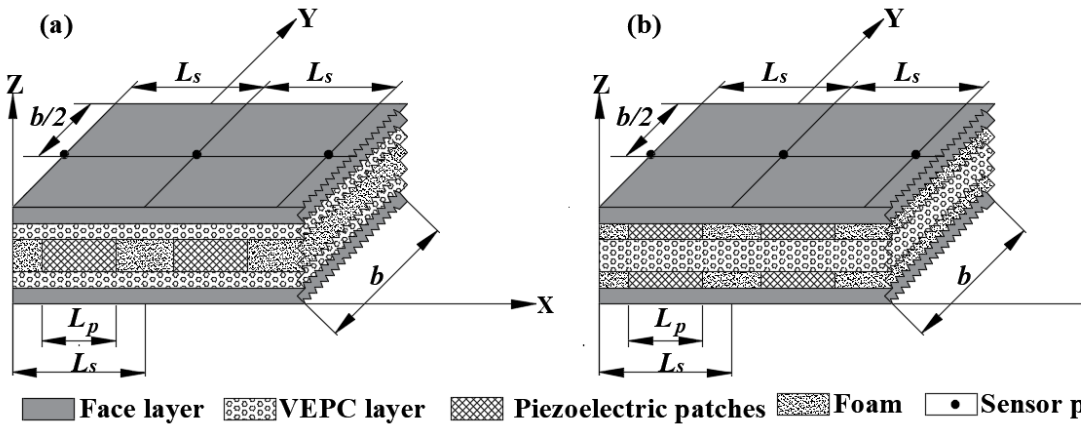

Fig. 5.4 Schematic diagrams for a part of the present sandwich plate-strip with the locations of velocity sensors over the top surface; (a) Core-config#1 and (b) Core-config#2.

segment is taken as the feedback parameter to supply the external electric field (E_z^s) to that patch segment according to the velocity feedback control strategy. To implement this control strategy, the velocity sensors are located across the length (L_s) of every actuator patch segment as shown in Fig. 5.4. These sensors measure the transverse velocity and provide an estimation of the time-rate of change of the local slope of bending deformation around a patch segment (s) as,

$$\dot{\varphi}_s = \frac{{}^R\dot{w}_0^s - {}^L\dot{w}_0^s}{L_s}, \quad s = 1, 2, ...n_p \tag{5.10}$$

where, ${}^L\dot{w}_0^s$ and ${}^R\dot{w}_0^s$ are the transverse velocities sensed by the velocity sensors across the length (L_s) of s^{th} actuator patch segment. Now, according to the negative velocity feedback control law, the applied transverse electric field (E_z^s) to a typical actuator patch segment (s) can be written as follows,

$$E_z^s = -V^s / h_a \,, \; V^s = -k_d^s \dot{\varphi}_s \tag{5.11}$$

where, k_d^s is the velocity feedback control gain for the s^{th} actuator patch segment; $h_a = h_p$ for Core-config#1 (Fig. 5.2(a)) and $h_a = h_p / 2$ for Core-config#2 (Fig. 5.2(b)). The transverse velocities can be expressed in terms of the global nodal velocity vector ($\dot{\boldsymbol{X}}$) through a transformation row matrix ($\boldsymbol{N}_T^s$) as,

$$\left\langle {}^R\dot{w}_0^s - {}^L\dot{w}_0^s \right\rangle = \boldsymbol{N}_T^s \dot{\boldsymbol{X}} \tag{5.12}$$

Using Eqs. (5.12) and (5.10) in Eq. (5.11), and then substituting the resulting expression for E_z^s in Eq. (5.9), the closed-loop FE equations of motion of the sandwich plate-trip can be obtained in the form of Eq. (4.18a), where the damping matrix ($\boldsymbol{C}$) is given in Eq. (5.13).

$$\boldsymbol{M}\ddot{\boldsymbol{X}} + \boldsymbol{C}\dot{\boldsymbol{X}} + \boldsymbol{K}(\omega)\,\boldsymbol{X} = \boldsymbol{P}_M\, p(t) \tag{4.18a}$$

$$\boldsymbol{C} = \sum_{s=1}^{n_p} \left\langle \boldsymbol{P}_E^s\, k_d^s\, \boldsymbol{N}_T^s \big/ \left(h_a\, L_s\right) \right\rangle \tag{5.13}$$

The transverse harmonic point-load is considered in the form as $p(t) = p_0\, e^{j\omega t}$ ($j = \sqrt{-1}$) where p_0 and ω are the load-amplitude and operating frequency, respectively. For linear steady-state vibration of the sandwich plate-strip under the harmonic point-load, Eq. (4.18a) can be reduced in the form of Eq. (4.20). The solution of Eq. (4.20) at a given frequency (ω) provides the complex nodal displacement vector ($\bar{\boldsymbol{X}}$), and its ($\bar{X}$) absolute value appears for the nodal displacement-amplitude vector. Presently, the maximum transverse displacement amplitude from this nodal displacement-amplitude vector is taken at every frequency for the presentation of frequency responses of the plate-strip.

$$\left(-\omega^2 \boldsymbol{M} + j\omega \boldsymbol{C} + \boldsymbol{K}(\omega)\right)\bar{\boldsymbol{X}} = \boldsymbol{P}_M\, p_0 \tag{4.20}$$

Further, for the steady-state free vibration ($p_0 = 0$) of the plate-strip, Eq. (4.20) can be written in the form of a complex quadratic eigenvalue problem, as illustrated in Eq. (4.19). Since the stiffness parameters in this equation are dependent on the operating frequency, it is solved using direct iteration method following the same procedure illustrated in section 2.3. However, the corresponding solution provides complex natural frequency of the plate-strip, and it is subsequently reduced following Eq. (2.18) for computation of the natural frequency and modal loss factor.

$$\left(\boldsymbol{K}^R(\omega_i) + j\left\langle \boldsymbol{K}^I(\omega_i) + \omega_i \boldsymbol{C}\right\rangle\right)\boldsymbol{\psi}_i = \omega^2 \boldsymbol{M}\boldsymbol{\psi}_i \tag{4.19}$$

$$(\omega_i)^2 = \left(\omega_i^o\right)^2 \langle 1 + j\eta_i \rangle \tag{2.18}$$

The active, passive and active-passive damping in the plate-strip are analysed by evaluating the modal loss factor following the aforesaid procedure. In this concern, it may be noted here that the modal loss factor (η_i) appears due to the

passive damping only when the velocity feedback control gain (k_d^s) is taken with the zero-value. Similarly, for the assumption of the zero-value of the material loss factor (η_c) of VEPC, modal loss factor (η_i) appears due to the shear actuation-based active damping only. However, the modal loss factor (η_i) due to the total hybrid active-passive damping arises for none of the aforesaid assumptions ($k_d^s \neq 0, \eta_c \neq 0$).

5.4 Numerical results and discussion

In this section, first, the present formulation and the corresponding FE code for analysis of the sandwich plate strips are verified. Next, the usefulness of the inclusion of graphite particles within the viscoelastic layer for the shear actuation-based hybrid active-passive damping treatment is investigated. The geometrical dimensions of the plate strips are considered as, $L = 0.4$ m, $b = 0.05$ m, $h_f = 1$ mm, $h_v = 4$ mm and $h_p = 2$ mm. Unless otherwise mentioned, the number (n_p) of actuator patch segments over the length of the plate strips is taken as 4 while the volume fraction (v_p) of actuator patch in a typical patch segment is considered as 0.8.

The face layers are considered to be made of Aluminium ($E = 69$ GPa, $\nu = 0.3$, $\rho = 2740$ kg/m^3). The material properties of the foam are taken as $E = 35.3$ MPa, $G = 12.76$ MPa, $\rho = 32$ kg/m^3 (Aldraihem and Khdeir, 2003). The piezoelectric patches are made of PZT5H (Erturk and Inman, 2011) having the properties as, $C_{11} = 127$ GPa, $C_{12} = 80.21$ GPa, $C_{13} = 84.67$ GPa, $C_{33} = 117.84$ GPa, $C_{44} = 22.99$ GPa, $C_{66} = 23.47$ GPa, $\rho = 7500$ kg/m^3, $e_{31} = -6.6228$ C/m^2, $e_{33} = 23.24$ C/m^2, $e_{24} = 17.03$ C/m^2. It may be noted here that increased stiffness of foam causes a deterioration in the damping performance of the shear piezoelectric patches (Trindade and Maio, 2008). However, according to the aforesaid material properties of foam and shear piezoelectric patches, the shear modulus of foam is much less than that of the shear piezoelectric patches. The plate strips are considered to operate at room temperature (32^o C), and thus the frequency-dependent effective properties of the VEPC layer at the same temperature are taken from Chapter 2.

According to the present formulation for active control, the control gains (k_d^s , $s = 1,2,\ldots,n_p$) can be assigned with different values over the actuator patch segments. It involves a little difficulty in deciding the appropriate values of the control gains based on some factors like (a) mode of vibration to be controlled, (b) locations of maximum and minimum values of the transverse shear stress (τ_{xz}) over the length of the plate-strip, (c) permissible value of the applied control voltage in the use of the piezoelectric actuators, etc. However, for the sake of simplicity, presently all shear actuator patches are considered to be activated with the uniform value of the velocity feedback control gains ($k_d^s = k_d$, $s = 1,2,\ldots,n_p$). The ends of the sandwich plate strips are considered as fixed ends ($u = 0$, $v = 0$, $w = 0$ at $x = 0, L$), and the forced vibration responses of the plate strips are evaluated by applying transverse harmonic point-load ($p(t)$) at the middle point ($L/2, b/2, h$) as mentioned in section 5.3.

5.4.1 Verification of the present FE formulation

For verification of the present FE formulation in handling the shear mode piezoelectric actuation, the sandwich plate-strip (Fig. 5.2(a)) is taken with negligibly thin ($h_v \approx 0$) viscoelastic layers. The other geometrical properties, material properties, and boundary conditions of this sandwich plate-strip are taken as identical to that for a sandwich beam analysed in (Aldraihem and Khdeir, 2003). The transverse deflection of this sandwich beam is then computed for an applied transverse electric field across the thickness of the shear piezoelectric actuators at the core. This result is illustrated in Fig. 5.5, together with the similar result given in (Aldraihem and Khdeir, 2003). It may be observed from Fig. 5.5 that the present result is in good agreement with the reference result, and this comparison verifies the present FE formulation for handling the shear mode piezoelectric actuation.

For further verification of the present FE formulation in the computation of natural frequency and modal loss factor, the sandwich plate-strip is taken with negligibly thin ($h_p \approx 0$) and deactivated ($k_d = 0$) active layers where the core is made of a monolithic viscoelastic material. Further, this sandwich structure is taken with properties identical to that for a sandwich plate analysed in (Cupiał and Nizioł, 1995). The natural frequency ($\omega_{m,n}$) and modal loss factor ($\eta_{m,n}$) of this

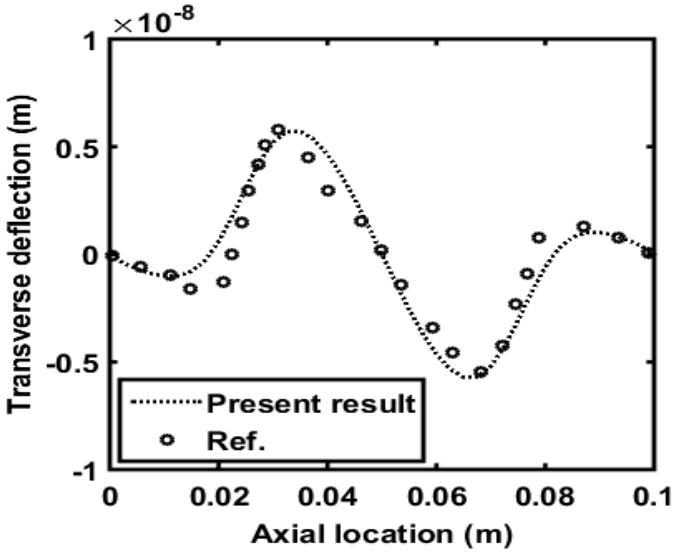

Fig. 5.5 Verification of the present FE formulation for handling the shear mode piezoelectric actuation (Ref. Aldraihem and Khdeir, 2003).

Table 5.1 Verification of the present FE formulation for the computation of natural frequency ($\omega_{m,n}$) and modal loss factor ($\eta_{m,n}$) (Ref. Cupiał and Nizioł, 1995).

Bending modes	Present FE results		Ref.	
(m,n)	$\omega_{m,n}$ (Hz)	$\eta_{m,n}$	$\omega_{m,n}$ (Hz)	$\eta_{m,n}$
(1,1)	60.246	0.1900	60.3	0.19
(1,2)	115.404	0.2028	115.4	0.203
(2,1)	130.559	0.1988	130.6	0.199
(2,2)	178.671	0.1802	178.7	0.181

Table 5.2 FE mesh convergence study for the sandwich plate-strips ($\phi = 0.2$, v_p = 0.8 and n_p = 8, k_d = 300).

No. of elements	Core-config#1		Core-config#2	
	ω_n (rad/s)	η	ω_n (rad/s)	η
640	507.658	0.28179	503.808	0.28904
1280	507.079	0.28181	503.725	0.28907
2048	506.857	0.28297	502.668	0.28771
3612	505.149	0.28486	502.349	0.28756
4992	505.141	0.28487	502.345	0.28756

sandwich plate are computed for the first four bending modes (m,n), and the results are furnished in Table 5.1 along with the similar reference results (Cupiał

and Nizioł, 1995). It may be observed from Table 5.1 that the present FE results are in good agreement with the reference results, thus verifying the present FE formulation for computation of natural frequency and modal loss factor

The FE mesh convergence study is performed to decide a suitable number of elements in evaluation of the present numerical results, where the fundamental natural frequency (ω_n) and the corresponding modal loss factor (η) of the sandwich plate-strips (Core-config#1 and Core-config#2) are evaluated by increasing the number of elements. These results are illustrated in Table 5.2. On the basis of these results (Table 5.2), the FE mesh of the sandwich plate-strips is considered for evaluation of the numerical results.

The geometry of the core of the present sandwich plate strips (Fig. 5.2(a) and 5.2(b)) seems to be a little complex, particularly for the embedded shear actuator patches. These actuator patches are to be included correctly in the FE code according to their specified locations and geometrical dimensions. It is presently verified through the computation of transverse shear strain (γ_{xz}) field within the domain of the sandwich plate-strip by applying an external transverse electric field (E_z) across the thickness of the shear piezoelectric actuator patches. For this static result, the Young's modulus of the viscoelastic layer is taken as 9.5 MPa while four actuator patch segments (n_p = 4) are considered with the volume fraction (v_p) of actuator patch as 0.5. The other geometrical properties, material properties, and boundary conditions of the sandwich plate-strip remain the same as those are given at the beginning of this section (section 5.4). The actuator patches within the left-half ($x = 0$, $L/2$) of the plate-strip are activated by applying 100 V while the other actuator patches are activated by applying -100 V. The corresponding distributions of the shear strain (γ_{xz}) for two different stacking sequences at the core (Core-config#1 and Core-config#2) are shown in Fig. 5.6(a)-5.6(d). Figures 5.6(a) and 5.6(c) show the distributions of γ_{xz} over the xz-plane of Core-config#1 and Core-config#2, respectively. The distributions of the same strain (γ_{xz}) over the middle plane of an active layer in Core-config#1 and Core-config#2 are illustrated in Figs. 5.6(b) and 5.6(d), respectively. Here, the strain (γ_{xz}) at a point in the plate-strip appears due to the electrically induced shear strain (γ_{xz}) in the actuator patches. So, the shear strain (γ_{xz}) would have its maximum magnitude over the actuator patches. Therefore, the zones of maximum

shear strain (γ_{xz}) in Figs. 5.6(a)-5.6(d) indicate the locations and geometrical dimensions of shear actuator patches. It may be observed that the zones of maximum shear strain in Figs. 5.6(a)-5.6(d) appear according to the specified locations and geometrical dimensions of actuator patches. These results verify the present FE code for accounting the actuator patches as per their specified locations and geometrical dimensions.

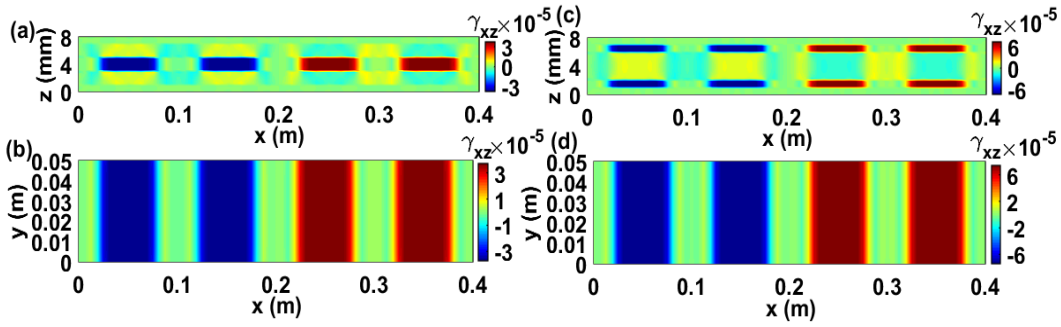

Fig. 5.6 Distribution of transverse shear strain (γ_{xz}) over the (a),(c) xz -plane of plate-strip, (b),(d) middle plane of the active layer in the plate-strip; (a), (b) Core-config#1 and (c), (d) Core-config#2.

5.4.2 Analysis of shear actuation-based hybrid active-passive damping

Initially, the influence of inclusion on the passive damping in the sandwich plate-strip (Fig. 5.2(a)) is studied considering negligibly thin ($h_p \approx 0$) and deactivated ($E_z^s = 0$) active layer. Here, the variation of modal loss factor (η) of the sandwich plate-strip corresponding to the fundamental bending mode of vibration is computed for different values of VFI (ϕ) in the VEPC layer at the core. Figure 5.7(a) illustrates this result where it can be observed that the passive damping in the sandwich plate-strip first increases and then decreases for the increasing VFI (ϕ) leading to an optimal value of VFI (ϕ) for the maximum passive damping in the sandwich plate-strip. This characteristic of passive damping using VEPC damping layer is also observed previously (Fig. 2.5) in the case of simply-supported/clamped-clamped sandwich beam; however, the optimal value of the VFI (ϕ) appears with different value for the plate-strip. The effect of this improved passive damping on the resonant transverse displacement-amplitude of the plate-strip is illustrated in Fig. 5.7(b) for the fundamental mode of vibration. This figure (Fig. 5.7(b)) shows that the attenuation of the resonant transverse displacement-

amplitude significantly improves due to the inclusion of graphite particles within the viscoelastic core.

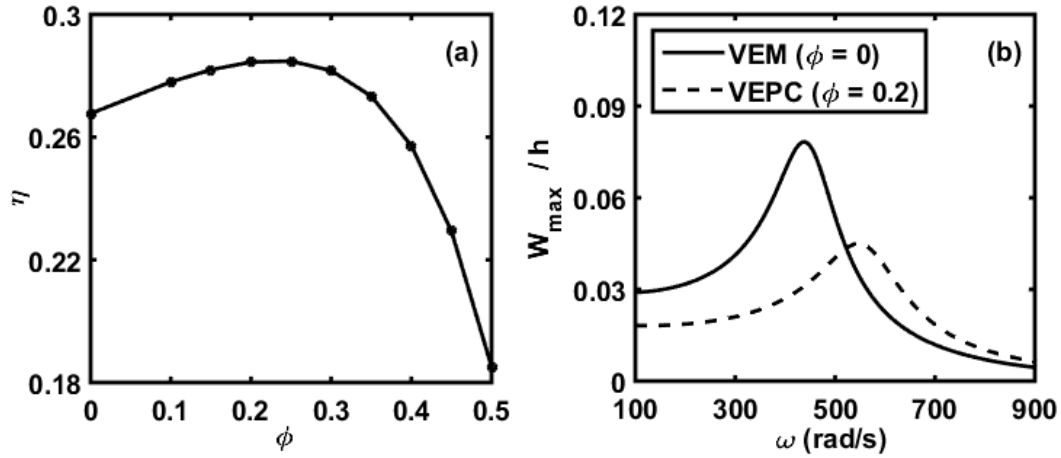

Fig. 5.7 (a) Variation of the modal loss factor (η) of the sandwich plate-strip ($h_p \approx 0$, $E_z^s = 0$) with VFI (ϕ); (b) variation of maximum transverse displacement-amplitude ($w_{\max}$) of the sandwich plate-strip with the operating frequency ($h_p \approx 0$, $E_z^s = 0$, $p_0 =$ 2 N).

Now, the shear actuators or active layers are stacked along with the VEPC layers at the core (Figs. 5.2(a)-5.2(b)) for achieving the shear actuation-based hybrid active-passive damping. According to the objectives of this study as stated in the introduction section, the analysis of the active-passive damping is mainly carried out by varying the VFI in the VEPC layer and considering two different stacking sequences of the component layers at the core (Figs. 5.2(a)-5.2(b)). First, to investigate the effect of the inclusion on the active counterpart of the total active-passive damping, the loss factor (η_c) of the passive damping layer is assumed to have zero-value ($\eta_c = 0$), and the variations of active damping (η for $k_d \neq 0$) with VFI (ϕ) are evaluated for the two different stacking sequences of layers at the core (Core-config#1 (Fig. 5.2(a)) and Core-config#2 (Fig. 5.2(b))). This result is illustrated in Fig. 5.8(a) where it is clear that the shear actuation-based active damping in the sandwich plate strips significantly increases with the increasing VFI. In fact, the inclusion of graphite particles improves the stiffness of the viscoelastic layer leading to better transfer of actuation force from the active layer to other layers. It leads to better utilisation of the shear piezoelectric actuators in Core-config#1 and Core-config#2 for attenuation of vibration of the sandwich plate strips. However, according to the results in Fig. 5.8(a), one would

prefer Core-config#2 as it provides significantly more active damping than that for the Core-config#1 for any value of the VFI (ϕ). Also, the rate of increase of active damping with the increasing VFI is more in the case of the Core-config#2 than that for the case of the Core-config#1.

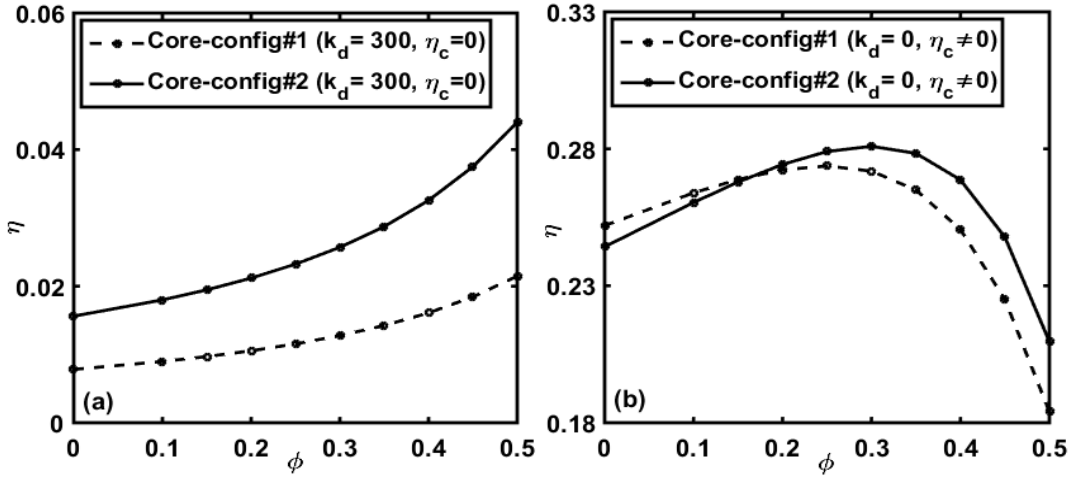

Fig. 5.8 Variation of the modal loss factor (η) with VFI (ϕ) for (a) only active damping ($k_d \neq 0$, $\eta_c = 0$); (b) only passive damping ($k_d = 0$, $\eta_c \neq 0$) in the sandwich plate strips.

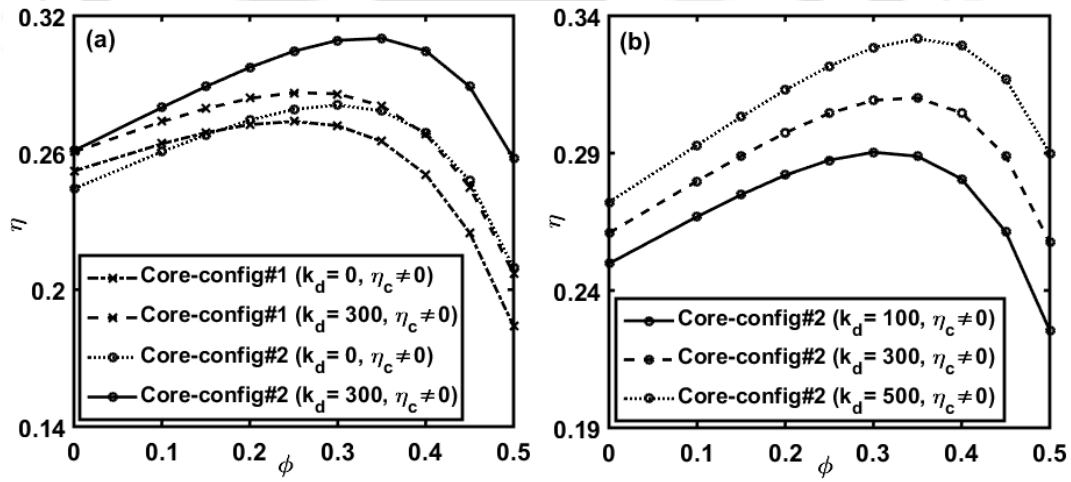

Fig. 5.9 Variation of the modal loss factor (η) with VFI (ϕ) for (a) only passive ($k_d = 0$, $\eta_c \neq 0$) and total active-passive ($k_d \neq 0$, $\eta_c \neq 0$) damping in the sandwich plate strips; (b) active-passive damping ($k_d \neq 0$, $\eta_c \neq 0$) in the sandwich plate-strip for Core-config#2 (Fig. 5.2(b)).

In parallel to the aforesaid active counterpart of the total active-passive damping, the variations of the passive counterpart with VFI are illustrated in Fig.

5.8(b) considering zero-value of the control gain ($k_d = 0$, $\eta_c \neq 0$). It may be observed by comparing the results in Figs. 5.8(b) and 5.7(a) that the characteristics of the passive damping in the sandwich plate strips do not change much for the incorporation of shear actuators in a stack with the viscoelastic layer. However, Fig. 5.8(b) shows that the Core-config#2 provides more passive damping than that for the Core-config#1 when the VFI (ϕ) is taken with its optimal value for maximum damping.

When both the active and passive counterparts of damping are combined ($k_d \neq 0$, $\eta_c \neq 0$), the variation of the corresponding shear actuation-based hybrid active-passive damping with VFI is illustrated in Fig. 5.9(a). It may be observed from Fig. 5.9(a) that the shear actuators significantly enhance the total damping ($k_d \neq 0$, $\eta_c \neq 0$) in the plate strips over the passive damping ($k_d = 0$, $\eta_c \neq 0$). Also, the inclusion of graphite particles enhances the effectiveness of both the shear mode actuator and viscoelastic layers so that an improved shear actuation-based hybrid active-passive damping is achieved due to the inclusion. However, if one compares the passive counterpart ($k_d = 0$, $\eta_c \neq 0$) with the total active-passive damping ($k_d \neq 0$, $\eta_c \neq 0$) through the results in Fig. 5.9(a), then the passive counterpart appears significantly more than the active counterpart. So, the variation of total active-passive damping with VFI (ϕ) is similar to that of the passive counterpart leading to an optimal value of VFI for the maximum active-passive damping. For this optimal value of VFI (ϕ), Core-config#2 provides significantly more active-passive damping than that for the Core-config#1. These observations indicate that the inclusion of graphite particles plays an important role to enhance the shear actuation-based hybrid active-passive damping while the actuator and viscoelastic layers are to be stacked according to Core-config#2. On the basis of this observation, further investigation is carried out considering the stack of component layers at the core according to the Core-config#2 (Fig. 5.2(b)).

For the results in Fig. 5.9(a), the total active-passive damping ($k_d \neq 0$, $\eta_c \neq 0$) is evaluated by taking a value of the control gain (k_d) as 300. However, similar results for different values of the control gain (k_d) are illustrated in Fig. 5.9(b). It can be observed from Fig. 5.9(b) that the shear actuation-based hybrid active-

passive damping (η) significantly increases with the increasing control gain (k_d) particularly when the VFI (ϕ) is taken with its optimal value for maximum damping. It may also be noted that a little change in the optimal value of VFI (ϕ) appears for the variation in the value of the control gain (k_d).

Figure 5.10 shows the variation of active-passive damping (η) in the sandwich plate-strip (Fig. 5.2(b)) with the thickness (h_v) of the viscoelastic damping layer where the actuator and viscoelastic layers at the core are stacked according to Core-config#2. For any thickness (h_v) of the viscoelastic damping layer, Fig. 5.10 shows that the shear actuation-based active-passive damping in the plate-strip significantly increases when the monolithic viscoelastic layer ($\phi = 0$) is replaced by the present VEPC layer ($\phi \neq 0$). More importantly, the active-passive damping in the plate-strip increases in a greater rate with the

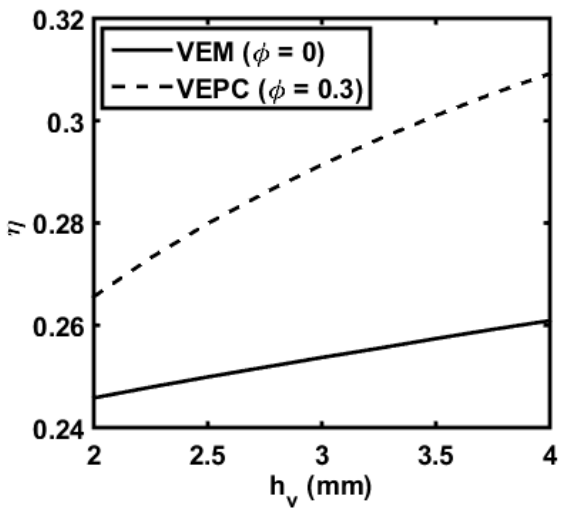

Fig. 5.10 Variation of the modal loss factor (η) with the thickness (h_v) of the viscoelastic damping layer in core-config#2 (Fig. 5.2(b)) ($k_d = 300$).

increasing thickness (h_v) of the passive damping layer when the damping layer is made of VEPC instead of the conventional monolithic viscoelastic material. However, since an increased thickness (h_v) of the passive damping layer results in improved damping (η) in the plate-strip, the VEPC layer may be taken with a suitable thickness (h_v) based on the design requirements in an application. In the present analysis, it (h_v) is taken as 4 mm. Besides the thickness (h_v) of the passive

damping layer, the thickness (h_p) of the shear piezoelectric actuators or active layer is also an important parameter. An active layer with too small thickness cannot provide a good shear actuation force. On the other hand, an active layer with high thickness requires more externally applied voltage to activate it with a specified transverse electric field (E_z). Presently, the total thickness of active layers is taken as 2 mm so that every active layer in Core-config#2 (Fig. 5.2(b)) is made with a thickness of 1 mm.

Apart from the thickness (h_p) of the active layers, the geometrical parameters (n_p and v_p) in the arrangement of shear actuator patches within the active layer may have a certain influence on the active-passive damping in the sandwich plate-strip. Further, the optimal values of these parameters (n_p, v_p) for maximum damping may also be dependent on the volume fraction (ϕ) of graphite particles in the viscoelastic damping layer. To investigate it, the number of patch segments (n_p), volume fraction (v_p) of actuator patch and volume fraction (ϕ) of graphite particles in the VEPC layer are chosen as the design variables with their bounds as, $2 \le n_p \le 8$, $0.6 \le v_p \le 0.9$ and $0 \le \phi \le 0.5$. According to these bounds of the parameters (n_p, v_p, ϕ), a three-dimensional domain is assumed, and the grid points are generated. The active-passive damping (η) in the plate-strip at its fundamental bending mode of vibration is computed at every grid point for a specified value of control gain (k_d) as 300. This result provides the variation of the active-passive damping with the three parameters (n_p, v_p, ϕ) where the optimal values of these parameters for maximum active-passive damping are obtained as, $\phi = 0.3$, $v_p = 0.8$ and $n_p = 2$. For interpretation of this result, one of the three parameters (n_p, v_p, ϕ) is taken with its optimal value while the variation of active-passive damping (η) with respect to the other two parameters is plotted in Figs. 5.11(a)-5.11(c). It may be observed from Fig. 5.11(a) that the active-passive damping at the fundamental mode of vibration of the sandwich plate-strip decreases as the number (n_p) of actuator patch segments increases. However, there is an optimal value of the volume fraction (v_p) of actuator patch for maximum active-passive damping and this optimal value of v_p does not

change significantly with n_p. Further, Figs. 5.11(b)-5.11(c) reveal that the optimal value of VFI (ϕ) for maximum damping is not much dependent on n_p or v_p.

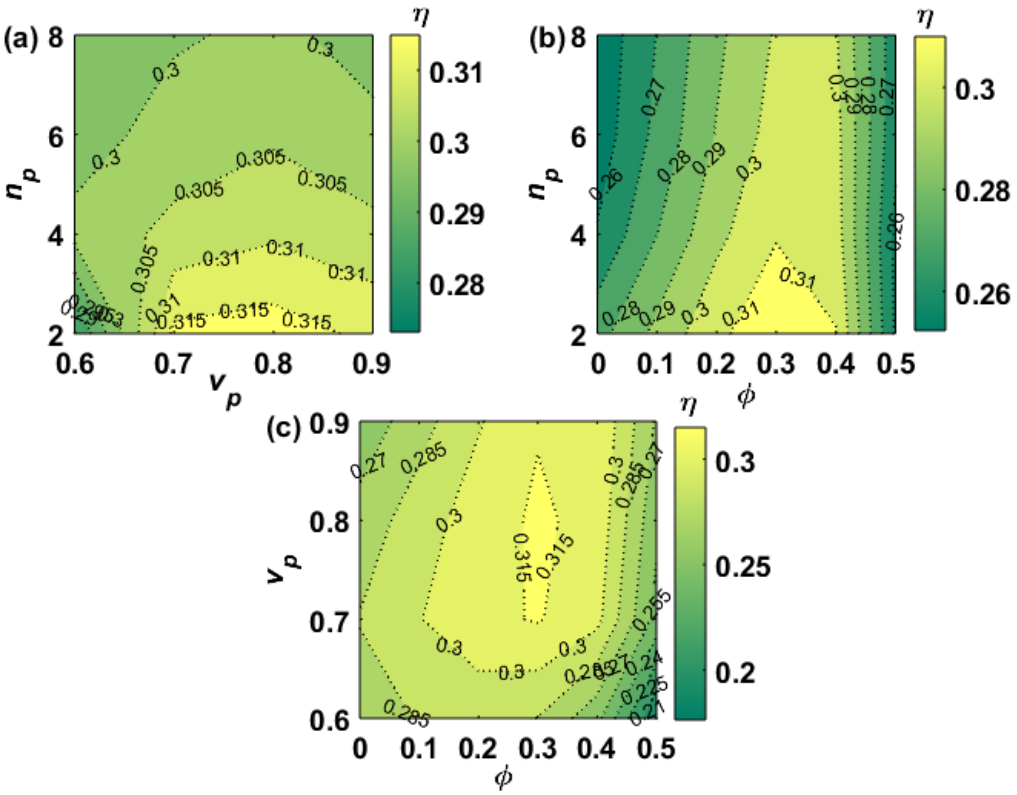

Fig. 5.11 Variation of the modal loss factor (η) in the two-dimensional domain of (a) v_p and n_p at optimal value of ϕ, (b) ϕ and n_p at optmal value of v_p, (c) ϕ and v_p at optimal value of n_p (Core-config#2).

It should be noted here that there is a practical limitation to the maximum length of the shear piezoelectric actuator patches (Benjeddou, 2007). According to this practical limitation, the arrangement of the shear actuator patches with the aforesaid optimal values of v_p and n_p may not be achievable in practice since the corresponding length of the actuator patches increases with the increasing length of the plate-strip. However, the results in Fig. 5.11(a) show that the modal damping (η) slowly decreases with the increase in the number (n_p) of actuator patch segments while another parameter (v_p) remains at its optimal value. So, following the aforesaid practical limitation, the number (n_p) of actuator patch segments may be increased without much deviation in the damping where the

volume fraction (v_p) of actuator patches and VFI (ϕ) can be kept with their optimal values. Considering such an arrangement (ϕ = 0.3, v_p = 0.8 and n_p = 6), the frequency response of the sandwich plate-strip (Core-config#2) around its fundamental bending mode of vibration is plotted in Fig. 5.12(a). Similar

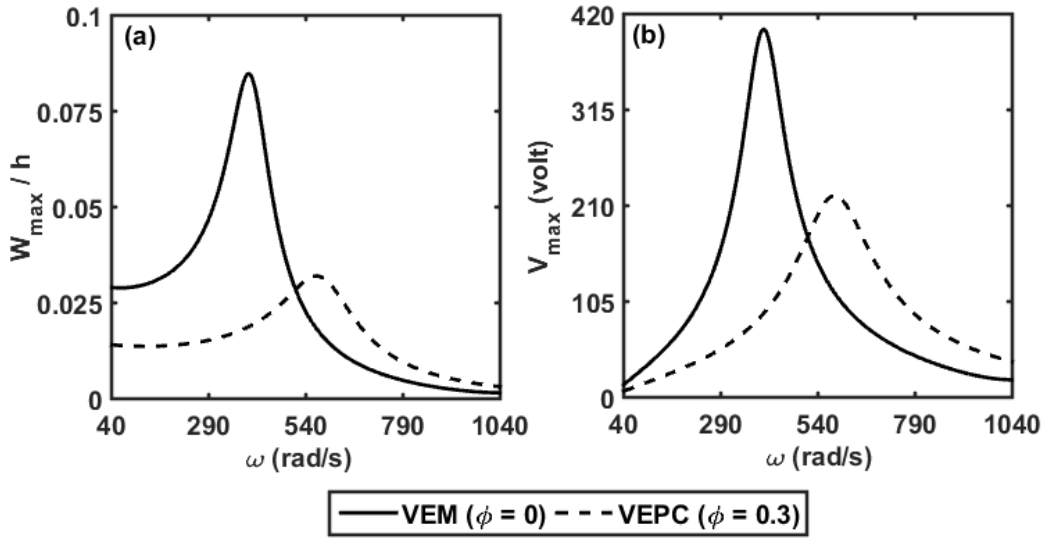

Fig. 5.12 Variations of (a) the maximum transverse displacement-amplitude and (b) the corresponding maximum control voltage (V_{max}) with the operating frequency (ω) around the fundamental bending mode of vibration of the sandwich plate-strip (p_0 = 5 N, k_d = 300, Core-config#2).

frequency response for the monolithic viscoelastic layer (ϕ=0) is also presented in the same figure (Fig. 5.12(a)). For every point on a frequency response curve in Fig. 5.12(a), the corresponding control voltage amplitudes are computed for all actuator patch segments, and the maximum one (V_{max}) is plotted in Fig. 5.12(b). It may be observed from these results (Figs. 5.12(a) and 5.12(b)) that the attenuation of the resonant displacement-amplitude significantly increases in the expense of less control voltage when the present VEPC layer replaces the monolithic viscoelastic layer. Therefore, this result corroborates the usefulness of the present VEPC layer where the inclusion of graphite particles enhances both the active and passive counterparts of total shear actuation-based hybrid active-passive damping. These observations imply an augmented shear actuation-based hybrid active-passive damping treatment of structural vibration by the use of the present VEPC layer.

5.5 Summary

The shear actuation-based hybrid active-passive damping in a sandwich plate-strip is investigated by incorporating the inclusion of graphite particles within the passive viscoelastic damping layer. The shear mode piezoelectric actuators are taken in the form of the patches that are embedded in the foam layer to form a composite active layer. The active layers are stacked along with the graphite particle-filled viscoelastic (VEPC) damping layers at the core of the sandwich plate-strip in two different stacking sequences that are named Core-config#1 and Core-config#2. In Core-config#1, an active layer is sandwiched between two identical VEPC damping layers, while for Core-config#2, a VEPC layer is sandwiched between two identical active layers. For every configuration of the core, the shear actuator patches are activated by the feedback of the time-rate of change of the local slope of bending deformation of the sandwich plate-strip for achieving the shear actuation-based hybrid active-passive damping. This active-passive damping is analysed by deriving a closed-loop FE model of the sandwich plate-strip.

The analysis is performed considering the fundamental bending mode of vibration of the sandwich plate-strip, and it reveals that the inclusion of graphite particles significantly enhances the transfer of shear actuation force from the active/actuator layer to other layers resulting in an improved active counterpart of the total active-passive damping. Besides the active damping, the passive damping capability of the viscoelastic layer also improves significantly. Therefore, an augmented shear actuation-based active-passive damping in the plate-strip is achieved by the inclusion of graphite particles in the viscoelastic layer. However, there is an optimal value of the volume fraction of inclusion (VFI) of graphite particles for the maximum shear actuation-based active-passive damping in the sandwich plate-strip. This optimal value of the VFI arises mainly depending on the increase in the effective storage modulus and the decrease in the effective loss factor of the viscoelastic layer due to the inclusion. It is observed that the shear actuation-based active-passive damping in the sandwich plate-strip with the Core-config#2 is more than that for the same plate-strip with the Core-config#1. This difference arises significantly when the graphite particles are incorporated with the optimal VFI for maximum active-passive damping.

Further study on the optimal geometrical configuration of shear actuator patches in the foam layer reveals that there is an optimal number of actuator patches across the length of the plate-strip for the maximum shear actuation-based active-passive damping. Also, the shear actuator patches are to be arranged with an optimal gap between any two consecutive ones. However, the optimal value of the volume fraction of inclusion of graphite particles is not much dependent on the geometrical configuration of shear actuator patches in the foam layer. The overall study reveals a fruitful viscoelastic particulate composite (VEPC) layer for an augmented shear actuation-based hybrid active-passive damping treatment of structural vibration where the inclusion of graphite particles not only enhances the active action but also provides improved passive damping capability of the viscoelastic damping layer.

Chapter 6

Comparative performance of VEPC and 0-3 VEC in the active/passive constrained layer damping treatment

6.1 Introduction

The performance of a graphite particle-filled viscoelastic damping layer in the CLD/ACLD treatment is studied in the previous chapters, and it is found that the inclusion of graphite particles within the passively/actively constrained viscoelastic damping layer significantly improves the damping effectiveness of CLD/ACLD treatment. This observation infers potential application of this viscoelastic particulate composite (VEPC) in control of structural vibration through the constrained layer damping arrangement. However, as mentioned in Chapter 1, another viscoelastic composite by the name of 0-3 VEC is also available in the literature for the improved CLD/ACLD treatment (Kumar et al., 2018a, 2018b), as shown in Fig. 6.1. This 0-3 VEC is basically comprised of a 1-3 VEC layer that is sandwiched between two identical monolithic viscoelastic layers. In Fig. 6.1, the 1-3 VEC layer and monolithic viscoelastic layers are identified by their thicknesses as h_g and h_v, respectively, and the gaps between any two consecutive graphite wafers within the 1-3 VEC layer are denoted by Δx and Δy along the x and y directions, respectively. This 0-3 VEC enables the CLD/ACLD treatment to have an excellent damping capability. But, the complex material arrangement in the 0-3 VEC may pose difficulties in its

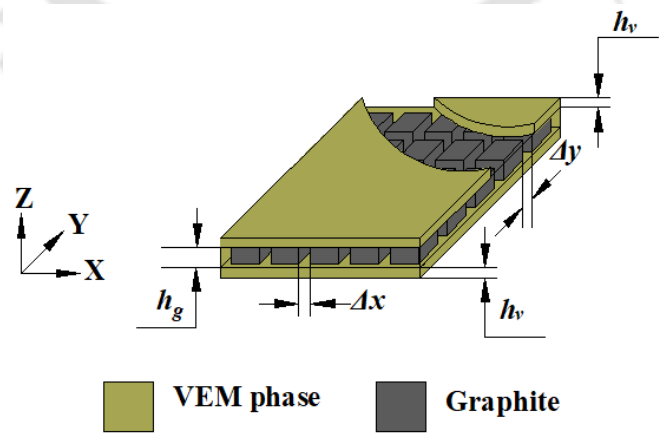

Fig. 6.1 Schematic diagram of 0-3 VEC layer.

fabrication resulting in an expensive CLD/ACLD treatment. In contrast, a low cost CLD/ACLD treatment with a good damping capability can be achieved by the use of the VEPC since this damping composite can be made easily using the conventional fabrication procedure (German, 2016; Sabu and Ranimol, 2010).

On this ground, it seems that the VEPC would be preferred over the 0-3 VEC. But, a comparative study on their damping performance in the CLD/ACLD treatment is not yet available in the literature. In this issue, a study on the comparative performance of 0-3 VEC and VEPC in the CLD/ACLD treatment is performed in the present chapter considering the damping treatment of vibration of a plate element. The overall study is presented in the following sections. First, in section 6.2, the CLD and ACLD arrangements are presented through the symmetric and asymmetric sandwich plate configurations. Next, an FE model is derived in section 6.3 for evaluation of the modal loss factor and frequency responses of the CLD/ACLD treated sandwich plates. Subsequently, in section 6.4, the numerical results are presented to analyse the comparative performance of the monolithic viscoelastic, 0-3 VEC and VEPC damping layers in the CLD/ACLD treatment. Finally, the overall comparative study is summarized in section 6.5.

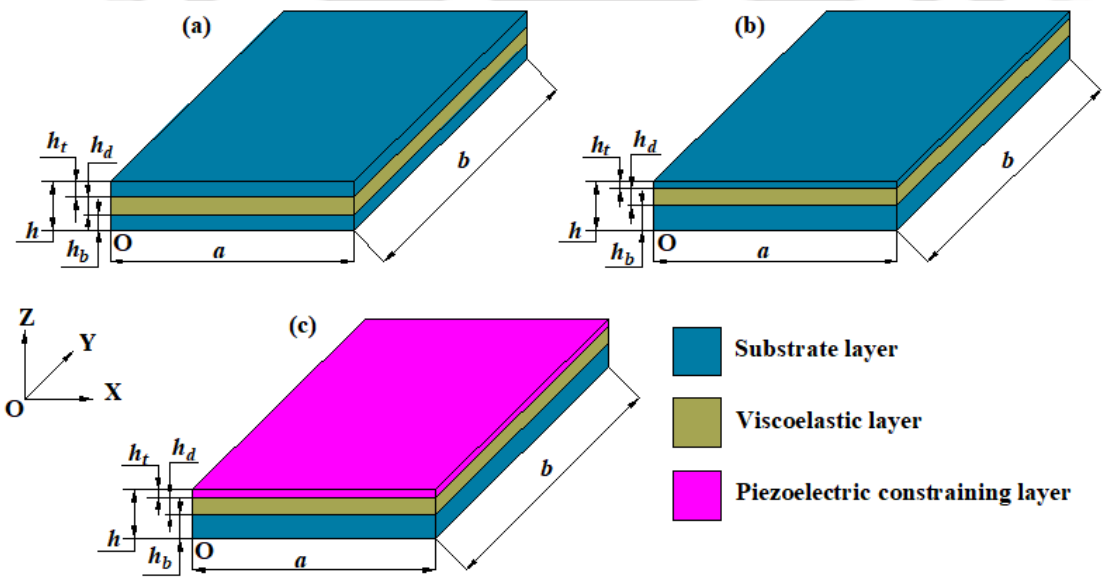

Fig. 6.2 Schematic diagrams of (a) symmetric sandwich plate with viscoelastic core, (b) asymmetric sandwich plate with passively constrained viscoelastic layer and (c) asymmetric sandwich plate with actively constrained viscoelastic layer.

6.2 Arrangement of layered plates for active/passive damping treatment

The available studies (Alam and Asnani, 1984a, 1984b; Cupiał and Nizioł, 1995; Veermani and Wereley, 1997) show two kinds of CLD arrangements in the sandwich plate configuration. The first one is a symmetric sandwich plate (Fig. 6.2(a)), where the bottom face layer is identical to the top face layer. However, in the second one (Fig. 6.2(b)), the thickness of the top face layer is significantly lesser than that for the bottom face layer. In this asymmetric sandwich plate, the bottom face layer primarily acts as the load-supporting member, whereas the thin top face layer mainly acts to constrain the viscoelastic layer for the CLD treatment. The present study is carried out considering both the symmetric and asymmetric sandwich plates separately. For each of these sandwich plates, the material for the viscoelastic damping layer is altered among the 0-3 VEC, VEPC, and monolithic viscoelastic materials. The corresponding changes in the damping characteristics of the symmetric/asymmetric sandwich plates (Figs. 6.2(a)-6.2(b)) are investigated towards a comparative study on the passive damping capabilities of the aforesaid three kinds of viscoelastic damping materials.

Similar comparison study in the use of these viscoelastic damping materials for the ACLD treatment is also performed considering the asymmetric sandwich plate configuration. Here, the viscoelastic damping layer is constrained by a thin extensional mode piezoelectric actuator layer, as shown in Fig. 6.2(c). This thin piezoelectric actuator layer is activated by supplying the external electrical voltage through its top and bottom fully electrode surfaces according to a control strategy. However, similar to the aforesaid CLD treatment, the material for the viscoelastic layer is altered among the three kinds of viscoelastic damping materials, and the corresponding changes in the active-passive damping characteristics of the ACLD treatment are investigated to address a comparative study on the damping effectiveness of the viscoelastic damping materials.

6.3 Mathematical formulation

The aforesaid three kinds of damping materials are separately used in each of the symmetric/asymmetric sandwich plates (Figs. 6.2(a)-6.2(c)). So, a total of

nine different types of material arrangements appear through these three kinds of symmetric/asymmetric sandwich plates. Among these different types of material arrangements, the most complex arrangement of component materials appears when the 0-3 VEC layer is used along with the piezoelectric constraining layer, as shown schematically in Fig. 6.3. So, the mathematical formulation for this kind of sandwich plate is presented in this section. However, the same formulation can also be used for the other kinds of sandwich plates by means of altering the material and geometrical properties of the constrained viscoelastic and constraining layers, as it is discussed at the end of this section.

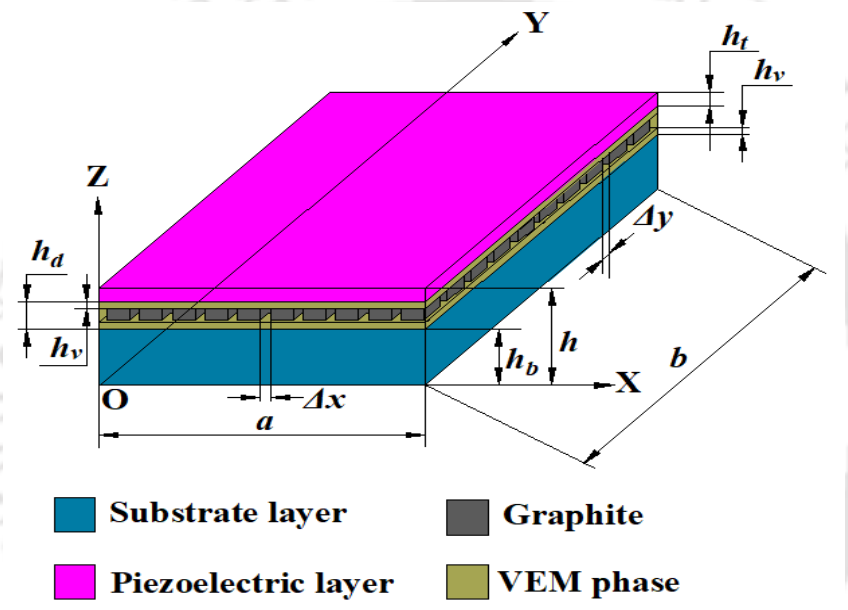

Fig. 6.3 Schematic diagrams of the plate with constrained 0-3 VEC layer and piezoelectric constraining layer.

For mathematical modelling of the layered plate with the 0-3 VEC layer, the origin (O) of the reference Cartesian coordinate system (xyz) is located at one corner of the plate (Fig. 6.3). The length, width and thickness of the overall laminated plate are denoted by a, b and h, respectively. The thicknesses of the bottom and top layers are denoted by h_b and h_t, respectively, while the thickness of the damping layer is symbolized by h_d (Fig. 6.2). The thicknesses of the monolithic viscoelastic and 1-3 VEC layers within the 0-3 VEC damping layer (Fig. 6.1) are specified with reference to the thickness (h_d, Fig. 6.3) of the damping layer by defining a ratio as $r_v = h_v / h_d$. Presently, a square layered plate

is considered and its damping characteristics are analysed for the fundamental bending mode of vibration. So, the graphite wafers within the 0-3 VEC layer are taken with the same gap ($\Delta x = \Delta y = \Delta$) for both the x and y directions. It also shows the same number (n_g) of graphite wafers along the x and y directions.

However, this layered plate (Fig. 6.3) appears similar to the earlier ACLD treated plate (Fig. 4.1), where the difference lies only in the material configuration within the damping layer. So, the analysis of the present layered plate (Fig. 6.3) can be carried out using the same formulation presented in section 4.2. However, in that formulation (section 4.2) using layer-wise (LW) theory, the displacement field in the viscoelastic damping layer is defined according to TSDT while FSDT is employed for the other two layers. It was considered to improve the accuracy in estimation of transverse shear deformation of the constrained viscoelastic layer. Because the transverse shear deformation in the viscoelastic layer is the key factor for passive damping in the overall plate. However, TSDT involves more complex formulation, as well as computational time, than that for FSDT. Looking into this aspect, the displacement field in every layer of a sandwich plate is defined here according to FSDT, while its suitability in comparison to TSDT is verified in the section for numerical results (section 6.4). Now, in the present layered plate (Fig. 6.3), the damping layer is composed of three thin layers, namely two monolithic viscoelastic layers and a 1-3 VEC layer (Fig. 6.1), and thus, the displacement field in each of these layers is defined according to FSDT. The corresponding mathematical expressions for the displacement components u^k, v^k and w^k at any point in the layered plate (Fig. 6.3) along the x, y and z directions, respectively, are given in Eq. (6.1).

$$u^k(x,\mathrm{y},z,t) = u_0(x,\mathrm{y},t) + \boldsymbol{z}^k \boldsymbol{\phi}_x(x,\mathrm{y},t),$$

$$v^k(x,\mathrm{y},z,t) = v_0(x,\mathrm{y},t) + \boldsymbol{z}^k \boldsymbol{\phi}_y(x,\mathrm{y},t),$$

$$w^k(x,\mathrm{y},z,t) = w_0(x,\mathrm{y},t)$$

$$\boldsymbol{\phi}_x = \left\{ \phi_x^1 \quad \phi_x^2 \quad \ldots \quad \ldots \quad \phi_x^{(N_L-1)} \quad \phi_x^{N_L} \right\}^{\mathrm{T}},$$

$$\boldsymbol{\phi}_y = \left\{ \phi_y^1 \quad \phi_y^2 \quad \ldots \quad \ldots \quad \phi_y^{(N_L-1)} \quad \phi_y^{N_L} \right\}^{\mathrm{T}}$$

$$\boldsymbol{z}^k = \left\{ z_1^k \quad z_2^k \quad \ldots \quad \ldots \quad z_{(N_L-1)}^k \quad z_{N_L}^k \right\} \tag{6.1}$$

In Eq. (6.1), the superscript k denotes the layer number starting from 1 for the bottom layer; N_L represents the total number of layers within the laminated plate; u_0, v_0 and w_0 denote the displacements at any point on the reference plane ($z=0$) along the x, y and z directions, respectively; ϕ_x^k and ϕ_y^k are the rotations of the normal to the bottom surface of the k^{th} layer with respect to the y and x axes, respectively. The different thickness coordinates (z_i^k) appearing in Eq. (6.1) are given in Eq. (3.2).

$$z_1^k = z \text{ or } h_1 \text{ for } k=1 \text{ or } k>1$$

$$z_2^k = 0 \text{ or } (z-h_1) \text{ or } h_2 \text{ for } k<2 \text{ or } k=2 \text{ or } k>2$$

$$z_3^k = 0 \text{ or } (z-h_1-h_2) \text{ or } h_3 \text{ for } k<3 \text{ or } k=3 \text{ or } k>3$$

.

.

$$z_{(N_L-1)}^k = 0 \text{ or } \left(z-h_1-h_2-h_3-\ldots\ldots-h_{(N_L-2)}\right) \text{ or } h_{(N_L-1)} \text{ for } k<(N_L-1) \text{ or } k=(N_L-1) \text{ or } k>(N_L-1)$$

$$z_{N_L}^k = 0 \text{ or } \left(z-h_1-h_2-h_3-\ldots\ldots-h_{(N_L-1)}\right) \text{ for } k<N_L \text{ or } k=N_L \tag{3.2}$$

The displacement components (u^k, v^k, w^k) at any point within the k^{th} layer can be expressed by Eq. (3.3a), where the displacement vector ($\boldsymbol{d}^k$) and other quantities are given in Eq. (6.2).

$$\boldsymbol{d}^k = \left(\boldsymbol{d}_t + \boldsymbol{Z}_r^k \boldsymbol{d}_r\right) \tag{3.3a}$$

$$\boldsymbol{d}^k = \left\{ u^k \quad v^k \quad w^k \right\}^{\mathrm{T}},$$

$$\boldsymbol{d}_t = \left\{ u_0 \quad v_0 \quad w_0 \right\}^{\mathrm{T}}, \; \boldsymbol{d}_r = \left\{ \boldsymbol{\phi}_x^{\mathrm{T}} \quad \boldsymbol{\phi}_y^{\mathrm{T}} \right\}^{\mathrm{T}},$$

$$\boldsymbol{Z}_r^k = \begin{bmatrix} \boldsymbol{z}^k & \boldsymbol{O}_{(1\times N_L)} & \boldsymbol{O}_{(1\times N_L)} \\ \boldsymbol{O}_{(1\times N_L)} & \boldsymbol{z}^k & \boldsymbol{O}_{(1\times N_L)} \end{bmatrix}^{\mathrm{T}} \tag{6.2}$$

The displacement components (u^k, v^k, w^k) can also be expressed in the form of Eq. (3.4a), where the generalized displacement vector ($\boldsymbol{d}$) and the transformation matrices ($\boldsymbol{T}_t, \boldsymbol{T}_r$) are given in Eq. (6.3).

$$\boldsymbol{d}^k = \left(\boldsymbol{T}_t + \boldsymbol{Z}_r^k \boldsymbol{T}_r\right)\boldsymbol{d} \tag{3.4a}$$

$$\boldsymbol{d} = \left\{u_0 \quad v_0 \quad w_0 \quad \phi_x^1 \quad \phi_x^2 \quad \ldots \quad \ldots \quad \phi_x^{(N_L-1)} \quad \phi_x^{N_L} \quad \phi_y^1 \quad \phi_y^2 \quad \ldots \quad \ldots \quad \phi_y^{(N_L-1)} \quad \phi_y^{N_L}\right\}^{\mathrm{T}},$$

$$\boldsymbol{T}_t = \left[\boldsymbol{I}_{3\times 3} \quad \boldsymbol{O}_{3\times 2N_L}\right], \quad \boldsymbol{T}_r = \left[\boldsymbol{O}_{2N_L\times 3} \quad \boldsymbol{I}_{2N_L\times 2N_L}\right] \tag{6.3}$$

In Eqs. (6.2) and (6.3), $\boldsymbol{I}$ and $\boldsymbol{O}$ denote the identity matrix and null matrix, respectively, and the subscript ($m\times n$) represents the size of a matrix. The state of strain (ε) and the state of stress (σ) at any point within the k^{th} layer can be written according to Eqs. (4.3a)-(4.3b).

$$\boldsymbol{\varepsilon}_b^k = \left\{\varepsilon_x^k \quad \varepsilon_y^k \quad \varepsilon_{xy}^k\right\}^{\mathrm{T}},$$

$$\boldsymbol{\varepsilon}_s^k = \left\{\varepsilon_{xz}^k \quad \varepsilon_{yz}^k\right\}^{\mathrm{T}} \tag{4.3a}$$

$$\boldsymbol{\sigma}_b^k = \left\{\sigma_x^k \quad \sigma_y^k \quad \sigma_{xy}^k\right\}^{\mathrm{T}},$$

$$\boldsymbol{\sigma}_s^k = \left\{\sigma_{xz}^k \quad \sigma_{yz}^k\right\}^{\mathrm{T}} \tag{4.3b}$$

According to the displacement field (Eq. (6.1)), the strain-displacement relations for the k^{th} layer can be written in the form of Eq. (4.4).

$$\boldsymbol{\varepsilon}_b^k = \left(\boldsymbol{\varepsilon}_{b0} + \boldsymbol{Z}_b^k \boldsymbol{\kappa}_b\right),$$

$$\boldsymbol{\varepsilon}_s^k = \left(\boldsymbol{\varepsilon}_{s0} + \boldsymbol{Z}_s^k \boldsymbol{\kappa}_s\right)$$

$$\boldsymbol{\varepsilon}_{b0} = \begin{Bmatrix} \dfrac{\partial u_0}{\partial x} \\ \dfrac{\partial v_0}{\partial y} \\ \dfrac{\partial u_0}{\partial y} + \dfrac{\partial v_0}{\partial x} \end{Bmatrix}, \quad \boldsymbol{k}_b = \begin{Bmatrix} \dfrac{\partial \boldsymbol{\phi}_x}{\partial x} \\ \dfrac{\partial \boldsymbol{\phi}_y}{\partial y} \\ \dfrac{\partial \boldsymbol{\phi}_x}{\partial y} + \dfrac{\partial \boldsymbol{\phi}_y}{\partial x} \end{Bmatrix},$$

$$\boldsymbol{\varepsilon}_{s0}=\begin{Bmatrix}\dfrac{\partial w_0}{\partial x}\\ \dfrac{\partial w_0}{\partial y}\end{Bmatrix},\ \boldsymbol{\kappa}_s=\begin{Bmatrix}\boldsymbol{\phi}_x\\ \boldsymbol{\phi}_y\end{Bmatrix},$$

$$\boldsymbol{Z}_b^k=\boldsymbol{I}_{(3\times3)}\otimes\boldsymbol{z}^k,\ \boldsymbol{Z}_s^k=\boldsymbol{I}_{(2\times2)}\otimes\left(\partial\boldsymbol{z}^k/\partial z\right) \tag{4.4}$$

For deriving the FE model of the sandwich plate (Fig. 6.3), the reference plane ($z=0$) is discretized using nine-node quadrilateral isoparametric elements, where a typical element appears in the rectangular shape having the edges in parallel to the x and y axes. Moreover, the reference plane is discretized following the edges of the rectangular graphite wafers in the 0-3 VEC core layer so that two types of elemental stacking sequences of the component layers appear as shown in Figs. 6.4(a)-6.4(b). Now, the material properties of different layers in an elemental stack of component layers can be defined. The substrate

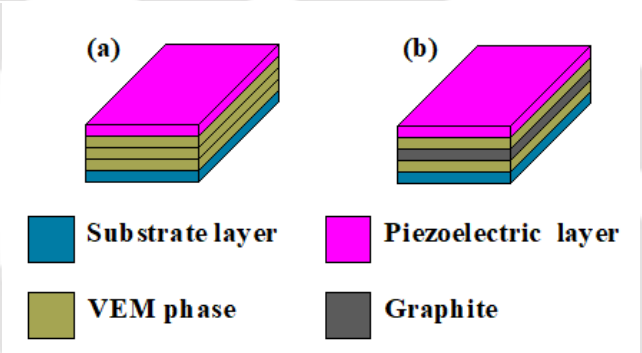

Fig. 6.4 Different elemental stacking sequences of the component layers.

plate or the bottom face layer is considered to be made of an isotropic material. The graphite wafers also possess isotropic material properties. Moreover, the viscoelastic phase in the 0-3 VEC is made of a monolithic viscoelastic material having the isotropic material properties. So, the constitutive relations for the k^{th} layer made of either of these materials can be written in the form of Eq. (4.7).

$$\boldsymbol{\sigma}_b^k=\boldsymbol{C}_b^k\boldsymbol{\varepsilon}_b^k,\ \boldsymbol{\sigma}_s^k=\boldsymbol{C}_s^k\boldsymbol{\varepsilon}_s^k$$

$$\boldsymbol{C}_b^k=\frac{E^k}{1-\left(\nu^k\right)^2}\begin{bmatrix}1 & \nu^k & 0\\ \nu^k & 1 & 0\\ 0 & 0 & \left(1-\nu^k\right)/2\end{bmatrix},\ \boldsymbol{C}_s^k=\frac{E^k}{2\left(1+\nu^k\right)}\begin{bmatrix}1 & 0\\ 0 & 1\end{bmatrix} \tag{4.7}$$

The material properties of the viscoelastic layers in an elemental stack of layers are usually dependent on the operating temperature and frequency (ω). Presently, the sandwich plates are considered to operate at the room temperature (32° C) so that the frequency-dependent material properties of the viscoelastic layers are taken at the same temperature. Further, since viscoelastic layers are presently modelled using complex stiffness method, the corresponding stiffness matrices ($\boldsymbol{C}_b^k(\omega)$, $\boldsymbol{C}_s^k(\omega)$) are frequency-dependent complex quantities.

Apart from these component materials in the sandwich plate (Fig. 6.3), the top face layer ($k = N_L$) is made of an extensional mode piezoelectric actuator for the ACLD treatment. This piezoelectric actuator layer is taken with a very small thickness, and it is activated by supplying the external voltage (V) across its top and bottom fully electrode surfaces. So, the electric fields E_x, E_y and E_z at any point in the piezoelectric layer along the x, y and z directions, respectively, are assumed as, $E_x \approx 0$, $E_y \approx 0$ and $E_z = -V/h_t$. Accordingly, the constitutive relations for the piezoelectric actuator layer can be written in the form of Eq. (4.6).

$$\boldsymbol{\sigma}_b^k = \boldsymbol{C}_b^k \boldsymbol{\varepsilon}_b^k - \boldsymbol{e}_b^k E_z, \quad \boldsymbol{\sigma}_s^k = \boldsymbol{C}_s^k \boldsymbol{\varepsilon}_s^k$$

$$D_z^k = \left(\boldsymbol{e}_b^k\right)^{\mathrm{T}} \boldsymbol{\varepsilon}_b^k + \in_{33}^k E_z$$

$$\boldsymbol{C}_b^k = \begin{bmatrix} \bar{C}_{11}^k & \bar{C}_{12}^k & 0 \\ \bar{C}_{12}^k & \bar{C}_{22}^k & 0 \\ 0 & 0 & C_{66}^k \end{bmatrix}, \quad \boldsymbol{C}_s^k = \begin{bmatrix} C_{55}^k & 0 \\ 0 & C_{44}^k \end{bmatrix}, \quad \boldsymbol{e}_b^k = \begin{Bmatrix} \bar{e}_{31}^k & \bar{e}_{32}^k & 0 \end{Bmatrix}^{\mathrm{T}},$$

$$\bar{C}_{11}^k = \left\langle C_{11}^k - \left(C_{13}^k\right)^2 / C_{33}^k \right\rangle, \quad \bar{C}_{22}^k = \left\langle C_{22}^k - \left(C_{23}^k\right)^2 / C_{33}^k \right\rangle,$$

$$\bar{C}_{12}^k = \left\langle C_{12}^k - C_{13}^k C_{23}^k / C_{33}^k \right\rangle,$$

$$\bar{e}_{31}^k = \left\langle e_{31}^k - C_{13}^k e_{33}^k / C_{33}^k \right\rangle, \quad \bar{e}_{32}^k = \left\langle e_{32}^k - C_{23}^k e_{33}^k / C_{33}^k \right\rangle \tag{4.6}$$

The displacement vector ($\boldsymbol{d}^k$) and strain vectors ($\boldsymbol{\varepsilon}_{b0}, \boldsymbol{\kappa}_b, \boldsymbol{\varepsilon}_{s0}, \boldsymbol{\kappa}_s$) at any point within an element can be expressed in terms of the shape function matrix ($\boldsymbol{N}$) and the elemental nodal displacement vector ($\boldsymbol{d}^e$), as given in Eq. (4.8) and

(3.11a), where the operator matrices ($\boldsymbol{L}_{b0}, \boldsymbol{L}_{b\kappa}, \boldsymbol{L}_{s0}, \boldsymbol{L}_{s\kappa}$) can be obtained from Eq. (4.4) and (6.1).

$$\boldsymbol{d}^k = \left(\boldsymbol{T}_t + \boldsymbol{Z}_r^k \boldsymbol{T}_r\right) \boldsymbol{N} \boldsymbol{d}^e \tag{4.8}$$

$$\boldsymbol{\varepsilon}_{b0} = \boldsymbol{B}_{b0}\boldsymbol{d}^e\,,\ \boldsymbol{\kappa}_b = \boldsymbol{B}_{b\kappa}\boldsymbol{d}^e\,,$$

$$\boldsymbol{\varepsilon}_{s0} = \boldsymbol{B}_{s0}\boldsymbol{d}^e\,,\ \boldsymbol{\kappa}_s = \boldsymbol{B}_{s\kappa}\boldsymbol{d}^e\,,$$

$$\boldsymbol{B}_{b0} = \boldsymbol{L}_{b0}\boldsymbol{T}_t\boldsymbol{N}\,,\ \boldsymbol{B}_{b\kappa} = \boldsymbol{L}_{b\kappa}\boldsymbol{T}_r\boldsymbol{N}\,,$$

$$\boldsymbol{B}_{s0} = \boldsymbol{L}_{s0}\boldsymbol{T}_t\boldsymbol{N}\,,\ \boldsymbol{B}_{s\kappa} = \boldsymbol{L}_{s\kappa}\boldsymbol{T}_r\boldsymbol{N} \tag{3.11a}$$

The sandwich plate is considered to operate under a uniformly distributed transverse harmonic load ($p(t)$) at the bottom plate-surface (z=0). For the corresponding vibration of the plate, the governing equations of motion are derived employing extended Hamilton's principle (Eq. (2.12)), where the first variations of the total potential energy (δT_p^e) and the total kinetic energy (δT_k^e) for a typical element are given in Eqs. (6.4) and (6.5), respectively.

$$\delta T_P^e = \int_0^{a^e}\int_0^{b^e}\left[\sum_{k=1}^{N_L}\int_{h_k}^{h_{k+1}}\left\langle(\delta\boldsymbol{\varepsilon}_b^k)^{\mathrm{T}}\boldsymbol{\sigma}_b^k + (\delta\boldsymbol{\varepsilon}_s^k)^{\mathrm{T}}\boldsymbol{\sigma}_s^k\right\rangle dz - \int_{h_k}^{h_{k+1}}\left(\delta E_z\right)^{\mathrm{T}} D_z^k\Big|_{k=N_L} dz - \left\langle\delta w_0\, p(t)\right\rangle\Big|_{z=0}\right] dydx \tag{6.4}$$

$$\delta T_K^e = \int_0^{a^e}\int_0^{b^e}\left[\sum_{k=1}^{N_L}\int_{h_k}^{h_{k+1}}\left\langle\left\{\delta(\dot{u}^k)\quad\delta(\dot{v}^k)\quad\delta(\dot{w}^k)\right\}\rho^k\left\{(\dot{u}^k)\quad(\dot{v}^k)\quad(\dot{w}^k)\right\}^{\mathrm{T}}\right\rangle dz\right] dydx \tag{6.5}$$

In Eqs. (6.4)-(6.5), a^e and b^e are the elemental lengths along the x and y directions, respectively; h^k and h^{k+1} represent the z coordinates at the bottom and top surfaces of the k^{th} layer, respectively. Using Eqs. (4.6), (4.7), (4.4), (4.8) and (3.11a) in Eqs. (6.4)-(6.5), and then substituting the resulting expressions in Eq. (2.12), the elemental equations of motion can be obtained in the form of Eq. (4.12), where the coefficient vectors and matrices are given in Eq. (6.6).

$$\boldsymbol{M}^e\ddot{\boldsymbol{d}}^e + \left(\boldsymbol{K}_b^e(\omega) + \boldsymbol{K}_s^e(\omega)\right)\boldsymbol{d}^e = \boldsymbol{P}_E^e V + \boldsymbol{P}_M^e\, p(t) \tag{4.12}$$

$$\boldsymbol{K}_b^e(\omega) = \int_0^{a^e}\int_0^{b^e}\left\langle\left(\boldsymbol{B}_{b0}\right)^{\mathrm{T}}\left(\boldsymbol{A}_{bL}(\omega)\boldsymbol{B}_{b0} + \boldsymbol{B}_{bL1}(\omega)\boldsymbol{B}_{b\kappa}\right) + \left(\boldsymbol{B}_{b\kappa}\right)^{\mathrm{T}}\left(\boldsymbol{B}_{bL2}(\omega)\boldsymbol{B}_{b0} + \boldsymbol{D}_{bL}(\omega)\boldsymbol{B}_{b\kappa}\right)\right\rangle dydx\,,$$

$$\boldsymbol{K}_s^e(\omega) = \int_0^{a^e}\int_0^{b^e}\left\langle\left(\boldsymbol{B}_{s0}\right)^{\mathrm{T}}\left(\boldsymbol{A}_{sL}(\omega)\boldsymbol{B}_{s0} + \boldsymbol{B}_{sL1}(\omega)\boldsymbol{B}_{b\kappa}\right) + \left(\boldsymbol{B}_{s\kappa}\right)^{\mathrm{T}}\left(\boldsymbol{B}_{sL2}(\omega)\boldsymbol{B}_{s0} + \boldsymbol{D}_{sL}(\omega)\boldsymbol{B}_{s\kappa}\right)\right\rangle dydx\,,$$

$$\boldsymbol{P}_E^e = \int_0^{a^e}\int_0^{b^e} \left\langle \left(\boldsymbol{B}_{b0}\right)^{\mathrm{T}} \boldsymbol{A}_{be} + \left(\boldsymbol{B}_{b\kappa}\right)^{\mathrm{T}} \boldsymbol{B}_{be} \right\rangle dydx,\ \boldsymbol{P}_M^e = \int_0^{a^e}\int_0^{b^e} \left\langle \left(\boldsymbol{N}\right)^{\mathrm{T}} \left(\boldsymbol{T}_t\right)^{\mathrm{T}} \{0 \quad 0 \quad 1\}^{\mathrm{T}} \right\rangle_{z=0} dydx,$$

$$\boldsymbol{M}^e = \int_0^{a^e}\int_0^{b^e} \left[\left(\boldsymbol{N}\right)^{\mathrm{T}} \left\langle \left(\boldsymbol{T}_t\right)^{\mathrm{T}} \left(\boldsymbol{m}_1\boldsymbol{T}_t + \boldsymbol{m}_2\boldsymbol{T}_r\right) + \left(\boldsymbol{T}_r\right)^{\mathrm{T}} \left(\boldsymbol{m}_3\boldsymbol{T}_t + \boldsymbol{m}_4\boldsymbol{T}_r\right) \right\rangle \boldsymbol{N} \right] dydx \tag{6.6}$$

In Eq. (6.6), the different rigidity matrices, mass parameters and electro-elastic coupling coefficient vectors are as follows,

$$\boldsymbol{A}_{bL}(\omega) = \sum_{k=1}^{5}\int_{h_k}^{h_{k+1}} \boldsymbol{C}_b^k(\omega)dz,\ \boldsymbol{B}_{bL1}(\omega) = \sum_{k=1}^{5}\int_{h_k}^{h_{k+1}} \boldsymbol{C}_b^k(\omega)\boldsymbol{Z}_b^k dz,$$

$$\boldsymbol{B}_{bL2}(\omega) = \sum_{k=1}^{5}\int_{h_k}^{h_{k+1}} \left(\boldsymbol{Z}_b^k\right)^{\mathrm{T}} \boldsymbol{C}_b^k(\omega)dz,\ \boldsymbol{D}_{bL}(\omega) = \sum_{k=1}^{5}\int_{h_k}^{h_{k+1}} \left(\boldsymbol{Z}_b^k\right)^{\mathrm{T}} \boldsymbol{C}_b^k(\omega)\boldsymbol{Z}_b^k dz,$$

$$\boldsymbol{A}_{bs}(\omega) = \sum_{k=1}^{5}\int_{h_k}^{h_{k+1}} \boldsymbol{C}_s^k(\omega)dz,\ \boldsymbol{B}_{sL1}(\omega) = \sum_{k=1}^{5}\int_{h_k}^{h_{k+1}} \boldsymbol{C}_s^k(\omega)\boldsymbol{Z}_s^k dz,$$

$$\boldsymbol{B}_{sL2}(\omega) = \sum_{k=1}^{5}\int_{h_k}^{h_{k+1}} \left(\boldsymbol{Z}_s^k\right)^{\mathrm{T}} \boldsymbol{C}_s^k(\omega)dz,\ \boldsymbol{D}_{sL}(\omega) = \sum_{k=1}^{5}\int_{h_k}^{h_{k+1}} \left(\boldsymbol{Z}_s^k\right)^{\mathrm{T}} \boldsymbol{C}_s^k(\omega)\boldsymbol{Z}_s^k dz,$$

$$\boldsymbol{m}_1 = \sum_{k=1}^{5}\int_{h_k}^{h_{k+1}} \rho^k dz,\ \boldsymbol{m}_2 = \sum_{k=1}^{5}\int_{h_k}^{h_{k+1}} \rho^k \boldsymbol{Z}_r^k dz,$$

$$\boldsymbol{m}_3 = \sum_{k=1}^{5}\int_{h_k}^{h_{k+1}} \left(\boldsymbol{Z}_r^k\right)^{\mathrm{T}} \rho^k dz,\ \boldsymbol{m}_4 = \sum_{k=1}^{5}\int_{h_k}^{h_{k+1}} \left(\boldsymbol{Z}_r^k\right)^{\mathrm{T}} \rho^k \boldsymbol{Z}_r^k dz,$$

$$\boldsymbol{A}_{be} = \int_{h_k}^{h_{k+1}} \boldsymbol{e}_b^k\left(-1/h_t\right)dz\Big|_{k=5},\ \boldsymbol{B}_{be} = \int_{h_k}^{h_{k+1}} \left(\boldsymbol{Z}_b^k\right)^{\mathrm{T}} \boldsymbol{e}_b^k\left(-1/h_t\right)dz\Big|_{k=5} \tag{6.7}$$

Assembling the elemental equations (Eq. (4.12)), the global equations of motion of the sandwich plate can be obtained in the form of Eq. (4.15).

$$\boldsymbol{M}\ddot{\boldsymbol{X}} + \boldsymbol{K}(\omega)\boldsymbol{X} = \boldsymbol{P}_E V + \boldsymbol{P}_M p(t),$$

$$\boldsymbol{K}(\omega) = \boldsymbol{K}_b(\omega) + \boldsymbol{K}_s(\omega) \tag{4.15}$$

The extensional mode piezoelectric actuator layer is activated by supplying the external electrical voltage according the velocity feedback control strategy. Here, the study is performed considering the fundamental bending mode of vibration of the sandwich plate where the maximum transverse velocity appears at the middle point of the plate. So, the transverse velocity at the middle

point on the top surface of the sandwich plate is sensed and fed back to the actuator layer in the form of voltage (V) according to Eq. (4.16).

$$V = -k_d \dot{w}_s \tag{4.16}$$

The transverse velocity ($\dot{w}_s$) at the sensing point can be expressed in terms of the global nodal velocity vector ($\dot{\boldsymbol{X}}$) through a transformation row vector ($\boldsymbol{N}_T$) as given in Eq. (4.17).

$$\dot{w}_s = \boldsymbol{N}_T \dot{\boldsymbol{X}} \tag{4.17}$$

Introducing Eqs. (4.16) and (4.17) in Eq. (4.15), the FE equations of motion of the overall sandwich plate can be obtained in the form of Eqs. (4.18a)-(4.18b).

$$\boldsymbol{M}\ddot{\boldsymbol{X}} + \boldsymbol{C}\dot{\boldsymbol{X}} + \boldsymbol{K}(\omega)\boldsymbol{X} = \boldsymbol{P}_M p(t) \tag{4.18a}$$

$$\boldsymbol{C} = \boldsymbol{P}_E k_d \boldsymbol{N}_T \tag{4.18b}$$

The above FE equations of motion of the sandwich plate (Fig. 6.3) are derived for its ACLD treatment using 0-3 VEC layer. However, for the use of the monolithic viscoelastic or VEPC layer instead of the 0-3 VEC layer in the ACLD treatment, the aforesaid FE formulation can be followed, where the FE equations of motion appear similar to Eq. (4.18a) by means of using only one elemental stacking sequence of the bottom face layer, monolithic viscoelastic/VEPC core layer, and piezoelectric constraining layer. Presently, the monolithic viscoelastic/VEPC core layer is taken in three identical mathematical layers so that the corresponding elemental stack of layers appears similar to that presented in Fig. 6.4(a).

However, in the case of the CLD treatment using either of the three kinds of viscoelastic damping layers, the piezoelectric constraining layer is replaced by the passive constraining layer (Fig. 6.2(b)) or top face layer (Fig. 6.2(a)). This passive constraining/top face layer is presently considered to be made of the same isotropic material as that is taken for the bottom face layer. Therefore, the aforesaid formulation for every kind of viscoelastic damping layer can be repeated by removing the active control strategy and assigning the material properties of the top face/constraining layer identically to that of the bottom face layer. This modification in the formulation for every kind of viscoelastic damping layer yields the FE equations of motion in the form, as given in Eq. (2.14).

$$\boldsymbol{M}\ddot{\boldsymbol{X}} + \boldsymbol{K}(\omega)\boldsymbol{X} = \boldsymbol{P}_M \; p(t) \tag{2.14}$$

6.4 Numerical results and discussion

In this section, the damping characteristics of the CLD and ACLD treatments are investigated for the separate use of the monolithic viscoelastic, 0-3 VEC and VEPC damping layers in the symmetric/asymmetric sandwich plates (Figs. 6.2(a)-6.2(c)). This investigation is carried out by evaluating the numerical results for the modal loss factor and frequency responses of the sandwich plates having the aforesaid CLD or ACLD arrangement. For evaluation of the modal loss factor, the above FE equations of motion for the ACLD and CLD treatments of sandwich plates are solved following the same procedure as described in sections 4.3 and 2.3. Besides the modal loss factor, the frequency responses of a CLD/ACLD treated sandwich plate are evaluated around the fundamental natural frequency, where the uniformly distributed transverse harmonic load ($p(t)$) is taken in the form as, $p(t) = p_o e^{j\omega t}$ ($j = \sqrt{-1}$, p_o and ω are the load-amplitude and excitation frequency, respectively). For the linear steady-state vibration of a sandwich plate under this harmonic load, the corresponding solutions are obtained following the procedure as mentioned in sections 4.3 and 2.3. From this solution, the maximum transverse displacement-amplitude is presented for every operating frequency in the following results for the frequency responses.

For the numerical results, the bottom face layer in all the sandwich plates (Figs. 6.2(a)-6.2(c)) is considered to be made of Aluminium ($E = 69$ GPa, $\nu = 0.3$, $\rho = 2740$ kg/m^3). The top face/constraining layer of the symmetric/asymmetric sandwich plate with CLD arrangement (Figs. 6.2(a)-6.2(b)) is also made of Aluminium. The extensional mode piezoelectric actuator layer in the ACLD treatment (Fig. 6.2(c)) is considered to be made of PZT5H, and its material properties are given in section 4.3. The material properties of graphite wafers/particles in the 0-3 VEC/VEPC are considered as $E_d = 250$ GPa, $\nu_d = 0.3$, $\rho_d = 1400$ kg/m^3 (Jones, 1998). The viscoelastic phase in any kind of damping layer is considered to be made of Butyl rubber. However, the sandwich plates are presently considered to operate at the room temperature (32^o C), and thus the frequency-dependent material properties of the Butyl rubber are taken from

(Jones, 2001). It may be noted from the aforesaid formulation that the 0-3 VEC layer is presently modelled without computation of effective properties of the composite since this viscoelastic composite is made of macro-sized graphite wafers. However, the VEPC layer is modelled through its effective material properties that are computed and presented in section 2.4.

Apart from the aforesaid material properties of the component materials in the sandwich plates, the lengths of the edges of any sandwich plate are taken as, a = 0.4 m and b = 0.4 m. In the case of the symmetric sandwich plate (Fig. 6.2(a)), the thickness of the top and bottom face layers are taken as, $h_b = h_t = 2.5$ mm; however, for the asymmetric sandwich plates (Figs. 6.2(b)-6.2(c)), the thicknesses of the bottom substrate layer and the top passive/active constraining layer are taken as, h_b = 4.5 mm and h_t = 0.5 mm, respectively. The symmetric/asymmetric sandwich plates (Figs. 6.2(a)-6.2(b)) are taken with the clamped edges. However, for the ACLD treated plate (Fig. 6.2(c)), the edges of the substrate layer are clamped. All sandwich plates are considered to operate under the uniformly distributed transverse harmonic load as mentioned above.

In order to achieve sufficient numerical accuracy in the present FE results, FE mesh convergence study is performed where the fundamental natural frequency (ω_n) and the corresponding modal loss factor (η) of every sandwich plate are computed by increasing the number of elements. These results for the case of the sandwich plate with the actively constrained 0-3 VEC layer are illustrated in Table 6.1. Similar results for other sandwich plates are not presented here. However, this FE mesh convergence study is followed to decide the FE mesh of a sandwich plate in evaluation of further results with sufficient numerical accuracy.

Table 6.1 FE mesh convergence study for the sandwich plate with actively constrained 0-3 VEC layer (n_g = 12, r_v = 0.05, Δ = 100 μm, h_d = 2.5 mm, p_0 = 1000 N/m², k_d = 200).

No. of elements	ω_n (rad/s)	η
1225	1737.037	0.16591
2209	1732.313	0.16714
3481	1728.517	0.16764
4189	1727.894	0.16770
5041	1727.882	0.16771

Table 6.2 Verification of the present FE formulation for the computation of natural frequency ($\omega_{m,n}$) and modal loss factor ($\eta_{m,n}$) of sandwich plates with the viscoelastic core (m and n are the bending mode numbers along the x and y directions, respectively).

Bending modes (m,n)	FE results (FSDT)		FE results (TSDT)		Ref. (Cupiał and Nizioł, 1995)	
	$\omega_{m,n}$ (Hz)	$\eta_{m,n}$	$\omega_{m,n}$ (Hz)	$\eta_{m,n}$	$\omega_{m,n}$ (Hz)	$\eta_{m,n}$
(1,1)	60.236	0.1901	60.235	0.1901	60.3	0.190
(1,2)	115.226	0.2034	115.224	0.2034	115.4	0.203
(2,1)	130.429	0.1992	130.427	0.1992	130.6	0.199
(2,2)	178.466	0.1806	178.463	0.1806	178.7	0.181

Table 6.3 Natural frequency ($\omega_{m,n}$) and model loss factor ($\eta_{m,n}$) of a sandwich plate for different thicknesses of the viscoelastic core layer (ϕ = 0, $m=1$, $n=1$).

h_d (mm)	Present FE results (FSDT)		Present FE results (TSDT)	
	$\omega_{m,n}$ (Hz)	$\eta_{m,n}$	$\omega_{m,n}$ (Hz)	$\eta_{m,n}$
0.5	1127.975	0.1583	1127.951	0.1583
1.5	1007.757	0.1430	1.007.732	0.1430
2.5	971.117	0.1432	971.093	0.1432

The FE formulation for the layered plates in this chapter is carried out using layer-wise deformation theory, where the displacement field in every layer is defined according to FSDT. Similar formulation is also presented in Chapter 4 by defining the displacement field in the viscoelastic layer according to TSDT. The corresponding changes in the results for the natural frequency and modal loss factor are illustrated in Table 6.2 for a sandwich plate with the monolithic viscoelastic core. The same sandwich plate is also analysed in (Cupiał and Nizioł, 1995) employing FSDT for every layer, and these reference results are also given in Table 6.2. It may be observed from this table (Table 6.2) that there is an insignificant change in the results for the consideration of FSDT instead of TSDT. However, in the comparison study presented in Table 6.2, the thickness of the viscoelastic layer is considered as that is taken in (Cupiał and Nizioł, 1995). Now, in the case of a thicker viscoelastic core layer, as considered in the present study, similar results are demonstrated in Table 6.3, where the same observation arises as that was obtained from the previous comparison study

(Table 6.2). Therefore, the displacement field in the viscoelastic layer of the present layered plates may be defined according to FSDT, where the advantages of simpler formulation and less computational cost can be achieved.

However, the comparative damping performance of the monolithic viscoelastic, 0-3 VEC and VEPC damping layers are analysed in the following three subsections. In the first subsection, the CLD treatment of the symmetric sandwich plate (Fig. 6.2(a)) is analysed using all three viscoelastic damping layers separately. Similar analysis is presented in the second subsection for the CLD arrangement through the asymmetric sandwich plate configuration (Fig. 6.2(b)). Third subsection is devoted for the ACLD treatment of the asymmetric sandwich plate (Fig. 6.2(c)) using the aforesaid viscoelastic damping layers.

6.4.1 Symmetric sandwich plate with different damping layers

In this section, the 0-3 VEC, VEPC and monolithic viscoelastic layers are separately used in the symmetric sandwich plate (Fig. 6.2(a)), and the corresponding damping characteristics of the sandwich plate are analysed considering three different values of thickness (h_d) of every damping layer as 0.5 mm, 1.5 mm and 2.5 mm. The damping performance of the 0-3 VEC layer is significantly dependent on the geometrical dimensions (n_g, r_v and Δ) in the arrangement of graphite wafers within the viscoelastic matrix (Kumar et al., 2018a, 2018b). Therefore, the present study is carried out by taking the optimal geometrical configuration of graphite wafers in the 0-3 VEC layer, where the concerned parameters (n_g, r_v, Δ) are taken optimally based on the maximum modal loss factor of the sandwich plate at its fundamental mode of vibration. Further, the optimal values of these parameters (n_g, r_v, Δ) may appear differently as the thickness of the 0-3 VEC layer changes. So, for every thickness (h_d), the parameters are taken with the bounds as $3 \le n_g \le 12$, $0.02 \le r_v \le 0.4$ and $50\ \mu\text{m} \le \Delta \le 200\ \mu\text{m}$, and their optimal values are determined for the maximum modal loss factor (η) following the same procedure as described in (Kumar et al., 2018a, 2018b). Here, it is observed that the variation of the gap (Δ) within its aforesaid bounds has not much influence on the modal loss factor for any thickness of the 0-3 VEC layer, and thus this parameter (Δ) is presently taken with a value as 100 μm. However, the optimal values of the other two

parameters (n_g , r_v) for all the aforesaid three values of thickness of the 0-3 VEC layer are presented in Table 6.4.

Similar to the 0-3 VEC layer, the damping performance of the VEPC layer is also dependent on the volume fraction of inclusion (ϕ) of graphite particles, as it is observed from the results in Fig. 2.5. So, the optimal value of ϕ for each of the aforesaid values of thickness of the VEPC damping layer are evaluated. Here, the variation of the modal loss factor with ϕ is first computed within a span $0 \le \phi \le 0.5$, and then the optimal value of ϕ is chosen for the maximum value of the modal loss factor, as presented in Table 6.4.

Table 6.4 Optimal geometrical configuration of the 0-3 VEC and VEPC damping layers at the core of the symmetric sandwich plate.

h_d	0-3 VEC		VEPC
(mm)	n_g	r_v	ϕ
0.5	10	0.25	0.20
1.5	5	0.10	0.40
2.5	5	0.08	0.45

Table 6.5 Modal loss factor (η) at the fundamental mode of vibration of the symmetric sandwich plate (Fig. 6.2(a)) having either of the monolithic viscoelastic (VEM), 0-3 VEC and VEPC damping layers at the core.

h_d	Modal loss factor (η)		
(mm)	VEM	0-3 VEC	VEPC
0.5	0.1583	0.1710	0.1714
1.5	0.1430	0.2062	0.2180
2.5	0.1432	0.2076	0.2541

The 0-3 VEC or VEPC layer is taken with these optimal configurations (Table 6.4), and the corresponding modal loss factor (η) for the fundamental mode of vibration of the symmetric sandwich plate (Fig. 6.2(a)) is illustrated in Table 6.5. It may be observed from Table 6.5 that the modal loss factor (η) significantly increases as the 0-3 VEC or VEPC layer is used instead of the monolithic viscoelastic (VEM) layer. For a low thickness of damping layer (h_d = 0.5 mm), the modal loss factor changes insignificantly for the alteration between the VEPC layer and 0-3 VEC layer. However, as the thickness of the damping layer increases, the VEPC layer provides higher value of the modal loss factor

than that for the 0-3 VEC layer. Besides this variation in the modal loss factor, the changes in the resonant transverse displacement-amplitude at the fundamental resonant frequency are presented in Table 6.6. Table 6.6 illustrates the resonant transverse displacement-amplitude (W_f) at the middle point of the symmetric sandwich plate for the fundamental mode of vibration of the plate under the uniformly distributed transverse harmonic load. Here, the conventional monolithic viscoelastic (VEM) layer is considered as the basic damping layer, while the graphite wafers/particles are incorporated within the basic damping layer to obtain 0-3 VEC/VEPC damping layer. So, the change in the attenuation of the resonant displacement-amplitude (W_f) due to the use of 0-3 VEC or VEPC layer instead of the basic damping layer is presently quantified by defining percent attenuation (ΔW_f %) according to Eq. (6.8).

$$\Delta W_f\,(\%) = \frac{(W_f)_b - (W_f)_c}{(W_f)_b} \times 100 \qquad (6.8)$$

In Eq. (6.8), the subscript b or c indicates the resonant displacement-amplitude (W_f) for the use of the monolithic viscoelastic or viscoelastic composite (0-3 VEC or VEPC) damping layer. Table 6.6 illustrates the variation of the percent attenuation (ΔW_f %) due to the use of 0-3 VEC or VEPC layer instead of the monolithic viscoelastic/basic damping layer. It may be observed from this table (Table 6.6) that the attenuation of the resonant displacement-amplitude increases significantly due to the use of the 0-3 VEC or the VEPC layer instead of the monolithic viscoelastic layer. However, there is not much difference between the 0-3 VEC layer and the VEPC layer in the aspect of the attenuation of the resonant displacement-amplitude for any thickness of damping layer. Therefore, both the 0-3 VEC and VEPC layers are equally effective in attenuation of resonant displacement-amplitude of the symmetric sandwich plate even though the results in Table 6.5 indicate higher value of the modal loss factor in the case of the VEPC layer. It may be due to the fact that the stiffness of the 0-3 VEC layer differs from that of the VEPC layer so that the stored energy appears differently in these damping layers. Now, the dissipated energy appears in product of the loss factor and stored energy. So, although the VEPC layer provides higher value of the modal loss factor than that for the 0-3

VEC layer, the dissipated energy in the sandwich plate does not follow the same trend due to the difference in the stored energy.

Table 6.6 Transverse displacement-amplitude (W_f) of the symmetric sandwich plate at the fundamental resonance and the corresponding percent attenuation (ΔW_f (%)) for either of the monolithic viscoelastic (VEM), 0-3 VEC and VEPC damping layers at the core (p_0 = 1000 N/m²).

h_d (mm)	Parameter	VEM	0-3 VEC	VEPC
0.5	W_f (mm)	0.5962	0. 4175	0.4346
	ΔW_f (%)	-	29.97	27.09
1.5	W_f (mm)	0.7788	0. 2444	0.2532
	ΔW_f (%)	-	68.62	67.48
2.5	W_f (mm)	0.7901	0.1730	0.1695
	ΔW_f (%)	-	78.10	78.54

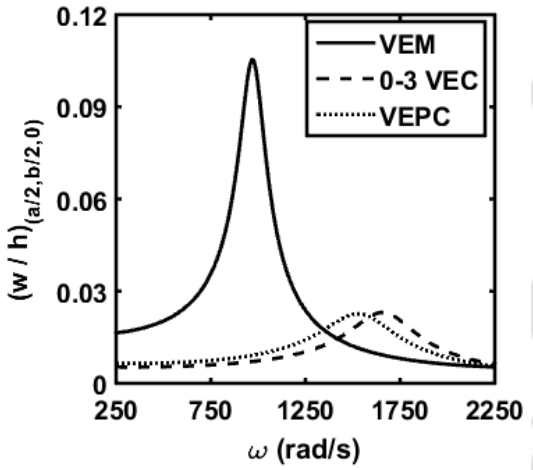

Fig. 6.5 Frequency responses of the symmetric sandwich plate around the fundamental resonant frequency for different viscoelastic damping layers at the core (h_d = 2.5 mm, p_0 = 1000 N/m²).

For further clarification of the passive damping capabilities of the monolithic viscoelastic, 0-3 VEC and VEPC damping layers in attenuation of vibration of the symmetric sandwich plate (Fig. 6.2(a)), the frequency responses at the middle point ($a/2, b/2, 0$) of the plate are illustrated in Fig. 6.5. It may be observed from this figure (Fig. 6.5) that the attenuation of vibration of the symmetric sandwich plate significantly improves as the monolithic viscoelastic

damping layer is replaced by the 0-3 VEC or VEPC layer. However, the passive damping capabilities of the 0-3 VEC and VEPC layers are almost equal as it is also observed from the previous results (Table 6.6). These results suggest that either of the 0-3 VEC and VEPC layers can be used for the improved CLD treatment of a plate through the symmetric sandwich configuration (Fig. 6.2(a)).

6.4.2 Asymmetric sandwich plate with different damping layers

In this section, the damping capabilities of the monolithic viscoelastic, 0-3 VEC and VEPC layers are compared in the CLD treatment through asymmetric sandwich plate configuration (Fig. 6.2(b)). Similar to the previous analysis, this comparison study is also carried out considering three different values of the thickness (h_d =0.5 mm, 1.5 mm and 2.5 mm) of every kind of damping layer, while the 0-3 VEC and VEPC layers are taken with their optimal configurations in the asymmetric sandwich plate. The corresponding optimal values of the geometrical parameters (n_g, r_v) for the 0-3 VEC layer and the volume fraction of inclusion (ϕ) in the VEPC layer are computed, as given in Table 6.7. With these optimal configurations of the 0-3 VEC and VEPC layers, Table 6.8 illustrates the variation of the modal loss factor (η) at the fundamental mode of vibration of the asymmetric sandwich plate for each of the damping layers. It may be observed from Table 6.8 that there is not much change in the modal loss factor if the monolithic viscoelastic layer is replaced by the VEPC layer particularly for a low thickness (h_d =0.5 mm) of damping layer. However, for any thickness (h_d) of damping layer, the modal loss factor increases significantly as the 0-3 VEC layer is used in place of the monolithic viscoelastic or VEPC layer.

Table 6.7 Optimal geometrical configurations of the 0-3 VEC and VEPC damping layers at the core of the asymmetric sandwich plate (Fig. 6.2(b)).

h_d	0-3 VEC		VEPC
(mm)	n_g	r_v	ϕ
0.5	4	0.2	0.1
1.5	4	0.08	0.3
2.5	4	0.05	0.4

Besides this variation of the modal loss factor due to the alteration of damping material, the corresponding changes in the attenuation of the resonant

transverse displacement-amplitude (W_f) are illustrated in Table 6.9. It may be observed from this table (Table 6.9) that the damping capability of the VEPC layer is significantly more than that of the monolithic viscoelastic layer although there is not much difference in the modal loss factor for these two damping layers (Table 6.8). It may be due to the difference in the stored energy within

Table 6.8 Modal loss factor (η) at the fundamental mode of vibration of the asymmetric sandwich plate having either of the monolithic viscoelastic (VEM), 0-3 VEC and VEPC damping layers at core.

h_d (mm)	Modal loss factor (η)		
	VEM	0-3 VEC	VEPC
0.5	0.0476	0.0729	0.0475
1.5	0.0564	0.1312	0.0745
2.5	0.0617	0.1525	0.1018

Table 6.9 Transverse displacement-amplitude (W_f) of the asymmetric sandwich plate at the fundamental resonance and the corresponding percent attenuation (ΔW_f (%)) for either of the monolithic viscoelastic (VEM), 0-3 VEC and VEPC damping layers (p_0 = 500 N/m²).

h_d (mm)	Parameter	VEM	0-3 VEC	VEPC
0.5	W_f (mm)	0.507908	0.26907	0.494670
	ΔW_f (%)	-	47.02	2.60
1.5	W_f (mm)	0.445374	0.114243	0.289331
	ΔW_f (%)	-	74.34	35.03
2.5	W_f (mm)	0.406837	0.069449	0.181930
	ΔW_f (%)	-	82.92	55.28

these two different (VEM and VEPC) damping layers. However, the results in Table 6.9 show that the 0-3 VEC layer is the best one among these three types of damping layers for the CLD treatment of plates through the asymmetric sandwich configuration (Fig. 6.2(b)). For further corroboration of these observations, the frequency responses of the asymmetric sandwich plate are illustrated in Fig. 6.6, where also it is clear that the 0-3 VEC layer provides more

passive damping in the asymmetric sandwich plate as compared to that for either of the other two damping layers.

However, if one compares the CLD treatment through symmetric sandwich configuration (Fig. 6.2(a)) with that through the asymmetric one (Fig. 6.2(b)), then the results in Tables 6.6 and 6.9 show that the 0-3 VEC damping layer is the best one in the asymmetric sandwich configuration while either of the 0-3 VEC, and VEPC layers can be used in the symmetric sandwich configuration for effective damping. Further, among these symmetric and asymmetric sandwich configurations, the asymmetric one would be preferred along with the 0-3 VEC layer for the most effective CLD treatment.

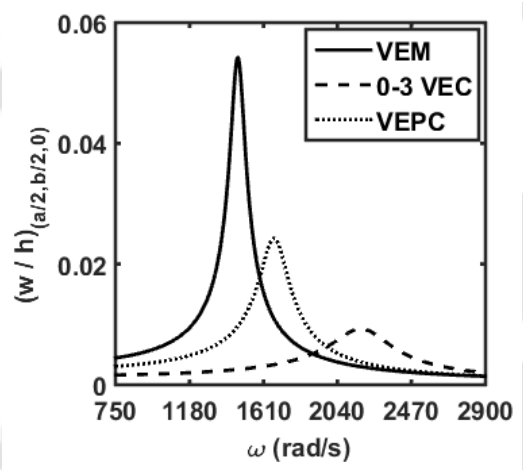

Fig. 6.6 Frequency responses of the asymmetric sandwich plate around the fundamental natural frequency for different viscoelastic damping layers at the core (h_d = 2.5 mm, p_0 = 500 N/m²).

6.4.3 ACLD treated plate with different damping layers

This section is devoted for a comparison study on the damping capabilities of the monolithic viscoelastic, 0-3 VEC, and VEPC layers in the ACLD treatment of a plate (Fig. 6.2(c)). For any kind of damping layer, the active-passive damping in the ACLD treatment changes with the variation in the control gain. However, the comparative performance of the three kinds of damping layers is presently studied considering a constant value of the control gain, while the type of damping layer in the ACLD treatment is altered only. Similar to the previous analysis for CLD treatment, a damping layer is taken with three different values of thickness as 0.5 mm, 1.5 mm, and 2.5 mm, and also, for every thickness, the VEPC and 0-3 VEC layers are taken with their optimal configurations in the

ACLD treated plate (Fig. 6.2(c)). The corresponding results are illustrated in Table 6.10, where a value of the control gain (k_d) is considered as 200, and the 0-3 VEC/VEPC layer is configured optimally for the maximum active-passive damping at the fundamental mode of free vibration of the plate (Fig. 6.2(c)).

Table 6.10 Optimal geometric configurations of the 0-3 VEC and VEPC damping layers in the ACLD treated asymmetric sandwich plate (Fig. 6.2(c)).

h_d (mm)	0-3 VEC		VEPC
	n_g	r_v	ϕ
0.5	4	0.15	0.1
1.5	4	0.05	0.35
2.5	4	0.05	0.425

According to these optimal configurations of the 0-3 VEC and VEPC layers, the attenuation of the resonant transverse displacement-amplitude (W_f) of the overall plate through the passive action only is illustrated in Table 6.11. Here, the damping through the passive action only is achieved by considering $\eta_c \neq 0$ and $k_d = 0$, where η_c is the material loss factor for the monolithic viscoelastic layer or VEPC layer or viscoelastic phase in 0-3 VEC. It may be noted from the results in Table 6.11 that the damping in the plate (Fig. 6.2(c)) due to the passive action only appears in the same manner as that is observed from Table 6.9 for the CLD treatment with the asymmetric sandwich configuration (Fig. 6.2(b)). Because the ACLD treated plate (Fig. 6.2(c)) becomes similar to the CLD treated asymmetric sandwich plate (Fig. 6.2(b)) in the case of the deactivated ($k_d = 0$) piezoelectric constraining layer.

However, the influence of the active action in the piezoelectric actuator layer on the resonant displacement-amplitude (W_f) is illustrated through the results in Table 6.12. Here, the passive action is not considered ($\eta_c = 0$), and the actuator layer is activated with a control gain (k_d) as 200. It may be observed from Table 6.12 that the active damping in the plate improves as the monolithic viscoelastic layer is replaced by the 0-3 VEC or VEPC layer. It may be due to the fact that the stiff inclusion causes improved effective stiffness of a composite damping layer leading to better transfer of actuation force from the actuator layer to the bottom substrate layer. However, in this transfer of actuation force,

the 0-3 VEC layer performs well compared to the VEPC layer although this difference reduces as the thickness (h_d) of damping layer increases.

Table 6.11 Transverse displacement-amplitude (W_f) of the ACLD treated plate at the fundamental resonance and the corresponding percent attenuation (ΔW_f (%)) for the passive action only ($\eta_c \neq 0, k_d = 0$).

h_d (mm)	Parameter	VEM	0-3 VEC	VEPC
0.5	W_f (mm)	1.8324	0.7474	1.7648
	ΔW_f (%)	-	59.20	3.68
1.5	W_f (mm)	1.4356	0.3338	1.0265
	ΔW_f (%)	-	76.74	28.49
2.5	W_f (mm)	1.1796	0.2523	0.6731
	ΔW_f (%)	-	78.61	42.93

Table 6.12 Transverse displacement-amplitude (W_f) of the ACLD treated plate at the fundamental resonance and the corresponding percent attenuation (ΔW_f (%)) for the active action only ($\eta_c = 0, k_d \neq 0$).

h_d (mm)	Parameter	VEM	0-3 VEC	VEPC
0.5	W_f (mm)	0.6731	0.5775	0.6529
	ΔW_f (%)	-	14.19	2.99
1.5	W_f (mm)	0.7070	0.3969	0.4853
	ΔW_f (%)	-	43.86	31.35
2.5	W_f (mm)	0.7529	0.3032	0.379
	ΔW_f (%)	-	59.73	49.57

Now, for the combined active and passive actions, similar results are illustrated in Table 6.13, where it is clear that the performance of the 0-3 VEC layer in augmentation of the active-passive hybrid damping in the ACLD treatment is more than that for the VEPC layer. This observation is also clarified by plotting the frequency responses of the ACLD treated plate, as shown in Fig 6.7(a). The variations of the corresponding control voltage amplitude

Table 6.13 Transverse displacement amplitude (W_f) of the ACLD treated plate at the fundamental resonance and the corresponding percent attenuation (ΔW_f (%)) for the active-passive damping.

h_d (mm)	Parameter	VEM	0-3 VEC	VEPC
0.5	W_f (mm)	0.4783	0.323	0.4656
	ΔW_f (%)	-	32.43	2.66
1.5	W_f (mm)	0.4571	0.1799	0.3213
	ΔW_f (%)	-	60.63	29.70
2.5	W_f (mm)	0.4462	0.1361	0.2366
	ΔW_f (%)	-	69.49	46.97

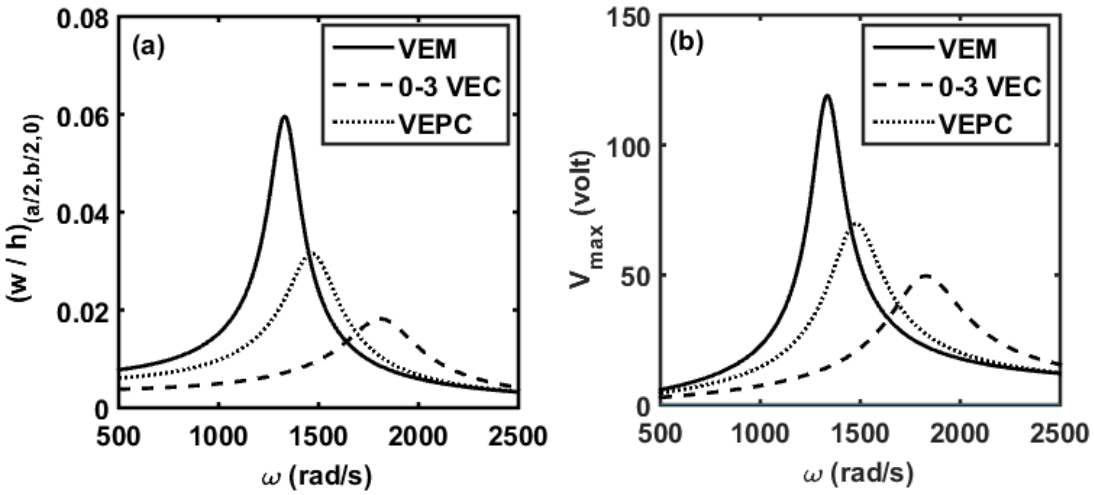

Fig. 6.7 (a) Frequency responses of the ACLD treated plate around the fundamental natural frequency for different damping layers and (b) the corresponding variations of the control voltage amplitude (h_d = 2.5 mm, p_0 = 1000 N/m², k_d = 200).

are also plotted in Fig. 6.7(b). It may be observed from this figure (Fig. 6.7) that the 0-3 VEC layer provides more active-passive damping in the sandwich plate than that for the VEPC layer. Also, the required control voltage reduces in the use of the 0-3 VEPC layer instead of the VEPC layer. These observations suggest 0-3 VEC layer for the ACLD treatment among the three types of viscoelastic damping layers.

6.5 Summary

In this chapter, a study on the comparative performance of monolithic viscoelastic, 0-3 VEC, and VEPC damping layers in the CLD/ACLD treatment of plate vibration are performed. The CLD treatment is achieved in both the symmetric and asymmetric sandwich plate configurations where the damping material lies at the core. However, the top face layer in the asymmetric sandwich plate configuration is made of an extensional mode piezoelectric actuator for the ACLD treatment. For the analysis of damping in these symmetric and asymmetric sandwich plates, a closed-loop FE model is first derived for the ACLD treatment in the asymmetric sandwich plate configuration. Subsequently, the utilization of the same FE model for the analysis of damping in the CLD treatment of the symmetric and asymmetric sandwich plates is demonstrated for each of the three kinds of damping layers. This FE model is first verified, and then the numerical results for the modal loss factor and frequency responses of the sandwich plates are presented for each of the three damping layers towards the comparative study.

It is found that the damping performance of the 0-3 VEC or VEPC layer in the CLD treatment is significantly more than that for the monolithic viscoelastic layer. Also, in the CLD treatment through symmetric sandwich configuration, the damping performance of the 0-3 VEC layer is almost equal to that for the VEPC layer. However, this observation alters when the CLD treatment is taken in the asymmetric configuration, where the performance of the 0-3 VEC is more than that for the VEPC layer. Therefore, the VEPC layer may be used for the CLD treatment in the symmetric sandwich configuration, while the 0-3 VEC is a suitable one for the same damping treatment through the asymmetric sandwich configuration. Further, among these symmetric and asymmetric sandwich configurations, the asymmetric one with the 0-3 VEC layer provides the most effective damping. In the ACLD treatment, the active-passive damping significantly improves as the monolithic viscoelastic damping layer is replaced by the 0-3 VEC or VEPC layer. However, the performance of the 0-3 VEC layer to augment the active-passive damping in the ACLD treatment is better than that for the VEPC layer. Although these observations indicate better damping in the use of the 0-3 VEC layer, the damping performance of the VEPC layer is not much less than that of the 0-3 VEC layer. Moreover, the VEPC layer can be

fabricated easily as compared to the 0-3 VEC. So, the present VEPC may be a potential passive damping material for a low cost CLD/ACLD treatment with a good damping capability.

Chapter 7

Conclusions and scope of future work

7.1 Conclusions

This dissertation deals with a novel viscoelastic particulate composite (VEPC) layer for improved CLD and ACLD treatments of vibration of basic structural elements like beams and plates. The VEPC layer is comprised of micro-sized graphite particles that are dispersedly distributed within the Butyl rubber matrix. Similar to the conventional particulate composite, the present VEPC is also characterized as a macroscopically homogeneous and isotropic material, and its frequency-dependent effective material constants are determined using a differential scheme in conjunction with the elastic-viscoelastic correspondence principle.

The damping performance of this new viscoelastic particulate composite is presently investigated through the CLD and ACLD treatments. First, the CLD treatment with the VEPC damping layer is applied for passive control of vibration of a sandwich beam, where the change of passive damping in the beam is investigated due to the inclusion of graphite particles in the constrained viscoelastic layer at the core. This study is further extended for the partial CLD treatment of the sandwich beam using VEPC patches at the core, where the main motive is to investigate the improvement of passive damping in the partial CLD treatment with respect to the increased weight of the overall sandwich beam when the graphite particles are incorporated dispersedly within the viscoelastic patches at the core. Both the aforesaid studies are carried out by deriving an FE model of the sandwich beam and also by proposing an optimization procedure in the FE framework to configure the partial CLD treatment in achieving maximum damping in the sandwich beam.

Next, the VEPC layer is applied for the CLD treatment of principal primary parametric instability of layered beams. Two different layered beams are considered for the CLD treatment using single or multiple VEPC damping layers. The first one is a three-layered beam having one VEPC damping layer between two identical substrate layers. The second one is a five-layered beam where two identical VEPC damping layers are constrained by three uniform substrate

layers. Generally, the constrained layer damping in these layered beams reduces the parametric instability region to stabilize the beams. However, the change in this functionally of the CLD treatment is analysed at present due to the use of the present VEPC layer instead of the conventional monolithic viscoelastic damping layer. Further, the change in the effectiveness of the CLD treatment is verified when the number of constrained VEPC layers increases without alteration of the volume of damping material. Besides the passive damping capability, the present VEPC layer offers an additional advantage of regulating its stiffness by the change of the volume fraction of inclusion. The usefulness of this feature of the VEPC layer in having a potential way of shifting the instability region out of the frequency range of interest is also investigated. All these investigations are carried out by deriving FE equations of motion of the layered beams based on the layer-wise deformation theory, while the same equations are solved using Bolotin's method to evaluate the principal primary parametric instability region.

Apart from the aforesaid uses of the present VEPC layer in the CLD treatment, the performance of this new viscoelastic particulate composite damping layer in the ACLD treatment is also demonstrated in the context of active-passive control of vibration of plates. The ACLD treatment is configured in the conventional layered form over the top surface of a substrate beam, where the active constraining layer is made of an extensional mode piezoelectric actuator. This piezoelectric actuator layer is activated by supplying external voltage across its top and bottom fully electrode surfaces according to the velocity feedback control law. However, the constrained damping layer is taken as the VEPC layer instead of the conventional monolithic viscoelastic damping layer, and the corresponding changes in the active-passive damping characteristics of the ACLD treatment are analysed. This analysis is performed by deriving a closed-loop FE model of the overall layered plate based on the layer-wise deformation theory, where the numerical results mainly explore the usefulness of the inclusion of graphite particles in the constrained viscoelastic layer to augment the active, passive, and active-passive actions in the ACLD treatment.

The damping performance of the VEPC layer is also studied in the shear actuation-based active-passive damping treatment for vibration control of a sandwich plate-strip, where the shear actuation force is achieved by the use of a shear mode piezoelectric actuator. The sandwich plate-strip is composed of a layered core that is made of a laminate of foam and viscoelastic layers. However, the shear mode piezoelectric actuator is used in the form of the patch, and the actuator patches are embedded in the foam layer to form an active composite layer. This active composite layer and the VEPC/viscoelastic layer are stacked within the core in two different stacking sequences. In the first one, an active layer is sandwiched between two identical VEPC damping layers, while, for the second one, a VEPC layer is sandwiched between two identical active layers. In both the layered configurations of the core, the volumes of the different phase materials are not altered. However, for every layered configuration of the core, the shear actuator patches are activated by the feedback of the time-rate of change of the local slope of bending deformation of the sandwich plate-strip for achieving the shear actuation-based hybrid active-passive damping. With this arrangements, a closed-loop FE model of the sandwich plate-strip is developed, and the numerical results are evaluated to illustrate (i) a fruitful stack of actuator and viscoelastic layers at the core for achieving improved active-passive damping and (ii) the advantages of the present VEPC layer with reference to the conventional monolithic viscoelastic layer in the shear actuation-based hybrid active-passive damping.

Finally, a comparative performance of 0-3 VEC, VEPC and monolithic viscoelastic damping layers in the CLD/ACLD treatment of plate vibration is performed. Here, the CLD treatment is arranged through both the symmetric and asymmetric sandwich plate configurations having the damping material at the core. However, for the ACLD treatment, the top face layer of the asymmetric sandwich plate is made of an extensional mode piezoelectric actuator layer. This actuator layer is activated by supplying the external voltage across its thickness according to the velocity feedback control strategy. For the analysis of damping in these symmetric and asymmetric sandwich plates, a closed-loop FE model is first derived for the ACLD treatment in the asymmetric sandwich plate configuration. Subsequently, the utilization of this FE model for the analysis of

damping in the CLD treatment of the symmetric and asymmetric sandwich plates is demonstrated for each of the three kinds of damping layers. Using this FE model, the numerical results for the modal loss factor and frequency responses of the sandwich plates are evaluated for each of the three damping layers towards the comparative study.

The following main observations are obtained from the aforesaid studies in this thesis.

1. The effective storage modulus of the VEPC increases significantly for an increase in the volume fraction of inclusion of graphite particles while the effective material loss factor of the same VEPC decreases. These material characteristics of the VEPC yield improved CLD treatment of sandwich beams. But, this improvement of passive damping in the CLD treatment is limited to a certain value of the increasing volume fraction of inclusion where the optimal value of the volume fraction of inclusion arises for the maximum passive damping.
2. The study on the optimal partial CLD treatment of the sandwich beam reveals that the optimal size and locations of the viscoelastic patches in the core do not change for the inclusion of graphite particles. Also, a minimal change of weight of the sandwich beam arises for the inclusion, while the same inclusion causes a significantly improved passive damping.
3. From the study on the CLD treatment of parametric instability of layered beams using the VEPC damping layer, it is observed that the inclusion of graphite particles significantly improves the critical buckling load or static stability of the beams. Also, the increased passive damping in the layered beams due to the inclusion yields significantly reduced principal primary parametric instability region resulting in augmented dynamic stability of the beams. However, the maximum reduction of the instability region appears corresponding to an optimal value of the volume fraction of inclusion where the passive damping in the layered beams arises with its maximum value. If the volume fraction of inclusion is lesser than its optimal value, then the dynamic stability of the layered beams can be improved by increasing the number of constrained VEPC layers. In contrast, the number of constrained

VEPC layers is to be reduced for the enhanced dynamic stability of the layered beams when the volume fraction of inclusion is greater than its optimal value. However, for an optimal value of the volume fraction of inclusion, there is no significant change in the instability region for the increasing number of damping layers. All these observations are obtained by keeping the constant volume of damping material in the layered beams for any number of damping layers.

4. Besides the improved static and dynamic stability of layered beams, the natural frequency of these beams can be regulated by tuning the volume fraction of inclusion in the constrained VEPC layers. It provides the advantage of shifting the instability region aside from the frequency range of interest by varying the volume fraction of inclusion. So, the appearance of the instability region within the operating frequency range can be reduced for achieving improved dynamic stability of layered beams.

5. The study on the ACLD treatment of plate vibration reveals that the inclusion of graphite particles within the viscoelastic layer causes improved transfer of actuation force from the actuator layer to the substrate plate. Also, the same inclusion yields increased passive damping capability of the constrained viscoelastic layer. However, the optimal volume fraction of inclusion for the maximum transfer of actuation force is almost equal to that for the maximum improvement of passive damping capability of the viscoelastic layer. So, a significant increase in the active-passive damping is observed for the optimal value of the volume fraction of inclusion in the constrained viscoelastic layer.

6. From the study on the shear actuation-based active-passive damping treatment of a sandwich plate-strip, it is observed that the stacking sequence of active and viscoelastic layers in the core has a significant influence on the active-passive damping in the plate-strip. Among the aforesaid two kinds of stacking sequences at the core of the sandwich plate-strip, the later one provides better active-passive damping where a viscoelastic layer is sandwiched by two identical active layers. However, for any of the stacking sequences of the component layers at the core, the inclusion of graphite

particles in the viscoelastic layer significantly improves the transfer of shear actuation force from the actuator to other layers. At the same time, the passive damping capability of the viscoelastic layer increases for the inclusion. So, the shear actuated active-passive damping in the plate-strip increases due to the inclusion, and similar to the previous study on ACLD treatment, there is an optimal value of the volume fraction of inclusion for the maximum improvement of the shear-actuated active-passive damping.

7. Further study on the optimal geometrical configuration of core of the sandwich plate-strip reveals that there is an optimal number of shear mode piezoelectric actuator patches across the length of the plate-strip for the maximum shear actuation-based active-passive damping. Also, the shear actuator patches are to be arranged with an optimal gap between any two consecutive ones. However, the optimal value of the volume fraction of inclusion of graphite particles is not much dependent on the geometrical configuration of shear actuator patches within the foam layer.

8. The study on the comparative damping performance of 0-3 VEC, VEPC and monolithic viscoelastic layers in the CLD treatment of a plate reveals augmented damping in the overall plate when the monolithic viscoelastic layer is replaced by the 0-3 VEC or VEPC layer. However, in the CLD treatment through the symmetric sandwich plate configuration, the damping performance of the 0-3 VEC layer is almost equal to that for the VEPC layer. But, in the asymmetric sandwich plate configuration, the damping performance of the 0-3 VEC layer is more than that for the VEPC layer. Further, among these symmetric and asymmetric sandwich plate configurations, the asymmetric one with the 0-3 VEC layer provides most effective damping.

9. From the study on the comparative performance of 0-3 VEC and VEPC layers in the ACLD treatment, it is found that the performance of the 0-3 VEC layer to augment the active-passive damping in the ACLD treatment is better than that for the VEPC layer.

10. The aforesaid comparative studies imply better damping in the use of the 0-3 VEC layer. However, the damping performance of the VEPC is comparable

to that of the 0-3 VEC. Moreover, the VEPC layer can be fabricated easily as compared to the 0-3 VEC. So, the present VEC may be a potential damping material for the low-cost CLD/ACLD treatment with a good damping capability. Further, the VEPC layer possesses an additional feature of regulating its stiffness by changing the volume fraction of inclusion. It provides a great advantage in controlling the parametric instability of flexible structures through the CLD treatment, as demonstrated in Chapter 3.

7.2 Scope of future work

Although the preceding chapters of this thesis fulfil the objectives of the present dissertation, further research on this VEPC damping layer may still be carried out in the context of CLD and ACLD treatments of structural vibration. Some of the future works which may be readily undertaken in line with the present work are as follows.

1. Performance of the VEPC layer in the CLD/ACLD treatment for control of large amplitude vibration of flexible structures.
2. Performance of the VEPC layer in passive or active-passive control of vibration of shell structures.
3. Usefulness of the VEPC layer for control of structural vibration under the thermal environment.
4. Experimental verification of the theoretical models developed in this thesis is also scope for further research work.

References

Al-Ajmi MA, Bourisli RI. Optimum design of segmented passive-constrained layer damping treatment through genetic algorithms. Mechanics of Advanced Materials and Structures 2008;15(3-4):250-7.

Alam N, Asnani NT. Vibration and damping analysis of a multilayered cylindrical shell, Part I: Theoretical analysis. AIAA Journal 1984a; 22(6):803-810.

Alam N, Asnani NT. Vibration and damping analysis of multilayered rectangular plates with constrained viscoelastic layers. Journal of Sound and Vibration 1984b;97(4):597-614.

Aldraihem OJ, Khdeir AA. Exact deflection solutions of beams with shear piezoelectric actuators. International Journal of Solids and Structures 2003;40(1):1-2.

Alvelid M, Enelund M. Modelling of constrained thin rubber layer with emphasis on damping. Journal of Sound and Vibration 2007;300(3-5):662-75.

Arafa M, Baz A. Dynamics of active piezoelectric damping composites. Composites Part B: Engineering 2000;31(4):255-64.

Attipou K, Nezamabadi S, Zahrouni H. A multiscale approach for the vibration analysis of heterogeneous materials: Application to passive damping. Journal of Sound and Vibration 2013;332(4):725-39.

Azvine B, Tomlinson GR, Wynne RJ. Use of active constrained-layer damping for controlling resonant vibration. Smart Materials and Structures 1995;4(1):1.

Baillargeon BP, Vel SS. Active vibration suppression of sandwich beams using piezoelectric shear actuators: experiments and numerical simulations. Journal of Intelligent Material Systems and Structures 2005;16(6):517-30.

Balamurugan V, Narayanan S. Active–passive hybrid damping in beams with enhanced smart constrained layer treatment. Engineering Structures 2002;24(3):355-63.

Batra RC, Geng TS. Comparison of active constrained layer damping by using extension and shear mode piezoceramic actuators. Journal of Intelligent Material Systems and Structures 2002;13(6):349-67.

Baz A, Ro J. Partial treatment of flexible beams with active constrained layer damping. ASME Applied Mechanics Division-Publications 1993;167:61.

Baz A, Ro J. Performance characteristics of active constrained layer damping. Shock and Vibration 1995;2(1):33-42.

Baz AM, Ro JJ. Active deflection control of multisegment traversing beams. Smart Structures and Materials 1993: Smart Structures and Intelligent Systems 1993; vol. 1917, pp. 144-156. International Society for Optics and Photonics.

Baz AM. Active and passive vibration damping. John Wiley & Sons; 2019.

Benjeddou A, Deu JF. Piezoelectric transverse shear actuation and sensing of plates, Part 1: A three-dimensional mixed state space formulation. Journal of Intelligent Material Systems and Structures 2001a;12(7):435-49.

Benjeddou A, Deu JF. Piezoelectric transverse shear actuation and sensing of plates, Part 2: Application and analysis. Journal of Intelligent Material Systems and Structures 2001b;12(7):451-67.

Benjeddou A, Trindade MA, Ohayon R. A unified beam finite element model for extension and shear piezoelectric actuation mechanisms. Journal of Intelligent Material Systems and Structures 1997;8(12):1012-25.

Benjeddou A. Shear-mode piezoceramic advanced materials and structures: a state of the art. Mechanics of Advanced Materials and Structures 2007;14(4):263-75.

Birman V, Kardomateas GA. Review of current trends in research and applications of sandwich structures. Composites Part B: Engineering 2018;142:221-40.

Bolotin VV. The Dynamic stability of elastic systems. Holden-Day; 1964.

Brahem M, Chouchane M, Amamou A. Active vibration control of a rotor bearing system using flexible piezoelectric patch actuators. Journal of Intelligent Material Systems and Structures 2020;31(10):1284-97.

Bruggeman DA. Dielectric constant and conductivity of mixtures of isotropic materials. Annals of Physics 1935;24:636-79.

Cady WG. Piezoelectricity: An introduction to the theory and applications of electromechanical phenomena in crystals. McGraw-Hill Press; 1946.

Cai C, Zheng H, Liu GR. Vibration analysis of a beam with PCLD patch. Applied Acoustics 2004;65(11):1057-76.

Cao XT, Zhang ZY, Hua HX. Free vibration of circular cylindrical shell with constrained layer damping. Applied Mathematics and Mechanics 2011;32(4):495-506.

Carrera E. Historical review of zig-zag theories for multilayered plates and shells. Applied Mechanics Reviews 2003;56(3):287-308.

Chaudhry Z, Rogers C. Actuators for smart structures. Fiber optic smart structures. John Wiley & Sons 1995:497-536.

Chawla KK, Meyers MA. Mechanical behavior of materials. Prentice Hall; 1999.

Chee CYK. Static shape control of laminated composite plate smart structure using piezoelectric actuators. PhD Thesis, The University of Sydney; 2000.

Chen LH, Huang SC. Vibration attenuation of a cylindrical shell with constrained layer damping strips treatment. Computers & Structures 2001;79(14):1355-1362.

Chen LH, Huang SC. Vibrations of a cylindrical shell with partially constrained layer damping (CLD) treatment. International Journal of Mechanical Sciences 1999;41(12):1485-1498.

Chen LW, Lin CY, Wang CC. Dynamic stability analysis and control of a composite beam with piezoelectric layers. Composite Structures 2002;56(1):97-109.

Chen TH, Baz AM. Performance characteristics of active constrained layer damping versus passive constrained layer damping with active control. Smart Structures and Materials 1996: Mathematics and Control in Smart

Structures 1996; vol. 2715, pp. 256-268. International Society for Optics and Photonics.

Cheng L, Lapointe R. Vibration attenuation of panel structures by optimally shaped viscoelastic coating with added weight considerations. Thin-Walled Structures 1995;21(4):307-26.

Christensen RM. Mechanics of composite materials. Courier Corporation; 2012.

Christensen RM. Theory of viscoelasticity: An introduction. Academic Press; 1982.

Cortés F, Elejabarrieta MJ. Structural vibration of flexural beams with thick unconstrained layer damping. International Journal of Solids and Structures 2008;45(22-23):5805-13.

Cunha-Filho AG, De Lima AM, Donadon MV, Leão LS. Flutter suppression of plates using passive constrained viscoelastic layers. Mechanical Systems and Signal Processing 2016;79:99-111.

Cupiał P, Nizioł J. Vibration and damping analysis of a three-layered composite plate with a viscoelastic mid-layer. Journal of Sound and Vibration 1995;183(1):99-114.

Dash P, Singh BN. Nonlinear free vibration of piezoelectric laminated composite plate. Finite Elements in Analysis and Design 2009;45(10):686-94.

Datta P, Ray MC. Smart damping of large amplitude vibrations of variable thickness laminated composite shells. Thin-Walled Structures 2018;127:710-27.

Datta P, Ray MC. Three-dimensional fractional derivative model of smart constrained layer damping treatment for composite plates. Composite Structures 2016;156:291-306.

Daya EM, Potier-Ferry M. A numerical method for nonlinear eigenvalue problems application to vibrations of viscoelastic structures. Computers & Structures 2001;79(5):533-41.

de Borbón F, Ambrosini D, Curadelli O. Damping response of composites beams with carbon nanotubes. Composites Part B: Engineering 2014;60:106-10.

Deng J, Liu Y, Zhang Z, Liu W. Stability analysis of multi-span viscoelastic functionally graded material pipes conveying fluid using a hybrid method. European Journal of Mechanics-A/Solids 2017;65:257-70.

DeValve C, Pitchumani R. Analysis of vibration damping in a rotating composite beam with embedded carbon nanotubes. Composite Structures 2014;110:289-96.

Dewa H, Okada Y, Nagai B. Damping characteristics of flexural vibration for partially covered beams with constrained viscoelastic layers. JSME International Journal Series 3: Vibration, Control Engineering, Engineering for Industry 1991;34(2):210-7.

Dey P, Singha MK. Dynamic stability analysis of composite skew plates subjected to periodic in-plane load. Thin-Walled Structures 2006;44(9):937-42.

Douglas BE, Yang JC. Transverse compressional damping in the vibratory response of elastic-viscoelastic-elastic beams. AIAA Journal 1978;16(9):925-

30.

Dwivedy SK, Sahu KC, Babu S. Parametric instability regions of three-layered soft-cored sandwich beam using higher-order theory. Journal of Sound and Vibration 2007;304(1-2):326-44.

El-Raheb M, Wagner P. Damped response of shells by a constrained viscoelastic layer. Journal of Applied Mechanics 1986;53:903.

El-Sabbagh A, Baz A. Topology optimization of unconstrained damping treatments for plates. Engineering Optimization 2014;46(9):1153-68.

Erturk A, Inman DJ. Piezoelectric energy harvesting. John Wiley & Sons; 2011.

Fang Y, Li L, Zhang D, Chen S, Liao WH. Vibration suppression of a rotating functionally graded beam with enhanced active constrained layer damping treatment in temperature field. Thin-Walled Structures 2021;161:107522.

Fasana A, Garibaldi L, Giorcelli E, Ruzzene M. Passive damping of beams with constrained viscoelastic material. Smart Structures and Materials 1997: Passive Damping and Isolation 1997; vol. 3045, pp. 184-189. International Society for Optics and Photonics.

Ferreira AJ, Araújo AL, Neves AM, Rodrigues JD, Carrera E, Cinefra M, Soares CM. A finite element model using a unified formulation for the analysis of viscoelastic sandwich laminates. Composites Part B: Engineering 2013;45(1):1258-64.

Filippi M, Carrera E, Regalli AM. Layerwise analyses of compact and thin-walled beams made of viscoelastic materials. Journal of Vibration and Acoustics 2016;138(6).

Filippi M, Carrera E. Bending and vibrations analyses of laminated beams by using a zig-zag-layer-wise theory. Composites Part B: Engineering 2016;98:269-80.

Filippi M, Carrera E. Various refined theories applied to damped viscoelastic beams and circular rings. Acta Mechanica 2017;228(12):4235-48.

Flügge W. Viscoelasticity. Mass Blaisdell Publishing Company; 1967.

Ganapathi M, Patel BP, Sambandam CT, Touratier M. Dynamic instability analysis of circular conical shells. Composite structures 1999;46(1):59-64.

Gao JX, Liao WH. Vibration analysis of simply supported beams with enhanced self-sensing active constrained layer damping treatments. Journal of Sound and Vibration 2005;280(1-2):329-57.

Garrison MR, Miles RN, Sun JQ, Bao W. Random response of a plate partially covered by a constrained layer damper. Journal of Sound and Vibration 1994;172(2):231-45.

Gentilman RL, Fiore DF, Pham HT, French KW, Bowen LJ. Fabrication and properties of 1-3 PZT-polymer composites. American Ceramic Society, Westerville, United States; 1994.

German RM. Particulate Composites. Springer; 2016.

Ghoneim H. Electromechanical surface damping using constrained layer and shunted piezoelectric. Smart Structures and Materials 1993: Mathematics in Smart Structures 1993; vol. 1919, pp. 78-89. International Society for Optics

and Photonics.

Golla DF, Hughes PC. Dynamics of viscoelastic structures-a time-domain, finite element formulation. Journal of Applied Mechanics 1985;52:897–906.

Granger D, Ross A. Effects of partial constrained viscoelastic layer damping parameters on the initial transient response of impacted cantilever beams: Experimental and numerical results. Journal of Sound and Vibration 2009;321(1-2):45-64.

Grewal JS, Sedaghati R, Esmailzadeh E. Vibration analysis and design optimization of sandwich beams with constrained viscoelastic core layer. Journal of Sandwich Structures & Materials 2013;15(2):203-28.

Grootenhuis P. The control of vibrations with viscoelastic materials. Journal of Sound and Vibration 1970;11(4):421-33.

Gu J, Dai B, Wang Y, Li M, Duan M. Dynamic analysis of a fluid-conveying pipe under axial tension and thermal loads. Ships and Offshore Structures 2017;12(2):262-75.

Haddad YM. Viscoelasticity of engineering materials. Springer; 1995.

Hagood NW, von Flotow A. Damping of structural vibrations with piezoelectric materials and passive electrical networks. Journal of Sound and Vibration 1991;146(2):243-268.

Hamdaoui M, Ledi KS, Robin G, Daya EM. Identification of frequency-dependent viscoelastic damped structures using an adjoint method. Journal of Sound and Vibration 2019;453:237-52.

Herdic PC, Houston BH, Marcus MH, Williams EG, Baz AM. The vibro-acoustic response and analysis of a full-scale aircraft fuselage section for interior noise reduction. The Journal of the Acoustical Society of America 2005;117(6):3667-3678.

Herrmann AS, Zahlen PC, Zuardy I. Sandwich structures technology in commercial aviation. Sandwich structures 7: Advancing with Sandwich Structures and Materials 2005; pp. 13-26. Springer.

Hsiao-Sheng C, Acrivos A. The effective elastic moduli of composite materials containing spherical inclusions at non-dilute concentrations. International Journal of Solids and Structures 1978;14(5):349-64.

Hu H, Belouettar S, Potier-Ferry M. Review and assessment of various theories for modeling sandwich composites. Composite Structures 2008;84(3):282-92.

Huang BW, Kuang JH. The parametric resonance instability in a drilling process. Journal of Applied Mechanics 2007;74(5):958-964.

Huang CY, Tsai JL. Characterizing vibration damping response of composite laminates containing silica nanoparticles and rubber particles. Journal of Composite Materials 2015;49(5):545-57.

Huang PY, Reinhall PG, Shen IY, Yellin JM. Thickness deformation of constrained layer damping: an experimental and theoretical evaluation. Journal of Vibration and Acoustics 2001;123(2):213-221.

Huang SC, Inman DJ, Austin EM. Some design considerations for active and passive constrained layer damping treatments. Smart Materials and

Structures 1996;5(3):301.

Huang Z, Qin Z, Chu F. Vibration and damping characteristics of sandwich plates with viscoelastic core. Journal of Vibration and Control 2016;22(7):1876-88.

Hwang WS, Park HC. Finite element modeling of piezoelectric sensors and actuators. AIAA Journal 1993;31(5):930-7.

Imaino W, Harrison JC. A comment on constrained layer damping structures with low viscoelastic modulus. Journal of Sound and Vibration 1991;149(2):354-9.

Jiang ZW, Chonan S, Abe H. Dynamic response of a read/write head floppy disk system subjected to axial excitation. Journal of Vibration and Acoustic 1990;112(1):53-58.

Jin G, Yang C, Liu Z, Gao S, Zhang C. A unified method for the vibration and damping analysis of constrained layer damping cylindrical shells with arbitrary boundary conditions. Composite Structures 2015;130:124-42.

Johnson CD, Kienholz DA. Finite element prediction of damping in structures with constrained viscoelastic layers. AIAA Journal 1982;20(9):1284-90.

Jones DI. Handbook of viscoelastic vibration damping. John Wiley & Sons; 2001.

Jones IW, Salerno VL. The effect of structural damping on the forced vibrations of cylindrical sandwich shells. Journal of Engineering for Industry 1966; 88(3):318-323.

Jones RM. Mechanics of composite materials. CRC Press; 1998.

Ke LL, Yang J, Kitipornchai S. Dynamic stability of functionally graded carbon nanotube-reinforced composite beams. Mechanics of Advanced Materials and Structures 2013;20(1):28-37.

Kerwin Jr EM. Damping of flexural waves by a constrained viscoelastic layer. The Journal of the Acoustical Society of America 1959;31(7):952-62.

Khalfi B, Ross A. Transient and harmonic response of a sandwich with partial constrained layer damping: A parametric study. Composites Part B: Engineering 2016;91:44-55.

Khan SU, Li CY, Siddiqui NA, Kim JK. Vibration damping characteristics of carbon fiber-reinforced composites containing multi-walled carbon nanotubes. Composites Science and Technology 2011;71(12):1486-94.

Khdeir AA, Aldraihem OJ. Deflection analysis of beams with extension and shear piezoelectric patches using discontinuity functions. Smart Materials and Structures 2001;10(2):212.

Korjakin A, Rikards R, Altenbach H, Chate A. Free damped vibrations of sandwich shells of revolution. Journal of Sandwich Structures & Materials 2001;3(3):171-96.

Krieger IM, Dougherty TJ. A mechanism for non-Newtonian flow in suspensions of rigid spheres. Transactions of the Society of Rheology 1959;3(1):137-52.

Kumar A, Panda S, Kumar A, Narsaria V. Performance of a graphite wafer-reinforced viscoelastic composite layer for active-passive damping of plate

vibration. Composite Structures 2018a;186:303-14.

Kumar A, Panda S, Narsaria V, Kumar A. Augmented constrained layer damping in plates through the optimal design of a 0-3 viscoelastic composite layer. Journal of Vibration and Control 2018b;24(23):5514-24.

Kumar A, Panda S. Design of a 1-3 viscoelastic composite layer for improved free/constrained layer passive damping treatment of structural vibration. Composites Part B: Engineering 2016;96:204-14.

Kumar N, Singh SP. Experimental study on vibration and damping of curved panel treated with constrained viscoelastic layer. Composite Structures 2010;92(2):233-43.

Kumar N, Singh SP. Vibration and damping characteristics of beams with active constrained layer treatments under parametric variations. Materials & Design 2009;30(10):4162-74.

Kumar R. Enhanced active constrained layer damping (ACLD) treatment using stand-off-layer: robust controllers design, experimental implementation and comparison. Journal of Vibration and Control 2013;19(3):439-60.

Kumar S, Kumar R, Sehgal R. Enhanced ACLD treatment using stand-off-layer: FEM based design and experimental vibration analysis. Applied Acoustics 2011a;72(11):856-872.

Kumar S, Sehgal R, Kumar R. Active vibration control of beams by combining precompressed layer damping and ACLD treatment: Theory and experimental implementation. Journal of Vibration and Acoustics 2011b;133(6).

Kung SW, Singh R. Vibration analysis of beams with multiple constrained layer damping patches. Journal of Sound and Vibration 1998;212(5):781-805.

Kwak SK, Washington G, Yedavalli RK. Active and passive vibration control of landing gear components. Adaptive Structures and Materials Systems 1999;59:269-75.

Lakes RS. Viscoelastic materials. Cambridge University Press; 2009.

Lakes RS. Viscoelastic solids. CRC Press; 1998.

Lall AK, Asnani NT, Nakra BC. Damping analysis of partially covered sandwich beams. Journal of Sound and Vibration 1988;123(2):247-59.

Lall AK, Asnani NT, Nakra BC. Vibration and damping analysis of rectangular plate with partially covered constrained viscoelastic layer. Journal of Vibration, Acoustics, Stress, and Reliability in Design 1987;109(3):241-247.

Lam MJ, Inman DJ, Saunders WR. Vibration control through passive constrained layer damping and active control. Journal of Intelligent Material Systems and Structures 1997;8(8):663-77.

Lam MJ, Saunders WR, Inman DJ. Modeling active constrained-layer damping using Golla-Hughes-McTavish approach. Smart Structures and Materials 1995: Passive Damping 1995; vol. 2445, pp. 86-97. International Society for Optics and Photonics.

Langthjem MA, Sugiyama Y. Dynamic stability of columns subjected to follower loads: a survey. Journal of Sound and Vibration 2000;238(5):809-51.

LaPlante WA. Vibration control of fluid-loaded cylindrical shells using active constrained layer damping. PhD thesis, Catholic University of America; 1998.

Lee DH, Hwang WS. Layout optimization of unconstrained viscoelastic layer on beams using fractional derivative model. AIAA Journal 2004;42(10):2167-70.

Lepoittevin G, Kress G. Optimization of segmented constrained layer damping with mathematical programming using strain energy analysis and modal data. Materials & Design 2010;31(1):14-24.

Lesieutre GA, Bianchini E. Time domain modeling of linear viscoelasticity using anelastic displacement fields. Journal of Vibration and Acoustics 1995;117(4):424-430.

Lesieutre GA, Lee U. A finite element for beams having segmented active constrained layers with frequency-dependent viscoelastics. Smart Materials and Structures 1996;5(5):615.

Lesieutre GA, Mingori DL. Finite element modeling of frequency-dependent material damping using augmenting thermodynamic fields. Journal of Guidance, Control, and Dynamics 1990;13(6):1040-50.

Lezgy-Nazargah M. Efficient coupled refined finite element for dynamic analysis of sandwich beams containing embedded shear-mode piezoelectric layers. Mechanics of Advanced Materials and Structures 2016;23(3):337-52.

Li FM, Kishimoto K, Wang YS, Chen ZB, Huang WH. Vibration control of beams with active constrained layer damping. Smart Materials and Structure 2008;17(6):065036.

Li H, Wang Z, Lv H, Zhou Z, Han Q, Liu J, Qin Z. Nonlinear vibration analysis of fiber reinforced composite cylindrical shells with partial constrained layer damping treatment. Thin-Walled Structures 2020;157:107000.

Li H, Yang Y. Dynamic response and active control of a composite cylindrical shell with piezoelectric shear actuators. Smart Materials and Structures 2007;16(3):909.

Li L, Liao WH, Zhang D, Guo Y. Dynamic modeling and analysis of rotating beams with partially covered enhanced active constrained layer damping treatment. Journal of Sound and Vibration 2019;455:46-68.

Li W, He Y, Xu Z, Zhang Z. A reduced passive constrained layer damping finite element model based on the modified improved reduced system method. Journal of Sandwich Structures & Materials 2019;21(2):758-83.

Liang L, Huang W, Lyu P, Ma M, Meng F, Sang Y. Impacts of PU foam stand-off layer on the vibration damping performance of stand-off free layer damping cantilever beams. Shock and Vibration 2020.

Liao WH, Wang KW. A new active constrained layer configuration with enhanced boundary actions. Smart Materials and Structures 1996;5(5):638.

Liao WH, Wang KW. Analysis of edge elements for a new active constrained layer treatment. Passive Damping and Isolation 1997;70.

Liu B, Zhao L, Ferreira AJ, Xing YF, Neves AM, Wang J. Analysis of viscoelastic sandwich laminates using a unified formulation and a differential quadrature hierarchical finite element method. Composites Part B:

Engineering 2017;110:185-92.

Liu Y, Wang KW. Active-passive hybrid constrained layer for structural damping augmentation. Journal of Vibration and Acoustics 2000;122(3):254-62.

Liu Y, Wang KW. Damping optimization by integrating enhanced active constrained layer and active-passive hybrid constrained layer treatments. Journal of Sound and Vibration 2002;255(4):763-775.

Liu Y, Wang KW. Enhanced active constrained layer damping treatment with symmetrically and non-symmetrically distributed edge elements. Smart Structures & Materials 1998;61-72.

Lu J, Wang P, Zhan Z. Active vibration control of thin-plate structures with partial SCLD treatment. Mechanical Systems and Signal Processing 2017;84:531-50.

Lu YP, Killian JW, Everstine GC. Vibrations of three layered damped sandwich plate composites. Journal of Sound and Vibration 1979;64(1):63-71.

Lu YP. Forced vibrations of damped cylindrical shells filled with pressurized liquid. AIAA Journal 1977;15(9):1242-9.

Lumsdaine A, Scott RA. Shape optimization of unconstrained viscoelastic layers using continuum finite elements. Journal of Sound and Vibration 1998;216(1):29-52.

Lunden R. Optimum distribution of additive damping for vibrating beams. Journal of Sound and Vibration 1979;66(1):25-37.

Madeira JF, Araújo AL, Soares CM, Soares CM, Ferreira AJ. Multiobjective design of viscoelastic laminated composite sandwich panels. Composites Part B: Engineering 2015;77:391-401.

Manconi E, Mace BR. Estimation of the loss factor of viscoelastic laminated panels from finite element analysis. Journal of Sound and Vibration 2010;329(19):3928-39.

Marcelin JL, Trompette P, Smati A. Optimal constrained layer damping with partial coverage. Finite elements in Analysis and Design 1992;12(3-4):273-80.

Markuš Š. Damping mechanism of beams partially covered by constrained viscoelastic layer. Acta Technica CSAV 1974;19(2):179-194.

Markuš Š. Damping properties of layered cylindrical shells, vibrating in axially symmetric modes. Journal of Sound and Vibration 1976;48(4):511-24.

Marra SP, Ramesh KT, Douglas AS. The mechanical properties of lead-titanate/polymer 0–3 composites. Composites Science and Technology 1999;59(14):2163-73.

Marsh ER, Hale LC. Damping of flexural waves with imbedded viscoelastic materials. Journal of Vibration and Acoustics 1998;120(1):188-193.

Masti RS, Sainsbury MG. Vibration damping of cylindrical shells partially coated with a constrained viscoelastic treatment having a standoff layer. Thin-Walled Structures 2005;43(9):1355-79.

MathWorks Inc. Choose an ODE Solver; 2020. Available at:

https://in.mathworks.com/help/matlab/math/choose-an-ode-solver.html.

McTavish DJ, Hughes PC. Modeling of linear viscoelastic space structures. Journal of Vibration and Acoustics 1993;115(1):103-110.

Mead DJ, Markus S. The forced vibration of a three-layer, damped sandwich beam with arbitrary boundary conditions. Journal of Sound and Vibration 1969;10(2):163-75.

Mead DJ, Pearce TG. The optimum use of unconstrained layer damping treatments. Southampton University, England; 1961.

Mead DJ. The measurement of the loss factors of beams and plates with constrained and unconstrained damping layers: A critical assessment. Journal of Sound and Vibration 2007;300(3-5):744-62.

Meirovitch L. Principles and techniques of vibrations. Prentice Hall; 1997.

Meunier M, Shenoi RA. Forced response of FRP sandwich panels with viscoelastic materials. Journal of Sound and Vibration 2003;263(1):131-51.

Mohanty SC, Dash RR, Rout T. Static and dynamic stability analysis of a functionally graded Timoshenko beam. International Journal of Structural Stability and Dynamics 2012;12(04):1250025.

Moita JS, Araújo AL, Martins PG, Soares CM, Soares CA. Analysis of active-passive plate structures using a simple and efficient finite element model. Mechanics of Advanced Materials and Structures 2011;18(2):159-169.

Moita JS, Araújo AL, Soares CM, Soares CA. Vibration analysis of functionally graded material sandwich structures with passive damping. Composite Structures 2018;183:407-15.

Moreira RA, Rodrigues JD, Ferreira AJ. A generalized layerwise finite element for multi-layer damping treatments. Computational Mechanics 2006;37(5):426-44.

Nakra BC. Structural dynamic modification using additive damping. Sadhana 2000;25(3):277-89.

Nakra BC. Vibration control in machines and structures using viscoelastic damping. Journal of Sound and Vibration 1998;211(3):449-66.

Nakra BC. Vibration control with viscoelastic materials-III. The Shock and Vibration Digest. A Publication of the Shock and Vibration Information Center, Naval Research Laboratory 1984;16(5):17-22.

Narayanan S, Verma JP, Mallik AK. Free vibration of thin-walled open section beams with unconstrained damping treatment. Journal of Applied Mechanics 1981; 48(1):169-173.

Nashif AD, Jones DI, Henderson JP. Vibration damping. John Wiley & Sons; 1985.

Nayfeh AH, Mook DT. Nonlinear oscillations. John Wiley & Sons; 2008.

Ni Q, Xiang Y, Huang Y, Lu J. Modeling and dynamics analysis of shells of revolution by partially active constrained layer damping treatment. Acta Mechanica Solida Sinica 2013;26(5):468-79.

Nikoei S, Hassani B. Study of the effects of shear piezoelectric actuators on the

performance of laminated composite shells by an isogeometric approach. Journal of Sandwich Structures & Materials 2020:1099636220942911.

Nokes DS, Nelson FC. Constrained layer damping with partial coverage. Shock and Vibration Bulletin 1968;38(3):5-12.

Oberst H, Frankenfeld K. Damping of the bending vibrations of thin laminated metal beams connected through adherent layer. Acustica 1952;2:181-94.

Ojha RK, Dwivedy SK. Dynamic analysis of sandwich plates with isotropic skins and viscoelastic core. International Journal of Structural Stability and Dynamics 2019;19(03):1950033.

Ojha RK, Dwivedy SK. Parametric instability analysis of sandwich plates with composite skins and LPRE based viscoelastic core. Journal of Sandwich Structures & Materials 2020:1099636220942472.

Okazaki A, Tatemichi A, Mirza S. Damping properties of two-layered cylindrical shells with an unconstrained viscoelastic layer. Journal of Sound and Vibration 1994;176(2):145-61.

Paidoussis MP. Fluid-structure interactions: slender structures and axial flow. Academic Press; 1998.

Pal R. New models for effective Young's modulus of particulate composites. Composites Part B: Engineering 2005;36(6-7):513-23.

Pan HH. Axisymmetrical vibrations of a circular sandwich shell with a viscoelastic core layer. Journal of Sound and Vibration 1969;9(2):338-48.

Panda S and Dubey MK. A balanced laminate of piezoelectric fiber composite for improved shear piezoelectric actuation of beams. Mechanics of Advanced Materials and Structures 2020;27(15):1291-1303.

Pandit MK, Singh BN, Sheikh AH. Buckling of laminated sandwich plates with soft core based on an improved higher order zigzag theory. Thin-Walled Structures 2008;46(11):1183-91.

Park CH, Baz A. Comparison between finite element formulations of active constrained layer damping using classical and layer-wise laminate theory. Finite Elements in Analysis and Design 2001;37(1):35-56.

Park CH, Baz A. Vibration control of bending modes of plates using active constrained layer damping. Journal of Sound and vibration 1999;227(4):711-734.

Parthasarathy G, Reddy CV, Ganesan N. Partial coverage of rectangular plates by unconstrained layer damping treatments. Journal of Sound and Vibration 1985;102(2):203-16.

Patel BP, Ganapathi M, Prasad KR, Balamurugan V. Dynamic instability of layered anisotropic composite plates on elastic foundations. Engineering Structures 1999;21(11):988-95.

Patel BP, Ganapathi M. Non-linear torsional vibration and damping analysis of sandwich beams. Journal of Sound and Vibration 2001;240(2):385-93.

Phan-Dao HH, Thai CH, Lee J, Nguyen-Xuan H. Analysis of laminated composite and sandwich plate structures using generalized layerwise HSDT and improved meshfree radial point interpolation method. Aerospace Science and

Technology 2016;58:641-60.

Plattenburg J, Dreyer JT, Singh R. Active and passive damping patches on a thin rectangular plate: a refined analytical model with experimental validation. Journal of Sound and Vibration 2015;353:75-95.

Plunkett R, Lee CT. Length optimization for constrained viscoelastic layer damping. The Journal of the Acoustical Society of America 1970;48(1B):150-61.

Popov EP. Engineering mechanics of solids. Prentice Hall; 1990.

Porfiri M, Gupta N. Effect of volume fraction and wall thickness on the elastic properties of hollow particle filled composites. Composites Part B: Engineering 2009;40(2):166-73.

Pradhan M, Dash PR, Pradhan PK. Static and dynamic stability analysis of an asymmetric sandwich beam resting on a variable Pasternak foundation subjected to thermal gradient. Meccanica 2016;51(3):725-39.

Pradyumna S, Bandyopadhyay JN. Dynamic instability behavior of laminated hypar and conoid shells using a higher-order shear deformation theory. Thin-Walled Structures 2011;49(1):77-84.

Pradyumna S, Gupta A. Dynamic stability of laminated composite plates with piezoelectric layers subjected to periodic in-plane load. International Journal of Structural Stability and Dynamics 2011;11(02):297-311.

Raja S, Sreedeep R, Prathap G. Bending behavior of hybrid-actuated piezoelectric sandwich beams. Journal of Intelligent Material Systems and Structures 2004;15(8):611-9.

Rajoria H, Jalili N. Passive vibration damping enhancement using carbon nanotube-epoxy reinforced composites. Composites Science and Technology 2005;65(14):2079-93.

Ramesh TC, Ganesan N. Finite element analysis of cylindrical shells with a constrained viscoelastic layer. Journal of Sound and Vibration 1994;172(3):359-70.

Ramesh TC, Ganesan N. Vibration and damping analysis of cylindrical shells with constrained damping treatment-A comparison of three theories. Journal of Vibration and Acoustics 1995;117:213.

Rao MD, He S. Dynamic analysis and design of laminated composite beams with multiple damping layers. AIAA Journal 1993;31(4):736-45.

Rao MD. Recent applications of viscoelastic damping for noise control in automobiles and commercial airplanes. Journal of Sound and Vibration 2003;262(3):457-74.

Ravi SS, Kundra TK, Nakra BC. Reanalysis of plates modified by free damping layer treatment. Computers & Structures 1996;58(3):535-41.

Ray K, Kar RC. Parametric instability of a sandwich beam under various boundary conditions. Computers & Structures 1995;55(5):857-70.

Ray K, Kar RC. Parametric instability of multi-layered sandwich beams. Journal of Sound and Vibration 1996;193(3):631-44.

Ray MC, Baz A. Optimization of energy dissipation of active constrained layer

damping treatments of plates. Journal of Sound and Vibration 1997;208(3):391-406.

Ray MC, Oh J, Baz A. Active constrained layer damping of thin cylindrical shells. Journal of Sound and Vibration 2001;240(5):921-935.

Reddy CV. Some studies on the effect of damping treatment on the vibration and noise attenuation in structures. Ph.D. Thesis, IIT Madras; 1979.

Reddy JN. Mechanics of laminated composite plates and shells: theory and analysis. CRC Press; 2003.

Ren S, Zhao G, Zhang S. A layerwise finite element formulation for vibration and damping analysis of sandwich plate with moderately thick viscoelastic core. Mechanics of Advanced Materials and Structures 2020;27(14):1201-12.

Rogers LC, Parin M. Experimental results for stand-off passive vibration damping treatment. Smart Structures and Materials 1995: Passive Damping 1995; vol. 2445, pp. 374-383. International Society for Optics and Photonics.

Ross D, Ungar EE, Kerwin EM. Structural damping. Journal of the American Society of Mechanical Engineers 1959;42(7):272-279.

Roy PK, Ganesan N. Dynamic studies on beams with unconstrained layer damping treatment. Journal of Sound and Vibration 1996;195(3):417-27.

Roy PK, Ganesan N. Dynamic studies on plates with unconstrained layer treatment. Computers & Structures 1993;49(3):473-80.

Sabu T, Ranimol S. Rubber nanocomposites: preparation, properties, and applications. John Wiley& Sons; 2010.

Sadd MH. Elasticity: theory, applications, and numerics. Academic Press; 2009.

Sahu NK, Biswal DK, Joseph SV, Mohanty SC. Vibration and damping analysis of doubly curved viscoelastic-FGM sandwich shell structures using FOSDT. Structures 2020;26:24-38.

Saito H, Otomi K. Parametric response of viscoelastically supported beams. Journal of Sound and Vibration 1979;3(2):169-78.

Şakar G, Sabuncu M. Buckling and dynamic stability of a rotating pretwisted asymmetric cross-section blade subjected to an axial periodic force. Finite Elements in Analysis and Design 2004;40(11):1399-415.

Sankar A, Natarajan S, Ganapathi M. Dynamic instability analysis of sandwich plates with CNT reinforced facesheets. Composite Structures 2016;146:187-200.

Saravanan C, Ganesan N, Ramamurti V. Semianalytical finite element analysis of active constrained layer damping in cylindrical shells of revolution. Computers & Structures 2001;79(11):1131-1145.

Seubert SL, Anderson TJ, Smelser RE. Passive damping of spinning disks. Journal of Vibration and Control 2000;6(5):715-25.

Shi J, Song Q, Liu Z, Wan Y. Formulating a numerically low-cost method of a constrained layer damper for vibration suppression in thin-walled component milling and experimental validation. International Journal of Mechanical Sciences 2017;128:294-311.

Shi Y, Hua H, Sol H. The finite element analysis and experimental study of beams with active constrained layer damping treatments. Journal of Sound and Vibration 2004;278(1):343-363.

Shih YS, Yeh ZF. Dynamic stability of a viscoelastic beam with frequency-dependent modulus. International Journal of Solids and Structures 2005;42(7):2145-59.

Shin YS, Maurer GJ. Vibration response of constrained viscoelastically damped plates: Analysis and experiments. Finite Elements in Analysis and Design 1991;7(4):291-7.

Sisemore CL, Darvennes CM. Transverse vibration of elastic-viscoelastic-elastic sandwich beams: compression-experimental and analytical study. Journal of Sound and Vibration 2002;252(1):155-67.

Stevens KK, Evan-Iwanowski RM. Parametric resonance of viscoelastic columns. International Journal of Solids and Structures 1969;5(7):755-65.

Sun CT, Sankar BV, Rao VS. Damping and vibration control of unidirectional composite laminates using add-on viscoelastic materials. Journal of Sound and Vibration 1990;139(2):277-87.

Sun CT, Zhang XD. Use of thickness-shear mode in adaptive sandwich structures. Smart Materials and Structures 1995;4(3):202.

Sun D, Tong L. A compressional-shear model for vibration control of beams with active constrained layer damping. International Journal of Mechanical Sciences 2004;46(9):1307-1325.

Sun D, Tong L. Modelling and vibration control of beams with partially debonded active constrained layer damping patch. Journal of Sound and Vibration 2002;252(3):493-507.

Sun J, Kari L. Coating methods to increase material damping of compressor blades: Measurements and modeling. Turbo Expo: Power for Land, Sea, and Air 2010; vol. 44014, pp. 1157-1165.

Sun W, Yan X, Gao F. Analysis of frequency-domain vibration response of thin plate attached with viscoelastic free layer damping. Mechanics Based Design of Structures and Machines 2018;46(2):209-24.

Suzuki K, Kageyama K, Kimpara I, Hotta S, Ozawa T, Kabashima S, Ozaki T. Vibration and damping prediction of laminates with constrained viscoelastic layers--numerical analysis by a multilayer higher-order-deformable finite element and experimental observations. Mechanics of Advanced Materials and Structures 2003;10(1):43-75.

Swallow W. An improved method of damping panel vibrations. British Patent Specification 1939;513:171.

Sylwan O. Shear and compressional damping effects of constrained layered beams. Journal of Sound and Vibration 1987;118(1):35-45.

Thakkar D, Ganguli R. Dynamic response of rotating beams with piezoceramic actuation. Journal of Sound and Vibration 2004a;270(4-5):729-53.

Thakkar D, Ganguli R. Helicopter vibration reduction in forward flight with induced-shear based piezoceramic actuation. Smart Materials and Structures 2004b;13(3):599.

Thomson WT. Theory of vibration with applications. CRC Press; 1993.

Tian S, Xu Z, Wu Q, Qin C. Dimensionless analysis of segmented constrained layer damping treatments with modal strain energy method. Shock and Vibration 2016;2016: 8969062

Tomlinson GR. Overview of active/passive damping techniques employing viscoelastic materials. 3rd International Conference on Intelligent Materials and 3rd European Conference on Smart Structures and Materials 1996; vol. 2779, pp. 656-669. International Society for Optics and Photonics.

Tomlinson GR. The use of constrained layer damping in vibration control. International Journal of Mechanical Sciences 1990;32(3):233-42.

Tornabene F, Brischetto S, Fantuzzi N, Viola E. Numerical and exact models for free vibration analysis of cylindrical and spherical shell panels. Composites Part B: Engineering 2015;81:231-50.

Torvik PJ, Strickland DZ. Damping additions for plates using constrained viscoelastic layers. The Journal of the Acoustical Society of America 1972;51(3B):985-91.

Trindade MA, Benjeddou A, Ohayon R. Finite element modelling of hybrid active–passive vibration damping of multilayer piezoelectric sandwich beams-part I: Formulation. International Journal for Numerical Methods in Engineering 2001;51(7):835-854.

Trindade MA, Benjeddou A. Parametric analysis of effective material properties of thickness-shear piezoelectric macro-fibre composites. Journal of the Brazilian Society of Mechanical Sciences and Engineering 2012;34:352-61.

Trindade MA, Benjeddou A. Refined sandwich model for the vibration of beams with embedded shear piezoelectric actuators and sensors. Computers & Structures 2008;86(9):859-69.

Trindade MA, Maio CE. Multimodal passive vibration control of sandwich beams with shunted shear piezoelectric materials. Smart Materials and Structures 2008;17(5):055015.

Trindade MA. Experimental analysis of active-passive vibration control using viscoelastic materials and extension and shear piezoelectric actuators. Journal of Vibration and Control 2011;17(6):917-29.

Trindade MA. Simultaneous extension and shear piezoelectric actuation for active vibration control of sandwich beams. Journal of Intelligent Material Systems and Structures 2007;18(6):591-600.

Trompette P, Fatemi J. Damping of beams. Optimal distribution of cuts in the viscoelastic constrained layer. Structural Optimization 1997;13(2):167-71.

Tzou HS, Lee HJ, Arnold SM. Smart materials, precision sensors/actuators, smart structures, and structronic systems. Mechanics of Advanced Materials and Structures 2004;11(4-5):367-93.

Ungar EE, Kerwin Jr EM. Plate damping due to thickness deformations in attached viscoelastic layers. The Journal of the Acoustical Society of America 1964;36(2):386-92.

Van Nostrand WC, Knowles GJ, Inman DJ. Finite element model for active constrained-layer damping. Smart Structures and Materials 1994: Passive

Damping 1994; vol. 2193, pp. 126-137. International Society for Optics and Photonics.

Vasiliev VV, Barynin VA, Razin AF. Anisogrid composite lattice structures-Development and aerospace applications. Composite Structure 2012;94(3):1117-27.

Vasques CM, Mace BR, Gardonio P, Rodrigues JD. Arbitrary active constrained layer damping treatments on beams: Finite element modelling and experimental validation. Computers & Structures 2006;84(22):1384-1401.

Vaz MA, Rizzo NA. A finite element model for flexible pipe armor wire instability. Marine Structures 2011;24(3):275-91.

Veermani S, Wereley NM. Modeling and experimental validation of a sandwich plate with isotropic face plates and viscoelestic core. Smart Structures and Materials 1997: Passive Damping and Isolation 1997; vol. 3045, pp. 329-339. International Society for Optics and Photonics.

Veley DE, Rao SS. A comparison of active, passive and hybrid damping in structural design. Smart Materials and Structures 1996;5(5):660.

Walpole LJ. The elastic behaviour of a suspension of spherical particles. The Quarterly Journal of Mechanics and Applied Mathematics 1972;25(2):153-60.

Wang S, Zhang J, Li Q, Su J, Liang S. Free vibration of co-cured composite structures with different numbers of viscoelastic damping membranes. Composite Structures 2020;247:112434.

Whittier JS. The effect of configurational additions using viscoelastic interfaces on the damping of a cantilever beam. Wright Air Development Command, US Air Force; 1959.

Wilson CJ, Carnevali P, Morris RB, Tsuji Y. Viscoelastic damping calculations using a p-type finite element code. Journal of Applied Mechanics 1992;59(3):696-699.

Xiang Y, Huang YY, Lu J, Yuan LY, Zou SZ. New matrix method for analyzing vibration and damping effect of sandwich circular cylindrical shell with viscoelastic core. Applied Mathematics and Mechanics 2008;29(12):1587-600.

Xie Z, Shepard Jr WS. An enhanced beam model for constrained layer damping and a parameter study of damping contribution. Journal of Sound and Vibration 2009;319(3-5):1271-84.

Xu Z, Li H, Wang WY, Wen BC. The analysis of vibration characteristics of fiber metal laminated thin plate with partial constrained layer damping patches treatment. Meccanica 2020;55(1):227-43.

Yang C, Jin G, Liu Z, Wang X, Miao X. Vibration and damping analysis of thick sandwich cylindrical shells with a viscoelastic core under arbitrary boundary conditions. International Journal of Mechanical Sciences 2015;92:162-77.

Yeh JY, Chen LW, Wang CC. Dynamic stability of a sandwich beam with a constrained layer and electrorheological fluid core. Composite Structures 2004;64(1):47-54.

Yeh ZF, Shih YS. Dynamic stability of a sandwich beam with magnetorheological

Core. Mechanics based Design of Structures and Machines 2006;34(2):181-200.

Yellin JM, Shen IY. A self-sensing active constrained layer damping treatment for a Euler-Bernoulli beam. Smart Materials and Structures 1996;5(5):628.

Yildiz A, Stevens K. Optimum thickness distribution of unconstrained viscoelastic damping layer treatments for plates. Journal of Sound and Vibration 1985;103(2):183-99.

Yin TP, Kelly TJ, Barry JE. A quantitative evaluation of constrained-layer damping. Journal of Engineering for Industry 1967;89(4):773-782.

Young TH, Shiau TN, Kuo ZH. Dynamic stability of rotor-bearing systems subjected to random axial forces. Journal of Sound and Vibration 2007;305(3):467-80.

Yu YY. Viscoelastic damping of vibrations of sandwich plates and shells. Polytechnic Institute of Brooklyn New York; 1963.

Yuan L, Xiang Y, Huang Y, Lu J. A semi-analytical method and the circumferential dominant modal control of circular cylindrical shells with active constrained layer damping treatment. Smart Materials and Structures 2010;19(2):025010

Zarraga O, Sarría I, García-Barruetabeña J, Cortés F. Dynamic analysis of plates with thick unconstrained layer damping. Engineering Structures 2019;201:109809.

Zener CM. Elasticity and anelasticity of metals. University of Chicago Press; 1948.

Zhai Y, Su J, Liang S. Damping properties analysis of composite sandwich doubly-curved shells. Composites Part B: Engineering 2019;161:252-62.

Zhai Y, Wang S, Liang S. Structural optimization of composite beams with multilayered viscoelastic cores. Mechanics of Advanced Materials and Structures 2020;27(2):119-27.

Zhang SH, Chen HL. A study on the damping characteristics of laminated composites with integral viscoelastic layers. Composite Structures 2006;74(1):63-9.

Zhang Y, Jin G, Chen M, Ye T, Yang C, Yin Y. Free vibration and damping analysis of porous functionally graded sandwich plates with a viscoelastic core. Composite Structures 2020;244:112298.

Zhang Y, Lu TF, Al-Sarawi S. Formulation of a simple distributed-parameter model of multilayer piezoelectric actuators. Journal of Intelligent Material Systems and Structures 2016;27(11):1485-91.

Zhao J, Wong PK, Ma X, Xie Z, Xu J, Cristino VA. Simplification of finite element modeling for plates structures with constrained layer damping by using single-layer equivalent material properties. Composites Part B: Engineering 2019;157:283-8.

Zheng H, Cai C, Pau GS, Liu GR. Minimizing vibration response of cylindrical shells through layout optimization of passive constrained layer damping treatments. Journal of Sound and Vibration 2005;279(3):739-756.

Zheng H, Pau GS, Wang YY. A comparative study on optimization of constrained

layer damping treatment for structural vibration control. Thin-Walled Structures 2006; 44(8):886-896.

Zheng L, Qiu Q, Wan H, Zhang D. Damping analysis of multilayer passive constrained layer damping on cylindrical shell using transfer function method. Journal of Vibration and Acoustics 2014;136(3).

Zheng L, Zhang D, Wang Y. Vibration and damping characteristics of cylindrical shells with active constrained layer damping treatments. Smart Materials and Structures 2011;20(2):025008.

List of Publications

The work presented in this thesis has led to the following publications:

1. Gupta A, Panda S, Reddy RS. Improved damping in sandwich beams through the inclusion of dispersed graphite particles within the viscoelastic core. Composite Structures 2020; 247:112424.

2. Gupta A, Panda S, Reddy RS. An actively constrained viscoelastic layer with the inclusion of dispersed graphite particles for control of plate vibration. Journal of Vibration and Control 2020:1077546320956533.

3. Gupta A, Panda S. Hybrid damping treatment of a layered beam using a particle-filled viscoelastic composite layer. Composite Structures 2021:113623.

4. Gupta A, Panda S, Reddy RS. Shear actuation-based hybrid damping treatment of sandwich structures using a graphite particle-filled viscoelastic layer. Journal of Intelligent Material Systems and Structures 2021:1045389X211002649.

5. Gupta A, Panda S, Reddy RS. Passive control of parametric instability of layered beams using graphite particle-filled viscoelastic damping layers. Mechanics of Advanced Materials and Structures 2021:1-6.

6. Gupta A, Panda S, Reddy RS. A comparative study on the damping capabilities of different viscoelastic composites in active/passive control of structural vibration. (Manuscript under preparation).